

University of Southampton Research Repository

Copyright © and Moral Rights for this thesis and, where applicable, any accompanying data are retained by the author and/or other copyright owners. A copy can be downloaded for personal non-commercial research or study, without prior permission or charge. This thesis and the accompanying data cannot be reproduced or quoted extensively from without first obtaining permission in writing from the copyright holder/s. The content of the thesis and accompanying research data (where applicable) must not be changed in any way or sold commercially in any format or medium without the formal permission of the copyright holder/s.

When referring to this thesis and any accompanying data, full bibliographic details must be given, e.g.

Thesis: Author (Year of Submission) "Full thesis title", University of Southampton, name of the University Faculty or School or Department, PhD Thesis, pagination.

Data: Author (Year) Title. URI [dataset]

UNIVERSITY OF SOUTHAMPTON

FACULTY OF MEDICINE

Academic Unit of Human Development and Health

**Spontaneous 3D Micropatterning of BMP-2 in Self-
assembling Nanoclay Gels**

by

Roxanna Sharon Ramnarine Sanchez

Thesis for the degree of Doctor of Philosophy

October 2019

UNIVERSITY OF SOUTHAMPTON

ABSTRACT

FACULTY OF MEDICINE

Human Development and Health

Thesis for the degree of Doctor of Philosophy

Spontaneous 3D Micropatterning of BMP-2 in Self-assembling Nanoclay Gels

Roxanna Sharon Ramnarine Sánchez

Limitations of current clinical treatments for critical size bone defects have motivated the development of new strategies for bone tissue engineering. In this regard, emulating the three dimensional (3D) hierarchical organisation of biochemical cues found in the native cellular microenvironment is likely to be key to generate anisotropic biomaterials with distinct levels of functionality. However, despite advances in tissue engineering (TE), achieving stable structures incorporating 3D micropatterning of biochemical cues, particularly that preserve resolution with an increase in size has proven challenging. Self-assembling nanoclay-gels have established potential in TE due to their capacity to sequester proteins for sustained localised bioactivity. This thesis explores the hypothesis that bottom-up self-assembly of nanoclay/protein structures can be harnessed to achieve a gradient of proteins, allowing the delivery of localised spatio-temporal niches for enhanced bone tissue regeneration. Addition of nanoclay-gels into high concentration protein solutions promoted self-assembly of a structure with 3D micropatterning of proteins. Polarised light and scanning electron microscopy confirmed that a reaction-diffusion process was responsible for the scaffold assembly, where the proteins (or gelator) reacted with the clay nanoparticles and simultaneously diffused through the clay-gel in a concentration-dependent manner. The process led to the formation of a protein-clay complex structure with a periodical arrangement. Furthermore, confocal images demonstrated that the diffusion front or the interface between the reacted and unreacted clay-gel region was responsible for the 3D localisation of loaded proteins. By changing the assembly parameters, such as concentration, ionic strength, incubation time and temperature. Also, the solute size and net charge it was possible to control the diffusion coefficient of the assembly solution, and as a result, the localisation of proteins loaded. Tuning of the assembly and loading process allowed the generation of scaffolds with punctuated or gradual gradients of different proteins. Also, the versatility of the system supported the assembly of structures at scale with a range of dimensions (0.2 to 1 mm) and shapes (droplets, cylinders and strings) while preserving the resolution of protein patterning. Finally, a subcutaneous mouse model revealed that the punctuated localisation of BMP-2 inside the scaffold had the potential to control the spatio-temporal formation of mature bone. Thus, this novel system provides the opportunity to design customised scaffolds with complex biochemical gradients, dimensions and shapes for bone with clinical relevance.

Contents

Contents	i
List of Tables.....	iv
List of Figures	v
Declaration of Authorship.....	x
Contributors	xii
Acknowledgements	xiii
Abbreviations	xiv
Chapter 1 INTRODUCTION.....	1
<i>Overview</i>	2
1.1 Bone tissue engineering and regenerative medicine (TERM).....	2
1.1.1 Current state of the art in biomaterials and nanotechnology for tissue engineering.....	7
1.2 Fundamental of bone biology	11
1.2.1 Bone structure, composition and functionality	11
1.2.2 Bone development	19
1.2.3 Fracture healing	20
1.3 BMP at bone development and regeneration.....	22
1.3.1 BMP gradients	24
1.3.2 Therapeutic application of BMP.....	30
1.3.3 Current state of the art in biomaterials and nanotechnology to deliver BMP and other growth factors	32
1.4 Clay-gel nanoparticles as a therapeutic delivery system.....	40
1.4.1 Clay nanoparticles.....	40
1.4.2 Opportunities of clay-gel nanoparticles for TERM.....	49
Hypothesis and Aims	55
Chapter 2 METHODOLOGY	56
2.1 Materials and Methods	57
2.1.1 Laponite® gel or clay-gel preparation.....	57
2.1.2 Clay-gel droplet assembly	57
2.1.3 Nanoclay/protein scaffold.....	58
2.1.4 Structural characterisation of the nanoclay/protein scaffold	59
2.1.5 Statistical analysis.....	62
Chapter 3 FABRICATION OF NANOCLAY/PROTEIN SCAFFOLDS.....	63

3.1 Introduction	64
3.2 Materials and Methods	73
3.3 Results	76
3.3.1 Initial attempts at stratified nanoclay/protein scaffolds	76
3.3.2. Formation of fluorescent-layered structures	81
3.4 Discussion	94
3.5 Conclusions	105
Chapter 4 OPTIMISATION OF FABRICATION PARAMETERS	106
4.1 Introduction	107
4.2 Materials and Methods	109
4.3 Results	111
4.3.1 Effect of assembly variables on nanoclay/protein scaffold structure	111
4.3.1.1 Protein concentration of the assembly solution	111
4.3.1.2 Presence of ions in the assembly solution.....	114
4.3.1.3 Assembly time.....	118
4.3.1.4 Assembly temperature.....	120
4.3.1.5 Assembly with different types of proteins	122
4.3.2 Effect of loading variables on the nanoclay/protein scaffold structure ...	127
4.3.2.1 Protein absorbed as a function of time	127
4.3.2.2 Effect of temperature.....	129
4.3.2.3 Loading globular proteins	130
4.3.3 Effect of storage variables on the nanoclay/protein scaffold structure....	134
4.3.3.1 Effect of the storage solution	134
4.3.3.2 Effect of storage temperature	136
4.3.3.3 Stability as a function of time	138
4.4 Discussion	139
4.5 Conclusions	154
Chapter 5 CHARACTERISATION OF THE ARCHITECTURE AND THE ASSEMBLY MECHANISM OF THE NANOCCLAY/PROTEIN SCAFFOLD	155
5.1 Introduction	156
5.2 Materials and Methods	163
5.2.1 Scaffold assembly	163
5.2.2 Characterisation techniques	163
5.3 Results	167
5.3.1 Assembly mechanism of the nanoclay/protein scaffold	167

5.3.2 Characterisation of the nanoclay/protein scaffold nano to macroarchitecture.....	169
5.3.2.1 Scanning Electron Microscopy	169
5.3.2.2 Polarised Light Microscopy	171
5.3.2.3 Transmission Electron Microscopy.....	177
5.3.2.4 Maximum adsorption capacity of the clay-gel droplet	179
5.4 Discussion	181
5.5 Conclusions	192
Chapter 6 EXPLORING THE VERSATILITY AND FUNCTIONALITY OF THE NANOCCLAY/PROTEIN SCAFFOLDS.....	193
6.1 Introduction	194
6.2 Materials and Methods	197
6.2.1 Assembly of nanoclay/protein scaffolds.....	197
6.2.2 Biological activity assessment of nanoclay/protein scaffolds	200
6.3 Results	205
6.3.1 Assembly of nanoclay/protein scaffolds with multiple protein patterns .	205
6.3.2 Scalable and mouldable clay-gels.....	209
6.3.3 Functionalization of clay-gel prior to assembly	211
6.3.4 Biological activity of nanoclay/protein scaffolds	212
6.4 Discussion	218
6.5 Conclusions	222
Chapter 7 DISCUSSION AND FUTURE DIRECTIONS FOR RESEARCH.....	224
7.1 Discussion	225
7.1.1 Achievements of this study.....	225
7.1.2 A discussion of main findings and their context.....	228
7.1.3 Limitations of the study and indications for future research	229
7.2 Concluding remarks	232
<i>Appendix</i>	233
<i>References</i>	238

List of Tables

Table 2.1 General Leica TCS SP5 CLSM hardware settings.....	60
Table 2.2 General Carl Zeiss AxioVert 200 Inverted Fluorescence Microscope hardware settings.....	61
Table 2.3 Format of p-value according to GraphPad.....	62
Table 3.1 Protocol to make a nanoclay/protein LBL polyelectrolyte.....	74
Table 3.2 Upgraded protocol to make a Laponite®/protein LBL polyelectrolyte.....	75
Table 3.3 Constituents of serum.....	90
Table 5.1 General Polarised Light Microscope (80i, Nikon) settings.....	165
Table 6.1 Experimental setup to assembled nanoclay/protein scaffolds with multiple punctuate gradient of proteins.....	197
Table 6.2 Experimental setup to assembled nanoclay/protein scaffolds of different size and shape.....	200
Table 6. 3 BMP-2 Infuse™ standards dilutions.....	201

List of Figures

Figure 1.1 Tissue engineering at different levels.....	7
Figure 1.2 Illustration of hierarchical biology concept framework.....	9
Figure 1.3 The 7 hierarchical levels of organisation of the mature bone.....	15
Figure 1.4 Functionality of the bone at each hierarchical level.....	18
Figure 1.5 BMP-2 structure.....	23
Figure 1.6 Dorsal-Ventral patterning of the neural tube	24
Figure 1.7 BMP reporter activity during the mid-gestation stage of a mouse embryo.....	26
Figure 1.8 Spatio-temporal restricted patterns of BMP expression during bone healing.....	27
Figure 1.9 Morphogen transport models illustrations.....	29
Figure 1.10. Top-down and bottom-up techniques used to the assembly of hydrogels with 3D patterns of macromolecules.....	39
Figure 1.11 The structure of smectites.....	42
Figure 1.12 Double layer model.....	43
Figure 1.13 Zeta potential of colloidal dispersions.....	44
Figure 1.14 Behaviour of colloidal solutions with changes in pH and addition polymers or surfactants.....	45
Figure 1.15 Metastable state of colloidal clays.....	47
Figure 1.16 Phase diagram of Laponite® clay nanoparticles colloidal suspensions as a function of clay nanoparticles concentration (weight/weight %) and salts (Molar).....	48
Figure 1.17 Sorptive capacity of clay nanoparticles.....	50
Figure 1.18 Self-assembly of Laponite® suspensions via thixotropy and in response to an ionic medium.....	52
Figure 1.19. Osteogenic differentiation promoted by clay nanoparticles.....	54
Figure 2.1 General protocol to make nanoclay/protein scaffolds.....	59
Figure 2.2 LAS X software measurements.....	60
Figure 3.1. Morphogen gradient formation by diffusion.....	64
Figure 3.2 Schematic illustration of BMP-2 delivery approaches.....	66
Figure 3.3 Nanoclay/protein LBL polyelectrolyte self-assembly.....	77

Figure 3.4 Nanoclay/protein LBL polyelectrolyte stabilisation.....	78
Figure 3.5 Nanoclay/protein scaffold structure conceptual vs actual results....	79
Figure 3.6 Nanoclay/protein scaffold dimensions.....	80
Figure 3.7 Nanoclay/protein scaffold self-assembly, fluorophores deposition vs diffusion.....	82
Figure 3.8 Fluorescent-layered structure formation.....	84
Figure 3.9 Preferential localisation of fluorophores within the nanoclay/protein scaffold.....	85
Figure 3.10 Tissue culture solutions and clay-gel droplet interaction.....	87
Figure 3.11 Clay-gel droplets assembled in DMEM FCS.....	88
Figure 3.12 Diffusion of FITC BSA facilitated by FCS.....	89
Figure 3.13 Protocol to self-assemble nanoclay/protein scaffolds with different serum.....	91
Figure 3.14 Assembly of clay-gel droplets in different FCS components.....	93
Figure 3.15 Hydrogel generic filtering principles.....	96
Figure 3.16 Diffusion process of FCS and FITC BSA molecules in the clay- gel.....	97
Figure 3.17 Natural and synthetic patterned structures.....	98
Figure 3.18 Reaction-diffusion models through physical gels matrix.....	99
Figure 3.19 Reaction-diffusion gelation of physical gels by “one mobile and one static phase” model.....	101
Figure. 3.20 Diffusion-reaction mechanism to assemble 3D micropatterned structures.....	103
Figure 4.1 3D micropatterned clay-gel assembly hypothesis.....	107
Figure 4.2 Fabrication of nanoclay/protein scaffolds steps.....	109
Figure 4.3 Assembly of nanoclay/protein scaffold as a function of protein concentration.....	112
Figure 4.4 Linear dimensions of nanoclay/protein scaffold assembled as a function of BSA concentration.....	113
Figure 4.5 Effect of ions in the assembly of nanoclay/protein scaffold, experiment setup	114
Figure 4.6 Effect of ions in the assembly of nanoclay/protein scaffold.....	115

Figure 4.7 Effect of ions in the linear dimensions of nanoclay/protein scaffold.....	117
Figure 4.8 Assembly of nanoclay/protein scaffolds as a function of time.....	119
Figure 4.9 Assembly of nanoclay/protein scaffolds as a function of time and concentration of the assembly solution.....	120
Figure 4.10 Effect of temperature on the scaffold assembly.....	121
Figure 4.11 Assembly of the nanoclay/protein scaffold with fibril protein vs globular protein.....	123
Figure 4.12 Assembly of the nanoclay/protein scaffold with different globular proteins.....	125
Figure 4.13 Effect of assembly and loading protein interaction in the fluorescent pattern distribution.....	126
Figure 4.14 Maximum loading capacity of the nanoclay/protein scaffold.....	128
Figure 4.15 Effect of loading temperature on the fluorescent pattern distribution.....	130
Figure 4.16 Loading different globular proteins into the nanoclay/protein scaffold.....	131
Figure 4.17 Diffusion and localisation of proteins loaded governed by electrostatic interactions.....	133
Figure 4.18 Effect of the solvent storage in the nanoclay/protein scaffold.....	135
Figure 4.19 Effect of the storage solvent in the nanoclay/protein scaffold.....	137
Figure 4.20 Effect of the storage time in the nanoclay/protein scaffold.....	138
Figure 4.21 Diffusion of charged macromolecules through a charged diffusive media.....	146
Figure 4.22 Secondary diffusion and localisation of macromolecules governed by clay/protein interaction.....	147
Figure 4.23 Surface patch binding of human serum albumin with Laponite® clay nanoparticles.....	149
Figure 4.24 Secondary diffusion and localisation of macromolecules governed by protein-clay complex/protein interaction.....	151
Figure 5.1 The reaction-diffusion fronts with one static and one diffusion reactant.....	156
Figure 5.2 Assembly of physical gels by ionotropic gelation.....	157

Figure 5.3 Physical gels set by a reaction-diffusion process.....	158
Figure 5.4 SEM characterisation of physical gels cross-linked by diffusion-reaction.....	159
Figure 5.5 Polymer distribution of physical gels assembled by reaction-diffusion characterised by SEM.....	160
Figure 5.6 TEM imaging analysis of physical gels assembled by reaction-diffusion.....	161
Figure 5.7 Homemade well plate fabricated to analyse the assembled scaffolds under polarised light microscopy.....	164
Figure 5.8 Polarised light experiment settings.....	166
Figure 5.9 Assembly mechanism of nanoclay/protein scaffold.....	168
Figure 5.10 Scanning electron microscopy of nanoclay/protein scaffolds.....	170
Figure 5.11 Microstructure of clay-gel assembled with BSA.....	171
Figure 5.12 Cross-polarised light images of nanoclay/protein scaffolds.....	172
Figure 5.13 Optical analysis of 2D nanoclay/protein scaffolds anisotropic structure.....	173
Figure 5.14 Optical analysis of 2.8 % clay-gel anisotropic structure.....	173
Figure 5.15 Crossed polarising images of clay dispersions presented as a function of autoclave treatment and concentration.....	175
Figure 5.16 Crossed polarising images of 2.8% clay-gel.....	175
Figure 5.17 Crossed polarising images of clay dispersions after one month of storage.....	176
Figure 5.18 Optical analysis of 3D nanoclay/protein scaffolds assembled with different clay-gel concentrations.....	177
Figure 5.19 Transmission electron microscopy of nanoclay/protein scaffolds.	178
Figure 5.20 Maximum adsorption capacity of the clay-gel droplet.....	180
Figure 5.21 Mechanism of external gelation for bead formation.....	186
Figure 5.22 Estimated adsorbed protein per clay nanoparticles.....	188
Figure 5.23 Density of proteins per clay-nanoparticles 3D models.....	189
Figure 5.24 Hierarchical levels of organisation of the nanoclay/protein scaffold.....	191
Figure 6.1 Signalling patterning during development.....	195

Figure 6.2 Experimental setup to assemble nanoclay/protein scaffolds with dual gradual protein patterns.....	198
Figure 6.3 Assembly of nanoclay/protein scaffolds with a punctuated concentration of protein gradients.....	206
Figure 6.4 Assembly of nanoclay/protein scaffolds with a punctuated concentration of protein gradients.....	207
Figure 6.5 Assembly of nanoclay/protein scaffolds with a gradual concentration of protein gradients.....	208
Figure 6.6 Assembly of nanoclay/protein scaffolds of different size and shape.....	210
Figure 6.7 Assembly of nanoclay/protein scaffolds with functionalized clay-gel.....	212
Figure 6.8 Optimisation of the scaffolds' fabrication parameters.....	215
Figure 6.9 Biological activity of nanoclay/protein scaffolds.....	217

Declaration of Authorship

Print name: Roxanna Sharon Ramnarine Sanchez

Title of thesis: Spontaneous 3D Micropatterning of BMP-2 in Self-assembling Nanoclay Gels

I declare that this thesis and the work presented in it is my own and has been generated by me as the result of my own original research.

I confirm that:

1. This work was done wholly or mainly while in candidature for a research degree at this University;
2. Where any part of this thesis has previously been submitted for a degree or any other qualification at this University or any other institution, this has been clearly stated;
3. Where I have consulted the published work of others, this is always clearly attributed;
4. Where I have quoted from the work of others, the source is always given. With the exception of such quotations, this thesis is entirely my own work;
5. I have acknowledged all main sources of help;
6. Where the thesis is based on work done by myself jointly with others, I have made clear exactly what was done by others and what I have contributed myself;
7. Parts of this work have been published as: [please list references below]:

Paper

Shi P, Kim Y, Mouse M, Ramnarine R, Oreffo R, Dawson J. "Self-Assembling Nanoclay Diffusion Gels for Bioactive Osteogenic Microenvironments" Published in: *Advanced Healthcare Materials*, 7(15):1-11, doi: 10.1002/adhm.201800331. I contributed to the experimental design, understanding and writing of the clay-gel self-assembly in tissue culture media.

Abstracts

“Self-Assembling Laponite® Hydrogel Scaffolds with Spontaneous 3D Micropatterning of Bioactive Factors for Bone Tissue Regeneration”; *Tissue Engineering and Regenerative Medicine International Society* 2019, Rhodes, Greece. TERMIS-EU.

“Self-Assembling Laponite® Hydrogel Scaffolds with Spontaneous 3D Micropatterning of Bioactive Factors for Bone Tissue Regeneration”; *Tissue and Cell Engineering Society and UK Society for Biomaterial meeting* 2019, Nottingham, UK TCS UKSB.

Patent

Ramnarine R, Dawson J, Oreffo R and Evans N (filled 2018). Currently at PCT - Case Ref 18458/PCT.

Signature

Date

Contributors

All experiments and data analysis were performed by the author in the Bone and Joint Group laboratory, Academic Unit of Human Development and Health, Faculty of Medicine, Southampton University Hospital, University of Southampton, with the following exceptions:

Section 3.3.1 & 3.3.2

Confocal imaging was performed by Dr. David Johnston, in the Institute of Developmental Sciences, University of Southampton.

Section 4.3.1.3

Dr. Jeroen Van Duijneveldt helped to plot the data acquired, in the School of Chemistry, University of Bristol.

Section 5.4

Illustration of nanoclay protein interaction was modelled by Dr. Jonathan Dawson, in the Institute of Developmental Sciences, University of Southampton.

Section 6.2.4.5

Micro CT imaging and analysis were performed by Dr. Stuart Lanham, in the Biomedical Research Facility and Institute of Developmental Sciences, University of Southampton.

Section 6.2.4.5

Animal surgery was performed by Dr. Janos Kanczler (personal license I8CEF3D50), in the Biomedical Research Facility, University of Southampton.

Acknowledgements

The PhD has been a great life experience that allowed me to improve as a person and a professional.

I want to express my deepest gratitude to the people that have been part of this great journey. I am very thankful to my supervisors, Dr. Jonathan Dawson, Dr. Richard Oreffo and Dr. Nicholas Evans for giving me the opportunity to work on this project and for offering me all their support. Very special thanks to Dr. Jonathan Dawson, who guided and helped me to become a researcher. I will always be grateful for his dedication, patience and wise advice. I also want to thank Dr. Richard Oreffo for his guidance and encouraging words, for making an amazing and harmonious working environment for all of us.

It was a great pleasure to work in the B&J group during these years. I especially want to thank you the people who were always ready to help and offer me their support in the lab: David, Janos, Julia and Juan.

Many thanks to my great friends Juan, Maria, Julia and Nev, for being there to listen and to encourage. I will always treasure your friendship and kindness.

A special thanks to my family, in special Ronald, Yoly and Sharmila for supporting me to achieve my life goals, for their time, dedication and prays, for being my dearest source of love, values and advice.

To the practice of Nichiren Buddhism that enables me to draw on inexhaustible inner reserves of courage, hope and resilience to surmount challenges and go beyond what we thought was possible.

“A great revolution in just one single individual will help achieve a change in the destiny of a society and, further, will enable a change in the destiny of humankind”.

— Daisaku Ikeda, *The Human Revolution*

Abbreviations

2D	two-dimensional
3D	three-dimensional
AER	apical ectodermal ridge
AB/AM	antibiotic/antimycotic
AF	alexa fluor
AFM	atomic force microscopy
Ag	silver
Al	aluminium
ALP	alkaline phosphatase
As	assembly
A&S	alcian blue/sirius red
BD	bovine serum albumin and dulbecco phosphate buffer
BMP	bone morphogenic protein
BSA	bovine serum albumin
BW	bovine serum albumin and water
Ca ²⁺	calcium
CaCl ₂	calcium chloride
CLSM	confocal laser scanner microscopy
CPD	critical point drier
DAPI	4'6-diamidino - 2 - phenylindole
DHA	docosaheptaenoic acid 22:6 (n-3)
DLVO	Derjaguin-Landau-Verwey-Overbeek
DMEM	dulbecco's modified eagle medium
DNA	deoxyribonucleic acid
DPBS	dulbecco's phosphate buffer saline
DPX	p-xylene bis-pyridinium bromide
EDTA	ethylenediaminetetraacetic acid
eGFP	enhanced green fluorescent protein
EMA	european medicines agency
Fe	iron
Fe ₃ O ₄	iron oxide

FITC	fluorescein isothiocyanate
FB	fluorescein isothiocyanate and bovine serum albumin
FCS	foetal calf serum
FDA	food and drug administration
FGF	fibroblast growth factor
GAGs	proteoglycans
GelA	gelatin
GelMA	gelatin-methacryloyl
Glu	glucose
GRGDS	glycine-arginine, glycine, glutamic acid, serine peptide
HBA	human serum albumin
HH	Hamburger & Hamilton
hMSCs	human bone marrow stem cells
IgG	immunoglobulin G
LBL	layer-by-layer
LFM	light fluorescence microscopy
Ln	loading
MAPK	mitogen-activated protein kinase
Micro CT	micro computed tomography
MUA	mercaptoundecanoic acid
MD	molecular dynamics
Mg	magnesium
MSC	mesenchymal stem cell
NaOH	sodium hydroxide
NCPs	non-collagenous proteins
PEG	polyethylene glycol
PEGDA	poly(ethylene glycol) diacrylate
PEGDA-GelA	poly(ethylene glycol) diacrylate -gelatin
PBDT	poly (2,2'-disulfonyl-4,4'-benzidine terephthalamide)
PCL	polycaprolactone
PGA	poly(glycolic acid)
PLA	poly(lactic acid)
PLGA	(poly(lactic-co-glycolic acid))

PLM	polarised light microscopy
PPi	pyrophosphate
RA	retinoic acid
RGDS	arginine, glycine, glutamic acid, serine
rhBMP	recombinant human bone morphogenetic protein
RT	room temperature
ROI	region of interest
RNA	ribonucleic acid
SAXS	small-angle x-ray scattering
SEM	scanning electron microscopy
SD	standard deviation
SPB	surface patch binding
TE	tissue engineering
TEM	transmission electron microscopy
TERM	tissue engineering and regenerative medicine
TC	tissue culture
TGF- β	transforming growth factor-beta
TMA	N, N, N-trimethyl (11-mercaptoundecyl) ammonium chloride
TPP	tripolyphosphate
TRITC	tetramethylrhodamine isothiocyanate
UV	ultraviolet
VEGF	vascular endothelial growth factor
β -Lg	β - lactoglobulin

Chapter 1 INTRODUCTION

Overview

Osteoporosis is a health condition that deteriorates the bone mass and micro-architecture, making it fragile and prone to fractures. In 2000, worldwide was estimated at nearly 9 million osteoporotic fractures involving the hip, forearm and vertebra (Johnell & Kanis, 2006). Alarmingly, in 2004, US Surgeon General's report suggested that 1 in 2 women and 1 in 5 men will experience a fracture over the age of 50 (U.S. Dept. of HHS, 2004). This major public health issue costs the European economy €37 billion each year and owing to the ageing population, and an increase of 25% of the global cost of osteoporotic fracture is expected during the period 2010 and 2025 (Hernlund et al. 2013). Moreover, the management of complex fractures possess a risk of mal-union, delayed union and non-union (Ekegren et al. 2018). The use of BMP growth factor is the current gold standard alternative to autologous bone graft for bone reconstruction, fracture repair and fusion. However, while widely used in the absence of effective alternatives, its use presents significant limitations, such as inflammatory complications, radiculopathy, ectopic bone and wound complications (James et al. 2016). To address this health problem, new regenerative medicine and tissue engineering approaches towards bone healing are imperative. This thesis explores the development of a new self-assembly approach for effective therapeutic delivery of BMP-2 at the fracture site using clay nanoparticles. After an introduction to the biology of bone and bone tissue engineering strategies, this chapter will discuss current BMP-2 delivery strategies and the potential of clay nanoparticles to provide new opportunities for bone repair.

1.1 Bone tissue engineering and regenerative medicine (TERM)

Regenerative medicine is an interdisciplinary field that aims at the replacement or regeneration of damaged cells, organs or tissues. Generally, it comprises different approaches, such as therapeutic (induced pluripotent) stem cells, gene therapies, tissue engineering or the fabrication of artificial organs. For the purpose of this study, it will be discussed the tissue engineering approach.

Tissue engineering (TE) is a platform that emerged about 30 years ago intending to restore the structure and functionality of tissues that have been severely damaged beyond their self-healing capacity. For this purpose, three distinct components are used: cells to synthesise the new tissue, scaffolds to serve as an artificial niche for cells and growth factors to provide the necessary biochemical cues to elicit specific cells response, though all components are not necessarily used simultaneously (Ikada 2006 and O'Brien 2011).

It is essential to recognise that the approach mentioned above is based on biomimetic design principles. This concept “grew its usage, particularly amongst material scientists in 1980s” to solve practical problems by understanding and emulating nature's designs (Aziz & El Sherif, 2015). In this regard, the considerable efforts made to understand the biological principles underlying the form, composition, self-assembly, developmental or regeneration process and function of tissues, not only allowed establishing the general component necessary for TE but as well to the development of numerous methods for restoring tissues functionality.

For example, current orthopaedic bone grafting is fundamentally biomimetic in its approach since it implicates emulating the macro and microstructure, composition and regeneration processes observed in bone tissue. For this purpose, grafts or implants with natural or synthetic biomaterial are commonly built to provide the mechanical, physical and biochemical cues necessary to repair skeletal defects by following validated principles of osteogenesis, osteoinduction and osteoconduction. The result is the design of bioactive grafts with osteogenic, osteoconductive and osteoinductive properties (Elsalanty & Genecov, 2009 and Roberts & Rosenbaum, 2012).

Thus, a graft with osteogenic properties augments bone formation and remodelling by providing viable bone-forming cells, an osteoinductive graft delivers biomolecular signalling required for recruitment and differentiation of bone-forming cells, and an osteoconductive graft stimulates cell adhesion and proliferation to guide the growth of new bone along its surfaces (Bose et al. 2012 and Jan et al. 2013).

Following this biomimetic concept, numerous grafts for bone repair has been designed and successfully approved by the FDA. Ideally, they should be sufficient to guide bone regeneration. Nevertheless, the clinical practice has shown some pitfalls mainly related to the graft composition, which include reduced cellular proliferation and differentiation, inadequate mechanical strength, uncontrolled degradation profile, reduced bone formation, inefficient bone formation and immune rejection (Walmsley et al. 2015 and Fernandez-Yague et al. 2015). In this regard, a brief overview of the main bone grafts used and their advantages, limitations and new TE strategies will be discussed. For this purpose, the grafts are grouped rendering their primary component into bone grafts, cells, organic matrix, growth factors, ceramic and polymer.

Bone grafts

Despite decades of innovation in tissue engineering and regenerative medicine, autograft continues being the “gold standard” implantable material for bone regeneration, since it fulfils the three principles for bone grafting (osteogenesis, osteoinduction and osteoconduction) and also possess suitable histocompatibility and non-immunogenic properties (Amini et al. 2013). This graft is harvested from the same patient (usually from the posterior iliac crest) and transplanted to reconstruct another site of interest. However, the use of autograft is attended by significant limitations. For example, it cannot be used to repair long bone defects (> 5 cm) because the available volume to harvest is limited. Furthermore, the patient can experience chronic pain and post-surgical infections at the donor site (Polo-Corrales et al. 2014).

Alternative treatments to autograft to increase the quantity of available tissue and to eliminate the harvesting procedure include bone allografts and xenografts. These grafts are harvested from human cadavers and animals, respectively and then treated to remove the cells and antigens. Nevertheless, they lack osteoinductive capacity owing to the treatment and still have the risk of carrying infectious agents or immune rejection (Meijer et al. 2007).

Cellular and Organic matrix components

Other biomimetic approaches involve using the cellular and organic matrix components of the bone. The cellular component is harvested by “bone marrow aspiration” technique. It is used to treat joints, delayed union and non-union fractures by placing concentrated mesenchymal stem cell (MSC) in the damaged area to enhance the osteogenesis. Harvesting MSCs is less invasive compared to the autograft. However, the amount of MSC obtained can be limiting (instead, more red blood cells are harvested), and they are not able to repair extensive bone fractures by themselves. As a result, significant effort has been put into determining the appropriate delivery system, the sufficient number of cells with osteogenic capacity and the factors necessary to enhance the osteogenic response (Fei et al. 2012).

Regarding the organic bone matrix, it is obtained from allograft by removing the mineral component, and they are available in different commercial presentations, such as putty, powder and sponge. It should retain the collagen and non-collagenous proteins, including growth factor and act as an osteoinductive agent. However, the in vitro and clinical studies have shown that it is mainly osteoconductive and that possesses low osteoinductive capacity. It is suggested to be related to the allograft pre-treatments. Moreover, they have poor mechanical properties, the bioactivity depends on the allograft quality and still has the risk of carrying infectious agents (Campana et al. 2014).

Growth factor

To augment the osteoinductive properties of natural or synthetic grafts, they are usually enriched with a supra-physiological concentration of growth factors, such as transforming growth factor-beta (TGF- β) and bone morphogenetic protein (BMP). Nevertheless, their short biological half-life and fast local clearance are not favourable, since the bone healing process takes longer periods of time; thus, it is required a steady and slow release of growth factors (Bose et al. 2012). Moreover, the high concentrations used have been related to important side effects. For example, the use of BMP-2 in spine surgery has shown that high dosage (2 - 4.2 mg/patient) support bone formation, but as well produces ectopic bone formation,

osteolysis, graft subsidence, dysphagia and soft - tissue swelling (Tannoury & An, 2014).

Bioceramics and polymers

To overcome the limitation of grafts based on the naturally occurring components, including the risk of disease transmission, infection and immunogenicity and low availability, synthetic alternatives, such as ceramics and polymer grafts are used. In this regard, the calcium phosphate-based ceramics are available in a wide variety of forms, such as powder, putty, pellets and as implant coating (to promote their osseointegration). Generally, they are osteoconductive, but some have shown osteoinductive properties, such as bioglasses. Nevertheless, they are brittle materials, unable to maintain their structural integrity before the adequate substitution with new bone occurs. Furthermore, it is difficult to control their degradation kinetic without compromising, even more, their mechanical properties (Roberts & Rosenbaum 2012 and Henkel et al. 2013).

Finally, another synthetic approach involves the use of naturally occurring and synthetic polymers that can be degradable and non-degradable. These grafts are designed to deliver growth factors and/or supports tissue ingrowth. In general, the clinical results indicate that they possess osteoconductive and osteoinductive properties. Nevertheless, they are not completely efficient. For example, the naturally occurring polymers, such as collagen, alginate and gelatin are inherently biocompatible, though it is a challenge to make reproducible structures and they have poor mechanical properties. Regarding the synthetic polymers, such as poly (lactic acid) (PLA), poly(glycolic acid) (PGA) and polycaprolactone (PCL), their architecture, degradation kinetic and mechanical properties can be easily tuned. However, their main drawbacks are the risk of rejection (Henkel et al. 2013 and Campana et al. 2014).

To conclude, there is an extensive list of currently available grafts approved by the FDA for bone repair, but their clinical performance is not entirely efficient interns of bioactivity, biocompatibility and mechanical properties (Fernandez-Yague et al. 2015). In this regard, it could be argued that this TE approach was focused on the

investigation and reproduction of macro-level structures to build “the essential gross morphology and generate real-size organ systems”, failing to reproduce the natural microenvironments cues necessary to enhance bone formation (Wen et al. 2005).

Moreover, there is a need for exploring other biomaterials to improve the biocompatibility and mechanical properties of the grafts (Fig. 1.1).

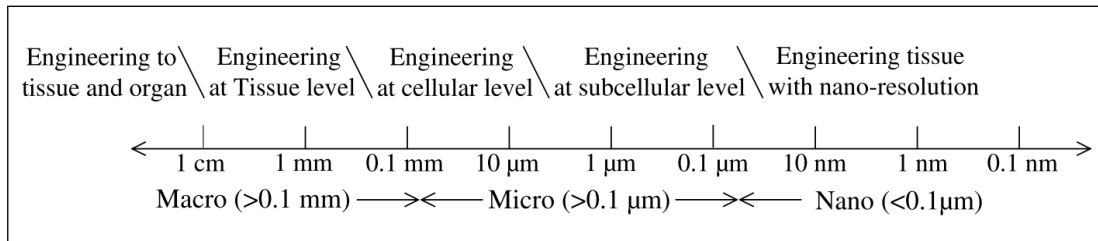


Figure 1.1 Tissue engineering at different levels. Figure from Wen et al. (2005).

In the last decades, the interdisciplinary advances in nanotechnology, tissue engineering and biomaterial fields have provided the opportunity to characterise the nano- and microstructure, and functionality of bone tissue across different length scales. Also, the development of new techniques and biomaterials to manipulate and organise matter systematically for emulating cellular microenvironments. This seems to be a promising approach for the development of more biomimetic, effective and conservative treatments for bone regeneration. In this regard, the main concepts and advances in the area will be discussed.

1.1.1 Current state of the art in biomaterials and nanotechnology for tissue engineering

Biomimicry involves the imitation of nature by studying its composition, processes, model and systems to understand the underlying principle and implement them to help to solve human challenges. For centuries, designers and architects have looked to nature as a source of inspiration to create aesthetic, functional, lightweight structures and with optimum material and energy usage. For example, Leonardo Da Vinci’s inventions were inspired by the observation of nature, Gustave Eiffel emulated the hierarchical structure of trabecular bone to build the skeleton of the Eiffel Tower. It is a tall and lightweight structure that was meant to stand for at least 20 years and has already 130 (Vincent, 2008). Similar to Gaudi and all his masterpieces like La Sagrada Familia and La Casa Batlló. Eventually, the concept

was applied at smaller length scales, such as Velcro, which was designed by George de Mestral after burrs of the Burdock plant.

The materials scientists only adopted this approach in the 1980s. However, significant interest surged in the last fifteen years in different fields like biological-science (Aziz & El Sherif, 2015). Since then, the advances in physicochemical techniques to characterise nanomaterials lead to an unprecedented understanding of the composition and the hierarchical levels of organisation omnipresent in biological systems spanning from nano to macro length scales (Lin et al. 2014).

Moreover, this fact reoriented various research field, including biomaterials, nanotechnology and tissue engineering, which scope has broadened exploring novel materials and techniques to design biomimetic and functional structures with nano and micro size for tissue engineering. For this purpose, the working area was outlined around basic concepts briefly discussed below (Fig. 1.2):

- Hierarchy: is the arrangement of fundamental units into different asymmetrical level of order.
- Hierarchical levels: is a standard organisation scheme used to label the arrangements found in a structure at different length scales. Generally, they are presented from the lowest level to the highest levels, where the lowest represent the fundamental building units and the highest levels the maximum and stable arrangement achieved. For example, the lamellar bone can be divided into 7 hierarchical levels (Fig. 1.3).
- Molecular self - assembly process: is the spontaneous ordered assembly or aggregation of molecular units through non-covalent interactions to form complex structures that are usually in equilibrium or metastable states. Moreover, no human intervention is required since the assembly process is determined by the chemical properties of the molecular unit (G. M. Whitesides & Boncheva, 2002).

- **Supramolecular self - assemblies:** are complex structures that result from molecular self - assembly processes. Usually, the organised structure formed are sphere-, rod- or sheet-like species, which dimensions range from nanometres to micrometres.
- **Building blocks:** is the fundamental or molecular unit that forms a structure. They are held either by covalent or non-covalent interactions. For example, the electron, protons and neutrons are the building blocks that make the atoms, the atoms make the matter, and the nucleotides are the main component to assemble the deoxyribonucleic acid (DNA).

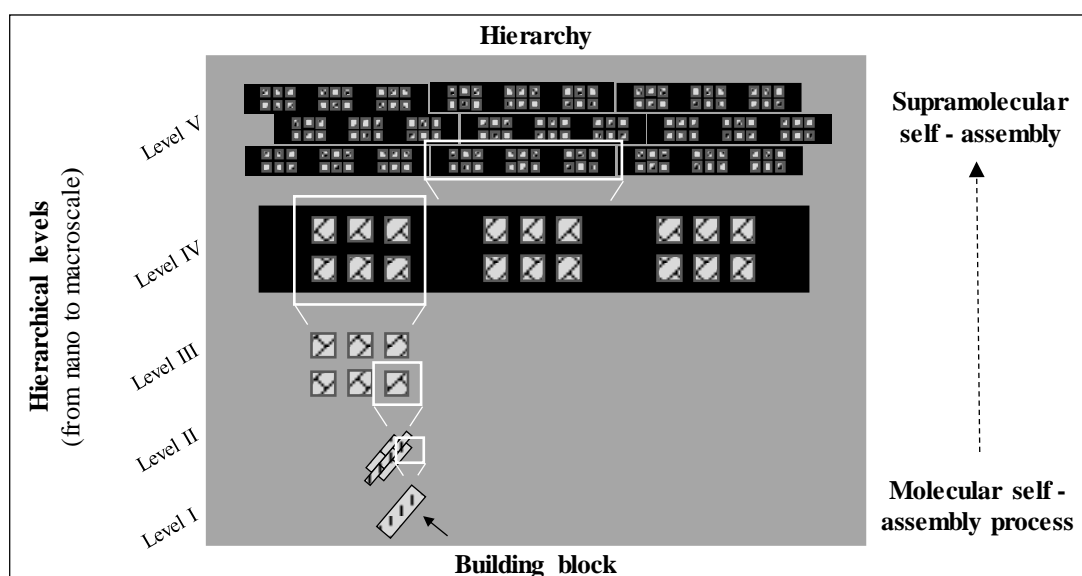


Figure 1.2 Illustration of hierarchical biology concept framework.

The simultaneous blooming of the different engineering fields above mentioned has supported the development of numerous nano and microfabrication techniques, such as nanotemplating, electrostatic deposition, molecular self-assembly, electrospinning, photolithography, emulsion templating and micromachining in order to build complex or supramolecular frameworks that mimic features of biological systems (Santo et al. 2012). All these techniques can be grouped according to the assembly process into top-down and bottom-up approaches.

The top-down approach involves the miniaturisation or scaling down of existing materials into micro- and nanostructures. It is a directed process that uses tools to

cast the desired size, shape and order (Santo et al. 2012). In contrast, the bottom-up approach consists in the self-guided assembly of smaller building blocks to form organised nanostructure. This is a spontaneous process mediated by non-covalent forces, such as electrostatic interactions and affinity-based binding, hence the chemical properties of the building block is crucial (Güven et al. 2015).

The bottom-up approach presents more advantages since it attains higher resolution at nanoscale levels, uses building blocks with similar size to the native nanoscale components and enables localised spatial array of biochemical cues (Santo et al. 2012). Moreover, it is a more biomimetic approach, since nature relies on it to build hierarchical and functional structures that span from the nano- to macroscale level.

It has taken nature's billion years of evolution to achieve remarkable self-assemble performance toward very complex structures (Thiruvengadathan et al. 2013), and this still remains a challenge to man. In the laboratory, the "hierarchy mostly occurs inadvertently, and it is rarely designed into a structure" (Vincent, 2008), and when achieved, the hierarchy does not translate to higher length scales. For example, dendron assembly, self-assembly peptides, electrostatic deposition and Langmuir Blodgett deposition.

Further in vitro analysis of these bioinspired nano and micro frameworks (either built with top-down or bottom-up approaches) have revealed that the cell response can be modulated by multi-dimensional arrays of morphological, structural, mechanical and biochemical cues. In this regard, topographical factors, such as size, shape and geometrical patterns resulted in being important nano- and microscale cues to modulate the cell adhesion, migration, alignment and differentiation. Though optimum parameters strongly depend on the cell type (Nguyen et al. 2016 and Limongi et al. 2017). Stiffness is an important mechanical cue that cells can sense at microscale levels, supporting their "migration, proliferation, differentiation and alterations in cell-cell and cell-matrix adhesion" (Mason et al. 2012). Furthermore, it can enhance the efficacy of biochemical stimuli (Breuls et al. 2008).

Regarding the biochemical cues, such as growth factors, peptides, chemical moieties and synthetic molecules can be used to functionalize the surfaces of 2D and 3D

scaffolds. Usually, when combined with physical and mechanical cues, they show a synergistic effect. Moreover, it has been designed nanoparticulate carriers to control and facilitate the transport of growth factors or synthetic molecules across cell membranes (Santo et al. 2012 and Samorezov & Alsberg 2015). These strategies seem to enhance the local cell response by binding or controlling the delivery of the biochemical cues.

Thus, the nanotechnology has allowed an unprecedented understanding of cellular microenvironments and their emulation with predictable biological, physical and mechanical properties to control the cells' responses. This seems to be a promising approach for TE. Nevertheless, many challenges still need to be addressed, like the assembly of structures with different hierarchical levels and high resolution from nano- to macroscale and 3D protein micropatterning.

Thus, the present study aims to self-assemble a biomimetic scaffold that incorporates features of the bone structure. For this, a review of the fundamental of bone biology at different length scales will be presented in the next section.

1.2 Fundamental of bone biology

1.2.1 Bone structure, composition and functionality

Bone is a hard connective tissue that forms the skeleton of adult vertebrates. Its major functions include 1) locomotion and protection of soft tissues, 2) storage and homeostasis of ions, 3) harbouring the bone marrow and 4) aiding the haemopoiesis (Datta et al. 2008).

Moreover, it possesses unique mechanical properties and remodelling capacity, which have been linked to its composition and structure at the molecular level (Liu et al. 2016). In this regard, this heterogeneous tissue comprises an intricate network of bone-forming cells embedded in a specialised inorganic/organic framework, which has various anisotropic arrangements at multiple length scales.

The cellular component form 2% of the bone mass and they aid in maintaining the bone integrity and vitality by means of four type of cells. The 1) osteoblast synthesises and mineralises the new bone. During this process, some osteoblast becomes embedded in the organic framework that they have secreted transforming into 2) osteocytes, these cells are “primary mechanosensors” that help to orchestrate the remodelling process. Once the bone is formed, a group of osteoblast changes its morphology (flattens) and localises at the bone surface, forming the 3) bone-lining cells, their function is not well understood. However, they have been associated with the calcium and phosphate homeostasis, the protection of the surface from any adventitious resorptive activity and to participate in initiating the bone remodelling (Florencio-Silva et al. 2015). Finally, a key cell involved in the bone (longitudinal) remodelling, and (bulk) turnover are the 4) osteoclast, these cells have the capacity to demineralise and degrade the inorganic and organic bone framework respectively (Datta et al. 2008 and Fogelman et al. 2012).

In 1998, Weiner & Wagner proposed that the inorganic/organic framework, also known as the extracellular matrix, had some degree of order spanning from the nano- to the macroscale; thus, they divided the mature bone (lamellar bone) into seven hierarchical levels, as briefly outlined here (Fig. 1.3):

- **Level I** (sub - nanostructure 1 nm): here it is found the main components of bone. 1) The organic framework forms ~30 % (dry weight), of which 90 % is collagen, mainly type I and the rest non-collagenous proteins (NCPs) and proteoglycans (GAGs). 2) The inorganic framework forms ~60 % (dry weight) and is made of carbonated hydroxyapatite crystals with plate-like shape, which average lengths and widths are 50×25 nm with a thickness is 2 - 3 nm and the last component is 3) water, forming the remaining 10 % (Palmer et al. 2008 and Feng 2010).
- **Level II** (nanostructure 0.5 µm): interaction of the main components guides the formation of mineralised collagen fibrils, which in turn forms the building blocks of bone (Sabet et al. 2015). In this regard, once the type I collagen fibril has been synthesised and assembled, the hydroxyapatite crystals nucleate and grow initially within the hole zones inside the fibrils and then in the adjacencies.

The result is a collagen fibril with minerals that “span the cross-section of the fibril” (Reznikov et al. 2014).

- **Level III** (sub - microstructure): it should be observed the internal structural organisation and interaction of individual and neighbouring fibril arrays that will form fibril bundles (collagen fibres). This is poorly understood, but two possible orders have been proposed respect to the orientation of the crystalline structure and the fibril axes. The first would be fully orthotropic, where the mineralised fibrils align respect to the crystal layers and the fibril axes. The second arrangement, transversely isotropic, would be only with respect to the fibril axes (Weiner & Wagner, 1998).

- **Level IV** (microstructure): it is found a diversity in organisational patterns of fibril bundles (collagen fibres). In this regard, Weiner & Wagner (1998) described two patterns, which they named “woven fibre structure” and “plywood like structure”. The former pattern the in woven bone, it is made of fibres with a wide range of diameters (up to 30 μm), which are poorly packed and oriented. In addition, it is found an important amount of non-collagenous proteins and osteocytes. Moreover, the plywood like structure is present in lamellar bone. Here, sets of parallel fibrils form discrete layers, but the orientation of each layer is different. It is suggested that layers rotate with a specific angle and in one direction, resulting in an asymmetric lamellar unit.

- **Level V** (microstructure 10 - 200 μm): here, the osteoclast and osteoblast play an important role. Initially, the osteoclasts would excavate a long tunnel that then the osteoblasts would refill by depositing the lamella unit above described. During this process, osteoblast results trapped transforming into osteocytes. They will reside in spaces called lacunae, which are connected through canaliculi (Florencio-Silva et al. 2015). At this point, it can be formed two types of structures:
 - 1) Cylindrical osteon or Haversian systems (100 - 200 μm). In a cross-section, they look like onions assembled of lamellae layers surrounding a central hole or Haversian canal, through which the blood vessels run.

- 2) Rods or plates - like structures (100 - 200 μm) assembled from lamellae layers, but with no Haversian canal (Parkinson & Fazzalari, 2013).
- **Level VI (mesostructure):** at this level, two different types of bone will form, compact and spongy bone (Clarke, 2008).
 - 1) The compact bone is a dense structure made of numerous and well-packed osteons, which are irrigated by interconnected Haversian canals.
 - 2) The spongy bone is porous; thus, less dense than the compact bone. It is formed by a trabecular network of interconnected rod and plate-like structures. Since they lack of Haversian systems and canals, the irrigation is provided by the red bone marrow found between the trabeculae.
 - **Level VII (macroscale):** finally, the compact and spongy (trabecular) bone will form the outer and inner layer of the whole bone, respectively. Further detail of the gross anatomy of bone is beyond the scope of this review. For an overview of the subject referred to (Clarke, 2008).

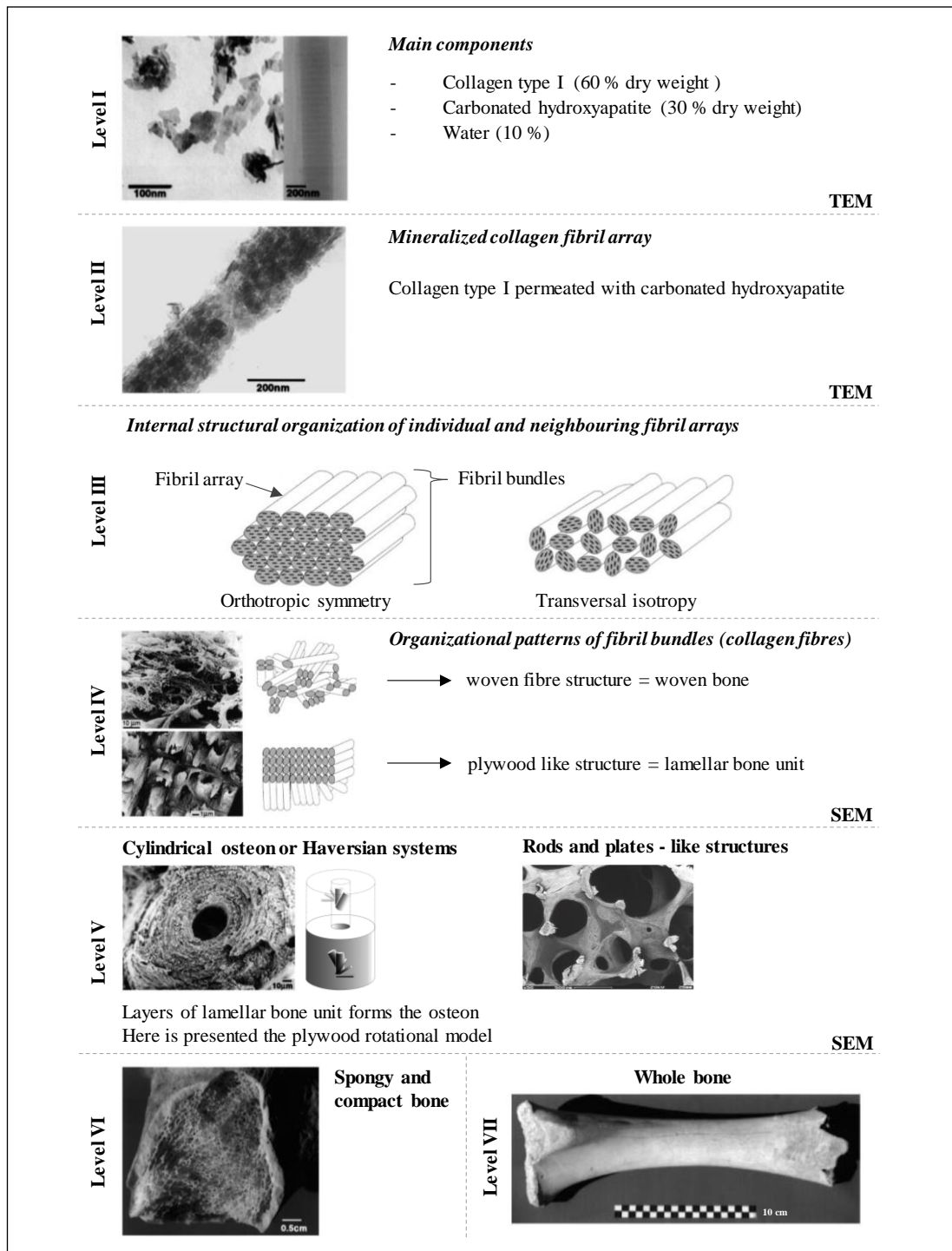


Figure 1.3 The 7 hierarchical levels of organisation of the mature bone. These are modified images from Weiner & Wagner (1998) except for the rods and plate-like structure, which was retrieved from Boyde (2012).

The study of the bone architecture, specifically the physical (e.g. porous, osteons) and chemical (e.g. collagenous and non-collagenous proteins) features found at each scale level have allowed evaluating their role in the biochemical and biomechanical

functions of the bone at specific hierarchical levels, which are briefly described below (Fig.1.4).

At macroscale level (mm - cm):

The whole bone shows interesting anisotropic macro-mechanical properties, primarily owing to the distribution of fundamental components (collagen type 1, carbonated hydroxyapatite and water) which make some areas stiffer and tougher than others. As well, the anatomical localisation of both compact and spongy bone, the orthogonal orientation of the spongy bone trabeculae and the osteonal structures size and orientation make the bone resistant mainly to compressive forces (Wang et al. 2010).

At the microscale level (10 - 500 μm):

It can be observed different biomechanical and biochemical functions related to the microstructure features found in the compact and spongy bone.

- The compact bone architecture and composition makes it a solid and dense structure. It is stiffer compared to the spongy bone owing to its intrinsic and higher content of carbonated hydroxyapatite. Moreover, features, such as osteons, cement lines, Haversian canals or any extensive discontinuities control its fracture toughness (Augat & Schorlemmer 2006 and Sabet et al. 2015).
- The spongy bone is the main load-bearing bone and its trabeculae are organised to optimize load transfer from the joints to the compact bone of long bones (Oftadeh et al. 2015).
- The compressive strength at this level is lower than at the macroscopic level. In contrast, the torsional strength is significantly higher (Wang et al. 2010).
- The porosity (size and interconnectivity) of both types of bones affect as well the elastic modulus (Augat & Schorlemmer 2006).
- At this level initiates the mechanotransduction process, where the bone lining cells and osteocytes sense the physical forces and control the process of adaptive remodelling by regulating osteoblast and osteoclast function (Oftadeh et al. 2015).

- The bone porosity, interconnectivity, Haversian canals, lacuno-canalicular network support the cell migration, vascularization and nutrients delivery, respectively (Jabbarzadeh et al. 2012).

At the nanoscale level (1 nm): distinct biochemical and biomechanical functions are recognised, including:

- The mechanotransduction or conversion of physical forces into biochemical signals for bone remodelling (Oftadeh et al. 2015).
- The biomineralization process is facilitated and controlled by different biochemical factors. It involves two main events: 1) the release of mineral - matrix vesicles from the osteogenic cells and 2) the nucleation and growth of hydroxyapatite crystals (Weiner & Addadi 1997 and Mann 2001).
- The processes above-mentioned trigger cell adhesion, migration, differentiation and function supported by biochemical factors.
- Moreover, mechanical properties of the whole bone are not only defined by the anisotropic arrangement of the material in the space at the micro- and macroscale levels but as well by the fundamental components and their organisation at the nanoscale level. For example, the carbonated hydroxyapatite is a stiff material with good compressive strength. On the contrary, the collagen has a low elastic modulus, poor compressive strength but good tensile strength. However, both make the collagen fibril a stiff and tough material (Weatherholt et al. 2013).
- The density and quality of the inorganic/organic framework affect the whole bone mechanical properties. For example, an agile animal requires bones with high elasticity and optimum but low mineral content, such a deer. On the contrary, the bones of a large animal, like a whale or a cow, are very stiff bones with high hydroxyapatite content (Mann, 2001). Moreover, in pathological conditions, such as osteogenesis imperfect, it has been shown that the quality of the collagen type I affects significantly the hydroxyapatite size, shape, orientation and localisation with respect the collagen fibril, which in turns makes the bone weak and brittle (Landis, 1995).

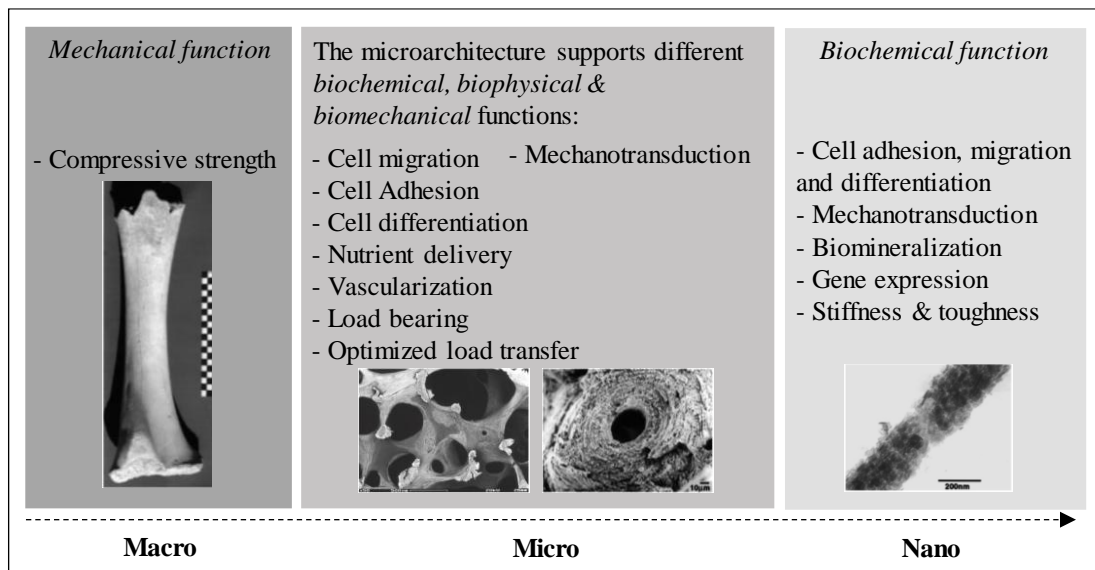


Figure 1.4 Functionality of the bone at each hierarchical level. Images from Weiner & Wagner (1998) and Boyde (2012).

This brief review provides some insides about the bone structure functionality in relation to the distinct physical, mechanical and chemical cues found across different length scales. Interestingly, the chemical cues are the primordial signalling found at the lowest level, setting the structural bases for the self-assembly of this hierarchical mineralised structure. In this regard, Mann (1988) and Weiner & Addadi (1997) proposed that the proteins were not only responsible for the cell's response but in the modulation of the biomineralization or process by which biological systems selectively incorporate minerals from the local environment and under strict biological control to create functional structures with hierarchical organisation and improved mechanical and biological properties, such as bone or seashell. The same authors have highlighted some principles. However, the process still remains unknown.

Thus, the incorporation of chemical cues into the design of the scaffolds for bone tissue regeneration seems to be crucial. However, further research is required to understand their presentation format that triggers the formation of such complex structure.

1.2.2 Bone development

During early embryonic development, the embryo's skeleton is constituted by a fibrous membrane and hyaline cartilage. However, the actual bone formation or osteogenesis starts by the sixth or seventh week of embryonic life. The process may follow two different osteogenic pathways, intramembranous or endochondral ossification, but the mature bone formed is the same regardless of the pathway.

At the intramembranous ossification, *de novo* bone develops directly from the connective tissue of mesenchymal (undifferentiated) cells. The first event consists in the formation of an ossification centre within the connective tissue membrane by recruitment and differentiation of mesenchymal cells into capillaries and other osteogenic cells and osteoblasts. Next, the osteoblasts secrete an uncalcified matrix consisting of collagen precursors and other organic proteins within the connective tissue, known as osteoid or bone matrix, which calcifies a few days later by deposition of apatite crystals. The entrapped osteoblasts become osteocytes and the surrounding cells in the connective tissue condensate and differentiate into osteoblast at the edges of the new growing bone, becoming the cellular layer of the periosteum, which is a vascular connective tissue that surrounds the bone. Then, the deposition of several osteoid clusters between the capillaries and subsequent mineralisation forms a network of trabecular bone containing a dense vascular tissue that becomes the red bone marrow. In contrast, the osteoblast localised at the surface secretes the compact bone (reviewed by Setiawati & Rahardjo, 2018).

Regarding the endochondral ossification, the bone tissue forms by systematic replacement of growing hyaline cartilage. In this process, the mesenchymal cells condense and differentiate into chondrocytes or cartilage cells to form a template of hyaline cartilage. A membrane of connective tissue known as perichondrium surrounds the avascular matrix of cartilage, whose main function is supplying nutrients and removing metabolic waste via diffusion. As the cartilaginous template increases in size, the chondrocytes in the centre undergo hypertrophy and eventual death. These changes are accompanied by vascular invasion and differentiation of the perichondrium cells into osteoblasts that will deposit a ring of bone or bone collar at the edges of the hypertrophic cartilage (reviewed by Long & Ornitz, 2013). Further

vascularisation supports the invasion and differentiation osteoprogenitors into osteoblasts establishing an ossification centre to generate the trabecular bone (Maes et al. 2010).

Both ossification pathways, either intramembranous or endochondral, are finely coordinated by the spatio-temporal presentation of systemic and locally secreted factors. Generally, gradients of these factors play a vital role in the fate of mesenchymal cells at different stages of the ossification pathways by triggering their migration, proliferation or differentiation in a concentration dependent manner. The systemic factors may be growth hormone and thyroid hormone, and local factors, such as insulin-like growth factors, Indian hedgehog, parathyroid hormone, bone morphogenetic proteins, Wnt family or fibroblast growth factors (FGF) (Mackie et al. 2008 and Long & Ornitz, 2013). For this reason, some of them have been actively reviewed for bone tissue engineering applications (Mehta et al. 2012).

1.2.3 Fracture healing

Bone tissue has the capacity to fully regenerate after trauma without forming scars by following different pathways based on the anatomical characteristics of the fracture. In this regard, reduction and rigid stabilisation of the fracture allow direct intramembranous healing. The process consists in the initial remodelling of the lamellar bone by cutting cones or tunnel of osteoclast that crosses the fracture line leaving longitudinal cavities, which are later filled with new bone produced by the osteoblast residing in the rear of the cutting cone. This result in the simultaneous bone bridging and restoration of the Haversian system without the formation of any external tissue or callus. This type of healing is fast. However, it is not commonly observed during the natural process of fracture healing (Marsell & Einhorn, 2011).

In contrast, non-rigidly stabilised fracture, exposed to micro-motion and weight-bearing heals through a more complex and indirect process that involves both endochondral and intramembranous bone formation. Briefly, the first event that follows the trauma is an acute inflammatory response. At this point, a hematoma is formed and stabilised in the fracture gap. Simultaneously, several pro-inflammatory mediators are significantly elevated in the first few days, having a chemotactic effect

on other inflammatory cells. In this regard, macrophages phagocytise necrotic areas of the bone fracture, releasing signalling factors that are responsible for subsequent recruitment and differentiation of mesenchymal cells into angioblasts, chondroblasts, fibroblasts, and osteoblasts. These cells will then participate in filling and stabilising the fracture gap through the formation of a primary cartilaginous callus. Next, the callus is gradually replaced by woven bone via intramembranous and endochondral bone formation. Usually, the osteoblasts synthesise intramembranous bone distal to the fracture sites. On the contrary, endochondral bone formation is observed in regions that are less mechanically stable. Finally, reabsorption and mineralisation of the woven bone lead to the formation of mature bone, which is later remodelled back to its original shape and size (Mountziaris & Mikos, 2008, Marsell & Einhorn, 2011 and Oryan et al. 2015).

Despite the potential of bone tissue to remodel and heal without scarring, there are cases where this capacity is not sufficient to regenerate the lost tissue, either owing to the type of defect (e.g. non-union fractures, spinal fusions or alveolar bone augmentation for dental implants) or to the patient physical state (e.g. age, medication, immune system or concomitant diseases). Thus, medical/surgical intervention is required to support the bone healing process. As discussed in the previous section, the gold standard treatments for bone regeneration are the implantation of autograft and BMP-2 growth factor delivered in concomitant with the autograft or a collagen sponge.

As described in the previous section 1.1, the autograft possesses important osteogenic, osteoconduction and osteoinductive properties. However, its use is attended by significant limitations. For example, it cannot be used to repair long bone defects (> 5 cm) because the available volume to harvest is limited. Furthermore, the patient can experience chronic pain and post-surgical infections at the donor site (Polo-Corrales et al. 2014). Regarding the BMP-2, supra-physiological concentrations enhance the osteoinductive properties of natural and synthetic grafts. However, such dosages have been related to important side effects. For example, the use of BMP-2 in spine surgery has shown that high dosage (2 - 4.2 mg/patient) support bone formation, but as well produces ectopic bone formation, osteolysis, graft subsidence, dysphagia and soft - tissue swelling (Tannoury & An, 2014).

Despite the reported side effects of BMP-2, this growth factor is still widely used. Therefore, a significant effort has been made to generate the appropriate delivery system to exploit their strong osteoinductive properties but without the side effects. In the next section will be studied the significance of BMP-2 during bone development and regeneration and current delivery systems.

1.3 BMP at bone development and regeneration

In 1965, Urist demonstrated that demineralised bone segments had the capacity to induce ectopic formation of cartilage and bone tissue. Later in 1971, he postulated that this morphogenetic property was related to the presence of bioactive factor(s), which he named “Bone Morphogenetic Protein” (BMP) (Urist, 1965 and Urist & Strates, 1971). The advances in molecular biology allowed the sequencing and cloning of BMP proteins, and to date, around 20 BMPs have been identified (Bragdon et al. 2011). They represent the largest subgroup of the transforming growth factor β (TGF - β) super-family, except for BMP-1, which is a metalloprotease (Carreira et al. 2014).

BMPs play a critical role in the development and maintenance of skeletal tissues in vivo by regulating cell migration, proliferation, differentiation and death (Goldstein et al. 2005 and Katagiri & Watabe, 2016). In this regard, BMP-2 and BMP-7 are the strongest inducers of bone and cartilage formation, while BMP-4, BMP-5, BMP-6, BMP-8, BMP-9, and BMP-10 contribute to the bone formation as well, BMP-3 and BMP-13 act as BMP inhibitors (Daluiski et al. 2001, Shen et al. 2009, Yang et al. 2014 and El Bialy et al. 2017). They may transduce their signals via classical BMPs/Smads pathway or by Smad-independent pathways. With regards the former, BMPs dimers bind to two different types of transmembrane receptors that possess intrinsic serine/threonine kinase activity, forming a receptor complex that can phosphorylate the intracellular downstream effectors, which are the Smad proteins. The translocated complex into the nucleus cooperates with other transcriptional factors (e.g. Runx2/Cbfa1, Osx, Dlx5, and Msx2) to direct the transcription of genes to induce osteogenesis. Another regulatory pathway is the non-classical Smads-independent, which follows the mitogen-activated protein kinase (MAPK) pathway

and regulates the expression of target genes to fulfil their roles in the differentiation of osteoblast as well (Bragdon et al. 2011 and Yang et al. 2014).

It is important to recognise that BMP bioactivity is not limited to osteogenesis, other BMP members have been recognised as critical in the development of various organs, including the brain, muscle, kidney, blood vessels and tooth (Ducy & Karsenty 2000 and Javier et al. 2012).

The structural basis of BMP family members is highly conserved. The mature monomer possesses seven cysteine residues, of which six form a cysteine knot by three intramolecular disulfide bonds (Griffith et al. 1996 and Scheufler et al. 1999). These sites interact with heparin/heparin sulfate macromolecules present on cell surfaces and the extracellular matrix, which is essential in the regulation process of osteogenesis (Gandhi & Mancera 2012). The remaining cysteine is involved in the stabilisation of the dimeric structure through an intermolecular cysteine bridge. This dimeric conformation of approximately 120 amino acids is vital for their biological bioactivity (Carreira et al. 2014) (Fig. 1.5 - A).

Regarding other physical and chemical properties of BMPs, they are globular proteins with a molecular weight ranging from 15 to 30 kDa. These basic molecules possess isoelectric points ranging from 7.7 to 9, and characteristically present abundant hydrophobic patches on the surface (Scheufler et al. 1999, Carreir et al. 2014 and El Bialy et al. 2017) (Fig. 1.5 - B).

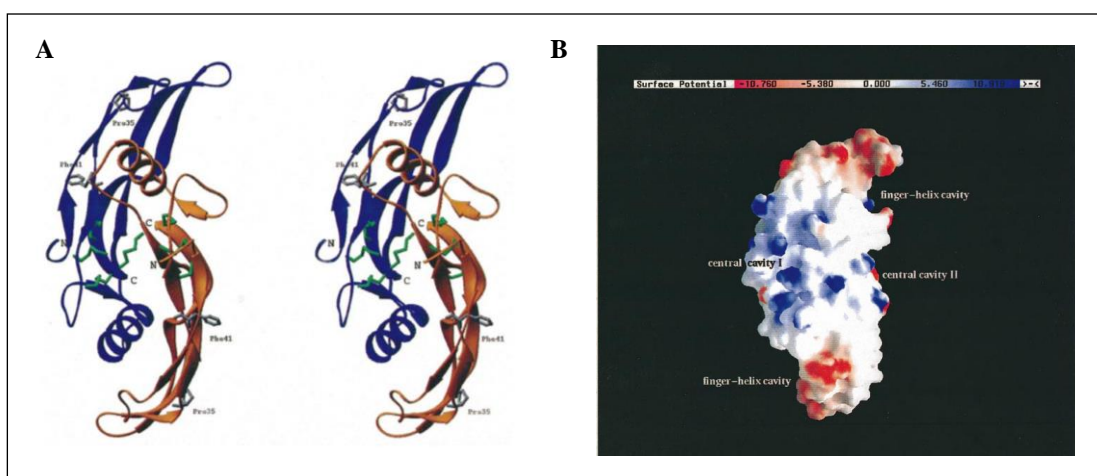


Figure 1.5 BMP-2 structure. (A) Stereo view of native BMP-2 dimer reveals the folding topology. Each subunit (blue and orange) consist of α -helices (spiral), β -strands (arrow) and internal disulfides bridges (green). Interaction between the Cys 78 residue of each subunit forms a bridge that stabilises the dimeric structure. Furthermore, the intersubunit contact is formed by interactions of helix $\alpha 3$ with the β -sheets of the neighbouring molecule, specifically through the cis-Pro35 and Phe41 (dark grey) residues. (B) Illustration of the BMP-2 surface reveals the distribution of the surface charge density, where red and blue colours indicate negative and positive electrostatic potential, respectively; and the white colour the hydrophobic regions (Scheufler et al. 1999).

1.3.1 BMP gradients

During embryogenesis, spatiotemporal gradients of signalling molecules pattern developing tissues by instructing the formation of distinct cell types along the dorsal and ventral axis of the organism in a concentration-dependent manner. In this process, a limited number of signalling pathways (e.g. BMP, Wnt, Shh and Notch) coordinate the cell fate and interaction leading to organogenesis (Sanz-Ezquerro et al. 2017) (Fig. 1.6 - A). Interestingly, the signals and mechanisms utilised throughout development have been found to be very conserved through evolution (Fig. 1.6 - B). They are recapitulated at different times and places in the embryo and are involved in adult tissue homeostasis and regeneration (Le Dréau & Martí, 2012 and Zagorski et al. 2017) (Fig. 1.6 - C & D).

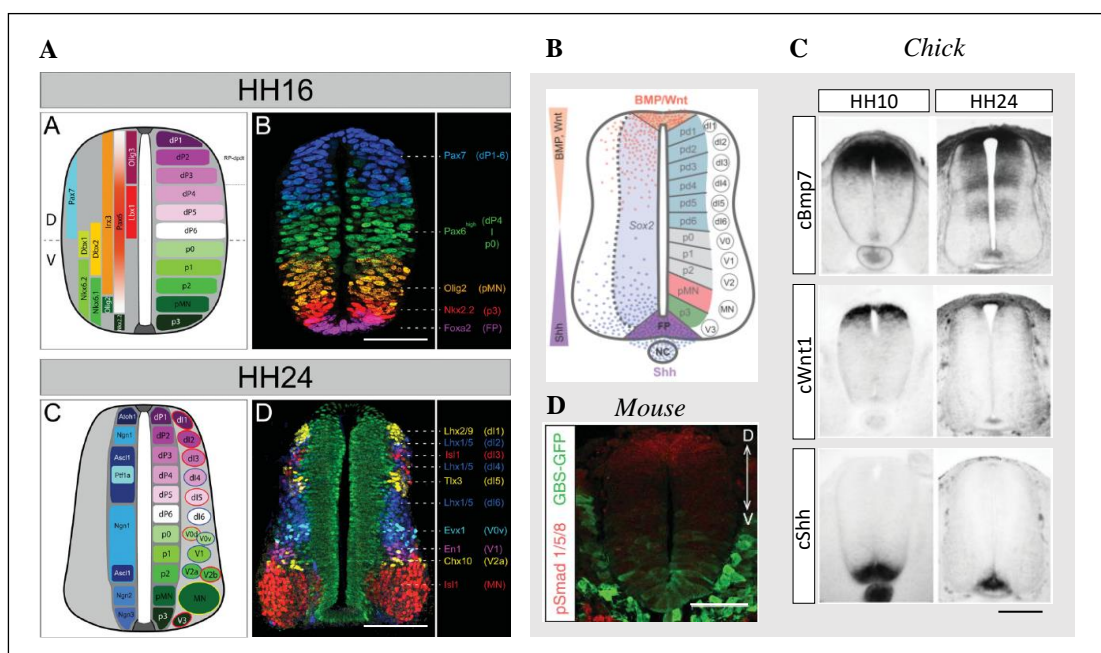


Figure 1.6 Dorsal-Ventral patterning of the neural tube. (A) Schematic illustration of the transversal section of a chick neural tube at Hamburger & Hamilton (HH) development stage 16 (51-

56 h) and 24 (4 days) reveals distinct ventral and dorsal progenitor proteins patterning distributed throughout the neural tube along the dorsal-ventral axis (left). Respective reconstruction of immunostaining images shows the subdivision of the neural tube into 11 distinct domains of neural progenitors, which then migrates laterally to form the mantle zone (right) (Le Dréau & Martí, 2012). (B) Moreover, the ventral and dorsal patterning of neural progenitors during the neural tube development is controlled not only by the spatiotemporal distribution of factors but their graded signalling, including BMP, Wnt and Shh (Briscoe & Small, 2015). For example, neural tube development of (C) chicks and (D) mouse, where secreted factors: Shh emanating from the ventral pole (notochord), and Wnt and BMP signalling dorsally (Le Dréau & Martí, 2012 and Zagorski et al. 2017). Scale bar corresponds to 50 μm .

Spatial and temporal gradients of BMP signalling are crucial in embryogenesis and skeletal development as they influence naïve cells' fate during early dorsal-ventral axis patterning and subsequent subdivision for correct formation, positioning and shape of bones, respectively (Wilson et al. 2013 and Bier & De Robertis, 2015). In this regard, studies exploring the dynamics of embryonic BMP signalling in transgenic mice through reporter (LacZ) systems revealed that BMP signalling was restricted to the apical ectodermal ridge (AER) during early limb development, and later was localised to pre-cartilage condensations and sides of endochondral ossification throughout the skeleton (Javier et al. 2012) (Fig. 1.7 - A & B). Similarly, BMP reporter (eGFP) in transgenic zebrafish and *Xenopus* embryos revealed a strong expression in the ventral pharyngeal arches during early dorsal-ventral axis patterning (Bubnoff et al. 2005 and Alexander et al. 2011). Collectively, these findings demonstrate a direct relationship between the spatial and temporal restricted patterns of BMP signalling and the specific morphogenic events during embryogenesis and development of cartilage and bone.

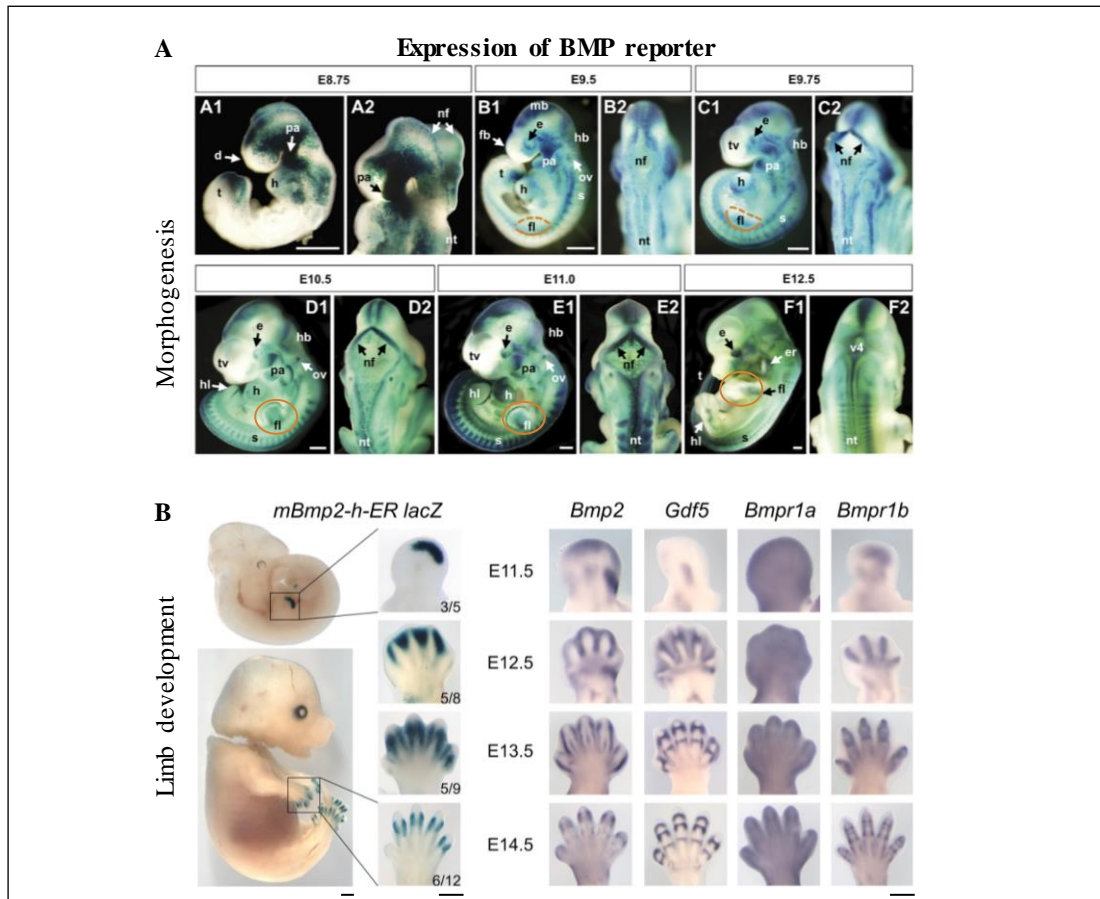


Figure 1.7 BMP reporter activity during the mid-gestation stage of a mouse embryo. (A) X-gal staining reveals BMP expression in different regions and tissues (neural structures, pharyngeal arches, heart, limbs and ectodermal appendage) throughout development. The yellow circle points out the limb bud development at different stages and expression of BMP at the apical ectodermal ridge, which is a specialised epithelium located at the distal edge of the limb bud that directs the outgrowth. (Javier et al. 2012). Further analysis reveals that (B) a fine balance in the expression BMP in a dosage-dependent manner is crucial for the normal development of the phalanges and their joints (Dathe et al. 2009). The scale bar corresponds to 0.5 μm .

In addition to the role of BMP patterning in development, BMPs exhibit spatial and temporal restricted activity during bone healing (Wilson et al. 2013). Time course studies of a non-stabilised bone fracture in mouse reveal BMP expression in multiple cell types (e.g. chondrocytes, osteoblasts/osteocytes, endothelial cells, periosteal cells, inflammatory cells), which varies during the process of bone healing via endochondral ossification (Yu et al. 2010). In this scenario, BMP-2 is considered the leader of the signalling pathway as it initiates the repair cascade with its mRNA expression peaking at 24 h after bone injures (Cho et al. 2002). It also regulates the expression of other BMP members (Edgar et al. 2007) and its presence at early

stages of fracture healing is imperative for the differentiation of mesenchymal progenitors into osteoblasts or chondrocytes (Tsuji et al. 2006).

Analysis of temporal patterns over a 28 day period of fracture healing in mouse tibias reveals upregulation of BMP-2 and 8 at early stages around the injured periosteum (day 1 - 3). Later a second peak of BMP-2 with BMP-3, 4, 7 and 8 is detected during the osteogenic stage of bone healing (day 14 - 21) when the resorption of calcified cartilage, osteoblastic recruitment, and bone formation are most evident (Cho et al. 2002 and Yu et al. 2010). Finally, when the wound-healing resolves, BMP expression returns to baseline levels. Similar temporal fluctuation has been observed in transitional studies of human tissue (Kloen et al. 2003) (Fig. 1.8 - A & B).

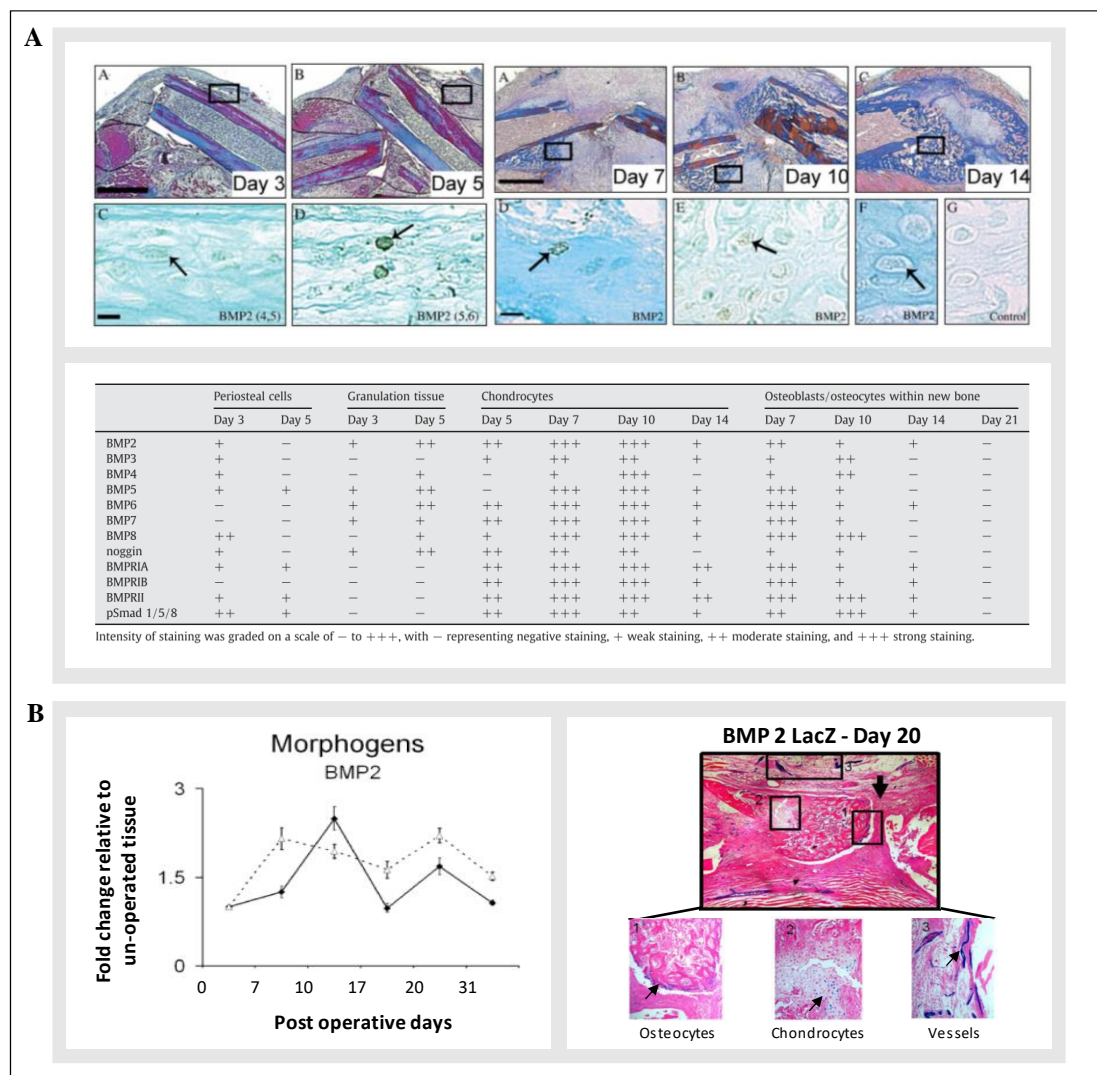


Figure 1.8 Spatio-temporal restricted patterns of BMP expression during bone healing. (A) Milligan's Trichrome of a non-stabilised long bone fracture in the mouse (upper panel) shows the healing progression from day 3 to 14. Moreover, respective immunohistochemical staining (lower

panel) shows distinct spatio-temporal expression of BMP-2 in different tissues and cells types (e.g. periosteal tissue, granulation tissue, chondrocytes and osteocytes). Scale bars of upper and lower panels correspond to 100 μm and 10 μm , respectively (Yu et al. 2010). (B) Time course mRNA analysis of a human bone fracture and surrounding muscle reveals the expression of BMP-2. Staining for β -galactosidase indicate that the BMP-2 is expressed primarily by osteocytes, chondrocytes and endothelial cells (40X and 200X, top and bottom images magnification) (Matsubara et al. 2013).

Thus, the graded distribution of signalling molecules, commonly termed morphogens, is crucial during embryonic development and tissue regeneration. Studies indicate that the movement of morphogens from the source throughout the target field creates the gradients (Lander et al. 2002) (Fig.1.9 - A). However, the transport and localisation mechanism has been under debate for decades, and several models have been proposed. They can be generally grouped into the extracellular diffusion-based mechanism (e.g. free, hindered or facilitated) or cell based-mechanism (e.g. transcytosis or cytonemes) (Muller et al. 2013). Given the importance of gradient patterning for this thesis, these various models will briefly be described (reviewed more fully by Muller et al. 2013).

The free diffusion model is the simple case of morphogen dispersal, in which morphogens diffuse freely from the source through the target field, and their fast clearance (relative to the diffusion) generates a gradient. In this scenario, the clearance could be achieved by rapid degradation (due to their short lifetime) or permanent immobilisation of the morphogen by the target cell (Zhou et al. 2012) (Fig. 1.9 - B).

The hindered diffusion model postulates that obstacles and transient binding interactions hinder the extracellular diffusion of molecules. In this scenario, the cell packing generates a tortuosity, which strongly influences the movement of extracellular molecules, as they must go around the cells reducing their overall dispersal. Moreover, transient binding to receptors or extracellular matrix components might further hinder morphogen movement generating a spatio-temporal gradient (Nicholson & Syková, 1998) (Fig. 1.9 - C & D).

The facilitated diffusion model is an extension of the hindered diffusion model since a negative diffusion regulator immobilises the morphogens until a positive diffusion

regulator interferes with the former binding allowing their mobilisation (Fig. 1.9 - E). Another scenario involves shuttle molecules. When they are produced at a localised source, the immediate morphogens bind forming a shuttle complex that diffuses away. However, as the shuttle degrades, the morphogen is immobilised again creating a gradient (Sawala et al. 2012) (Fig. 1.9 - F).

Alternative to the extracellular diffusion mechanisms. The morphogens could be transported by two distinct intracellular mechanisms, transcytosis or cytonemes. In the transcytosis model, the morphogen is uptaken (endocytosis) and released (exocytosis) by the cells. Repetition of this event leads to the graded dispersion of morphogens throughout the target field (Fig.1.9 - G) (Gallet et al. 2008). In the cytonemes model, the cells use filopodial-like structures, known as cytonemes to transport morphogens. In this scenario, the target cells project cytonemes to the morphogen-producing cells. The morphogen transport through this extracellular extension forms a concentration gradient (Kornberg, 2012) (Fig. 1.9 - H).

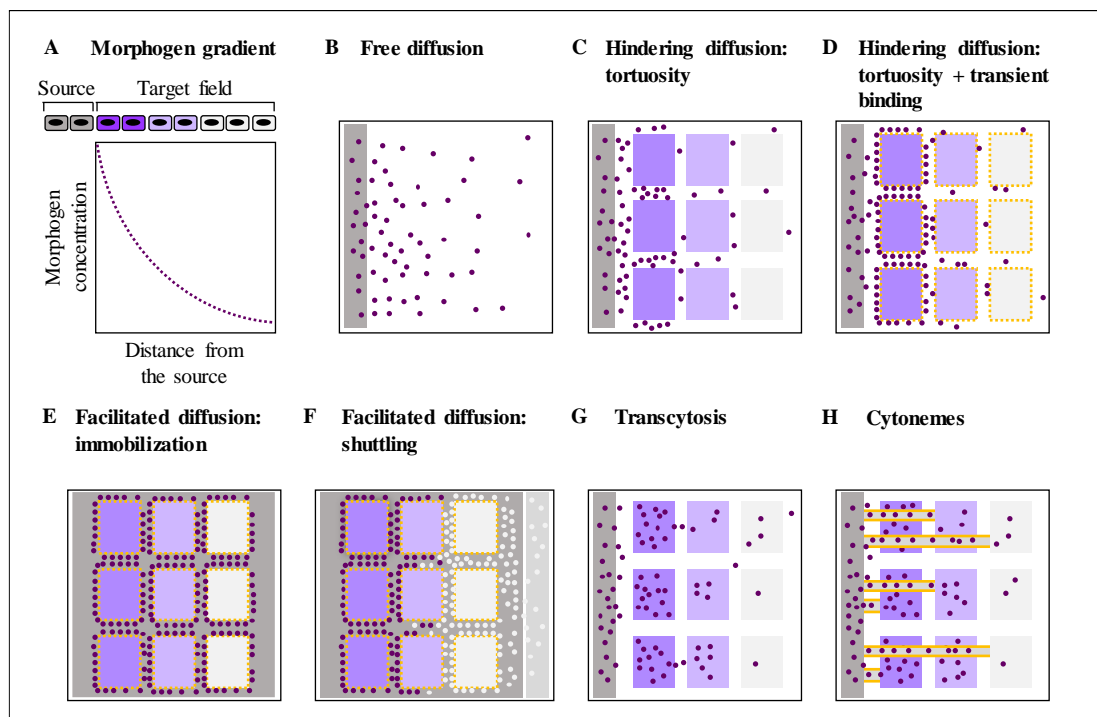


Figure 1.9 Morphogen transport models illustrations. (A) Morphogens secreted from a source of cells (dark grey) diffuse through the target field exposing the cells to different concentrations and based on the threshold they will exhibit distinct responses (purple, lilac and light grey) (Kicheva & González-Gaitán, 2008). Here are illustrated distinct diffusion or transport mechanisms that generate morphogen's gradients. (B) In the free diffusion model, morphogens (purple dots) diffuse from the source (dark grey) through the target field (white) where their clearance due to short life or cell

binding creates a gradient. (C & D) Regarding the hindered diffusion, morphogens movement is restricted by obstacles and/or binding to a receptor or extracellular components. (E) Similarly, in a facilitated diffusion, the diffusion of morphogens is restricted and enhanced by interaction with negative and positive diffusion regulators, respectively. (F) A special case utilises shuttle molecules that bind, diffuse away the morphogens and when they degrade, the morphogen is immobilised again generating a gradient. Finally, an alternative to the extracellular diffusion mechanism, morphogens may be transported through the cells (transcytosis) or along cellular extensions (cytonemes). Illustrations modified from (Muller et al. 2013).

The significance and relevance of these various mechanisms for BMP-2 gradient formation remain to be clarified. However, it is evident that the gradients are crucial for bone development and regeneration. Thus, understanding and replicating such spatio-temporal distribution of morphogens in the design of novel and biomimetic gels will likely be of critical importance for more effectively harnessing BMP-2 in regenerative medicine.

1.3.2 Therapeutic application of BMP

Understanding of the molecular biology of the bone and more specifically the role of BMPs signalling in bone healing has led to the identification and characterisation of more than 30 family members, of which BMP-2 and BMP-7 have shown the strongest osteoinductive capacity. Today, these molecules referred to as human recombinant BMP-2 and BMP-7 are produced and purified for therapeutic applications (Ducy & Karsenty, 2000, Agrawal & Sinha 2016 and El Bialy et al. 2017). In this section, their clinical application will be discussed, along with the benefits and limitations of existing and new delivery strategies.

In 2001, the Food and Drug Administration (FDA) and the European Medicines Agency (EMA) approved the use of BMP-7, marketed as OP-1® for the treatment of long bone fracture. To deliver the product into the defect, a powder containing 3.5 mg of BMP-7 with 1 g of bovine collagen (type I) was reconstituted with 3 to 5 ml of sterile saline with further addition of carboxymethylcellulose to make a putty (Agrawal & Sinha, 2017). Despite the claimed osteoinductive capacity, this product failed to demonstrate a higher efficacy in comparison with autogenous bone graft (Vaccaro et al. 2008). For this reason, in 2014, its use was discontinued in the United

States (El Bialy et al. 2017). Although it is still used in other countries for long bone fracture and alveolar cleft reconstruction (Moghaddam et al. 2016 and Ayoub et al. 2016).

Another morphogenic protein approved by the FDA in 2002 to treat long bone fracture, lumbar spine fusion and maxillofacial reconstruction was BMP-2, marketed as infuse™ (Krishnakumar et al. 2017). The lyophilised formulation contains 1.5 mg/ml BMP-2 after reconstitution, which is delivered into the defect along with an absorbable collagen sponge (El Bialy et al. 2017). As bone graft, the BMP-2 has shown a superior performance than BMP-7. For example, a study performed in 2014 by Conway et al. demonstrated BMP-7 having less efficacy than BMP-2 in the treatment of long bone fracture since the patients treated with BMP-2 showed better healing and faster recovery.

Furthermore, the use of BMP-2 augmented the success of numerous procedures, including dental surgeries, articular cartilage damage, open tibia fractures, cancer and paediatric use. It showed a positive effect on the consolidation of osteogenic defects, with no sign of rejection or infection. Patient morbidity and hospital stay were also reduced in comparison to bone grafting treatment (Gautschi et al. 2007 and Poon et al. 2016), becoming the second-line treatment in non-union bone defect after autogenous iliac crest bone graft (Agrawal & Sinha, 2017).

Maintaining spatio-temporal concentrations of BMP is crucial for bone repair. However, owing to its fast clearance from the collagen sponge and proven short half-life, supra-physiological doses are usually applied to maintain effective local concentrations. As a result, the excess of protein circulating in the system caused numerous unforeseen side effects, such as postoperative inflammation, ectopic bone formation, osteolysis, excessive immune response, postoperative neurological impairment, compromised airways and cancer (Zara et al. 2011, Hustedt & Blizzard 2014, Suliman et al. 2015, James et al. 2016 and El Bialy et al. 2017).

Regardless of the side effect, owing to the vital function of BMPs, especially BMP-2 during development and bone healing, substantial research effort has been focused towards developing an effective delivery system to lower the administered dose,

localise and prolong its retention time at the site of action. Also, to preserve the protein stability with the aim of improving its bioactivity and therapeutic potential (El Bialy et al. 2017).

1.3.3 Current state of the art in biomaterials and nanotechnology to deliver BMP and other growth factors

Current delivery systems research not only pursues to localise and reduce BMP dosage to prevent side effects but to recapitulate other essential features of the bone healing process, including the spatio-temporal localisation of BMP signalling. Their deliberate incorporation into the design aims to enable and allow greater control over cellular responses.

Thus, in order to mimic the spatio-temporal signalling, different physical and chemical immobilisation techniques have been developed to localise and control BMP, and other growth factor release from a substrate carrier. Such carriers include hydrogels, microspheres, nanoparticles, fibres or solid structures made of metals, ceramics, polymers and composites (Mehta et al. 2012 and Agrawal & Sinha, 2017). Next, will be reviewed various approaches to immobilising growth factors, hydrogels as a biomimetic carrier of growth factors' gradients and 3D patterning techniques.

1.3.3.1 Immobilisation of growth factors

Physical entrapment

Physical entrapment of BMP-2 takes advantage of electrostatic interactions, hydrophobic interactions or hydrogen bonds to bind proteins to a substrate and regulate their release by either protein desorption, swelling or degradation of the substrate (King & Krebsbach 2012 and Li & Mooney 2016). Generally, the loading techniques of proteins based on physical entrapment are quite simple, versatile and do not require expensive equipment (Migliorini et al. 2016). Next, some techniques are briefly described.

Physical adsorption is considered the simplest form to deliver proteins where the substrate carrier is soaked into the protein solution. For example, loading of BMP-2 into collagen (infuse™) or gelatin sponge. A similar approach can be used to functionalize substrate surfaces, such as ceramics, bovine or coral derived hydroxyapatite and tricalcium phosphate (Uludag et al. 1999). Another technique involves mixing the protein with the substrate carrier. For example, homogenisation of BMP-2 with polyethylene glycol hydrogel and synthetic bone substitute (Cha et al. 2018), collagen paste (OP-1®) or clay-gel (Gibbs et al. 2016) leads to the entrapment of the molecules. Nevertheless, the main limitations of these techniques are the loading efficiency and/or poor control of the release kinetics in vitro and in vivo (King & Krebsbach 2012 and Draenert et al. 2013).

Some degree of retention and/or release could be attained by varying specific properties of the material substrate, including surface charge, wettability, roughness and the presence of functional groups (King & Krebsbach 2012). For example, functionalized smooth titanium surface with heparin facilitates the physical adsorption of BMP-2 owing to their binding affinity. This system demonstrated a controlled release of the growth factor and enhancement of bone formation and osseointegration compared to pristine titanium in vivo (Yang et al. 2017). However, significant control over the BMP-2 release profile was achieved when the protein was entrapped into a layer-by-layer polyelectrolyte film that could be assembled either over polymeric or metallic substrates (Macdonald et al. 2011, Shah et al. 2011). For example, Bouyer et al. (2016) coated a (poly(lactic-co-glycolic acid) (PLGA) tube with a polyelectrolyte film made of poly(L-lysine) and hyaluronic acid, which was later cross-linked and loaded with BMP-2. In this study, the release profile of BMP-2 was successfully regulated by tuning the degree of crosslinking of the film. Moreover, the in vivo study revealed a complete bridging of a rat femoral critical-size defect after two weeks.

Another technique that has shown control over the protein release profile is the incorporation of encapsulated BMP-2 in nano or microparticles into a substrate carrier (Jeon et al. 2008, Patel et al. 2008 and Hettiaratchi et al. 2017). For example, Wei et al. (2007) demonstrate that encapsulated BMP-7 in PLGA nanospheres

incorporated into a polylactic acid (PLA) structure was able to control the release of BMP-7 as a function of time, inducing effective bone formation in a rat model.

The physical entrapment techniques are promising; however, it should be considered that the bioactive state of the protein can be affected by the orientation, conformation, and accessibility of its bioactive site when adsorbed on the substrate surface (Thyparambil et al. 2015).

Chemical crosslinking

Another approach is, therefore, to use chemical crosslinking, which tends to allow a more stable and sustained release in comparison to physical entrapment. In this type of immobilisation, both the protein and the substrate carrier are usually functionalized with reactive groups so that the protein can be covalently coupled to the substrate. Thus, the protein can be chemically modified or genetically engineered containing reactive groups, such as thiols, acrylates and azides (Lienemann et al. 2012) and the substrate with hydroxyl, amine and carboxyl groups. For example, azide functionalized BMP-derived peptide biomolecules were grafted to a poly(lactide-co-ethylene oxide fumarate) hydrogel via click chemistry (He et al. 2008). Finally, upon chemical immobilisation of the protein, the release can be mediated by either hydrolysis or reduction reaction or cells mediated enzymatic cleavage (Censi et al. 2012).

However, the stability of the biological activity of the protein still represents an issue since controlling the modification site have proven difficult and could potentially block the active sites or alter the protein conformation. Moreover, it is time and cost consuming, and the chemistry used may affect the protein activity and the overall biocompatibility of the carrier (Migliorini et al. 2016 and De Witte et al. 2018).

1.3.3.2 Biomimetic carrier

Hydrogels are attractive candidates for various tissue engineering and regenerative medicine applications since their innate biocompatibility, hydrophilicity and aqueous permeability allows the fabrication of structures that mimic the native extracellular

matrix of different tissues or delivery systems of bioactive factors with controlled release profile (Hoare & Kohane 2008, Lee et al. 2008 and Geckil et al. 2010). Advances in materials science have led to the design of “smart hydrogels” that may swell, self-assemble or degrade at defined rate upon response to specific physical and chemical stimuli by simply altering their composition, crosslinking and fabrication method (Vermonden et al. 2012 and Ahmed, 2015).

Conventionally, their water-swollen polymeric 3D network consists of hydrophilic polymers, and based on their source, the properties of the hydrogel may vary, showing different advantages and limitations. In this regard, synthetic polymers consist of a basic structural unit that allows the design of synthetic hydrogels with tuned mechanical properties and porosity, controlled degradation rate, potentially long shelf lives and higher strength and capacity for water content (Khansari et al. 2017 and Bai et al. 2018). These hydrogels are prepared by chemical polymerization techniques. For example, polyacrylamide, polyethylene glycol and poly (2-hydroxyethyl methacrylate) (Khansari et al. 2017). However, poor biological activity and adverse tissue response to acidic degradation are their main limitations (Fu et al. 2000 and De Witte et al. 2018). Alternatively, natural hydrogels seem to be better candidates since they show superior chemical biocompatibility and bioactivity owing to the presence of protein-ligands and can be absorbed through metabolic or enzymatic-controlled degradation (Bai et al. 2018). Generally, they are extracted from natural sources, such as polysaccharide (glucan, hyaluronic acid, chitosan agarose and alginate) and proteins (collagen, gelatin, fibrin and silk). (Van Vlierberghe et al. 2011 and Ruedinger et al. 2015). However, some limitations include reduced control over the degradation rate, poor mechanical strength and stability, batch variability, inactivation induced by sterilisation, potential immunogenicity, and fabrication cost (Zhao et al. 2013 and Agrawal & Sinha, 2016).

Combination of both natural and synthetic polymers allows the synthesis of hybrids or semisynthetic hydrogels with modifiable physical, electrical and chemical properties and improved mechanical properties. However, further work is required to evaluate the long-term biocompatibility, nanotoxicity and mechanical strength. (Khansari et al. 2017).

There is another group of materials that lie between natural and synthetic polymers. It includes self-assembly peptides and artificial proteins. These materials are not naturally occurring yet composed of natural building blocks. The self-assembly peptides can be synthesised via solid-phase chemistry. Generally, they consist of hydrophobic and hydrophilic domains of residues and/or lipid chains strategically placed to support self-assembly of well-defined structures (nanofibers, nanotubes or nanovesicles) via non-covalent interactions, such as hydrogen bonding, electrostatic attraction and van der Waals forces, and the process can be triggered by external stimuli, such as electrolytes, temperature, and pH (Dehsorkhi et al. 2014 and Chen & Zou, 2019). This nanomaterial has shown good biocompatibility, controlled degradation and the possible introduction of self-healing, shape memory and shear-thinning properties. However, there are several challenges. The stability and consistency need to be improved, further understanding of the immunogenic mechanism is required, synthesis of proteins with hundreds of residues remains a challenge (Cui et al. 2010 and Chen & Zou, 2019).

Regarding the artificial proteins, also known as “recombinamers” are synthesised by bacterial expression of artificial genes. These macromolecules consist of multidomain or complex monomers that repeat few times generating artificial proteins with a molecular mass comparable to that of conventional polymers. Moreover, they undergo reversible gelation in response to changes in pH or temperature (Petka, 1998 and Rodríguez-Cabello et al. 2009). These materials are biocompatible, biodegradable, non-immunogenic, stimuli-responsive, bioactive and with self-assembly properties. However, the concatenation of genes encoding for large macromolecules over 100 kDa remains a challenge and the incorporation of phosphorylated sites (Despanie et al. 2016).

As well as the nature of the polymer itself, the crosslinking method between the polymer chains affects various properties of the hydrogel. In this regard, a chemical or permanent crosslinking allows control over the degree of porosity and interconnectivity, which directly influence the mechanical properties, degradation rate and perfusion of the hydrogels. However, the organic solvent, unreacted chemical cross-linkers and by-product may be detrimental for the hydrogel cytocompatibility (Hu et al. 2019). Thus, another option is the self-assembly of

hydrogels through physical interactions. This type of crosslinking, such as electrostatic interaction, hydrogen bonds and hydrophobic/hydrophilic interactions gives reversible hydrogels that can flow and assemble in situ in response to different environmental triggers (e.g. pH, ionic strength or temperature). However, it is difficult to control the degree of porosity and pore size, and mechanical properties (Hoare & Kohane, 2008).

Finally, careful selection of the fabrication method is crucial as it determines the effective time and cost. For example, the use of equipment, such as electrospinning and 3D printers to modulate the micro and macrostructure of the hydrogel increases the manufacturing cost and creates challenges for clinical translation. In this regard, self-assembling gels that form in situ are attractive. However, these approaches often rely on the design and synthesis of molecules, such as genetically engineered proteins, which can also increase the cost and present challenges for clinical development and regulation (Xu et al. 2005).

1.3.3.3 3D patterning techniques

Notwithstanding the challenges above mentioned, a substantial amount of research has sought to generate spatio-temporal control over signalling on a substrate carrier in order to recapitulate the complex 3D patterning of bioactive factors observed during tissue development and regeneration. In this regard, hydrogels have emerged as a powerful candidate material since their polymeric three-dimensional network not only generates a structure similar to the extracellular matrix but also allows the loading of proteins with 3D spatial localisation, which can be achieved through different top-down and bottom-up techniques, including photo-patterning, electrophoresis, 3D printing, reaction-diffusion and microfluidics. Next, will briefly be presented some techniques; however, further details, advantages and limitations can be found in the introduction of the results' chapter 4.

The 3D photo-patterning technique consists in the 3D patterning of a hydrogel bulk with activated photosensitive groups, which later serves to anchor proteins, creating a gradient. For example, photosensitive molecules present in an agarose matrix were

activated using a laser light source. The exposure of functional groups allowed the coupling of cell-adhesive RGDS peptide (Luo & Shoichet, 2004) (Fig. 1.10 - A).

Another approach takes advantage of the electrophoresis technique commonly used in molecular biology to separate and analyse macromolecules (e.g. DNA, RNA and proteins). However, for this application, a mask is placed between the protein source (e.g. Immunoglobulin G, elastin and fibronectin) and the hydrogel (e.g. poly(ethylene glycol) diacrylate (PEGDA) pristine or containing gelatin (PEGDA-GelA) to guide the 3D spatial distribution of proteins that migrates along the direction of the electric field (Aguilar et al. 2018) (Fig. 1.10 - B).

Regarding the extrusion-based 3D printing technique, it allows printing viscoelastic fluids or gels containing growth factor by depositing then layer by layer with a pre-determined design assisted by a computer. For example, Liu et al. (2017) were able to print multiple biomaterials (e.g. hydroxyapatite, gelatin-methacryloyl (GelMA)/alginate bioink) to make complex 3D constructs using a seven-channel printer-head that is connected to individual reservoirs (Fig. 1.10 - C).

Reaction-diffusion systems play a key role in the spontaneous formation of patterned structures in nature, from the embryonic development to sand ripples (Ball, 2015). Researches have used the principles of this system to develop a bottom-up technique for the 3D patterning of biomolecules. In this regard, two reactants (e.g. hydrazide and aldehyde) positioned at opposite sides of a hydrogel matrix (e.g. agar) diffuses towards each other, and their chemical reaction at the diffusion fronts leave a pattern inside the hydrogel, which can be potentially used to anchor proteins (Lovrak et al. 2017) (Fig. 1.10 - D).

Finally, open microfluidics has been recently used to assembled free-standing hydrogels with gradients concentration of macromolecules, which could be potentially used for the 3D patterning of growth factors in the near future. In this regard, Lee et al. (2019) designed a device that allows the progressive deposition of hydrogel layers (e.g. agarose) with different concentrations manually (Fig. 1.10 - E).

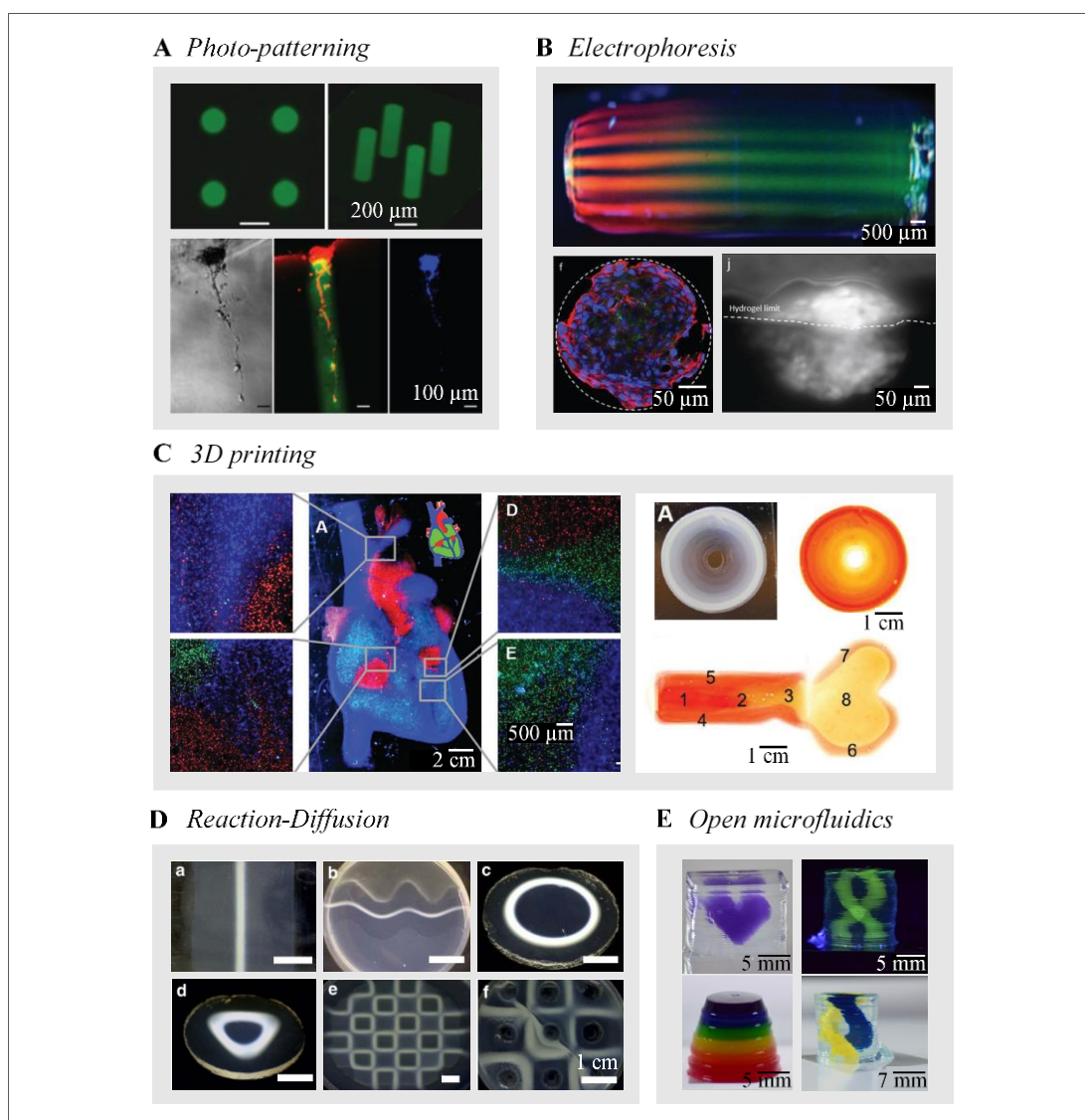


Figure 1.10 Top-down and bottom-up techniques used for the assembly of hydrogels with 3D patterns of macromolecules. (A) Fluorescent images of photo-patterned agarose matrix with channels of GRGDS oligopeptide-modified (green fluorophore) reveals the migration and extension of primary rat dorsal root ganglia cells (red fluorophore) into the channel (Luo & Shoichet, 2004). (B) A modified electrophoresis machine (3DEAL) was used to print Immunoglobulin G (red) and elastin (green) gradients within polyacrylamide-GelA hydrogel (top image). Moreover, NIH-3T3 cells seeded onto polyacrylamide-collagen hydrogel functionalized with fibronectin localised into the patterned regions. However, their migration into the hydrogel was not significant after 14 days (Aguilar et al. 2018). (C) 3D printing by extrusion with a multiple channel print-head was used to build layer by layer a heart-like structure with a bioink of GelMA and alginate containing microbeads (blue and red fluorophores) and human dermal fibroblast (green fluorophore). Also, a cylinder and bone-like structure were printed with GelMA/alginate bioink containing a gradient of hydroxyapatite as revealed by the alizarin red staining (Liu et al. 2017). (D) A free-standing hydrogel was assembled by reaction-diffusion of hydrazide and aldehyde reactants, which were placed in different reservoirs of an agar matrix to obtain patterns with distinct shapes (Lovrak et al. 2017). (E) Various agarose structures built

using rail-based open microfluidics. A purple agarose heart inside colourless agarose (top, left), cylindrical structure with double helix-like internal space filled with inks for visualisation (top & bottom, right) and structure with multiple agarose concentration containing different dyes to visualise the gradient (Lee et al. 2019).

These techniques are promising for the 3D patterning of bioactive factors. However, they are on an early stage of design and optimisation. Thus, further work is required to evaluate the functionality of patterned hydrogels *in vivo* in comparison to the protein release systems, and more specifically for bone tissue engineering applications. Up to now, their main disadvantage is the time and cost associated with the hydrogel manufacture and equipment.

Note that the layer-by-layer polyelectrolyte was not included in this review because the technique does not generate a free-standing macrostructure. Also, in this scenario, they are mainly used to control the release profile of bioactive factors.

1.4 Clay-gel nanoparticles as a therapeutic delivery system

1.4.1 Clay nanoparticles

Some clay nanoparticles are able to generate highly hydrated colloidal gels, which offer similar advantages to certain physically cross-linked polymeric hydrogels. In this regard, colloid gels consist of colloidal network immersed in a fluid that forms soft-solid materials characterised by finite shear viscosity regardless of their disorderly molecular organisation and their capacity to exhibit viscoelastic stress relaxation (Kavanagh & Ross-Murphy, 1998 and Douglas, 2018).

Interestingly, colloidal clay gels have emerged as a promising alternative material for the design of drug delivery systems due to their high sorptive capacity, biocompatibility and bioactivity (Dawson & Oreffo, 2013).

Clay nanoparticles are crystalline structures built up of one or more phyllosilicate minerals or alternating silicate tetrahedral sheet and octahedral sheet containing either Mg, Al or Fe. The structure and composition of naturally occurring clays vary

significantly depending on their geological origin. They are often categorised according to the composition and arrangement of their octahedral and tetrahedral sheets into different families, such as kaolinite, smectite (or bentonite) and palygorskite-sepiolite family (Gaharwar et al. 2019). Clays have been widely used for curative and protective purposes by humans since ancient times, and more recently, the advantages of clay nanoparticles, in particular, the smectite groups have been investigated and exploited for different biomedical applications including the formulation of pharmaceutical products as active principle or excipient or cosmetics (Tomás et al. 2018). More recently, their use in regenerative medicine has gained interest since their synthetic option, known as Laponite® (XLG) produced by BYK Additive and Instruments, eliminated the inhomogeneity and impurities of naturally occurring clays that made them unsuitable and risky for parenteral administration or implantation, providing a material with highly controlled purity, composition and dimensions (Tomás et al. 2018 and Gaharwar et al. 2019). Also, with low levels of heavy metals and as a result, proven minimal toxic effects (Gaharwar et al. 2013).

Laponite® is a synthetic clay mineral that belongs to the smectite group of phyllosilicates. It is constituted by 2:1 crystalline layered units, where two tetrahedral silica sheets sandwich one magnesium octahedral sheet, giving rise to a disk-shaped particle of approximately 25 nm in diameter and 0.92 nm in height with an empirical formula of $\text{Na}^{+0.7}[(\text{Si}_8\text{Mg}_{5.5}\text{Li}_{0.3})\text{O}_{20}(\text{OH})_4]^{-0.7}$ (Mousa et al. 2018). The chemical structure provides them with a dual distribution of charges, specifically a permanent negative charge on the surface and a positive charge at the edges, which changes with the surrounding pH (Dawson & Oreffo, 2013) (Fig. 1.11).

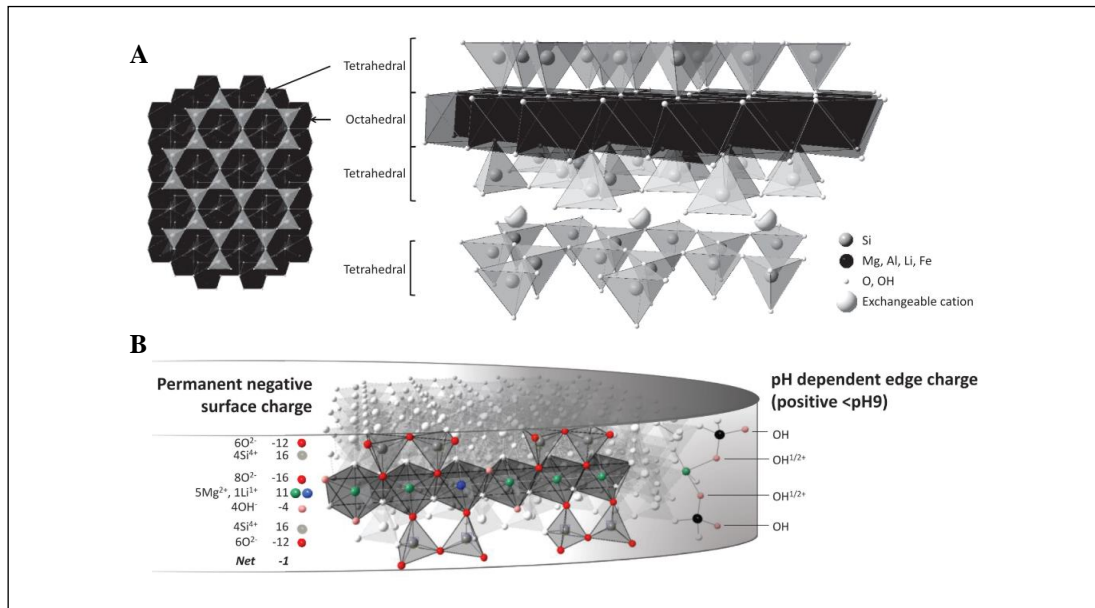


Figure 1.11 The structure of smectites. (A) In this case, clays are constituted by two tetrahedral silica sheets sandwiching an octahedral sheet of metal oxides, usually Al^{3+} or Mg^{2+} . (B) Smectites exhibit dual charge distribution, a permanent negative surface charge generated from isomorphic cation substitution in the crystal structures and a pH-dependent positively charged edge due to broken Si-O, Al-OH and Mg-OH groups. (Dawson & Oreffo, 2013 and Mousa et al. 2018).

The anisotropy related to the geometrical shape and charge distribution attributes distinctive characteristics to clay nanoparticles dispersions (or colloidal solutions), as their interactions can lead to a variety of structural arrangements (or phases), which may undergo spontaneous evolution (or ageing) towards the equilibrium or a more stable state, implying that the observable physical characteristic of the system, such as nanoparticles diffusion and viscosity of the dispersion evolves with time (Jabbari-Farouji et al. 2008).

Generally, the behaviour of the colloidal system comprising charged particles like clay nanoparticles can be explained by the classical Derjaguin-Landau-Verwey-Overbeek (DLVO) theory, which postulates that the stability/instability of colloidal particles in suspension is determined by the balance of electrostatic interaction (repulsive) and van der Waals interaction (attraction) between particles (Ohshima, 2014). The repulsive electrostatic interaction is produced by a cloud of counter-ions and co-ions that builds around a colloidal particle, also known as electric double-layer (Ohshima, 2014). Thus, when the repulsive electrostatic interaction becomes

significant, the colloids remain stable and separate, forming a dispersion (Fig. 1.12 - A). However, when the electrostatic repulsion is screened, the colloids undergo steady aggregation and settle out of suspension (flocculation) or form an interconnected matrix (gelation) under the influence of the van der Waals attraction (Fig. 1.12 - B).

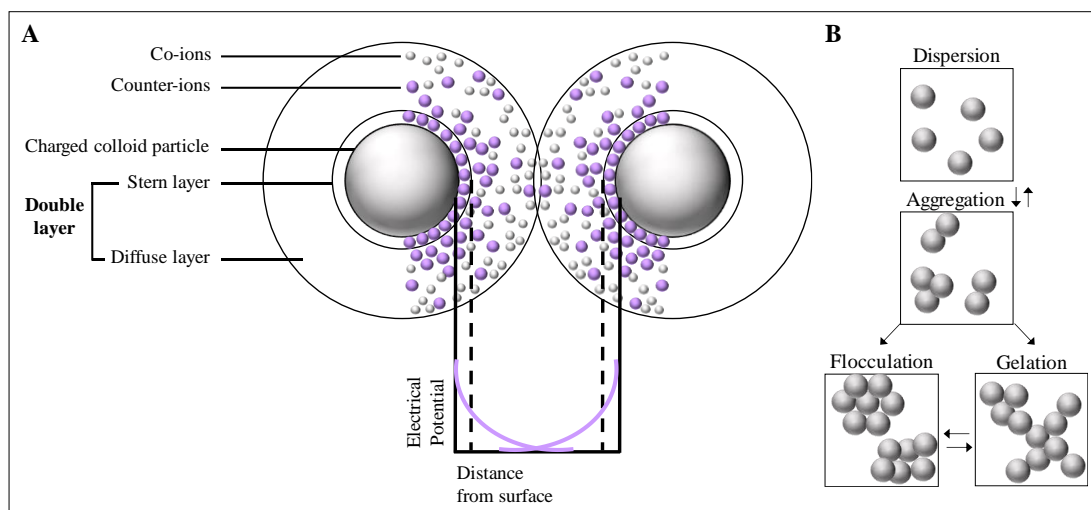


Figure 1.12 Double layer model. (A) In an ionic environment, a double layer of ions forms around individual charged colloidal particles creating a “like” electrical charge, which determines the interparticle interaction and, therefore, the characteristic of the suspension. The electrical double layer is constituted by a (Stern) layer of counter-ions firmly attached to the surface of the colloid and a second (diffusive) layer of counter-ions and co-ions gradients. The figure shows a colloid surrounded by a charged atmosphere, which thickness will depend upon the type and concentration of ions in the solution and subsequent overlapping of the electrical double layers of two particles causes their repulsion (Adair et al. 2001). (B) However, screening of the electrostatic interactions triggers the aggregation of the dispersion that may undergo flocculation or gelation.

Upon movement of a colloidal particle in the dispersion medium, a layer of the surrounding liquid remains bound to the particle. The boundary of this layer is called the slipping plane (shear plane) (Fig. 1.13). The magnitude of the electrical potential or zeta potential at the slipping plane of an individual colloidal particle is often used as an indicator to predict their interaction and the colloid stability. Generally, colloidal particles with zeta potential values greater than ± 25 mV are in a dispersed state and have high degrees of stability as the repulsion forces between neighbouring particles are enough to keep them separate. On the contrary, dispersions with low zeta potential value ($< \pm 25$ mV) will eventually aggregate due to van der Waals inter-particle attractions. For example, 0.5 and 1wt% Laponite® dispersions display

liquid-like behaviour, which suggests that the nanoparticles must be interacting repulsively to form a liquid-sol. This assumption is supported by corresponding high negative zeta potential values, - 49.2 mV (at 0.23 mS/cm and pH 8.2) and - 62.5 mV (at 0.39 mS/cm, pH 10.0), respectively (Au et al. 2015).

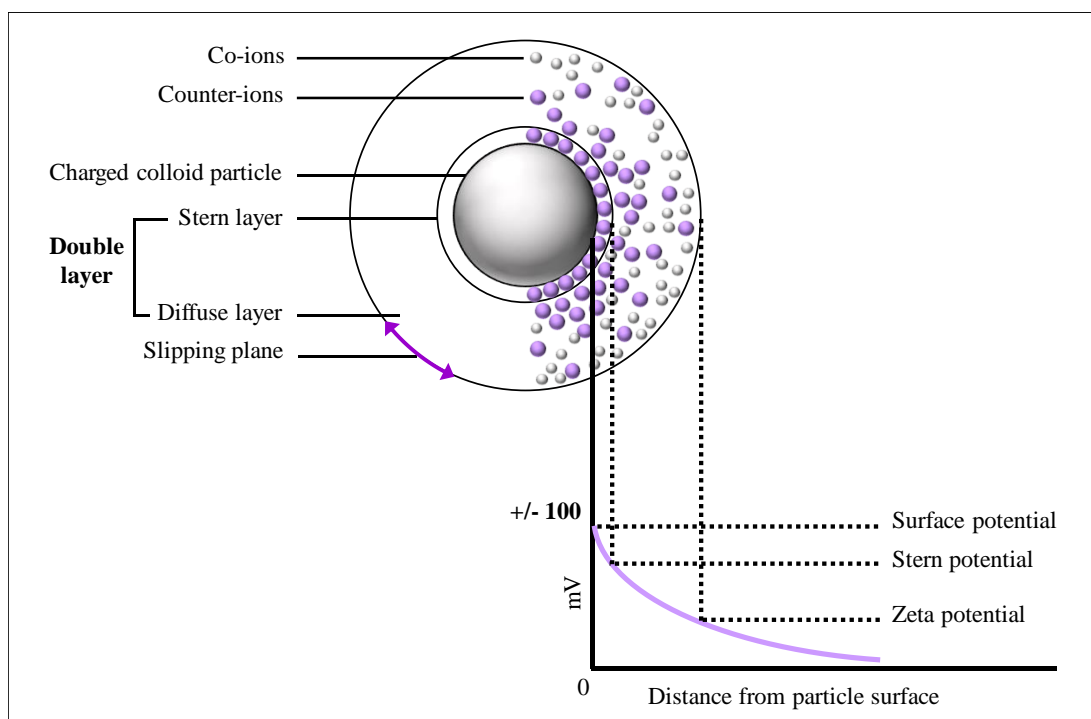


Figure 1.13 Zeta potential of colloidal dispersions. Generally, the magnitude of the electrical potential or zeta potential of colloidal particles at the slipping plane is often used as an indicator to predict their interaction and the colloid stability. In this regard, zeta potential values over +/- 25 mV suggest that the particles are dispersed and stable. On the contrary, the values under +/- 25 mV indicate that the particles will eventually aggregate. Illustration modified from Park & Seo, 2011.

The interactions between the charged colloidal nanoparticles can be tailored by adjusting the pH, ionic strength or by addition of polymers or surfactants as they affect the range of the double-layer interaction. In this regard, with increasing salt concentration, the surface potential decreases as electrostatic screening suggests. In turn, this will increase the attraction between the colloidal nanoparticles leading to their aggregation (Adair et al. 2001). Interestingly, the absorption of polymers or surfactants onto the colloidal particle may stabilise the colloidal dispersion by creating a steric barrier around the particle that prevents their aggregation or on the contrary, trigger their flocculation by forcing the aggregation of the particle through depletion or bridging (Adair et al. 2001 and Gong et al. 2014) (Fig. 1.14 - A). Again,

measurement of the zeta potential can be used to predict the particles interaction and the stability of the system as a function of the environment changes. For example, a study performed by Au et al. (2015) on the zeta potential-pH behaviour of 1wt% Laponite® dispersions with and without pyrophosphate peptizer shows that the zeta potential is negative across the whole pH range 3 - 12.5 and increases with pH (-10mV at pH 3 and -40mV at pH 10). They suggest that the aggregation could be triggered by the incorporation of ions as the pH decreases or that the nanoparticles undergo degradation releasing cations that causes their aggregation. Interestingly, the addition of peptizer increases the negative zeta potential at any given pH. Thus, at high pH, the system is stable as the nanoparticles repel each other. However, as the pH decreases, the z-potential becomes less negative; therefore, the nanoparticles can agglomerate becoming unstable (Fig. 1.14 - B).

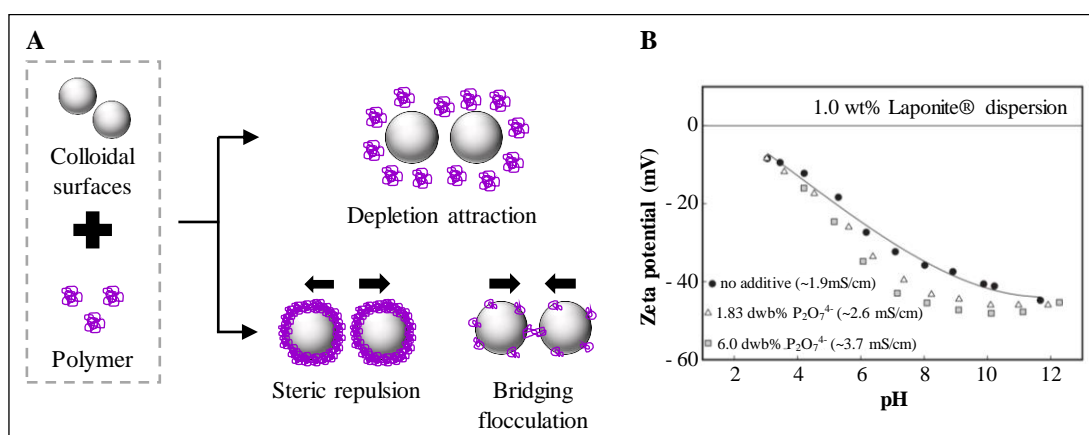


Figure 1.14 Behaviour of colloidal solutions with changes in pH and addition polymers or surfactants. (A) Incorporation of polymers or surfactants into a colloidal dispersion may stabilise it by preventing aggregation via steric barrier or trigger flocculation through depletion (where non-absorbed polymers generate gradients throughout the dispersion forcing the displacement and aggregation of the colloidal particles or bridging (where the ends of a polymer chain absorb onto different particles drawing them together) (Gong et al. 2014). (B) For example, the zeta potential of 1wt% Laponite® dispersion decreases or becomes less negative with the decrease in pH (-10mV at pH 3 and -40mV at pH 10), which leads to aggregation. Further addition of pyrophosphate peptizer (1.83 and 6.0 dwb% $P_2O_7^{4-}$) reveals a decrease in the zeta potential with respect the control, which may prevent aggregation. However, as the pH decreases, a progressive reduction of the steric repulsion effect is observed as well (Au et al. 2015).

In addition to the electrical potential, the analysis of other physical, chemical and mechanical properties of colloidal dispersions, such as pH, conductivity, light and x-

ray scattering and viscosity are performed alongside to understand the interparticle interaction and the overall behaviour of the system as a function of time or with changes on the colloid concentration, pH, ionic strength and temperature. Thus, in the next section, the metastable phase diagram of colloidal clay (Laponite®) as a function of clay concentration and ions will briefly be discussed, as understanding the material's internal structure and behaviour is crucial for the assembly of clay-based scaffolds.

1.4.1.1 Metastable phase diagram of colloidal clay (Laponite®)

Laponite® dispersions have shown a multiplicity of non-ergodic states, such as gels and glasses of different nature since the relative stability (or metastable state) is not able to reach equilibrium due to an arrest mechanism driven by different interparticle interactions (Awasthi & Joshi, 2009, Ruzicka & Zaccarelli, 2011, Rawat et al. 2014 and Au et al. 2015).

Thus, in pure water, clay nanoparticles dispersions form a liquid/sol phase at low clay concentrations ($< 1\%$). However, as the concentration increases from ~ 1 to 3% , this ergodic state (or state with the same behaviour averaged over time) transitions into different non-ergodic states, forming different gels and glasses as a function of concentration. In this regard, disordered gels are observed at low densities of between 1% to approximately 1.9% concentration. This is usually attributed to the formation of particle networks driven by face-to-edge attractive interactions. At densities between approximately 1.9% to 3% , the colloidal solution forms a disordered repulsive or Wigner glass. In this scenario, the particles do not form a network, but remain spatially disconnected and arrested in effective cages formed by (mainly repulsive) interaction with their neighbours (Tanaka et al. 2005, Cipelletti & Ramos 2005 and Jabbari-Farouji et al. 2008). Another type of Wigner glasses may form at lower concentrations, where clusters of clay particles are trapped in a disordered state by electrostatic repulsion. However, with the increase in density, competition between long-range repulsion and van der Waals attraction may lead to the transition of repulsive glasses into either attractive glasses or gels (Tanaka et al. 2004) (Fig. 1.15 - A to C).

Furthermore, the formation of ordered nematic gels has been observed over 2.8 % concentration. The gel exhibited a nematic-threaded texture under cross-polarised light caused by the periodic arrangement of the clay nanoparticles with the long axis roughly parallel (Lemaire et al. 2002, Mourad et al. 2006, Jabbari-Farouji et al. 2008, Shahin & Joshi, 2011) (Fig. 1.15 - D). Finally, a time-frame experiment of seven years showed the formation of empty liquids at concentrations under 1 % by separation of the clear liquid and the opaque gel phase, and also equilibrium gels over 1 % to 2 % concentration (Ruzicka et al. 2011) (Fig. 1.15 - E & F).

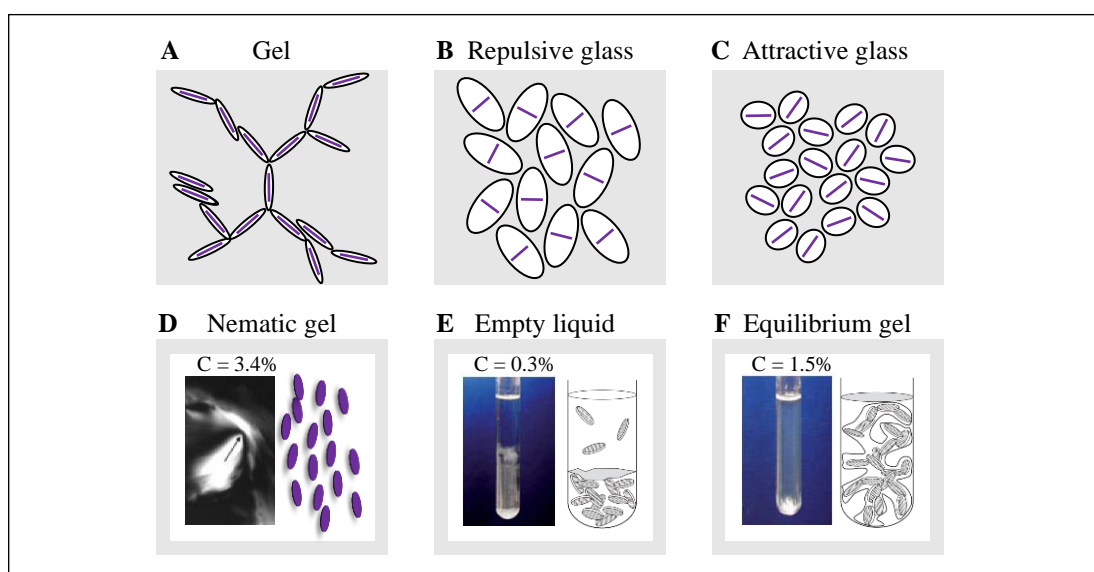


Figure 1.15 Metastable state of colloidal clays. Schematic illustrations of (A) gels' structure shows disordered clay nanoparticles (purple line) networks interconnected via face-to-edge by attractive interactions at low densities (1 - 1.9 %). On the contrary, (B) the repulsive or Wigner glass do not form networks (1.9 - 3 %). The clay nanoparticles are disconnected and arrested by long-range repulsive interactions with their neighbours (white ellipsoid represents the range of electrostatic repulsion). (C) The repulsive glass may transient into an attractive glass with an increase in density. Here the electrostatic repulsion range is shortened, so the clay nanoparticles are closer but still disconnected (Ruzicka & Zaccarelli, 2011). (D) Furthermore, ordered nematic gels were detected under at concentrations over 2.8 %. The gel exhibited a nematic-threaded texture under cross-polarised light (Lemaire et al. 2002). (E) Empty liquids were observed at concentrations under 1% by separation of a clear liquid and an opaque gel phase in a time-frame of seven years. (F) Also, equilibrium gels over 1 % to 2 % concentration (Ruzicka & Zaccarelli, 2011). The illustrations A, B and C were modified from Tanaka et al. (2004), D from Lemaire et al. 2002, and E & F from Ruzicka & Zaccarelli (2011).

Despite the mechanism governing the aggregation or transition between phases (gels and glasses) remains to be elucidated (Barbara Ruzicka & Zaccarelli, 2011), it is known that the temperature and additive, such as ions affect their phase transition or ageing similarly to the concentration matter above-described. In this regard, the ageing mechanism of the glass state of the colloidal clay becomes faster at higher temperatures (Awasthi & Joshi 2009). Furthermore, the increase of salt concentration may lead to the formation of attractive glasses as the attraction becomes dominant or to the macroscopic phase separation, also known as flocculation (Barbara Ruzicka & Zaccarelli, 2011) (Fig. 1.16).

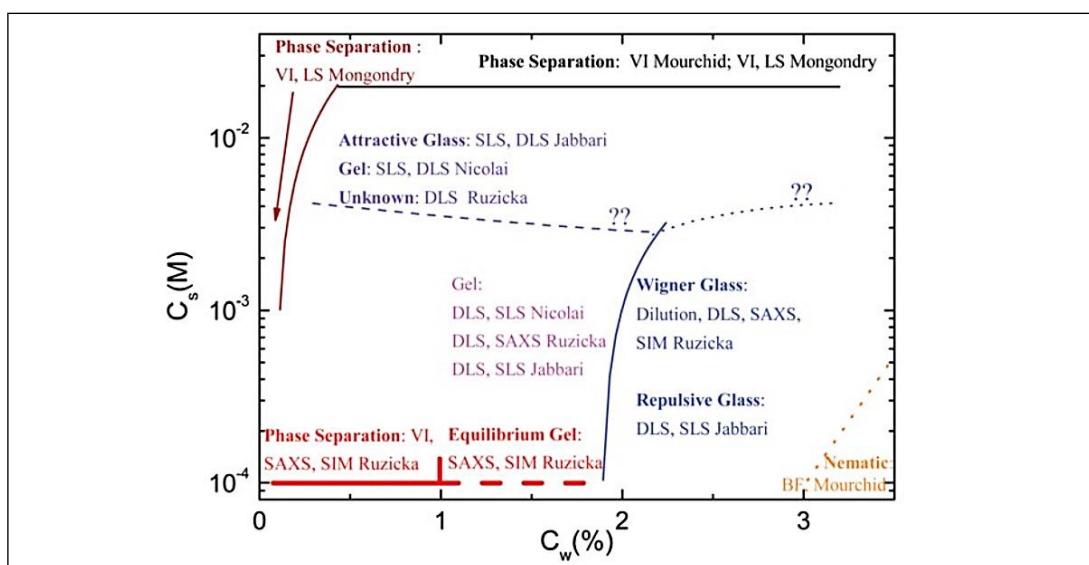


Figure 1.16 Phase diagram of Laponite® clay nanoparticles colloidal suspensions as a function of clay nanoparticles concentration (weight/ weight %) and salts (Molar). This graph compiles the data from different authors (Ruzicka & Zaccarelli, 2011).

Thus, understanding that colloidal clays may undergo distinct structural rearrangements is crucial for the design of scaffolds for tissue engineering applications, since their interaction with other molecules (e.g. ions, proteins, synthetic polymers) or exposure to physical factors (e.g. temperature, pressure) may alter their physical state and other properties. For example, Shi et al. (2018) reported that 2.8 % clay-gel stiffened into a stable gel via diffusion of concentrated ion solution. Interestingly, despite the system did not behave as expected and underwent flocculation, the approach was shown to have the potential for stem cell encapsulation and culture.

1.4.2 Opportunities of clay-gel nanoparticles for TERM

Laponite® XLG is a graded smectite clay with low heavy metal content potentially suitable for medical applications including in tissue engineering and regenerative medicine. In recent years, different formats of this material (e.g. nanoplatelet, sol or gel) have been exploited for numerous applications, such as a bioactive cell culture additive to modulate cells adhesion or differentiation, additive to crosslink or improve the mechanical properties of polymeric hydrogels or as a delivery system of drugs and biomolecules (Wang et al. 2010, Gaharwar et al. 2013 and Wang et al. 2013). The positive outcomes have been correlated to the distinct physico-chemical properties of the clay nanoparticles. Therefore, the next review will focus on describing the properties of clay nanoparticles that make them relevant for biomolecule delivery.

Sorptive capacity

In early studies, the main interest in clay nanoparticles was their sorptive capacity as delivery systems since their anisotropic structure and charge distribution supports distinct possible interactions with organic molecules, including the nanoparticle edges, surfaces, within the inter-layer pores or interparticle spaces through either cation-exchange, cation bridging, hydrophobic interactions, hydrogen bonding, anion exchange or proton transfer (reviewed by Dawson & Oreffo, 2013). Moreover, their high surface area ($> 350 \text{ m}^2 \text{ g}^{-1}$) provides them with a high chemical reactivity, which results positive for the sorption of biomolecules (Gaharwar et al. 2013) (Fig. 1.17 - A).

In this regard, a subcutaneous mouse model for ectopic bone formation demonstrated that gels of clay nanoparticles have the ability to bind and localise BMP-2 in space and time, restricting their diffusion from the implant site, improving their efficacy and reducing harmful ectopic effects. Moreover, the effective dose was significantly reduced, to sub-microgram per ml range, in comparison to those employed in clinical practice (1.5 to 2 mg/ml) and current carriers in research (Gibbs et al. 2016). Similarly, a construct of collagen sponge with clay-gel nanoparticles-containing BMP-2 and vascular endothelial growth factor (VEGF) revealed an enhancement in

neovascularization in a mouse femur segmental defect corroborating the capacity of the material to retain and localise the bioactivity of growth factors (Dawson et al. 2011) (Fig. 1.17 - B & C).

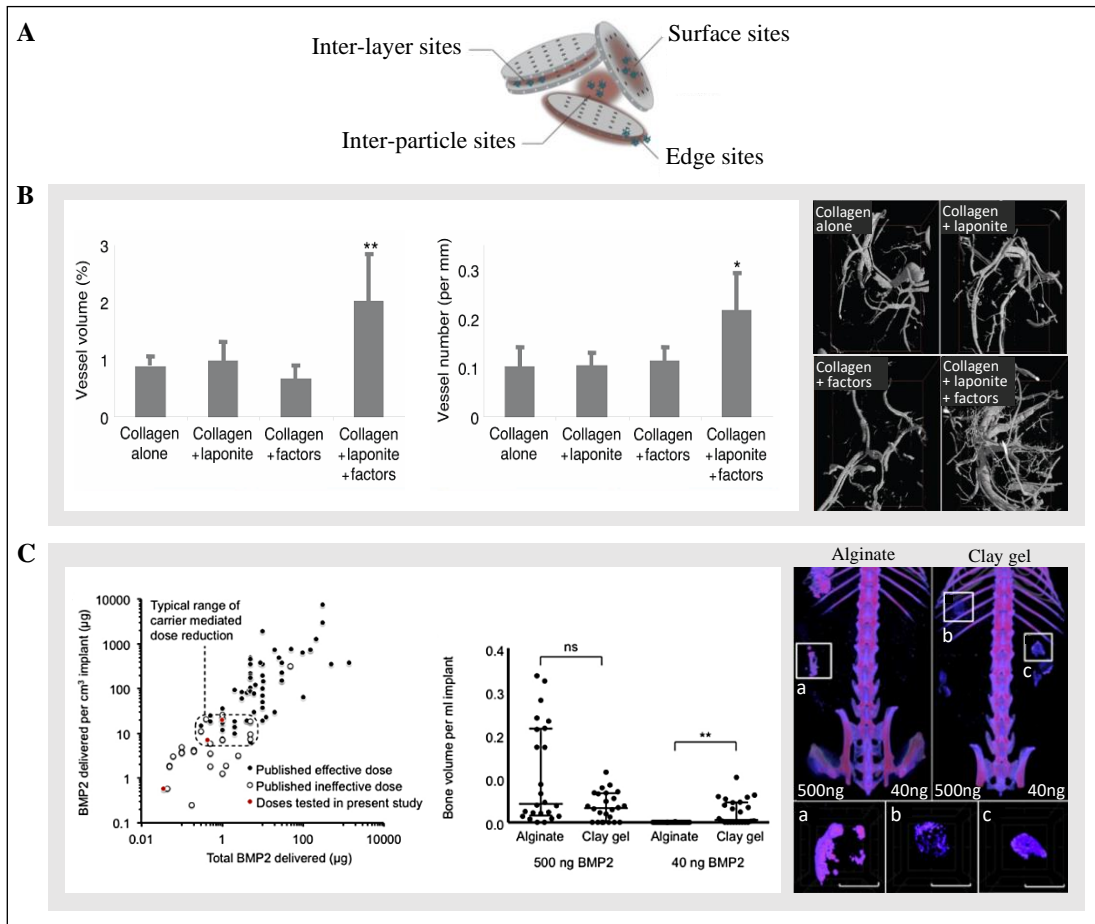


Figure 1.17 Sorptive capacity of clay nanoparticles. (A) Potential interactions between organic molecules and the clay particle surfaces, edges, inter-layer pores and inter-particle spaces involving a range of physical mechanisms. (B) Constructs of collagen sponge with clay-gel nanoparticles containing BMP-2 and VEGF were implanted in a murine critical-sized femoral defect. After 28 days, respective micro CT analysis revealed the formation of greater vessel volume in comparison to controls (area = 14 mm³). (C) 40 ng dose of BMP-2 encapsulated in clay-gel nanoparticles and perfused through a collagen sponge were implanted in a subcutaneous mouse model. After 28 days, they revealed localised and higher ectopic bone formation in comparison to the alginate control (scale bar 2.5 mm). Moreover, in contrast with the literature, the clay-gel significantly reduced the effective dosage (left graph). A & B figures were modified from Dawson et al. (2011) and C from Gibbs et al. (2016).

Self-assembly

Molecular self-assembly is ubiquitous in nature and has emerged as a new approach to fabricate novel supramolecular structures where molecules rearrange without guidance of an external source. As described on the previous section (1.1.1), the process consists in the spontaneous association of molecules by weak non-covalent bonds forming ordered structures with different size (micro- and submicrometre) and degrees of complexity (Whitesides et al. 1991), which is often determined by the shape and nature of the molecule.

In this scenario, the inherent anisotropic charge distribution of the Laponite® clay nanoparticles facilitate their delamination and self-assembly through mainly electrostatic interactions when dispersed in water, which leads to the formation of different structure, such as glass, gel or nematic. Moreover, the complexity of the self-assembled structures can be tuned by the addition of ions and polymeric molecules, making this material a good candidate to explore bottom-up approaches for tissue engineering and regenerative medicine.

For example, the pre-assembly of scaffolds outside the body with different shapes (e.g. droplets, rings and strings) via dropwise addition of clay-gel nanoparticles into an electrolyte solution (Dawson et al. 2011) (Fig. 1.18), or as injectable in-situ gelling material for local drug delivery (Page et al. 2019) since the reversible stress-induced fluidisation allows the clay-gel to pass through a needle with subsequent structural recovery.

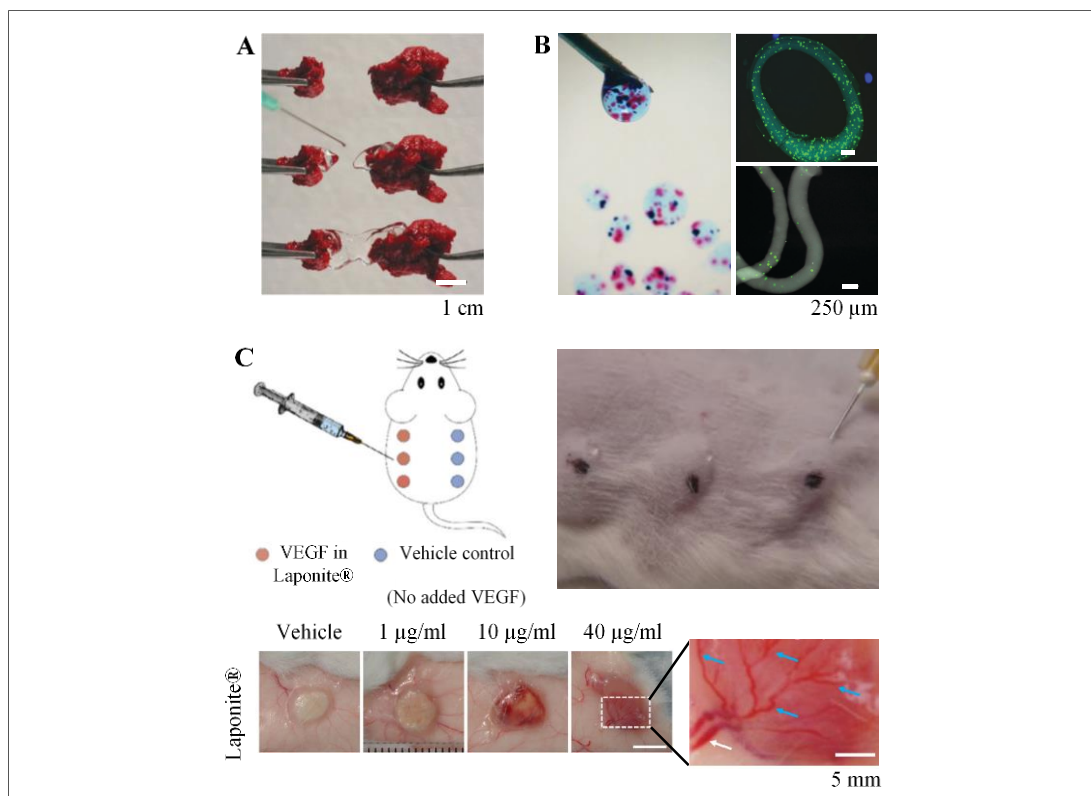


Figure 1.18 Self-assembly of Laponite® suspensions via thixotropy and in response to an ionic medium. (A) Thixotropic behaviour of clay-gels nanoparticles allows bridging gaps between tissues by stress-induced fluidisation through a needle and subsequent reestablishment of the cohesive microstructure (proof of concept image generated by Dawson et al. 2011). (B) Addition of clay-gel nanoparticles into electrolyte solutions resulted in the formation of structures with different shapes including microcapsules of clay-gel nanoparticles (red) sub-encapsulated in a larger host capsule (left image) (Dawson & Oreffo, 2013), rings or strings of clay-gel nanoparticles-containing hMSCs (right images) (Dawson et al. 2011). (C) Subcutaneous injection of clay-gel nanoparticles-containing vascular endothelial growth factor in a mouse model led to its in-situ gelation when in contact with the physiological fluids. After 21 days, the self-assembled structure maintained its localisation and integrity, and supported vessels formation as a function of VEGF concentration (Page et al. 2019).

Biocompatibility and bioactivity

Numerous biochemical assessments have been used to determine the cytocompatibility and bioactivity of clay nanoparticles (Gaharwar et al. 2019). In this regard, direct exposure of Laponite® XLG platelets was found non-toxic for human mesenchymal stem cells (hMSCs) when using concentrations lower than 1 mg/ml (Gaharwar et al. 2013). Moreover, clay nanoplatelets concentrations between 1 to 100 μg/ml were found to induce osteogenic differentiation in the absence of

osteoinductive factors in a dose-dependent manner (dexamethasone) (Gaharwar et al. 2013). Other studies indicate that the material has the capacity to modulate different cells response, including adhesion, proliferation and differentiation when added to a polymeric hydrogel. For example, the addition of clay nanoparticles to polyethylene glycol hydrogel enhanced the adhesion and proliferation of hMSCs (Gaharwar et al. 2012). Notably, Dawson et al. (2011) reported the viability and chondrogenic differentiation of encapsulated hMSCs in concentrated clay-gel nanoparticles (28 mg/ml) after 28 days, demonstrating the cytocompatibility of the material to deliver cells in a gel format.

Interestingly, despite all the biochemical assessments performed, the mechanisms underlying the bioactivity of clay nanoparticles remain to be elucidated. Some suggest that the clay nanoparticles may act directly as focal adhesion sites for cell attachment and spreading through the delivery of functional groups (e.g. $\text{Si}(\text{OH})_4$) (Gaharwar et al. 2012). Alternatively, cell adhesion could be indirectly enhanced via adsorption of adhesive proteins from the serum media. Another, mechanism could be that the release of Mg^{2+} ions via degradation promotes cell adhesion (Jain & Matsumura, 2016). It has also been proposed that the augment of local concentrations of divalent cations (e.g. Ca^{2+} or Mg^{2+}) on clay surfaces which are critical for the function of integrins that mediate cell interactions with extracellular matrix (Hynes, 2002).

Regarding the osteogenic differentiation promoted by clay nanoparticles, it has mainly been attributed to the degradation products. In the case of Laponite®, orthosilicic acid, magnesium and lithium ions are known to influence osteogenic cell function. For example, orthosilicic acid is connected to bone biomineralization and collagen type 1 synthesis (reviewed by Munjas et al. 2013). The magnesium ions play a crucial role in the activation of osteogenesis-regulating pathways (HIF-1a and PGC-1a) (Yoshizawa et al. 2014) and lithium ions activate the Wnt-responsive osteogenic genes (Hedgpeeth et al. 1997 and Williams et al. 2004). More recently, Mousa et al. (2018) postulated three more mechanisms by which clays could promote osteogenic commitment in skeletal cell populations, these include 1) the intracellular uptake of calcium phosphate minerals facilitated by clay nanoparticles and/or their ions 2) the interference of internalised clay nanoparticles in the signalling pathways

via clay-protein interaction and 3) the cellular uptake or receptor interaction of bioactive molecules facilitated by clay nanoparticles (Fig. 1.19).

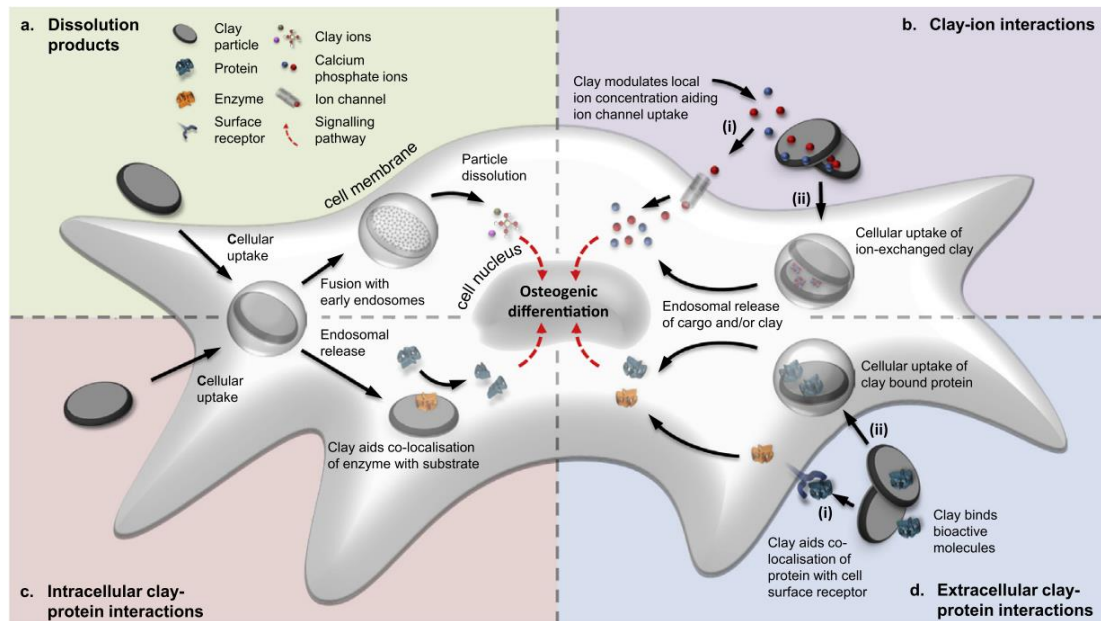


Figure 1.19. Osteogenic differentiation promoted by clay nanoparticles. The schematic illustration was acquired from Mousa et al. (2018).

Overall, the material shows potential for the fabrication of biocompatible structures to deliver growth factors effectively into the defect site. They can be either self-assembled in situ or prior to implantation. Moreover, growth factors can be loaded by adsorption or mixing. However, further work is required to optimise the spatio-temporal signalling to augment the bioactivity of the construct. To our knowledge, it has not been reported the use of clay gel nanoparticles or clay-composites to create spatio-temporal signalling similar to those observed during development and tissue regeneration through the 3D patterning of growth factor.

Hypothesis and Aims

The aim of this project is to engineer a scaffold with 3D micropatterning of biochemical cues similar to those found in the cellular microenvironments during bone development and regeneration with the goal of controlling the spatio-temporal formation of bone.

The overall hypothesis of this work is that the known self-assembly properties of clay nanoparticles and their interaction with proteins could be exploited to assemble nanoclay gel scaffolds incorporating 3D protein patterning at scale.

The specific objectives were as follow:

- To develop a method for assembling a clay-gel scaffold incorporating 3D patterning of proteins.
- To evaluate the effect of different fabrication parameters over 3D protein patterning.
- To characterise the structure of the assembled scaffolds.
- To study the assembly mechanisms by which the protein gradients are formed.
- To evaluate the versatility of the system to assemble scaffolds with different gradients, dimensions and shapes.
- To test the functionality for BMP-2 bone induction in a subcutaneous mouse model.

Chapter 2 METHODOLOGY

2.1 Materials and Methods

In this thesis, a general method section containing the procedures used throughout the study was described. However, individual methods' sections were also included in each chapter explaining the procedures and experimental setups used to design, optimise and characterise the engineered scaffold. Furthermore, the reagents, material and equipment used can be found in the Appendix, Tables A.1 to A.6.

2.1.1 Laponite® gel or clay-gel preparation

Different concentrations of clay-gel were prepared as a weight percentage (wt/wt%) of Laponite®/water following the protocol described by Dawson et al. (2011). In brief, type 1+ deionised water (18.2 MΩ, 25°C, pH 7) was added into a glass bottle, weighed and stirred vigorously until a vortex was formed. Weighed Laponite® XLG powder (BYK additive limited) was then slowly added and left to stir for 1 h at room temperature until the colloidal solution was clear before being weighed and autoclaved for 30 min at 121°C and 15 psi using a benchtop autoclave suitable for liquids sterilisation (Classic Media Extendable). After cooling the suspension was weighed again and the lost water added to adjust the concentration.

Note that the concentration n% is used throughout to describe w/w %.

2.1.2 Clay-gel droplet assembly

2.8 % clay-gel was vortexed vigorously for 20 seconds and then used to make 5 µl droplets with a 10 µl micropipette. Following, the scaffolds were assembled by placing a droplet directly into different tissue culture (TC) solutions as reported by Dawson et al. (2011), such as Dulbecco's Modified Eagle's Medium (DMEM) (Lonza), Dulbecco's phosphate-buffered saline without calcium and magnesium (DPBS) (Lonza) and foetal calf serum (FCS) (Thermo Fisher Scientific).

Assuming that the clay-gel droplet assembled has a spherical shape. The diameter expected could be calculated from the known volume, as follows:

The volume (V) of a sphere is derived from the equation

$$(1) \quad V = \frac{4}{3}\pi r^3$$

Solving for the radius (r) variable

$$(2) \quad r = \sqrt[3]{\frac{3V}{4\pi}}$$

Substitute the V by 5 mm³ into the formula solved (2) as the scaffold was made with 5 µl droplet of Laponite®.

$$r = \sqrt[3]{\frac{3(5\text{mm}^3)}{4\pi}} = 1.06 \text{ mm}$$

Consequently, the expected diameter of the scaffold assembled is 2.12 mm. However, taking into consideration a relative error that varies throughout the micropipette range, a 10 µl micropipette set at 5 µl yields a systematic error of ± 4 % (mean value) and less than ± 2 % random error (coefficient of variation). Therefore, the diameter of the scaffold would be 2.12 ± 0.02 mm mean value (Artel, 2019).

2.1.3 Nanoclay/protein scaffold

In the present study, a method to assemble nanoclay/protein scaffolds containing a 3D micropattern of molecules was developed. Thus, in this section, a general procedure to build the Laponite® scaffold will be described. However, further details of the different variable tested will be specified in each chapter with schematic figures.

Hence, a 5 µl droplet of clay-gel (high viscosity) was placed directly into a TC solution to assemble a clay-gel droplet and left to stabilise in the same solution. The scaffold was then rinsed to remove the excess tissue culture molecules and transferred to a solution containing the proteins of interest to be ‘loaded’. Finally, the scaffold was rinsed and stored in an aqueous solution for further analysis (Fig. 2.1).

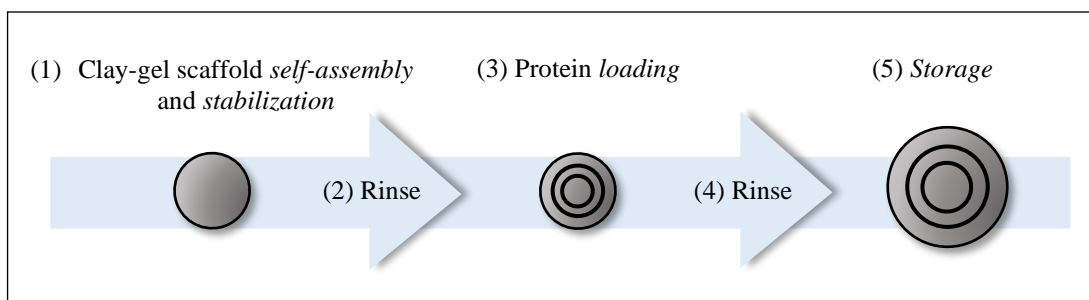


Figure 2.1 General protocol to make nanoclay/protein scaffolds. A well plate containing different treatment solutions was used to assemble the scaffolds, 1 per well. They were fabricated at 4°C and rinsed using an orbital shaker platform. The grey spheres represent the Laponite® gel droplet and the black rings inside the grey spheres the loaded molecules.

2.1.4 Structural characterisation of the nanoclay/protein scaffold

High water content and non-covalently cross-linked hydrogels are difficult to process for imaging analysis without resulting in substantial collapse, deformation or masking of important features. In this regard, only optical imaging techniques that did not require previous processing of the scaffolds were used to preserve the structure and prevent the introduction of artefacts, such as confocal laser scanning microscope (CLSM) and light fluorescence microscopy (LFM).

2.1.4.1 Confocal Microscopy

A Leica TCS SP5 CLSM was used to characterise the internal scaffold architecture by means of the fluorophores loaded, such as albumin from bovine serum conjugated with fluorescein isothiocyanate (FITC BSA) (Sigma-Aldrich) and 4',6-diamidino-2-phenylindole (DAPI) (Invitrogen, Fisher Scientific).

The scaffolds were scanned under wet conditions. To that end, they were transferred to a glass-bottom well plate (ibidi) containing 100 µl of aqueous solutions, such as DPBS or plain DMEM.

The general equipment settings used are described in this section (Table 2.1).

However, specific acquisition parameters, such as the gain and channels with their respective assigned pseudo-colours can be found in the experiment results chapter.

Table 2.1 General Leica TCS SP5 CLSM hardware settings.

Objective	HCX PL FLUOTAR 10.0 x /0.30 DRY	
Excitation wavelengths	Laser line (nm)	Power
	405	20.00 %
	458	0.00 %
	476	0.00 %
	488	30.00 %
	496	0.00 %
	514	0.00 %
	561	0.00 %
	594	0.00 %
633	0.00 %	
Emission wavelengths (channels)	begin - end	Offset
	1 420 nm - 473 nm	-1.0 %
	2 506 nm - 564 nm	-1.0 %
	3 600 nm - 699 nm	-1.0 %
	4 700 nm - 800 nm	-1.0 %
Transmitted light (channel)	5 Bright field	0.0 %
Image format	Width - 512 pixels	
	Height - 512 pixels	
	Resolution - 8 bits	
	File - LIF.	
Step Size	4.99 μm	
Scan Speed	600 Hz	

Furthermore, a free software Leica Application Suite X (LAS X) Core Offline version 3.0 was used to analyse the acquired images. To study the spatial localisation of the fluorescent molecules loaded into the nanoclay gel, their distance from the surface of the scaffold was manually measured (Fig. 2.2 - A), and the fluorescent intensity profile from the selected linear region of interest (ROI) (Fig. 2.2 - B).

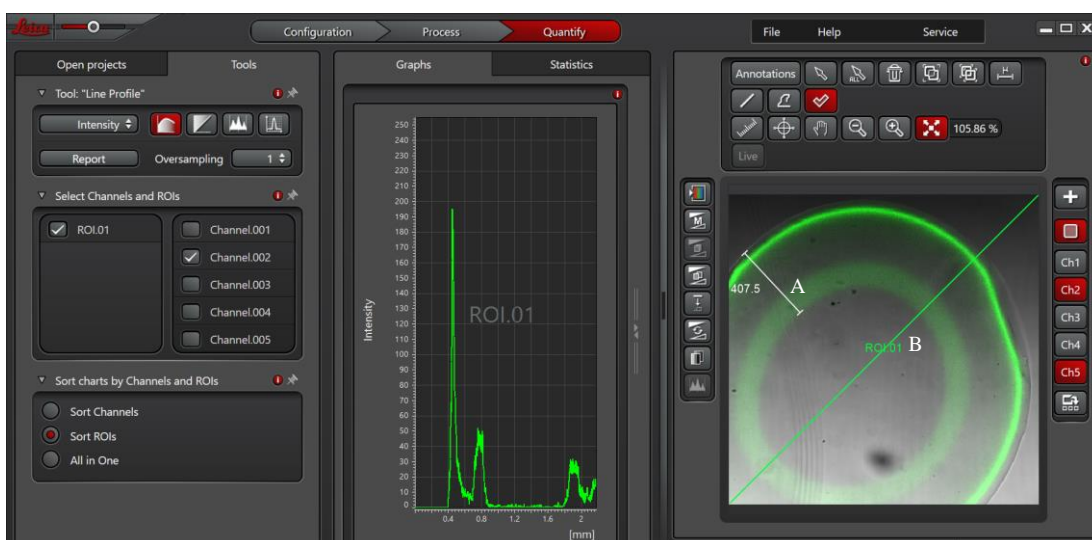


Figure 2.2 LAS X software measurements. (A) 3D spatial localisation of fluorescent molecules loaded into the nanoclay gel measured directly on the image using the scale bar tool, and (B) the ROI measured with the line profile tool.

The confocal images were presented throughout the text along the channel of excitation/emission, ROI graph and the gain or voltage (V) when considered appropriate.

2.1.4.2 Light Fluorescence Microscopy

A Carl Zeiss AxioVert 200 Inverted Microscope adapted for fluorescence imaging was employed to perform immediate analysis of the scaffolds structure and the spatial localisation of the fluorophores loaded. To this end, the scaffolds were stored in a 96-well microplate, U-bottom (Sigma Aldrich) containing 200 μ l of DPBS or DMEM to be imaged in wet conditions. The general equipment settings used are described in table 2.2.

Table 2.2 General Carl Zeiss AxioVert 200 Inverted Fluorescence Microscope hardware settings.

Objective	Fluar 2.5x/0.12 M27
Light source	HAL 100 halogen illuminator
Filter set	16
Excitation	BP 485/20
Beam splitter	FT 510
Emission	LP 515
Study identifiers assigned	FITC
Camera	AxioCam MRm (monochromatic)
Transmitted light	Bright field
Image format	Width - 1388 pixels Height - 1040 pixels Resolution - 16 bits File - zvi.

The grey-scale images acquired were analysed with AxioVision Rel. 4.8 software. Manual measurements of fluorescent gradients inside the clay-gel were performed on the LFM as well since the results showed similar to the CLSM imaging analysis. Moreover, the confocal can only image to $\sim 2/3$ of the scaffold because the lowest magnification of the equipment is 10X. Thus, the linear dimensions could not be studied from the CLSM images. In this regard, the LFM demonstrated to be more suitable since complete imaging of the scaffolds was possible.

It should be noted that the fluorescent images were presented throughout the text along the exposure time, millisecond (ms) when considered appropriate. Also, that in each figure, the features measured from the images acquired, either CLSM or LFM, in relation to the spatial localisation or patterning (termed from here on ‘localisation’) is described in the figure presenting the results.

2.1.5 Statistical analysis

Statistical significance ($p < 0.05$) was determined in GraphPad Prism version 8. The Student's t-test was conducted to compare two groups, in which data were normally distributed. Otherwise, Mann - Whitney ranks test for paired data was used. In order to compare between more than two groups, an analysis of variance ANOVA with Bonferroni's post hoc correction for normal distributed data was performed; otherwise, Kruskal Wallis test by mean rank with Dunn's post hoc was used. Finally, to evaluate the link between dependent and independent variables, a linear or exponential regression model regression was used. The data are presented and graphed as means \pm SD since replicates of the same scaffolds were analysed. Note that where the error bars are not visible in the graphs, they fall within the area occupied by the data point.

Furthermore, the p-value significance was reported with asterisks generally, at least the exact value was necessary (table 2.3).

Table 2.3 Format of p-value according to GraphPad.

Symbol	Meaning
****	< 0.0001
***	0.0001 to 0.001
**	0.001 to 0.01
*	0.01 to 0.05
ns	≥ 0.05

Chapter 3 FABRICATION OF NANOCLAY/PROTEIN SCAFFOLDS

3.1 Introduction

The aim of this chapter is to develop a scaffold comprising a 3D gradient of biochemical cues comparable to that found during development and regeneration of bone tissue through exploitation of the physicochemical properties of clay nanoparticles and proteins.

During development, gradients of morphogens set the initial path for the proliferation, differentiation, and pattern distribution of naïve cells to form hierarchically organised and functional structures (Ashe, 2006 and Christian, 2012). For decades, researchers have striven to elucidate the process by which this graded concentration of morphogens form and stabilise, and yet the precise mechanisms at play remain unknown (Entchev & González-Gaitán, 2002). Numerous passive and active transport models of morphogens have been proposed, such as “free or hindered extracellular diffusion to cell-mediated by transcytosis or cytonemes” (Yan & Lin 2009 and Muller et al. 2013). However, regardless the mechanism proposed, the various reports all concur that morphogens travel from their source through complex environments and somehow this process leads to the development of gradients in the target tissue (Entchev & González-Gaitán, 2002 and Muller et al. 2013) (Fig. 3.1).

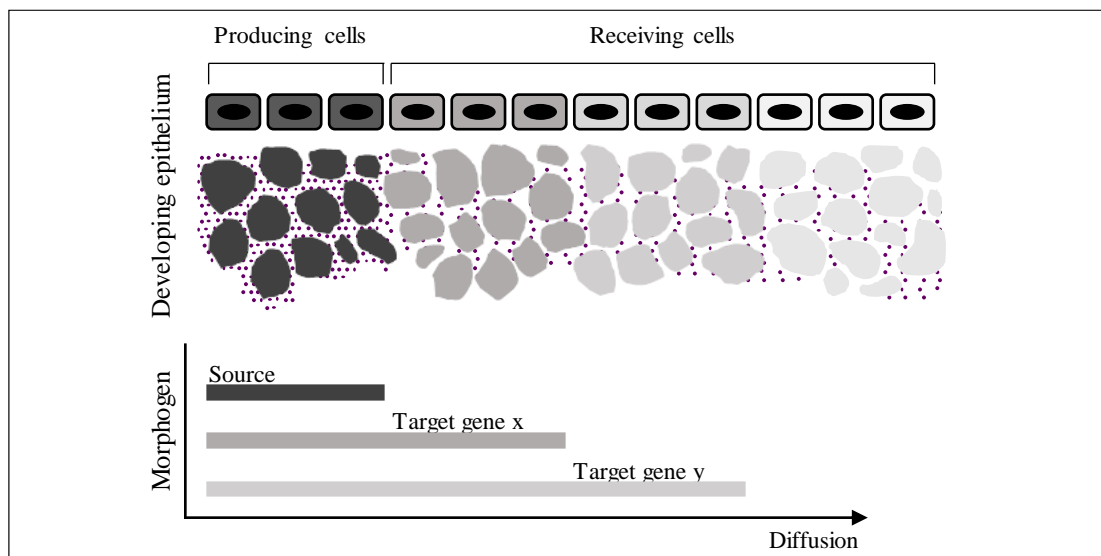


Figure 3.1 Morphogen gradient formation by diffusion. Secreted morphogen (purple dots) is released from a restricted region (producing cells) in the developing epithelium (receiving cells) and

forms a stable long-range concentration gradient. Modified illustration from Entchev & González-Gaitán, 2002.

The term morphogen is used to describe molecules that control cell fate in a concentration-dependent manner during morphogenesis (Christian, 2012) and are presented as a complex spatial and temporal signalling molecules (Tickle, 1999). Interestingly, morphogens are also found in regenerative processes (Ducy & Karsenty, 2000). For this reason, part of the regeneration process is considered a “recapitulation of embryonic development and morphogenesis” (Reddi, 2003), and based on this premise numerous tissue engineering strategies employ morphogenic molecules in the attempt to restore the structure and functionality of damaged tissues.

The morphogens that regulate bone development and repair are termed bone morphogenetic proteins (BMPs) and belong to a subgroup of transforming growth factors. To date, there are more than 30 members already described (Ducy & Karsenty, 2000). Among them, Bone Morphogenetic Protein-2 (BMP-2), has demonstrated strong osteoinductive properties and, in 2002, the Food and Drug Administration (FDA) and the European Medicines Agency (EMA) approved the use of BMP-2 for the treatment of long bone fracture and spinal fusion (Krishnakumar et al. 2017).

The use of BMP-2 augmented the success rate of numerous procedures (Gautschi et al. 2007 and Poon et al. 2016). In fact, it became “the second line of treatment in non-union bone defect” after autogenous iliac crest bone graft (Agrawal & Sinha, 2017). Nevertheless, unforeseen complications were encountered, such as postoperative inflammation, ectopic bone formation, osteolysis, excessive immune response, postoperative neurological impairment, compromised airways and cancer (Hustedt & Blizzard, 2014 and James et al. 2016) following off-label application.

Maintaining spatio-temporal concentrations of BMP-2 is crucial for bone repair, and the collagen sponges are the only carrier approved by the FDA (Agrawal & Sinha, 2017). However, owing to its fast clearance from the collagen sponge and proven short half-life, supra-physiological doses are usually applied (1.5 - 2.0 mg/ml) to maintain effective local concentrations of BMP-2. As a result, the excess of protein

circulating in the system causes the side effects above listed (Zara et al. 2011, Suliman et al. 2015 and Bialy et al. 2017).

Thus, to overcome the downsides of BMP-2, numerous delivery systems have been investigated to localise and reduce the dose, including hydrogels, microspheres, nanoparticles, and fibres made of metals, ceramics, polymers, and composites (Mehta et al. 2012 and Agrawal & Sinha, 2017). Overall, these delivery systems aim to achieve spatio-temporal gradients observed during bone development and repair through controlled and sustained release of BMP-2 or localised bioactivity by surface binding, which can be either in a 2D or 3D design (Fig. 3.2).

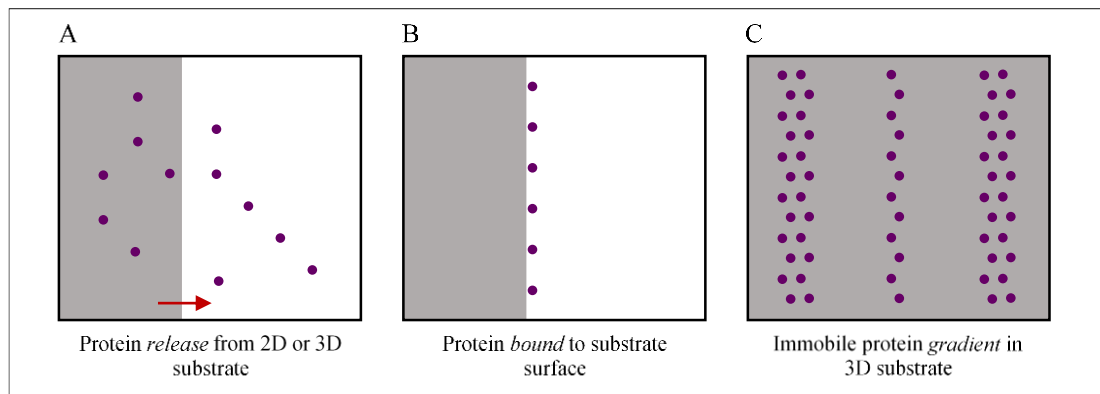


Figure 3.2 Schematic illustration of BMP-2 delivery approaches. (A) Controlled and sustained release, (B) localised bioactivity by binding the protein to a surface substrate, and (C) 3D gradients bound to a substrate. The grey square and dark-purple dots represent the substrate and proteins, respectively.

Hydrogels offer promising candidates to build a spatio-temporal gradient of proteins. Their three-dimensional polymeric network is similar to the natural extracellular matrix and allows carrying large quantities of proteins (Bae & Kurisawa, 2016). Hydrogels also provide an aqueous environment that retains proteins in their active form and prevents them from denaturation. Nevertheless, the high permeability of the hydrogels causes the burst release of proteins, which may lead to ineffective concentrations or different side effects (Vermonden et al. 2012). This has been tackled with different immobilisation techniques to prevent their diffusion (Suliman et al. 2015).

To date, significant effort has been generated in building hydrogels with 3D gradients of biochemical cues in the form of spatially localised patterns. For this purpose, several top-down and bottom-up techniques, including photo-patterning, electrophoresis, 3D printing, reaction-diffusion and microfluidics have been explored.

In principle, 3D photo-patterning focuses on shining a light beam through a transparent photosensitive hydrogel to expose the photo-initiators reactive groups. This provides the template for biomolecule immobilisation, which is chemically modified or designed to react with the photo-initiator reactive group.

Significant progress has been made in recent years to improve pattern resolution, hydrogel biocompatibility, and the ability to couple not only peptides but also proteins. For this, various light sources (UV, single-photon or two-photon excitation), hydrogels (agarose, hyaluronan and poly(ethylene glycol) modified) and photo-initiators have been investigated (Luo & Shoichet, 2004, Wosnick & Shoichet, 2008, Deforest et al. 2009, Ovsianikov et al. 2012, Mosiewicz et al. 2013, Torgersen et al. 2013, Li et al. 2013, Hernandez et al. 2016 and Shadish et al. 2019).

Moreover, some studies have demonstrated the functionality of patterned hydrogels in vitro. Luo & Shoichet (2004) seeded on top of GRGDS-patterned agarose hydrogel, primary rat dorsal root ganglia cells. After six days, the patterned channels promoted neurite extension and migration, and 76 ± 16 % out of channels contained neurites. Similarly, Hahn et al. (2006) seeded on top of RGDS-patterned collagenase PEG hydrogel HT-1080 fibrosarcoma cells, a commonly used cell type in migration studies. After four weeks, the cells migrated in the hydrogel following the peptide pattern.

The technique demonstrates excellent control over the localisation and concentration of biomolecules in the hydrogel, including peptides and proteins (Hahn et al. 2006 and Mosiewicz et al. 2013), as well as simultaneous patterning of two biomolecules (Wylie et al. 2011). Nevertheless, protein modification and conjugation with the hydrogel may affect its bioactivity (Spicer et al. 2018). The complete synthesis process is time-consuming as it may take approximately 1 to 3 days between the

immobilisation and the dialysis of the photo-reaction by-products and unbound biomolecules (Luo & Shoichet, 2004, Wylie et al. 2011 and DeForest & Tirrell, 2015). Furthermore, the microscope working distance may limit the thickness of the patterned hydrogel, and there is a high cost associated with the equipment.

Electrophoresis may offer opportunities for 3D patterning of hydrogels. However, this area remains underdeveloped. In 2012, Dai et al. adapted a blotting technique to generate a pattern of molecules in various media. This technique is routinely used in molecular biology to sort macromolecules. Using an electric field, the macromolecules can be made to migrate through a gel or sieving medium, which may assist their separation by size and/or charge.

Thus, to make the 3D patterned hydrogel, the authors placed between the doped gel and the receiving medium a screening mesh. These three structures were then sandwiched between two electrode plates, and by applying voltage, the charged molecules contained in the doped gel migrated to the receiving medium and formed a pattern guided by the screen mask.

In 2018, Aguilar et al. used a similar approach and demonstrated they could pattern a wide range of hydrogels. Nevertheless, the hydrogels showed not functionality *in vitro* since no significant migration of NIH-3T3 cells in polyacrylamide-collagen hydrogels patterned with fibronectin was observed after 14 days. The authors claimed that the low porosity of the gel may have affected cell migration and oxygen diffusion.

Compared to the photo-patterning technique, 3D electrophoresis is simple, rapid and cost-effective. In addition, two different types of protein can be patterned in the same hydrogel (Aguilar et al. 2018). The technique demonstrates control of the protein localisation and distribution, but the resolution and versatility are not comparable to the photo-patterning. Moreover, there is no proven control over the concentration of the proteins. It appears only biomolecules above 150 kDa can be patterned, but the morphogens for which patterning is of core relevance are typically between 30 to 70 kDa. Finally, more work needs to be done to evaluate the effect of the patterning

process in the protein bioactivity and verify the spatio-temporal localisation of the proteins as a function of time because they are not cross-linked with the hydrogel.

3D printing by extrusion has been used to create spatial gradients of bioactive molecules. In this technique, pneumatic forces are applied to dispense a viscoelastic fluid or gel containing biomaterials and/or cells through a nozzle that follows a computer-generated pattern (Ozbolat & Hospodiuk, 2016). With this platform, viscous gels ranging from 30 to 6×10^7 mPa s could be used to create complex 3D structures (Hölzl et al. 2016). Moreover, printed macrostructures may have internal gradients of different biochemical cues (Liu et al. 2017).

Although there are some limitations to be addressed, the structures generated are soft and, therefore, increasing the gel viscosity and/or gelation post-printing may be considered to prevent them from collapsing and improving their size, stability and resolution. Nevertheless, both cases have proven detrimental for nutrients and oxygen diffusion (Malda et al. 2013 and Hölzl et al. 2016). Moreover, the resolution of the biomolecules' gradients is significantly lower (100 - 500 μm) compared to the photo-patterning technique (0.1 to 5 μm). The printing process is slow and there is a high cost associated with the equipment (Miri et al. 2019).

Recently, reaction-diffusion systems have been explored to pattern organic molecules inside hydrogels. For this particular application, multiple reactants are positioned in a hydrogel matrix so that they diffuse towards each other and react at the crossing diffusion fronts. Finally, the byproducts form localised patterns or chemical gradients inside the hydrogel.

In 2017, Lovrak et al. reported the self-assembly of a free-standing macroscopic patterned structure through a reaction-diffusion system. The authors placed hydrazide and aldehyde at the opposite sides of an agar or alginate gel matrix. Both components diffused through the gel and reacted at the interception of the two diffusion fronts leading to the formation of trishydrazone. This byproduct reaches a critical concentration that triggers its self-assembly into fibres and the formation of non-transparent supramolecular patterns. The authors claimed that the patterned regions could be functionalized with bioactive molecules.

Similarly, others achieved patterning of enzymes and synthetic DNA in 2D hydrogels through the reaction-diffusion system (Semenov et al. 2013 and Abe et al. 2019).

This biomimetic approach recapitulates bottom-up self-assemblies observed during the morphogenesis of living tissues, as mentioned at the beginning of this introduction. Moreover, it has shown great potential to generate patterns and biocompatible structures with high levels of complexity and resolution. Moreover, bottom-up self-assembly allows building structures with controllable shape and size ranging from several hundred micrometres up to centimetres. Nevertheless, more work is required to create patterns of biochemical cues, such as peptides or proteins, so that it can be used for tissue engineering and regenerative applications.

Finally, open microfluidics was used to assemble free-standing hydrogels through the progressive deposition of hydrogel layers. According to Lee et al. (2019) this novel technique allows asymmetric designs with multiple components, such as agarose, type I collagen and PEG containing cell-laden regions.

Similar to the reaction-diffusion approach, it can be used to build structures of controllable shape and size from millimetres to centimetres with patterned layers of hydrogels ranging from tens to hundreds of micrometres thick. The process is performed with a simple pipette with minimum material waste and relatively fast compared to some of the techniques above described. For example, it takes 10 hours to fabricate an agarose cylinder of 14x14 mm containing 29 layers of approximately 480 μm thick. Drugs and factors may be introduced with along the printed hydrogel. For example, PEG functionalised with RGDS peptide. However, more work is required to generate patterns of growth factors and assess their functionality (Lee et al. 2019).

The top-down and bottom-up approaches discussed are promising. However, significant challenges remain to create a simple method following which: 1) immobilisation technique does not affect the protein bioactivity, 2) control is provided over the concentration of the protein patterned and 3) patterning proteins with molecular weights between 30 to 70 kDa is possible. Also, it is important that

these methods can 4) support the loading of multiple proteins, 5) use less chemicals to improve the biocompatibility, 6) favour a faster synthesis process, and 7) allow scaling up the hydrogel size. Satisfying these conditions could yield hydrogels with any desired 3D configuration of bioactive cues for tissue engineering applications.

To address these criteria, the sorptive capacity of Laponite® clay nanoparticles has been harnessed to design hydrogels with 3D immobilised proteins. This clay nanoparticle consists of a disk-shaped of approximately 25 nm diameter and 0.92 nm thickness, which chemical structure provides them with a negative surface charge and a weak positive rim charge. Owing to this reactive surface, the clay nanoparticles can interact between them when dispersed in water to form a thixotropic gel at given conditions or interact and sequester organic or inorganic molecules.

In the last years, Laponite® gel has shown great potential for bone tissue engineering applications due to its biocompatibility and capacity to 1) immobilise proteins preventing burst release, 2) localise proteins without affecting their bioactivity, and 3) decrease the concentrations to prevent side effects (Gaharwar et al. 2013, Dawson & Oreffo, 2013 and Gibbs et al. 2016).

Early work performed by Dawson et al. (2011) demonstrated the capacity of Laponite® gel to self-assemble into micro and macro-droplets, rings and long strings under physiological conditions and suggested their use as delivery systems of growth factors by premixing or adsorbing them over the droplet surface. Moreover, Gibbs et al. (2016) indicated that the localisation of growth factors with Laponite® gel (either premixed or adsorbed) enhances the bioactivity of physiological dosage of BMP-2 to achieve ectopic bone formation in a subcutaneous murine model. Both approaches highly the benefit of binding and localising proteins in space and time, restricting their diffusion from the implant site and improving their efficacy. Nevertheless, the construct failed to show any control over the 3D localisation of the protein, which is crucial to control its spatio-temporal bioactivity.

In this regard, Min et al. (2014) showed that Laponite® clay nanoparticles could be used to build a composite microstructure with 2D spatial localisation, organisation and controlled the release of macromolecules. The authors fabricated a polymer-

based self-assemble multi-layered structure loaded with rhBMP-2, gentamicin and Laponite® clay nanoparticles to coat orthopaedic implants using a spray layer-by-layer (LBL) polyelectrolyte technique. The in vitro study showed that the Laponite® barrier modulated the release profile of $\sim 300 \text{ ng/cm}^2/\text{day}$ of rhBMP-2 over a 40-day time course, which resulted in a physiologically relevant dosing to enhance implants osseointegration.

LBL technique is widely used to functionalize surfaces, control the release of drugs and improve biomaterials' biocompatibility (Vander Straeten et al. 2017). LBL involves alternated polyelectrolyte adsorption on a substrate where proteins can be trapped within hydrated polyelectrolyte layers. This versatile technique allows using a wide range of materials from metals, polymers and bio-macromolecules to nanoparticles and be assembled under mild conditions with simple procedures, such as immersion, spray and spin coating (Michel et al. 2012).

Similarly, colloid and hydrogel beads have been employed as templates to create 3D multilayer microstructures. The coating may contain proteins to improve the biocompatibility, but the primary purpose is to control the release of drugs loaded into the core (Del Mercato et al. 2014, Sakr et al. 2016 and Timin et al. 2017).

This approach looks promising, but the protein gradient bioactivity is subjected to the controlled release of proteins and not to their spatio-temporal localisation. To date, no one has explored building LBL of clay nanoparticles over a solid clay-gels structure to assemble free-standing micropatterned scaffolds with localised bioactivity.

Hence, the specific objective of this chapter is to develop a method for assembling scaffolds with 3D gradients of biochemical cues under mild conditions using Laponite® gel (or clay-gel) and proteins. For this purpose, the LBL polyelectrolyte technique will be explored to build functionalized macrodroplets. Here are presented initial attempts to assemble the nanoclay/protein scaffold followed by understanding and simplification of the system in terms of composition and fabrication.

3.2 Materials and Methods

3.2.1 Laponite®/protein layer-by-layer polyelectrolyte scaffold

In this experiment, an immersion LBL polyelectrolyte technique was employed to generate a nanoclay/protein scaffold containing stratified arrangements of proteins. For this purpose, a 5 μl droplet of 3 % clay-gel was placed into 100 $\mu\text{g/ml}$ FITC BSA-media solution to self-assemble a clay-gel droplet, which would then serve as a substrate for the subsequent deposition of nanoclay/protein “bilayers”. Note that owing to the sorptive properties of the clay, the deposition of FITC BSA “layer” at the clay-gel droplet surface was expected simultaneously to the assembly. Further to this, the assembled clay-gel droplet was rinsed with DPBS to remove the excess proteins from the surface and transferred to 1 % clay dispersion (low viscosity) in order to add a “spacer layer”. Again, a second rinse with DPBS took place to remove the excess clay, and the previous steps were repeated in order to add one more “bilayer” of nanoclay/protein. Finally, the samples were stored in DPBS and analysed with light fluorescence microscopy (LFM) to corroborate the binding of the protein layers at the clay-gel droplet surface.

This experiment was performed in a 24 well plate containing different treatment solutions (100 $\mu\text{g/ml}$ FITC BSA-media, DPBS and 1 % clay). One scaffold was assembled per well and transferred to the different treatments using a spatula. Furthermore, the procedure was performed at 4°C. Table 3.1 shows details of the volume, time and temperature that the scaffolds were exposed to at every step.

Table 3.1 Protocol to make a nanoclay/protein LBL polyelectrolyte

Assembly	“1 bilayer”				“2 bilayers”
Treatment	Step 1	Step 2	Step 3	Step 4	Repeat step 1 - 4
	Assembly & protein layer deposition	Rinse	Clay layer deposition	Rinse	
Solutions	FITC BSA-media	DPBS	Clay-gel	DPBS	
Concentration	100 µg/ml	---	1 %	---	
Time	20 min	30 secs	20 min	30 secs	
Volume	1 ml				
Temperature	4°C				

3.2.2 Upgraded protocol to make a Laponite®/protein LBL polyelectrolyte.

5 µl droplet of 2.8 % clay-gel was placed into DMEM 10 % FCS and left to stabilise for 1 h. Afterwards, the assembled clay-gel droplet was transferred to 100 µg/ml FITC BSA and 1 % clay solutions for 30 min and 1 h, respectively, to deposit “1 bilayer” of nanoclay/protein. Next, the clay-gel droplet was transferred to a (1:20) DAPI-DPBS solution to stain the previously deposited 1% clay layer, and in order to add a second “bilayer”, the procedure was repeated. Note that a rinsing step with plain DMEM took place between every treatment for 5 min - 50 rpm. Finally, the samples were stored in plain DMEM at 4°C to be analysed by CLSM.

The experiment was performed in a 48 well plate containing different treatment solutions (DMEM 10 % FCS, 100 µg/ml FITC BSA-media, DMEM plain, 1 % clay and 1:20 DAPI-DPBS). One scaffold was assembled per well and transferred to the different treatments using a spatula. Furthermore, the procedure was performed at 4°C. The table 3.2 shows details of the volume, time and temperature that the scaffolds were exposed to at every step.

Table 3.1 Upgraded protocol to make a Laponite®/protein LBL polyelectrolyte.

Assembly	“1 bilayer”								“2 bilayers”
Steps	1	2	3	4	5	6	7	8	
Treatment	Assembly	Rinse	Protein layer deposition	Rinse	clay layer deposition	Rinse	Clay staining	Rinse	
Solutions (400 μ l)	DMEM 10%FCS	plain DMEM	FITC BSA - media	plain DMEM	1% Clay- gel	plain DMEM	DAPI- DPBS	plain DMEM	Repeat Step 3 - 8
Time	1h	5min	30min	5min	1h	5min	20min	5min	
Temp.	4°C								

The next experiments were performed in 96 well plates containing 200 μ l volume of each treatment solution following similar setup above described. The concentration of FITC BSA (100 μ g/ml) was maintained throughout the study. However, further variations of the treatment solutions' concentrations and volumes, incubation time and temperature are described in the results.

3.3 Results

3.3.1 Initial attempts at stratified nanoclay/protein scaffolds

The aim of this study is to harness the properties of nanoclay for self-assembly and protein binding to construct scaffolds that incorporate spatially stratified arrangements of proteins. The ultimate aim is to generate 3D patterned presentations of growth factors in a gel environment able to host and direct stem cell-driven tissue regeneration. The preliminary strategy was to employ the immersion layer-by-layer polyelectrolyte technique using a 2 mm diameter clay-gel droplet as a core substrate for subsequent layer-by-layer deposition.

Initially, a droplet of 2.8 % clay-gel (high viscosity) was added drop-wise into FITC BSA-DPBS solution to assemble a clay-gel droplet. This structure would then serve as a substrate for the subsequent deposition of protein and clay “bilayers”. Note that owing to the sorptive properties of the clay, the deposition of FITC BSA “layer” at the clay-gel droplet surface was expected simultaneously to its assembly.

Further to this, the formed droplet was rinsed with DPBS to remove the excess proteins from the surface and then transferred to 1 % clay (low viscosity) in order to add a “spacer layer”. Again, a second rinse with DPBS took place to remove any excess of clay (Fig. 3.3 - A).

Finally, the whole process was repeated to add a second “bilayer” of protein and clay. The samples were analysed with confocal laser scanning microscopy and light fluorescence microscopy to corroborate the binding of the fluorescent labelled protein layers at the clay-gel droplet surface (further detail of the experimental setup can be found in the methods section - 3.2.1).

This initial attempt utilised clay-gel droplets gelled in DPBS as the core substrate for subsequent layer-by-layer addition of protein and clay “bilayers”. However, results indicate that the DPBS incubation alone was not sufficient to generate a stable clay-

gel core (4/8 clay-gels disintegrated during the second round of incubations) or preserve layer integrity through the wash steps (Fig. 3.3 - B).

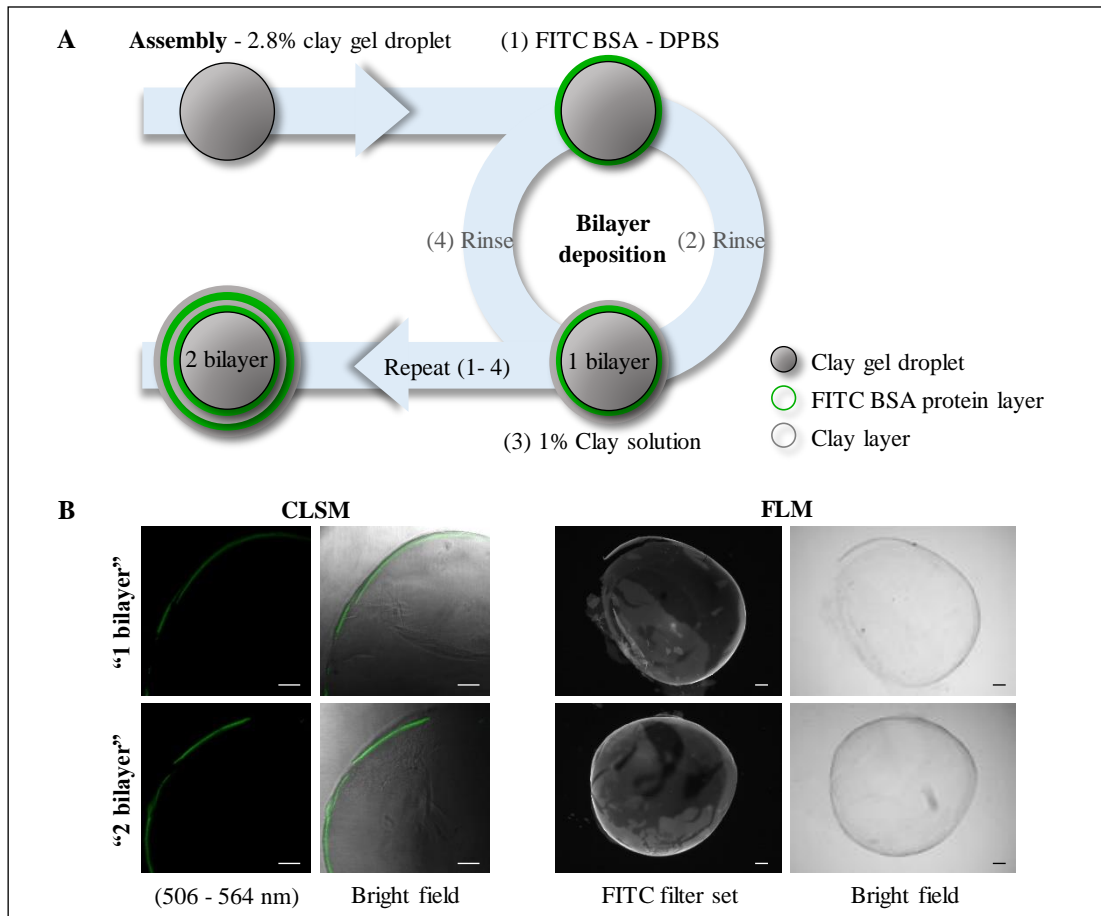


Figure 3.3 Nanoclay/protein LBL polyelectrolyte self-assembly. (A) Schematic illustration of the onion-like structure formation via a core-mediated immersion method. (B) The CLSM images revealed a fluorescent layer at the clay-gel droplet surface that could be associated with the binding of FITC BSA proteins, consistent with Dawson et al. (2011). Furthermore, the LFM images showed fragments of the layers' detachment from the clay-gel surface irrespective to the addition of "1 or 2 bilayers". The scale bars correspond to 200 μm ($n = 8$).

The results above indicated the fundamental need to improve the fabrication process to create a more stable core and "bilayer of protein and clay" that could withstand handling.

To address the lack of stability, the clay-gel droplet cores were formed in TC media containing FCS as previous studies have shown an increase in clay-gel strength under these conditions (Shi et al. 2018). An additional staining step with DAPI was applied to allow visualisation of the intermediate clay layer in the assembly as DAPI

shows a strong affinity for the clay nanoparticles. As above, single and double bilayer protocols were compared (Fig. 3.4 - A). Further details of the experimental setup can be found in the methods section - 3.2.2.

Analysis by confocal images of the clay-gel droplets treated with “1 or 2 bilayers” revealed the formation of comparable fluorescent-layered structures that were stable to handling. Well-defined, localised and symmetrical fluorescent bands were observed at the scaffold periphery, a single ‘red’ band (corresponding to the DAPI emission spectra, 420 - 472 nm) (Fig. 3.2 - D) and two distinct parallel ‘green’ bands (corresponding with the FITC BSA emission spectra 506 - 564 nm) (Fig. 3.4 - C).

Moreover, the bright-field images showed distinct bands that corresponded structurally with the localisation of the green fluorescent bands (3.4 - C & E).

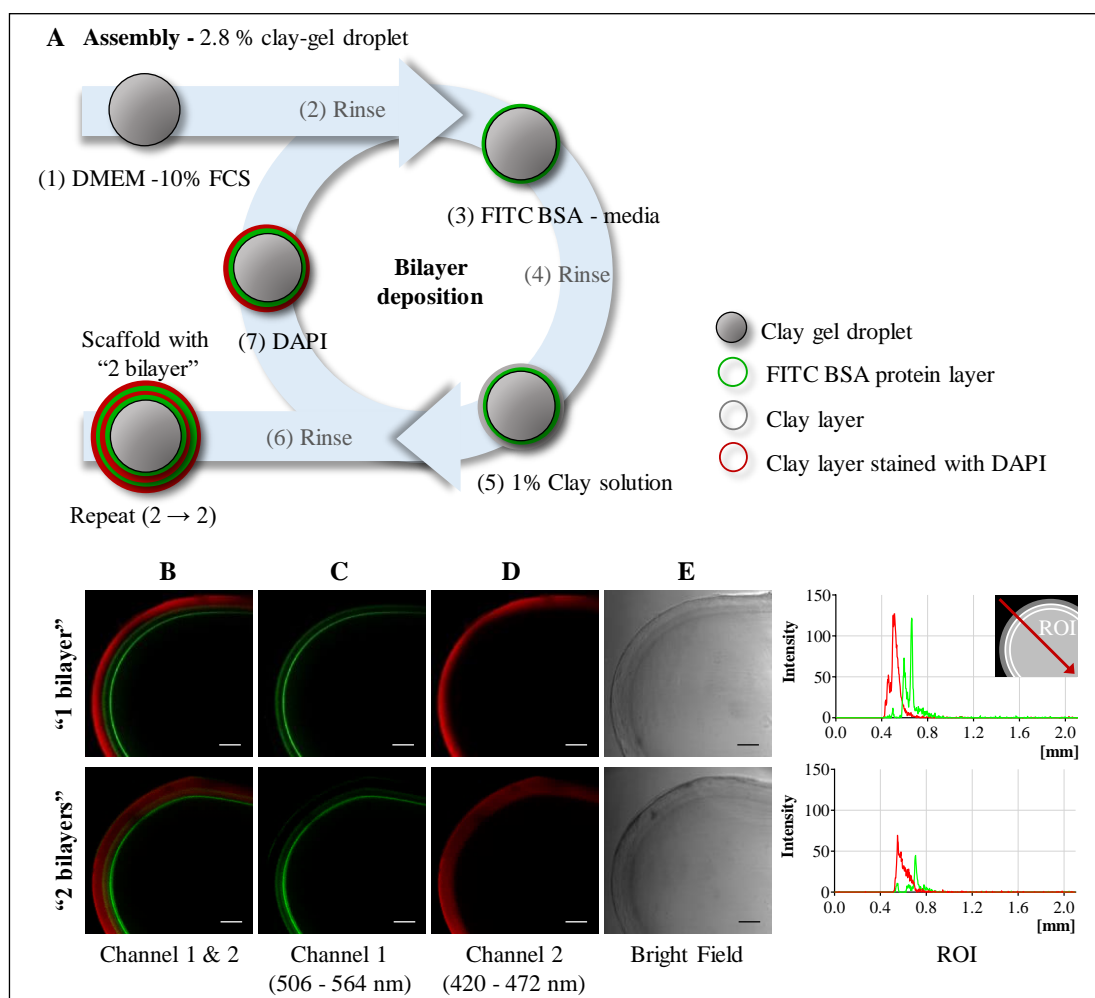


Figure 3.4 Nanoclay/protein LBL polyelectrolyte stabilisation. (A) Schematic illustration of the onion-like structure formation via a core-mediated immersion method. The CLSM images presented

by channel, overlay (B) or individual (C, D & E) alongside their line profile chart of the ROI. Observe that both scaffolds have similar fluorescent-layered structures despite the “1 & 2 bilayers” treatment. The scale bars correspond to 200 μm ($n = 3$).

Unexpectedly, the organisation of the fluorescent bands did not conform to that expected by a conventional LBL assembly mechanism. Sequential deposition of “1 and 2 bilayers” of protein and clay were expected in response to the treatments with a progressive increase in the number of the layers and overall thickness (Fig. 3.5 - A). However, the localisation of the fluorescent bands is similar irrespectively of the treatment, one red band and two green bands (Fig. 3.5 - B & C). No further increment in the number of the layers was observed, and the statistical analysis of the total thickness of the fluorescent-layered structure showed no significant differences (unpaired sample t-test, $p = 0.7531$, $n = 3$) between the scaffolds treated with “1 bilayer” (176.0 \pm 11.53 μm) and “2 bilayers” (194.7 \pm 8.96 μm) (Fig. 3.5 - D).

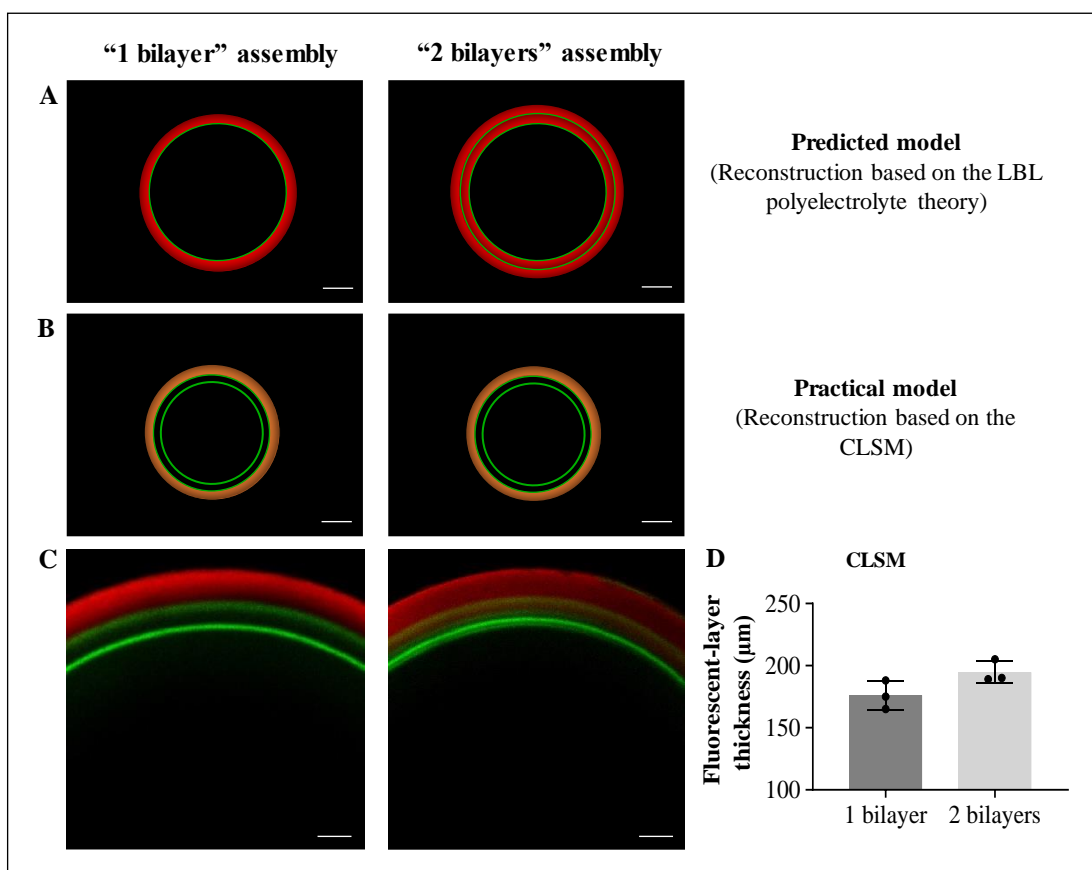


Figure 3.5 Nanoclay/protein scaffold structure conceptual vs actual results. Illustrations of “1 & 2 bilayers” of protein and clay order expected (A) and practical results (B) along with the corresponding confocal images (C). The green and red “layers” in the illustrations represent the FITC BSA and clay-DAPI “deposited” respectively over a clay-gel droplet (black core). (D) No significant differences

were observed in the total thickness of the fluorescent-layered structure of the scaffolds treated with “1 & 2 bilayers” (unpaired sample t-test, $p = 0.7531$, $n = 3$). Data presented as mean \pm SD. The illustration scale bars correspond to 500 μm and the CLSM images to 100 μm .

Further measurement of the diameter of the scaffolds treated with 1 bilayer ($2.37 \pm 0.10 \mu\text{m}$) & 2 bilayers ($2.36 \pm 0.10 \mu\text{m}$) showed no significant differences (unpaired sample t-test, $p = 0.9256$) (Fig. 3.6 - C) despite an expected increase in size by $\sim 8\%$ with the “deposition” of a second layer.

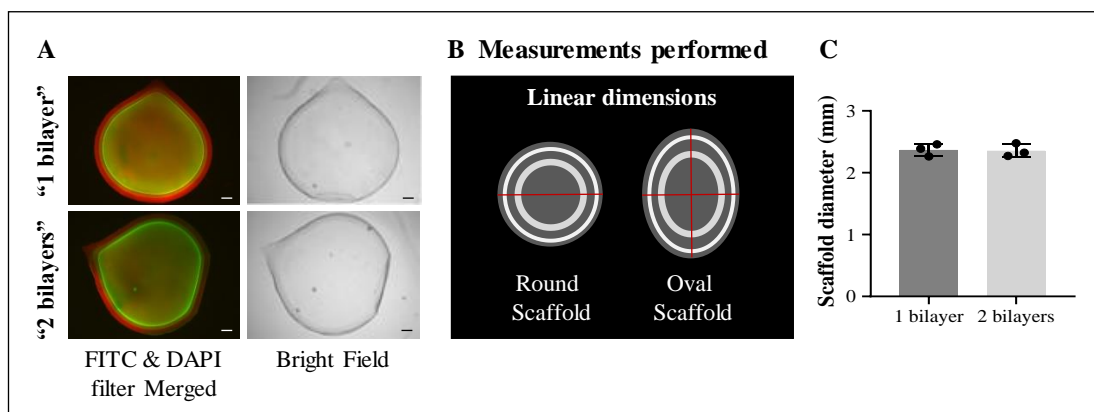


Figure 3.6 Nanoclay/protein scaffold dimensions. The bright field images (A) showed no significant differences in the size of the scaffold irrespectively of the “1 & 2 bilayers” treatment, this was confirmed by respective measurement (B) and statistical analysis (C) of both scaffolds (unpaired sample t-test, $p = 0.9256$, $n = 3$). Data presented as mean \pm SD. The scale bars correspond to 200 μm .

In summary, this new protocol facilitated the building of stable “bilayers” with defined 3D localisation of molecules and micron resolution from 6 to 200 μm that withstand handling. However, the patterning suggests that the LBL polyelectrolyte deposition does not account for the observed fluorophore distribution and that other mechanisms underlie this 3D localisation of protein around the periphery of the nanoclay gel droplet, such as diffusion.

Understanding this mechanism may open up new approaches to develop scaffolds for drug delivery with a high degree of protein localisation and resultant controlled bioactivity and/or release.

3.3.2. Formation of fluorescent-layered structures

In order to optimise the assembly protocol, the next experiments were set up to study the mechanism, process and factors that trigger and control the formation of the fluorescent-layered structures.

3.3.2.1. Formation of the fluorescent-layered structure due to diffusion and not the deposition of molecules.

Preliminary findings suggest that the phenomenon observed is not the result of a deposition process, but rather the diffusion and localisation of molecules within the clay-gel core structure (Fig. 3.5). In this regard, it was hypothesised that the addition of an intermediate clay spacer layer is not required to form the fluorescent-layered structure.

To test this, clay-gel droplets were treated as per the single bilayer protocol above (Fig. 3.4 - A) and compared the fluorophore distributions that result with and without an intermediate clay wash step (Fig. 3.7 - A).

Overall, the CLSM images revealed the formation of similar fluorescent-layered structure regardless of the addition of clay solution. A single red band (420 - 472 nm) and two green bands (506 - 564 nm), which presumably corresponds to DAPI and FITC BSA fluorophores, respectively (Fig. 3.7 - B).

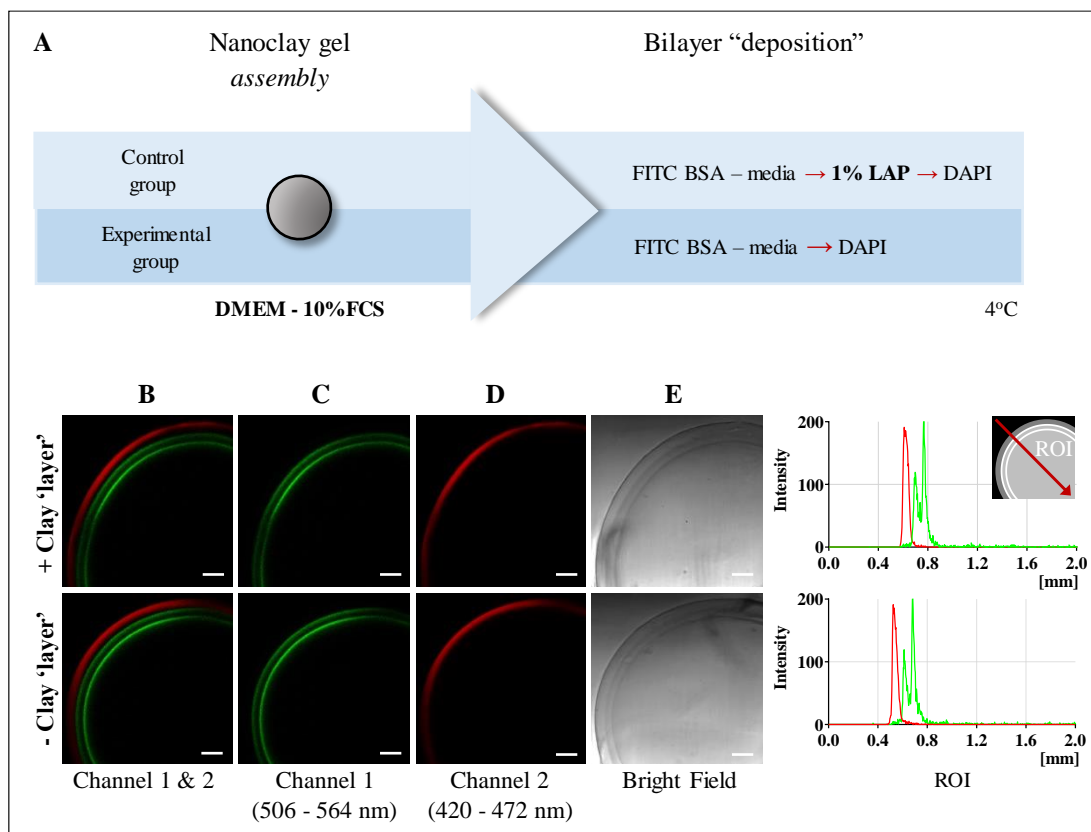


Figure 3.7. Nanoclay/protein scaffold self-assembly, fluorophores deposition vs diffusion. (A) Schematic illustration to make scaffolds with and without a clay wash. (B) The CLSM images and respective ROI revealed the formation of fluorescent-layered structures regardless of the clay wash step. The scale bars correspond to 200 μm (n = 3).

The results indicate that the additional step of rinsing in 1 % clay is not required to assemble the fluorescent-layered structure. This suggests a diffusion, rather than a layer deposition, in which the FITC BSA - media and DAPI molecules are absorbed and localised inside the originally assembled clay-gel droplet.

3.3.2.2. Absorption and preferential localisation of fluorophores into the clay-gel

An interesting feature of the pattern of the fluorophores is the sharp separation between bands. The DAPI band is separated at the clay-gel edge from the FITC band, which is internalised within the clay-gel core and separated into two clearly distinct bands (Fig. 3.7 - B). To evaluate the absorption and localisation process of the fluorophores, clay-gels were treated as above, but with FITC BSA and DAPI added in isolation from each other (Fig. 3.8 - A).

Image analysis of the scaffold assembled in DMEM 10 % FCS and subsequently treated with DAPI showed a fluorescent band localised next to the surface corresponding to the DAPI staining (420 - 473 nm) (Fig. 3.8 - 1D). Given the absence of added fluorophores (FITC BSA) emitting at the wavelength of 506 - 564 nm, one can assume that this arises from fluorescent molecules present in TC media (Fig. 3.8 - 1C).

Moreover, two fluorescent green bands were observed on the scaffolds treated with FITC BSA-media alone. A first band localised at $\sim 100 \mu\text{m}$ from the scaffold surface that could be associated to the FITC BSA, and the second band localised at $\sim 200 \mu\text{m}$ that could be associated to the TC media used to assemble the scaffold according to previous observation (Fig. 3.8 - 2C).

The subsequent addition of DAPI to the droplet treated with FITC BSA showed fluorescent patterns similar to the previously described scaffolds. Again, a single red band next to the scaffold surface, corresponding to the DAPI staining and two green bands localised at ~ 100 and $\sim 200 \mu\text{m}$ from the scaffold surface, which appears to be FITC BSA and TC media fluorophores, respectively (Fig. 3.8 - 3B).

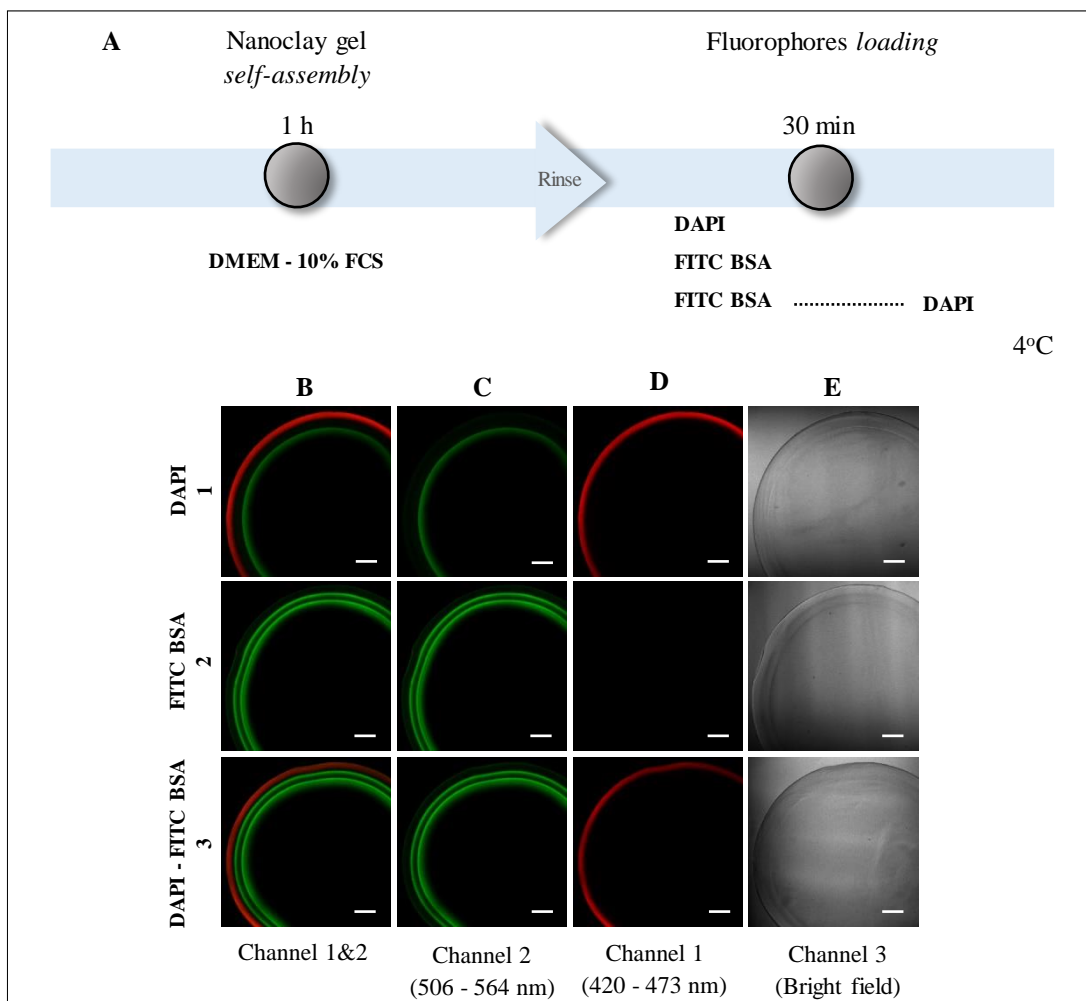


Figure 3.8 Fluorescent-layered structure formation. (A) Schematic illustration of scaffolds loading with individual fluorophores. The CLSM images presented by channel overlay (B) or individual (C & D). Observe the localisation of DAPI next to the surface (1 & 3 - B), the FITC BSA at $\sim 100 \mu\text{m}$ respect to the surface (2 & 3 - B) and unspecified fluorescent band at $\sim 200 \mu\text{m}$ (1, 2 & 3 - C). The images are representative of $n = 4$, and the scale bars correspond to $200 \mu\text{m}$.

To further evaluate if the distribution of fluorescent molecules in the FITC BSA - DAPI scaffold is related to the addition order (Fig. 3.6 - 3B), the loading treatment was inverted to DAPI - FITC BSA.

The CLSM images did not show any significant changes in the localisation of the fluorophore despite changes in their addition order (Fig. 3.8 - 3B & 3.9 - A). Moreover, it appears that the FITC BSA diffuses through the DAPI band without disturbing it.

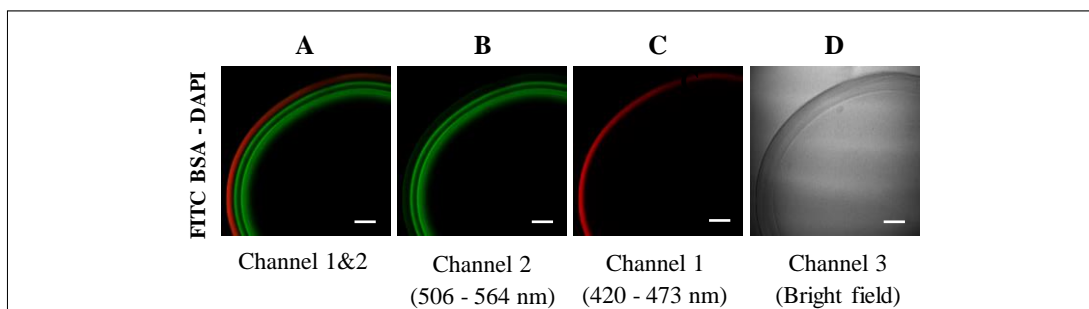


Figure 3.9 Preferential localisation of fluorophores within the nanoclay/protein scaffold. The CLSM images reveal the localisation of DAPI next to the clay-gel surface (A & C), FITC BSA at $\sim 100 \mu\text{m}$ respect to the surface and unspecified fluorescent band at $\sim 200 \mu\text{m}$ (B) although the addition order of DAPI and FITC BSA was inverted. The images are representative of $n = 4$, and the scale bars correspond to $200 \mu\text{m}$.

Overall, these results indicate that the distribution of patterned molecules is independent of the order of addition into the system, suggesting the absorption and preferential spatial localisation of the fluorophores into the scaffold. This phenomenon could be related to specific interactions between the assembled clay-gel and the fluorophores loaded because they localise in the same place regardless of their addition order.

Furthermore, the above experiments revealed that the clay-gel absorbs not only the FITC BSA and DAPI molecules but also fluorescent components of the media, which become visible at a wavelength (506 - 564 nm) similar to the FITC BSA.

3.3.2.3. Factors that trigger the fluorophores diffusion

Detailed analysis of the first experiments suggests that components in the tissue culture media may trigger the diffusion and localisation of fluorophores within the clay-gel (Fig. 3.4) since the direct assembly of the clay-gel in FITC BSA - DPBS, in the absence of DMEM FCS, resulted in protein adsorption on the surface (Fig.3.3). To evaluate this, gels were assembled in different permutations of tissue culture solutions, including DMEM, DPBS and FCS (Fig. 3.10 - A).

The fluorescent components present in the media were monitored to assess how the molecule localisation inside the clay-gel is affected by treatment. For this reason, no extra fluorophores were added in this experiment.

Overall, the confocal images revealed the emission of localised fluorescent bands (506 - 564 nm) on the scaffold assembled in DMEM 10% DPBS and DMEM 10% FCS. In contrast, no fluorescence emitted by the scaffolds treated with DPBS 10% FCS and DPBS was observed. These results identify the DMEM (components) as the primary contributor of the fluorescence observed (Fig. 3.10 - B, D & G).

The confocal images and ROI charts also revealed the different distribution of DMEM molecules in the clay-gels assembled with DMEM 10 % DPBS and DMEM 10 % FCS. They localised next to the surface and internally forming a ring, respectively. Further measurement of the DMEM diffusion path length (mean \pm SD, n = 4) were taken with respect to the scaffold surface (Fig. 3.10 - E). Descriptive statistics showed an increase of ~55 % in the diffusion path length in DMEM 10 % FCS ($232.0 \pm 1.83 \mu\text{m}$) compared with DMEM 10 % DPBS ($105.5 \pm 3.31 \mu\text{m}$) treatments (Fig. 3.10 - F).

Moreover, the bright field images revealed a distinct double-ring adjacent to the surface, but only in those scaffolds treated with 10 % FCS (Fig. 3.10 - C, red arrow). This feature seems to be related to the further diffusion and localisation of DMEM molecules into the clay-gel assembled with DMEM 10 % FCS.

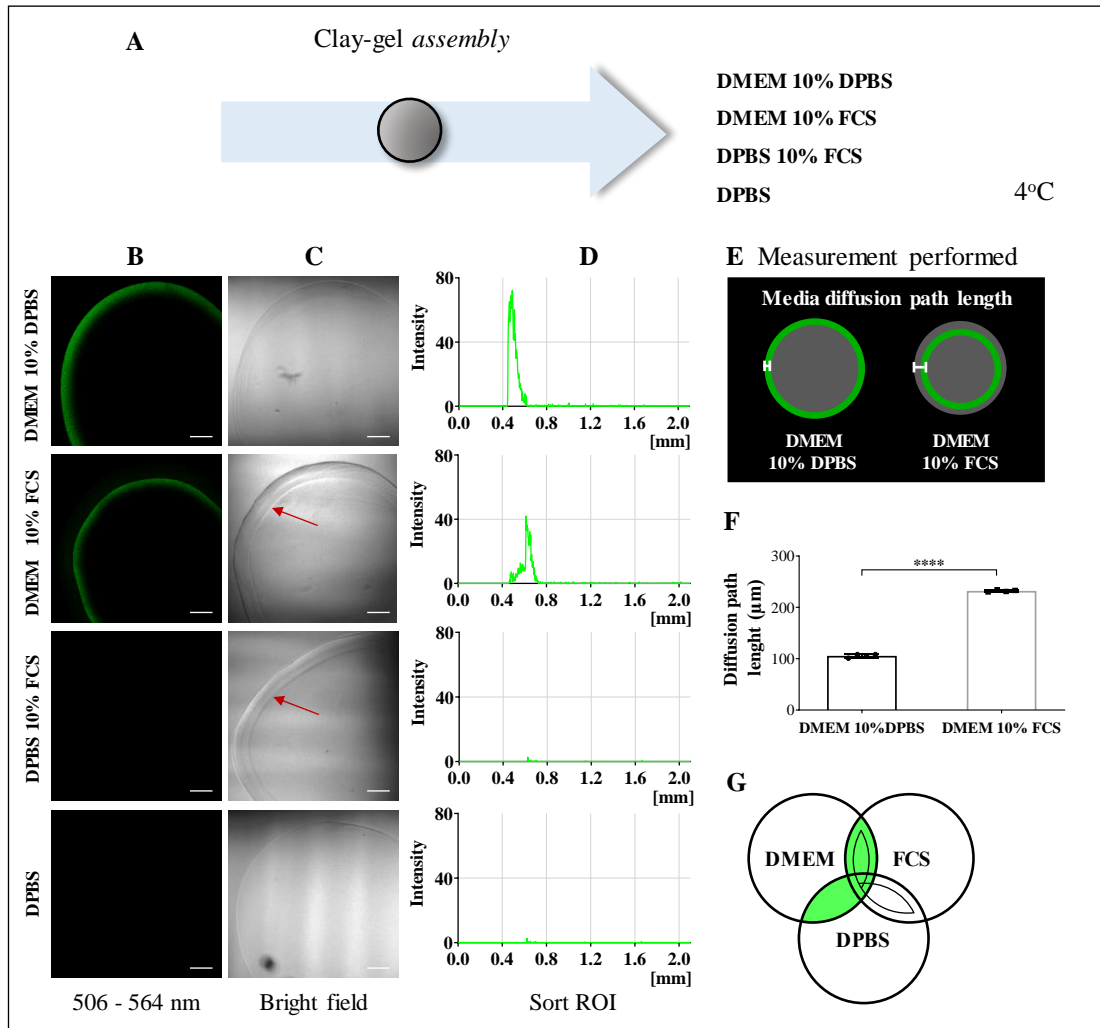


Figure 3.10 Tissue culture solutions and clay-gel droplet interaction. (A) Schematic illustration to assembled clay-gels in different TC media solution. The (B & G) CLSM images confirm that the FCS triggers the formation of the fluorescent ring within the clay-gel, also that the DMEM components are related to the fluorescent emission observed at 506 - 564 nm wavelength. (F) Measurement of the diffusion path length of the DMEM molecules shows that the addition of 10 % FCS increases their diffusion by ~55 % compared to DMEM diluted with 10% DPBS. The (C) bright field images of the clay-gel assembled with FCS reveals the formation of two symmetrical and parallel rings, which seems to be related to the fluorescent ring formation and localisation in the DMEM 10 % FCS scaffolds (C, red arrows). The (E & F) diffusion path lengths measured with respect to the gel surface were presented as the mean and standard deviation of $n = 4$. The scale bars correspond to 200 μm .

Interestingly, comparison of the fluorescent and bright field images of the clay-gel assembled with DMEM 10% FCS indicates that the fluorescent band observed starts right ($140 \pm 2.42 \mu\text{m}$) where the internal ring apparent in bright field localises ($140 \pm 2.90 \mu\text{m}$) (Fig. 3.11 - B & C).

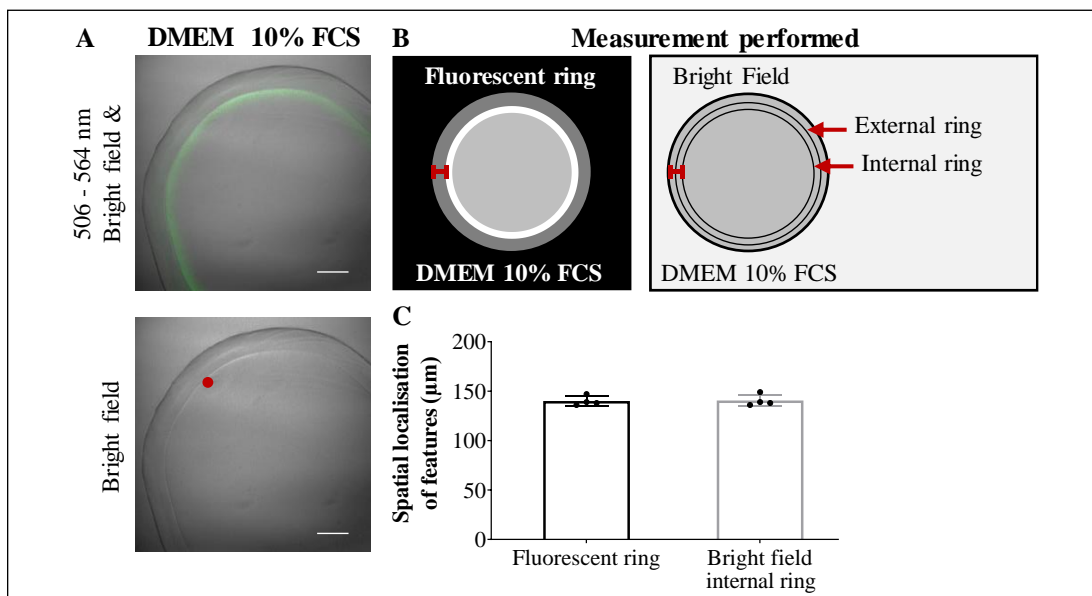


Figure 3.11 Clay-gel droplets assembled in DMEM FCS. Analysis of the (A) CLSM images reveals the colocalisation of the fluorescent ring and the internal ring observed in the bright field image (red dot, which indicates that the FCS regulates the localisation of DMEM molecules into the clay-gel. (B) The spatial localization of both features, fluorescent ring and bright field internal ring, within the gel was analysed with respect to the gel surface and (C) the results presented as the mean and standard deviation for $n = 4$. The scale bars correspond to $200 \mu\text{m}$.

These observations suggest that while molecules within DMEM cause the fluorescence, it is FCS (or rather, components therein) that influence the diffusion and localisation of molecules within the clay-gel droplet. To confirm this, clay-gels were assembled directly in 100 % FCS and then loaded with FITC BSA (Fig. 3.12 - A)

Different distributions of FITC BSA in the clay-gel droplet were observed depending on the treatment. In the presence of FCS, two distinct rings of FITC BSA were observed near to the core of the clay-gel droplet at ~ 850 and $\sim 320 \mu\text{m}$ from the surface (Fig. 3.12 - 2D & 2F), whereas in the absence of FCS, the FITC BSA was observed at the droplet surface (Fig. 3.12 - 3D, 3F & I). This layer of proteins bound to the surface was relatively unstable, and its fragmentation was observed throughout the experiment (Fig. 3.12 - 3B).

Interestingly, the bright field images of the clay-gel droplets treated with FCS - FITC BSA revealed the formation of two internal rings with similar localisation to the fluorescent rings previously described (Fig. 3.12 - 2B & 2C, red dots, & I).

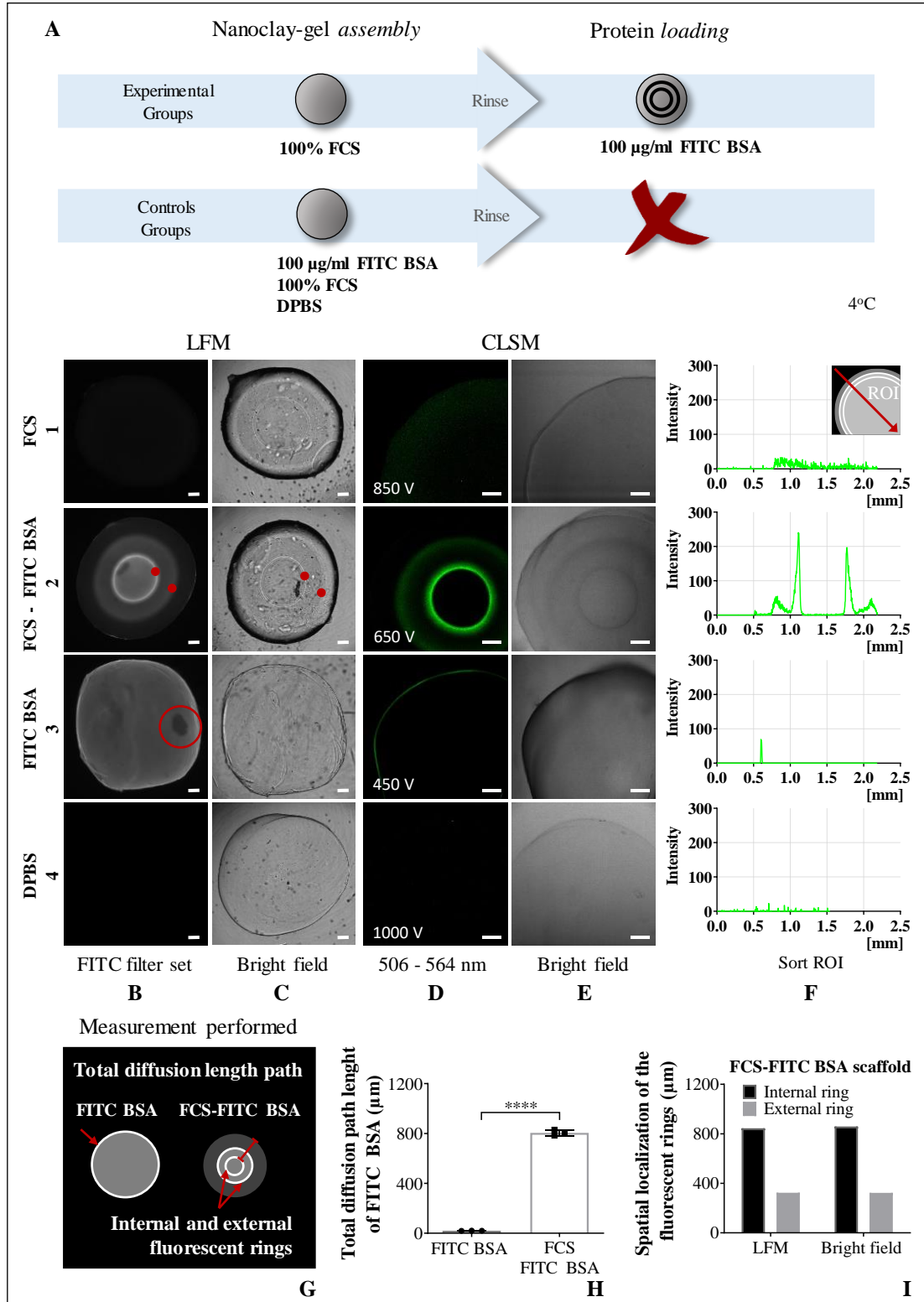


Figure 3.12 Diffusion of FITC BSA facilitated by FCS. The (2B & 2D) CLSM images showed the diffusion and localisation of FITC BSA into the clay-gel facilitated by FCS when compared to the

scaffolds assembled directly into FITC BSA, (3B & 3D) where the fluorescent proteins stayed next to the surface. (G & H) Further measurement of the diffusion path length supported this observation (unpaired sample t-test, $p < 0.0001$, $n = 3$). (I) Comparison of the fluorescent and bright field images of the clay-gel assembled with FCS indicates that the internal rings observed localise at $844.75 \pm 6.67 \mu\text{m}$ and $859.34 \pm 5.57 \mu\text{m}$ from the surface, respectively, and the external rings localise at $324.24 \pm 5.16 \mu\text{m}$ and $323.3 \pm 5.02 \mu\text{m}$, respectively. The results were presented as the mean and standard deviation of triplicates. The scale bars correspond to $200 \mu\text{m}$. Due to significant differences in fluorescent intensity, different gain settings were used, these are indicated at the bottom-left corner of the confocal fluorescent images.

These results confirm that the FCS facilitates the diffusion and localisation of FITC BSA into the clay-gel droplets. Nevertheless, the FCS is a complex solution, and in order to understand the phenomenon observed, it is essential determining the minimum FCS constituents necessary to assemble the scaffold. For this purpose, a bottom-up approach was used to simplify the solution and test the main constituents, this would allow better control over the variables studied and determine with more accuracy the individual component of the serum or combination that is responsible for the 3D localisation of molecules in the clay-gel.

To facilitate analysis, the FCS composition was assessed and divided into two major phases: organic and inorganic. The organic phase was constituted of mainly proteins, lipids and carbohydrates, and the inorganic phase of ions. Moreover, from each subgroup, the respective constituents were evaluated as shown in table 3.3.

Table 3.2 Constituents of serum. Table modified from Freshney (2005) and some data taken from Cheever et al (2017)*.

Constituents of serum			
Main phases	Components	Sub - components	Range of Concentrations
Organic	Proteins	Bovine Serum Albumin	20 - 50 mg/mL
		Globulin	1 - 15 mg/mL
		Growth factors	1 - 100 ng/mL
		Hormones	0.1 - 200 nM
		Lipids	Triglycerides *
		Cholesterol *	28.33 mg/dL
		Free Fatty Acids	0.1 - 1.0 μM
		Phospholipids	0.7 - 3.0 mg/mL

	Carbohydrates	Glucose	0.6 - 1.2 mg/mL
	Vitamins	Fat/water soluble	10 ng - 10 µg/ml
	Amino acids		0.01 - 1.0 µM
	Urea		170 - 300 µg/mL
Inorganic	Ions	Sodium	135 - 155 mM
		Potassium	5 - 15 mM
		Phosphate	2 - 5 mM
		Calcium	4 - 7 mM
		Magnesium	0.6 - 1.1 mmol/L
		Chlorides	100 µM

According to this brief review, BSA, docosahexaenoic acid 22:6 (n-3) (DHA), glucose (Glu) and DPBS were selected to represent the overall concentration of proteins, lipids, carbohydrates and ions present in serum. Different permutations of these solutions were used to assemble the clay-gels, and the concentrations were fixed to approximate the overall components' concentration (Fig. 3.13).

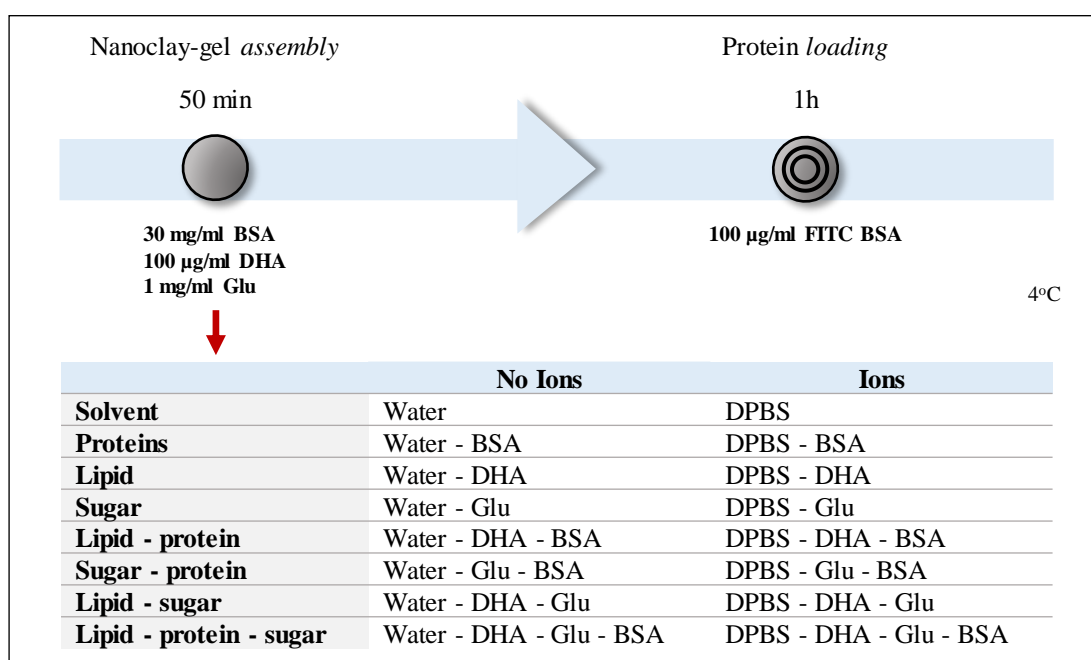


Figure 3.13 Protocol to self-assemble nanoclay/protein scaffolds with different serum constituents. Bovine serum albumin (BSA), docosahexaenoic acid 22:6 (n-3) (DHA), glucose (Glu) and Dulbecco phosphate buffer saline (DPBS) were used to represent the overall concentration of proteins, lipids, carbohydrates and ions present in serum, respectively. Different permutations were prepared with these components. Note that the DHA solution was prepared by reconstituting 1 g ampule of DHA (Sigma- Aldrich) with 95 % Ethanol to a concentration of 10 mg/ml as recommended by the supplier.

Only clay-gels assembled in water-based solutions containing BSA exhibited patterning of proteins upon loading. This seems to indicate that the protein fraction of the FCS is responsible for the phenomenon observed (Fig. 3.14 - A).

Interestingly, the clay-gels assembled with water - Glu - BSA solution did not show any protein patterning (Fig. 3.14 - 6A). Nevertheless, the 3D localisation of FITC BSA was observed again upon the addition of DHA (Fig. 3.14 - 8A), which suggest that the glucose has a detrimental effect on the protein patterning that could be reversed by the DHA.

Regarding the clay-gel droplets placed in DPBS-based solutions, all of them preserved their structures irrespective of the organic components. This is in contrast to gels prepared in water, which dissolved/dispersed in the absence of BSA. However, only those in DPBS that contained BSA formed a double fluorescent band of FITC BSA near the scaffold periphery (Fig. 3.14 - 2B, 5B, 6B & 8B).

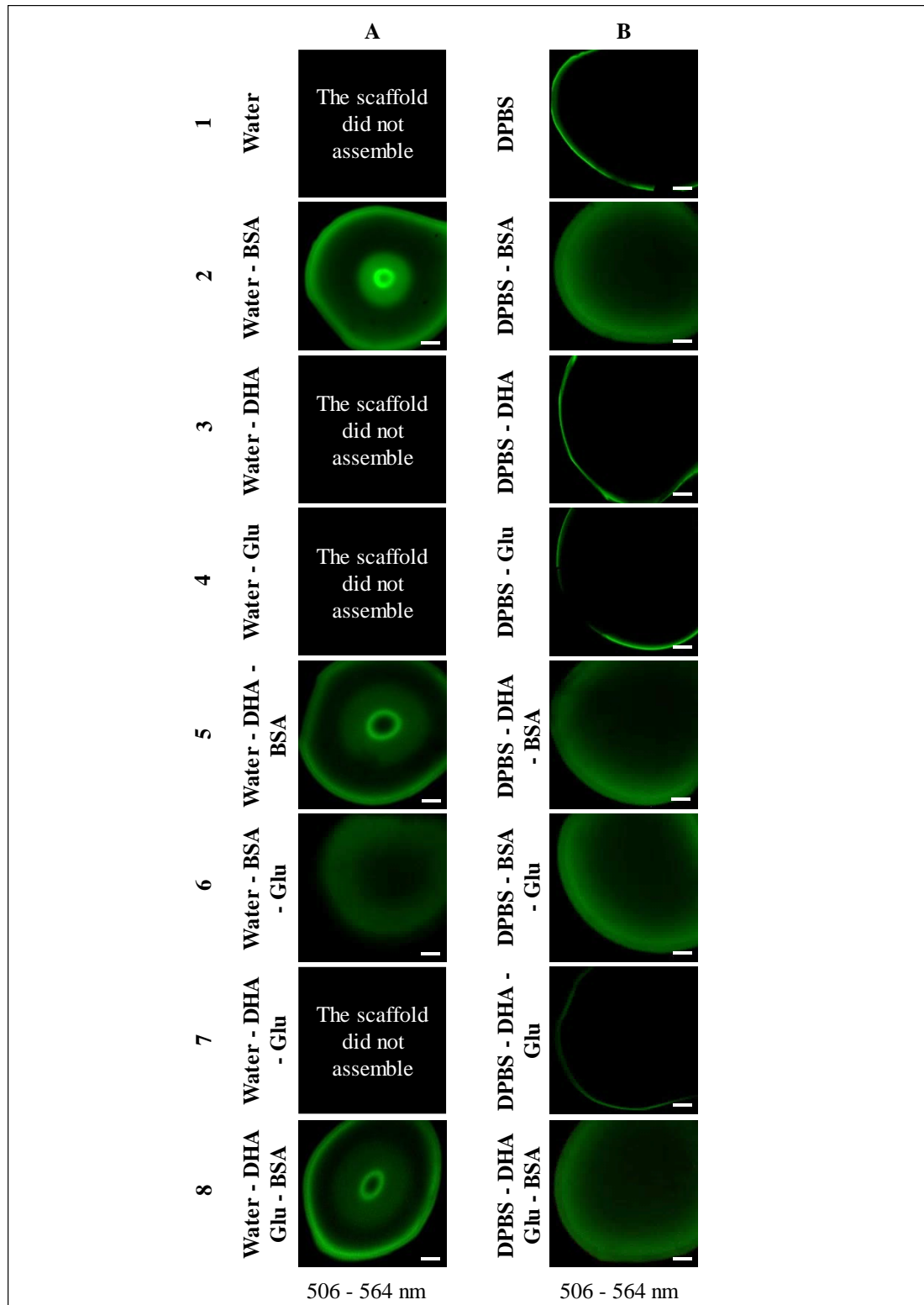


Figure 3.14 Assembly of clay-gel droplets in different FCS components. The CLSM images reveal the 3D localisation of FITC BSA in the core of water-based scaffolds containing BSA (A2, A5 & A8), except for the water - BSA - Glu (A6). The DPBS scaffolds containing BSA formed a double fluorescent band near the scaffold periphery (B2, B5, B6 & B8), this indicates that BSA plays the main role in the protein patterning and other components (DHA, Glu & ions) could be used to alter their localisation. The scale bars correspond to 200 μ m and the images to n = 4.

The protein patterning observed in the water-based, and DPBS-based scaffolds are significantly different. Nevertheless, one can conclude that the protein fraction of the FCS is the critical component for the 3D localisation of the fluorescent molecules into the clay-gel, and despite the presence of ions, DHA and glucose may not be necessary, both do affect the molecules localisation.

3.4 Discussion

This chapter aimed to develop a scaffold with a 3D gradient of biochemical cues as a first step to mimicking the extracellular microenvironment of the repairing bone callus. The strategy consisted of exploiting the physicochemical properties of clay nanoparticles and proteins to build non-covalent, bioactive and biocompatible scaffolds.

Initial attempts to build an LBL polyelectrolyte using 2.8 % clay-gel droplets for the sequential deposition of FITC BSA and 1 % clay - DAPI layers led to the fabrication of micron-sized layered structures with a distinctive anisotropic arrangement (Fig. 3.4). Interestingly, subsequent experiments showed that the structure assembled did not result from a deposition process, but the absorption and interaction of the clay nanoparticles with the molecules present in the DMEM - FCS, FITC BSA and DAPI solutions (Fig. 3.8). Further analysis of this structure revealed the preferential spatial localisation of FITC BSA and DAPI molecules inside the scaffolds irrespective of their addition order (Fig. 3.8 & 3.9).

This is the first study to describe the 3D micropatterning of molecules in clay-gels. Hence, to examine the nature of the assembled structure, other diffusion methods or phenomena that result in spontaneous patterns formation inside hydrogels were studied.

Hydrogels are characterised for their “ability to restrict the diffusive movement of solutes” (Amsden, 1998) by either size and/or interaction filtering. The process depends mainly on the physical and chemical properties of the hydrogels, such as the composition, crosslinking method, mesh size of crosslink, structure (homogenous or

heterogeneous), charge and polarity, but as well on the physicochemical properties of the solute.

The clay-gel used in this study is considered as a physical gel since it is stabilised by electrostatic interactions. In this regard, different authors indicate that the diffusion of a solute through a physically cross-linked hydrogel decreases with the increase of the solute size, increase in the crosslinking density and decrease in the volume fraction of water within the hydrogel (Johansson 1991 and Amsden 1998). For example, Dawson et al. (2003) reported that diffusion coefficient of polystyrene beads through human sputum mucus was significantly reduced as the particle size was increased from 100 nm to 500 nm, supporting the idea of size filtering (Fig. 3.15 - A).

Conversely, others have demonstrated that complex interactions between the hydrogel and the diffusing particle, such as electrostatics, hydrophobic interactions, and chemical binding result in a more intricate selection process called interaction filtering (Liegel et al. 2009 and Zhang et al. 2015). For example, Lai et al. (2007) found that polystyrene beads of 100 nm size were more effectively immobilised inside human cervicovaginal mucus than were 200 and 500 nm polystyrene beads contradicting the idea that the finite mesh size of cross-linked hydrogels is solely responsible for hindered diffusion in hydrogels (Fig. 3.15 - B).

As stated earlier, in this study, the diffusion and preferential spatial localisation of different molecules in the clay-gel was demonstrated. In this regard, the DAPI and FITC BSA localised next and at $\sim 100 \mu\text{m}$ from the clay-gel surface, respectively. (Fig. 3.8). Further comparison of the molecules localisation with respect their molecular weight suggest that they are not being filtered by size, but through complex interactions between the molecules and the clay nanoparticles, since the FITC BSA molecular weight (66.5 kDa) is 240-fold higher compared to the DAPI molecule (277.32 g/mol) and it diffused further into the gel.

Thus, based on these results, one could hypothesise that the separation of molecules within the clay-gel is the result of a selective diffusion barrier. However, further work would be needed to determine the mechanisms governing selective filtering,

whether it is size and/or interaction dependent since it is not possible to draw a conclusion based only on two molecules, DAPI and FITC BSA, and furthermore, they are significantly different in terms of composition and structure.

Also, in considering these results, it should be noted that the DAPI molecule itself will have a slight influence on the ionic strength of the system which may influence the gelation dynamics of the clay colloid. Though analysis of the gel structure in brightfield images reveals no differences between systems with and without DAPI (Figure 3.8).

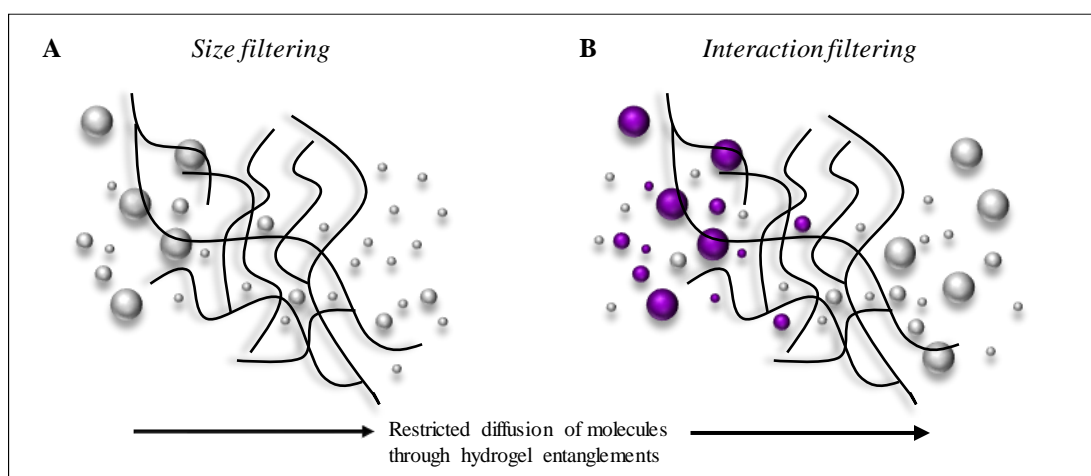


Figure 3.15 Hydrogel generic filtering principles. (A) Size filtering allows smaller molecules than the hydrogel (black curved lines) cut-off size to pass while larger molecules are rejected. (B) Interaction filtering allows the diffusion of molecules rendering to their surface properties. In this regard, a subset of molecules (purple) strongly interacts, either physically or chemically, with hydrogel entanglements and are trapped, while other molecules (grey) show weak interactions and thus are allowed to pass. Modified image from Lieleg & Ribbeck (2011).

In order to study the diffusion mechanism by which the patterned clay-gels are formed, recognising the tissue culture media components that trigger the process is crucial. Thus, the analysis of different TC solutions' interaction with the clay-gel demonstrated that the FCS facilitates the diffusion and localisation of fluorescent molecules within the scaffold (Fig. 3.10 & 3.11). Moreover, a confirmatory experiment revealed the diffusion of the FITC BSA inside the scaffold assembled with FCS compared to the DPBS control, whereas the FITC BSA stayed at the surface (Fig. 3.12).

A key feature observed in the bright field images of the scaffolds assembled with either 100 % FCS or 10 % FCS diluted with DMEM or DPBS was the formation of two rings, which were not apparent in the DPBS scaffolds or controls (Fig. 3.10 & 3.12). This might be due to changes in the structural density of the clay-gel along the diffusion process that bends or refracts the light becoming visible to the eye. Further study is required to understand this optical phenomenon. However, it is interesting that the rings colocalise with the spatial localisation of the loaded fluorescent molecule (Fig. 3.12 - 2D, 2E & I).

Overall, the final findings suggest that two distinct phenomena are taking place with corresponding fabrication steps: 1) a primary diffusion of FCS molecules through the clay-gel that creates a template (or apparent rings), which then guides 2) the secondary diffusion and localisation of FITC BSA (Fig. 3.16).

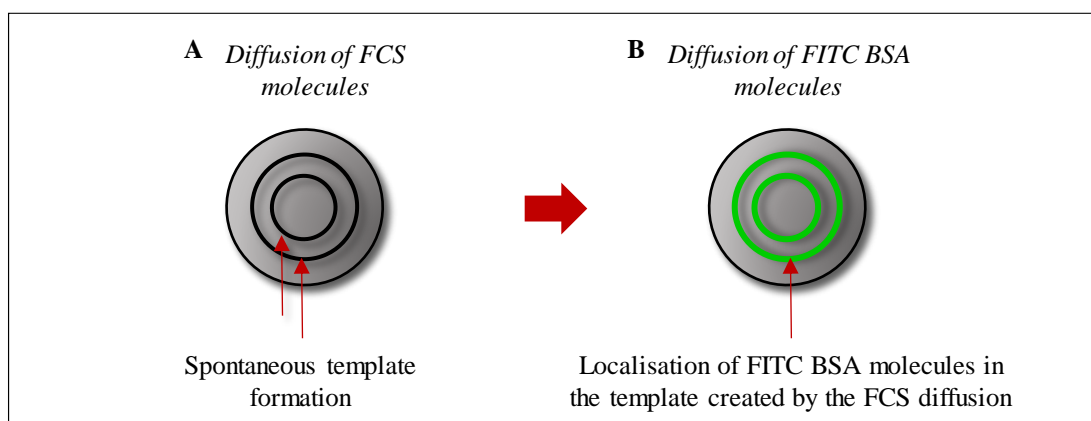


Figure 3.16 Diffusion process of FCS and FITC BSA molecules in the clay-gel. (A) Assembly of clay-gels in FCS solution leads to the formation of two visible rings, which then serve as a template for the (B) localisation of diffused FITC BSA molecules.

The FCS contains numerous components, including proteins, lipids, sugars, vitamins and ions, which still makes difficult studying in more detail the diffusion mechanism. Therefore, it has been sought to determine the specific components in the FCS related to the diffusion and 3D localisation of molecules. The results indicate that the BSA is the minimum component necessary to trigger the assembly and 3D micropatterning of molecules, though the presence of ions, DHA and glucose also affect the pattern distribution (Fig. 3.14).

a positive and negative surface charge respectively. The rings were formed by the periodic precipitation of AgTMA and AgMUA clusters (Lagzi et al. 2010). Regarding the (C) Belousov-Zhabotinskii Reactions, thin layers of ferroin-loaded resin use with a reactant solution containing malonic acid, potassium bromate, and sulphuric acid. An oscillating chemical reaction leads to the formation of oxidised ferroin catalyst patterns (Maselko et al. 1989).

Numerous reaction-diffusion models have been written to explain different patterning phenomena, but there are two main models that relate to physical gel matrices. One such model consists in the diffusion of reactants towards each other which then interact at the crossing diffusion fronts resulting in the formation of patterns (Semenov et al. 2013, Lovrak et al. 2017 and Abe et al. 2019) (Fig. 3.18 - A). An alternative model involves the interaction of multiple components, but one of them is static in the matrix gel (Maki et al. 2011, Wu et al. 2014 and Mredha et al. 2018) (Fig. 3.18 - B).

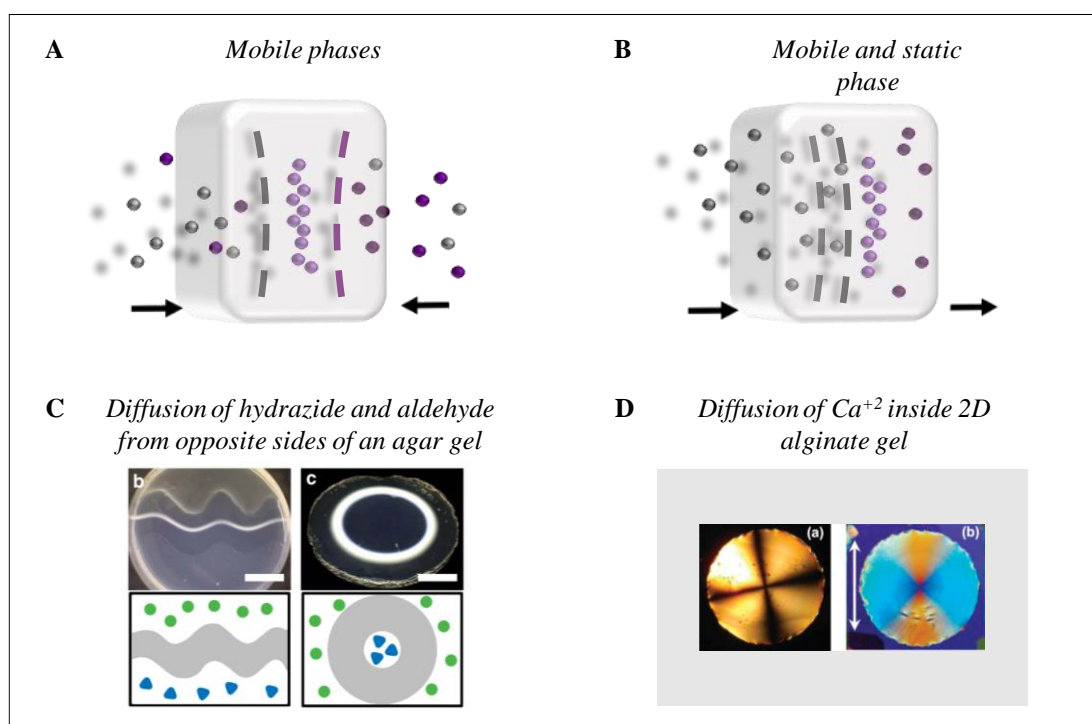


Figure 3.18 Reaction-diffusion models through physical gels matrix. (A) Schematic illustration of two mobile phases (grey and dark purple spheres) diffusing towards each other and interacting at the crossing diffusion fronts (dotted lines) forming patterns (lilac spheres) inside the gel matrix (translucid grey box). (B) Illustration of one mobile phase (grey spheres) diffusing through a gel matrix (translucid grey box) that holds a static phase (dark purple spheres). The interaction results in the formation of periodic patterns (lilac spheres). C and D are an example of both models, respectively. Thus, C illustrates a free-standing agar gel of 1.5 % (grey figure), which reservoirs (white area) were filled with hydrazide (green circles) and aldehyde (blue triangles). Interaction of both reactants at the

diffusion front led to the formation of a non-transparent supramolecular pattern in the gel, as shown in the images. Scale bar = 1 cm (Lovrak et al. 2017). Moreover, (D) crossed nicols (right) and polarised light (left) images revealed that reaction-diffusion of CaCl_2 through 2 % alginate gel triggers the formation of a structure with periodic arrangement (Maki et al. 2011).

Based on the above-described reaction-diffusion models, assembly of clay-gels in FCS seems to share some similarities with the “mobile and static phase” model. Hence, the diffusion of FCS (mobile phase) through the clay-gel (static phase) would lead to the self-assembly of a structure as it reacts with the clay nanoparticles. A similar strategy was reported by Wu et al. (2014). They described the self-assembly of a physical gel, poly (2,2'-disulfonyl-4,4'-benzidine terephthalamide (PBDT) governed by reaction-diffusion of calcium ions, which led to the formation of macroscopic anisotropic structure. Polarised light imaging revealed a progressive concentric alignment of the PBDT molecules simultaneously to the Ca^{2+} ions reaction-diffusion. “The electrostatic complexation between the cationic Ca^{2+} and anionic PBDT resulted in the self-assembly of PBDT molecules into mesoscopic fibrous bundles that align in parallel to the Ca^{2+} flux front” (Fig. 3.19 - B).

Interestingly, at the gelation front of concentrated PBDT gels (2 & 3 %), a visible ring was observed. Further characterisation with PLM and SEM confirmed that this structure was the diffusion front between the reacted and unreacted PBDT molecules, which displaced towards the core with time. The authors claim that the diffusion front became visible because the reacted gel contracted and stretched the unreacted gel (Wu et al. 2014). (Fig. 3.19 - B).

A similar study was reported by Maki et al. (2011). The authors studied the anisotropic structure of Ca-alginate gels assembled by diffusion setting method. Crossed polarised light revealed the radial structure, and small-angle x-ray scattering (SAXS) profile indicated the formation of rod-like fibrils of alginate that were aligned perpendicularly to the direction of the Ca^{2+} flow (Fig. 3.18 - D).

Moreover, Wu et al. (2014) suggest that the molecules that yield this type of assemblies possess negative charges and have a rigid or semi-rigid structure. For

example, PBDT and alginate, endowing them with the ability to form anisotropic structures by themselves or via electrostatic interaction with cations.

Recently, it has been shown the assembly of optically anisotropic gels by diffusion of gelation-inducing agents for various kinds of naturally occurring molecules, including κ -carrageenan (Narita et al. 2006 and 2008), carboxymethylcellulose (S. C. Lin et al. 2010), DNA (Dobashi et al. 2007) and fibril proteins (Furusawa et al. 2012). All of them possess the characteristic above described, except for the chitosan (Yamamoto et al. 2010) and curdlan (Dobashi et al. 2005), which are positively charged.

This type of reaction-diffusion process has been exploited in the last years as a mechanism to assemble physical gels with improved anisotropic properties known as dialysis-induced gelation, and also proposed as a possible mechanism for the mesoscopic self-assembly hard and soft tissue (Furusawa et al. 2012).

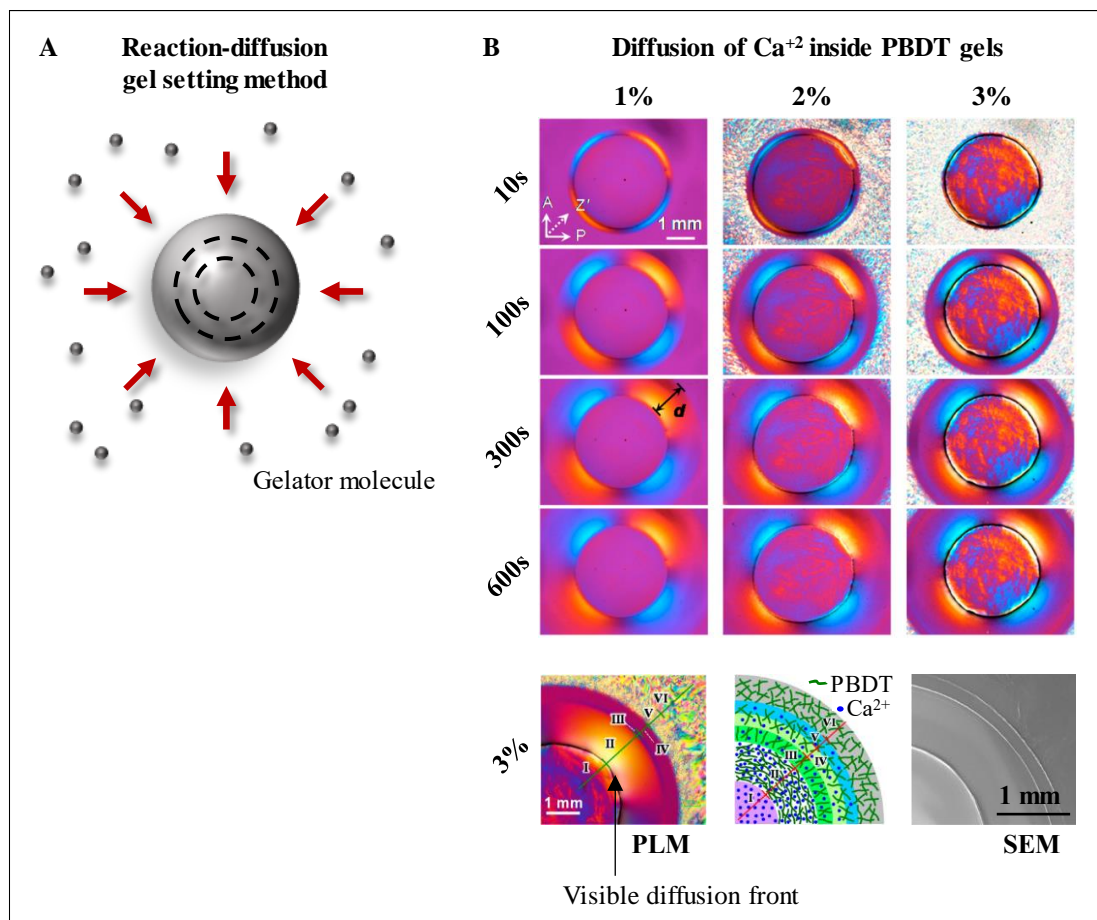


Figure 3.19 Reaction-diffusion gelation of physical gels by “one mobile and one static phase” model. (A) Schematic illustration of gelator molecule (small grey spheres) diffusing through (dashed line) the physical gel. (B) PLM images of different concentrations of PBDT reveals a radial birefringence corresponding to the reacted gel upon diffusion of calcium ions. Analysis of the PLM and SEM images reveals the development of an intricate periodic structure. Moreover, at 2 and 3 % gel, a ring corresponding to the diffusion front was observed moving towards the core with time (Wu et al. 2014).

The assembled clay-gel structure is similar to the reaction-diffusion system above discussed in term of procedure, structure and composition. Thus, 1) the gelation is triggered by the electrostatic interactions between the clay and diffusive FCS or BSA molecules. 2) The bright field images revealed the formation of two visible rings upon assembly with FCS, which could be the diffusion front of different components accordingly to Wu et al. (2014). Finally, 3) the clay nanoparticle is a rigid molecule that holds a permanent negative charged. Although the BSA is negatively charged, studies indicate that it binds to the clay-nanoparticle by surface patch binding, which depends on the protein surface charge anisotropy and not the overall protein net charge (Das et al. 2016). These last features fulfil the compositional requirement discussed.

To summarise, there are two different diffusion process taking place in the 3D micropatterned scaffolds; 1) the diffusion of FCS or BSA molecules through the clay-gel at the assembly step and, 2) the diffusion of FITC BSA or DAPI at the loading step. Thus, low concentration of BSA is not able to diffuse into the gel but high concentrations, which indicates that the concentration is the driving force as expected in a simple diffusion process. Nevertheless, this does not explain how the anisotropic structure is assembled. Therefore, it is assumed that a reaction process between the protein and the clay is occurring simultaneously to the diffusion process, forming an anisotropic structure, which then guides the localisation of the fluorescent loaded molecule. Further structural characterisation must be performed to confirm this assumption, such as PLM to evaluate if the clay-gel acquired an anisotropic arrangement upon diffusion of concentrated protein solution, SEM to evaluated changes in the microstructure of the assembled scaffold and TEM to visualize the spatial distribution and arrangement of the nanoparticles throughout the gel.

Regarding the diffusion of the loaded molecules, a selective diffusion barrier would explain their preferential spatial localisation by interaction with the assembled protein/clay-gel structure. Further work is required to verify this and what forces are interfering with the diffusion process. For example, evaluating the contribution of loaded protein' structure, size, shape and isoelectric point on its diffusion and spatial localisation within the assembled clay-gel.

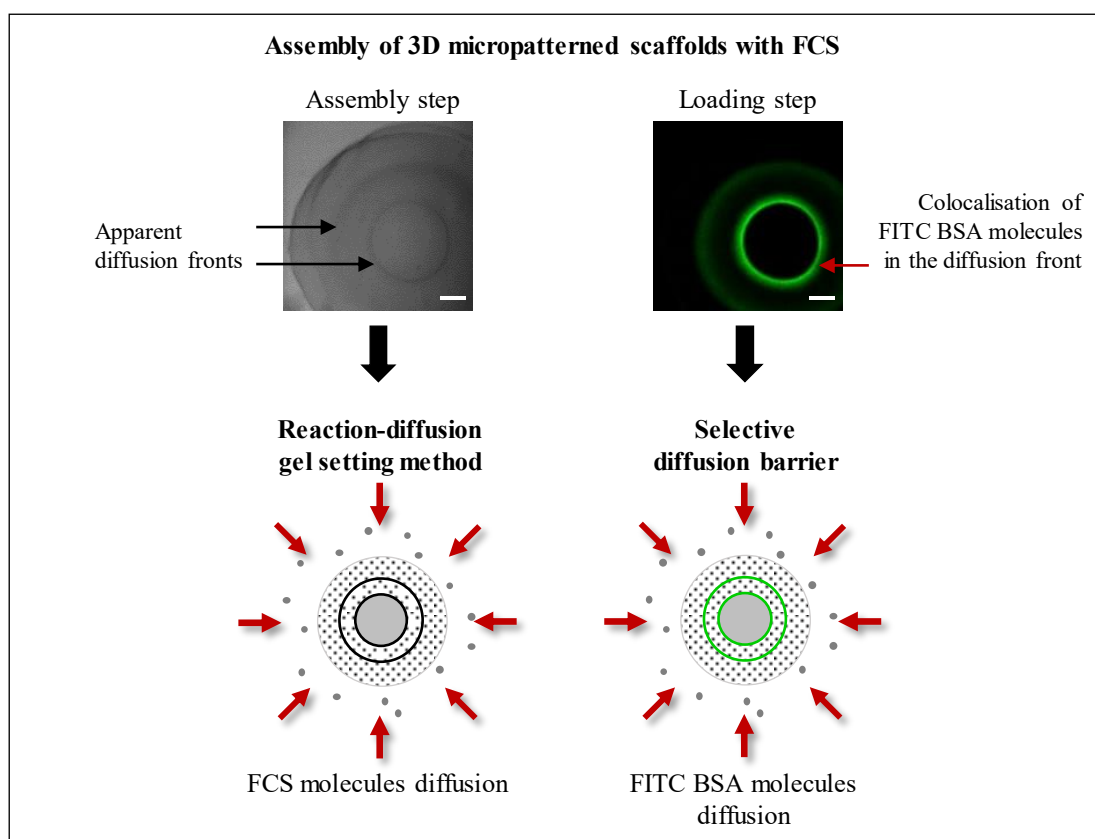


Figure. 3.20 Diffusion-reaction mechanism to assemble 3D micropatterned structures. It was hypothesised that the influx of FCS crosslinks the clay nanoparticles molecules intermolecularly by a “reaction-diffusion process”, resulting in the assembly of an anisotropic structure with a template that guides the secondary absorption and localisation of molecules through a “selective diffusion barrier” process.

Finally, the presence of FCS in the system represents an advantage for developing important knowledge base since the first event to take place upon the implantation of a biomaterial is the protein-surface interaction, which is crucial as it determines its ultimate fate and success. Several research groups have reported the positive biocompatibility of clay containing biomaterials in animal models (Herrera et al. 1995 and Li et al. 2010), and the ability of certain clay-gel systems to stimulate

regeneration through growth factor delivery (Dawson & Oreffo, 2013 and Gibbs et al. 2016). Understanding the early stage of plasma protein absorption will be necessary for characterising early cell responses to clay-gel biomaterials. In this regard, the scaffold built could serve as an “in vitro” model to study the interaction of high viscosity clay-gels with the proteins and ions found at the bloodstream, as the FCS is blood but without form elements (plasma).

Nevertheless, from the biomaterial design point of view, the FCS represents a disadvantage. This complex solution contains xenogenic species that might induce some infections (Louët, 2004) and despite it could be replaced by synthetic sera or human serum, it is not practical since the scaffold would carry proteins and molecules out of interest that could potentially interfere with the desired cell response. Moreover, the FCS contains numerous components, including proteins, lipids, sugars, vitamins and ions, which would then difficult studying in more detail the diffusion mechanism. Therefore, the next experiments will used BSA or other protein solution to study the phenomena.

It is important to recognise that current studies about the behaviour of Laponite® clay nanoparticles dispersion as a function of ionic strength are not comparable with the phenomena here observed. According to the metastable phase diagram presented in figure 1.12, preparation of 0.5 - 3 % Laponite® dispersion in 20 mM sodium chloride solution leads to phase separation of the clay nanoparticles in the form of flocculation (Mourchid et al. 1998 and Ruzicka & Zaccarelli, 2011). However, when concentrated Laponite® dispersion, 2.8 %, is drop-cast in a DPBS solution, which sodium chloride concentration is comparably high, 137.93 mM, the clay nanoparticles do not flocculate. This unforeseen behaviour could be potentially related to the method used to incorporate the ions into the system. In the first approach, the ions are incorporated by mixing them with the clay nanoparticles, and in the second approach, the ions are let to diffusion through. It could be argued that the concentrated Laponite® dispersion did not flocculate because it was initially dispersed with ultrapure water and underwent a heat treatment, which could potentially accelerate the ageing before the incorporation of the ions. However, Shi et al. (2018) reported that mixing of DPBS to equivalent system causes flocculation.

Further work is required to characterise the behaviour of clay nanoparticles upon ions diffusion. It could potentially be a new physical state the Laponite® dispersions with relevance in bulk soft matter assemblies, which properties could be exploited in different research fields, including biology, physics, material science or chemistry.

3.5 Conclusions

This is believed to be the first report describing the assembly of a scaffold with 3D gradient of molecules involving non-covalent clay-gel opening new avenues of research for biomimetic drug delivery systems.

Towards understanding the spontaneous patterning of molecules, it is evidently a result of a complex diffusion process, which is triggered by BSA molecules in a concentration dependent manner. In this regard, two distinct diffusion processes take place; 1) a primary diffusion of concentrated protein solution (FCS and BSA) through the clay-gel that then facilitates 2) a secondary diffusion and localisation of low concentrated FITC BSA molecules.

Thus, to elucidate the diffusion mechanism two main questions need to be addressed in the next experiments, how the concentrated protein solution diffuses into the clay-gel and creates a template for the secondary diffusion of low concentrated BSA, and what the type of binding interactions or molecular forces regulate the diffusion and selective trapping of low concentrated BSA.

Chapter 4 OPTIMISATION OF FABRICATION PARAMETERS

4.1 Introduction

In the previous chapter, the treatment of clay-gels with different tissue culture media and protein solutions resulted in the spontaneous assembly of structures with 3D micropatterning of molecules. Towards understanding the process, it was recognised that the phenomenon was the result of two distinct diffusion processes; 1) a primary diffusion of a concentrated protein solution (100 % FCS or 30 mg/ml - BSA) through the clay-gel that facilitated, 2) a secondary diffusion and localisation of lower concentration protein solutions (100 μ g/ml - FITC BSA) (Fig. 3.12 & 3.14).

Moreover, the mechanism leading to both diffusion processes were different. In this regard, it was suggested; 1) that the initial diffusion of concentrated protein solution into the clay-gel created an anisotropic structure, which serves as a template for the 3D localisation of molecules governed, potentially via a “reaction-diffusion process” and 2) a secondary diffusion of low concentrated protein solution by a “selective diffusion barrier” process (Fig. 4.1).

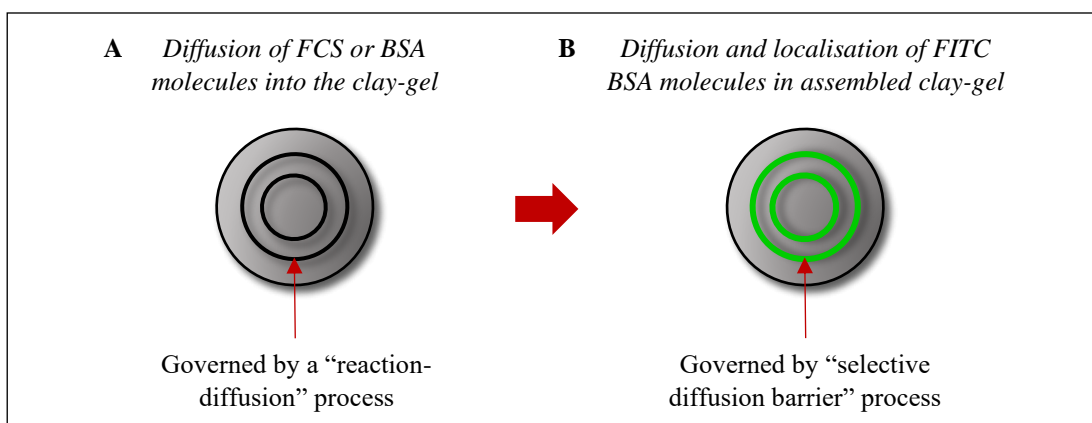


Figure. 4.1 3D micropatterned clay-gel assembly hypothesis. Schematic illustration of the clay-gel assembly by two different diffusion process. (A) Initial diffusion of concentrated protein solution diffuses into the scaffold creating an anisotropic structure governed by a “reaction-diffusion” process that serves as a template for the localisation of the loaded protein. (B) Then a “selective diffusion barrier” process, due to the interaction with the diffusive media, governs the diffusion of the loaded protein.

Diffusion is a physical process that refers to the movement of molecules from a region of high concentration to one of lower concentration. Numerous laws and equations have been written to describe the phenomena and the factors that may alter it, specifically, the diffusion coefficient (rate) and the diffusion length (distance

travelled). In this regard, the concentration and temperature are known to have a linear effect on the diffusion coefficient of solute in free solution. In contrast, diffusion time is inversely proportional to the diffusion coefficient, which means that the greater the coefficient, the shorter the time to travel from A to B. However, time would be proportional to the diffusion length. Moreover, other factors, such as the ionic strength, particle size and charge may influence the process by affecting the properties of either the solute or the diffusive media itself, in this case, the Laponite® gel (reviewed by Anderson et al. 1978 and Del Rió & Whitaker, 2016).

Thus, based on these norms and the fact that the scaffold assembly is the results of a diffusion process. The general objectives of this chapter are 1) to evaluate the effect of relevant factors on the diffusion coefficient and the diffusion length of the proteins in the clay-gel 2) to assess the utility of standard diffusion models to account for this system, also 3) to optimise the fabrication parameters. In doing so, it will test the hypothesis that introducing changes in the diffusion process may affect the 3D micropatterning of protein inside the clay-gel.

4.2 Materials and Methods

4.2.1 Scaffold assembly

Based on previous finding, the procedure to assemble the scaffolds was simplified into three main steps: assembly, loading and storage. In this regard, the 5 μ l droplet of 2.8 % clay-gel was placed in a concentrated protein solution and left to assemble. Next, the assembled structure was transferred to another solution containing the protein of interest to be loaded. Finally, the loaded scaffolds were stored and analysed (Fig. 4.2).

The procedure was performed in a 96-well plate containing 200 μ l of either the assembly, loading or storage solution. Moreover, only one scaffold was assembled per well and transferred to the different solutions using a spatula. Generally, a rinsing step with DPBS took place between the assembly and loading steps. Note that the rinsing step did not show a significant impact in the final localisation of the protein loaded, and for this reason, it was not included in this study. Also, most of the experiments were performed at 4°C, otherwise stated. Finally, to visualise the spatial localisation of the fluorescent protein, LFM and CLSM were used.

At every fabrication step, various parameters known to affect diffusion processes were assessed, such as protein concentration, ionic strength, incubation time and temperature or the isoelectric point and molecular weight of the protein. Details of the parameters evaluated, and experimental setup can be found in the results section.

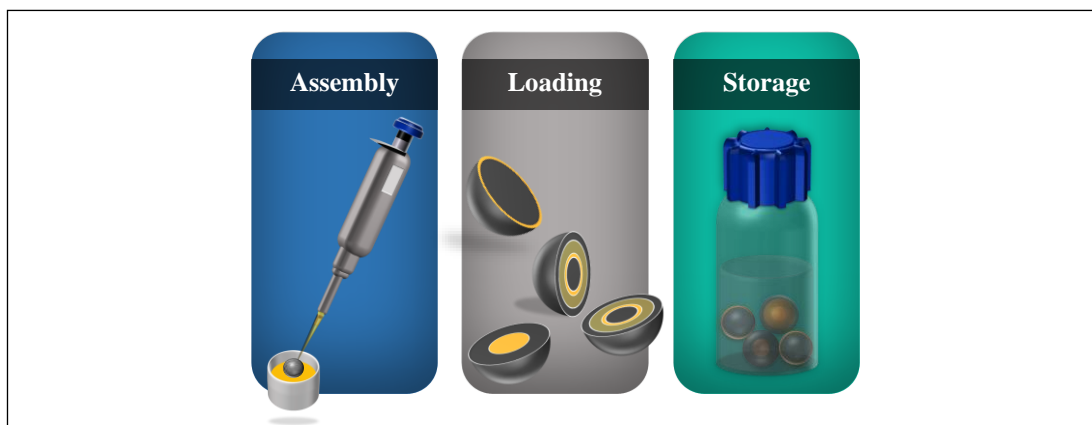


Figure 4.2 Fabrication of nanoclay/protein scaffolds steps.

4.2.2. Protein quantification

To quantify the amount of proteins depleted by the scaffold as a function of time, absorbance and fluorometric protein assays were carried out using a spectrophotometer (Promega).

Based on the Bradford dye-binding method, a protein assay was performed to determine the concentration of proteins in the media. Initially, a serial dilution ranging from 0 to 100 $\mu\text{g/ml}$ of FITC BSA was made using DPBS (pH 7.4) as a diluent to build a standard curve. Afterwards, 90 μl aliquots of samples (scaffolds incubated) and standard were pipetted to into a clear 96-microplate well in replicates of four and then mixed with 10 μl of Bio-Rad assay concentrated. Subsequently, the intensity of the light absorbed by the dye-protein bound at 595 nm was measured with the spectrophotometer. Final interpolation of the values acquired into the standard curve provided a relative measurement of protein concentration.

To perform the fluorometric protein assay, formerly, a serial dilution of FITC BSA (0 to 100 $\mu\text{g/ml}$) were made using DPBS. After dilution, 100 μl aliquots of samples (scaffolds incubated) and standards were pipetted into black 96-microplate wells ($n = 4$). Finally, the spectrofluorometer excitation was set up to 490 nm to detect the FITC BSA.

4.3 Results

4.3.1 Effect of assembly variables on nanoclay/protein scaffold structure

To optimise the assembly parameters and shed light on the mechanisms underlying the patterning process, the current section will evaluate various factors likely to influence the diffusion coefficient and length at the assembly process, including the following: i) protein concentration, ii) solvent ionic strength, iii) incubation time and temperature, and iv) protein size and net charge.

4.3.1.1 Protein concentration of the assembly solution

Towards evaluating the effect of BSA concentration on the protein patterning, clay-gels were assembled with gradients of BSA diluted in water and subsequently loaded with FITC BSA (Fig. 4.3 - A).

Qualitative analysis indicated that the clay-gels assembled only in concentrations of BSA over 20 mg/ml, which suggests that the assembly is concentration-dependent. Regarding the protein patterning, the confocal images revealed the formation of two fluorescent rings within the clay-gels; one localised next to the surface regardless of the concentration of the assembly solution and, one internal that localised closer to the core until it could not be observed anymore as the concentration of the assembly solution increased (Fig. 4.3 - B).

Measurement of the internal fluorescent ring was taken with respect to the scaffold surface to determine its spatial localisation (Fig. 4.3 - B). Then, a simple linear regression was carried out to test if the concentration of the assembly solution predicted the spatial localisation of the internal fluorescent ring. The results showed a significant regression equation ($p < 0.0001$), with an R^2 of 0.98, and the slope of the regression line predicted that the fluorescent ring displaced towards the core of the scaffold by an average of 11.61 μm for an increase in 1 mg/ml of BSA (Fig. 4.3 - C & D).

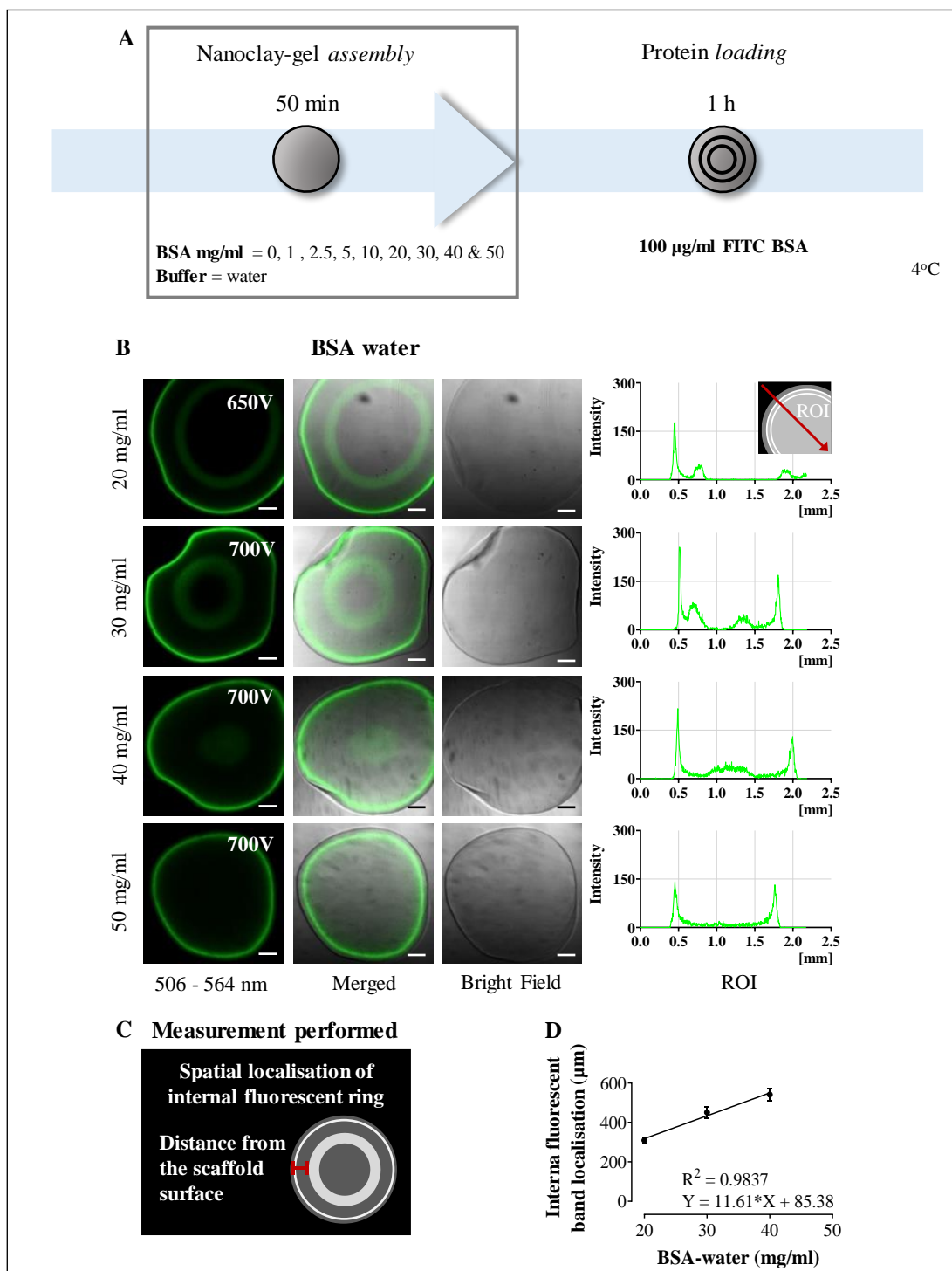


Figure 4.3 Assembly of nanoclay/protein scaffold as a function of protein concentration. (A) Schematic illustration to assemble clay-gels in different concentrations of BSA-water. The (B) CLSM images reveal two fluorescent rings inside the scaffolds. One localised next to the surface and one internal that localised closer to the core as the concentration of the assembly solution increased. Measurement (C) and statistical analysis (D) of the internal fluorescent ring with respect the clay-gel surface indicates that the displacement of the internal fluorescent ring is proportional to the increase in the protein concentration of the assembly solution (linear regression, $R^2 = 0.98$). The results represent mean \pm SD for $n = 4$ and the scale bars to 200 μm .

The results show that the concentration of the assembly solution not only plays an essential role in the localisation of the molecules loaded (FITC BSA) but in the stability of the clay-gel assembly itself since the clay-gel disintegrated in BSA concentrations of < 20 mg/ml.

Further analysis of the bright field images revealed a significant decrease in the scaffold size as the protein concentration increased (Fig. 4.4 - A). Analysis of the diameter of the scaffolds assembled with 20 and 50 mg/ml BSA-water demonstrated a decrease in size from 7.7 ± 4.2 % to 26.4 ± 1.3 %, respectively (Fig. 4.4 - B & D) when compared to the calculated theoretical size (see methods section - 2.1.2). A simple regression analysis confirmed an inverse correlation between the scaffold size and concentration of the assembly solution ($p < 0.0001$). The results showed a significant regression equation with an R^2 of 0.92, and an average decrease in the scaffold size by $13.49 \mu\text{m}$ was predicted for an increase in 1 mg/ml of BSA (Fig. 4.4 - C).

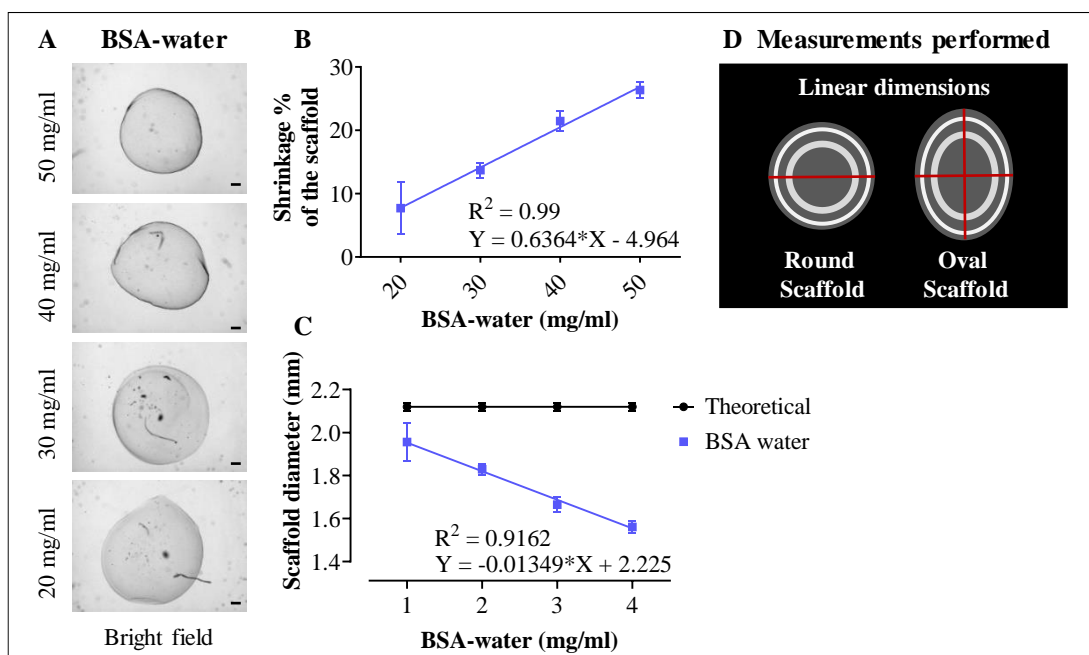


Figure 4.4 Linear dimensions of nanoclay/protein scaffold assembled as a function of BSA concentration. (A & B) The bright field images and respective statistical analysis reveals a significant decrease in the scaffold size with respect to the calculated theoretical size, from 7.7 ± 4.2 % to 26.4 ± 1.3 % when the scaffolds are assembled with 20 & 50 mg/ml BSA-water, respectively (C) The linear regression shows that the shrinkage is inversely proportional to the increase of protein concentration ($R^2 = 0.92$). The illustration (D) shows the measurement performed on the images. The results represent mean \pm SD for $n = 4$ and the scale bars to $200 \mu\text{m}$

Overall, these results indicate that the protein concentration of the assembly solution has a significant effect on the scaffold assembly, fluorescent pattern formation, as well as the linear dimensions of the clay-gel scaffold. In this regard, both the assembly and loading process was dependent on a specific range of protein concentration in the assembly solution since the scaffolds did not assemble under 20 mg/ml, and the internal fluorescent ring was only observed between 20 to 30 mg/ml BSA-water. Moreover, the scaffolds shrank as the concentration of the assembly solution increased.

4.3.1.2 Presence of ions in the assembly solution

Next, the effect of ions on the protein patterning was evaluated. Clay-gels were treated as above, but the BSA was diluted with DPBS instead of water (Fig. 4.5).

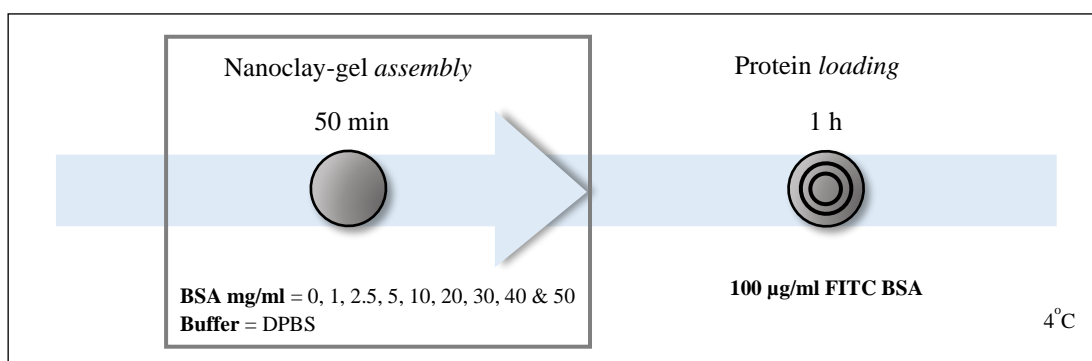


Figure 4.5 Effect of ions in the assembly of nanoclay/protein scaffold, experiment setup.

Schematic illustration to assemble clay-gels in different concentrations of BSA - DPBS.

In contrast to the previous experiment, in the presence of DPBS, the clay-gels did assemble irrespective of the presence or absence of proteins. Again, the confocal images revealed two fluorescent rings (506 - 564 nm) inside clay-gels, which corresponded to the FITC BSA emission. One of the fluorescent rings localised next to the surface and the other localised closer to the core until it could not be observed anymore as the concentration of the assembly solution increased (Fig. 4.6 - A).

Measurement of the internal fluorescent ring was taken with respect to the scaffold surface to evaluate the relationship between its spatial localisation and the concentration of the assembly solutions (Fig. 4.6 - B). As above, a simple regression analysis confirmed a linear relationship between both variables ($p < 0.0001$).

Moreover, the slope of the regression line predicted that the fluorescent ring displaced towards the core of the scaffold by an average of 41.35 μm for an increase in 1 mg/ml of BSA ($R^2 = 0.99$) (Fig. 4.6 - C).

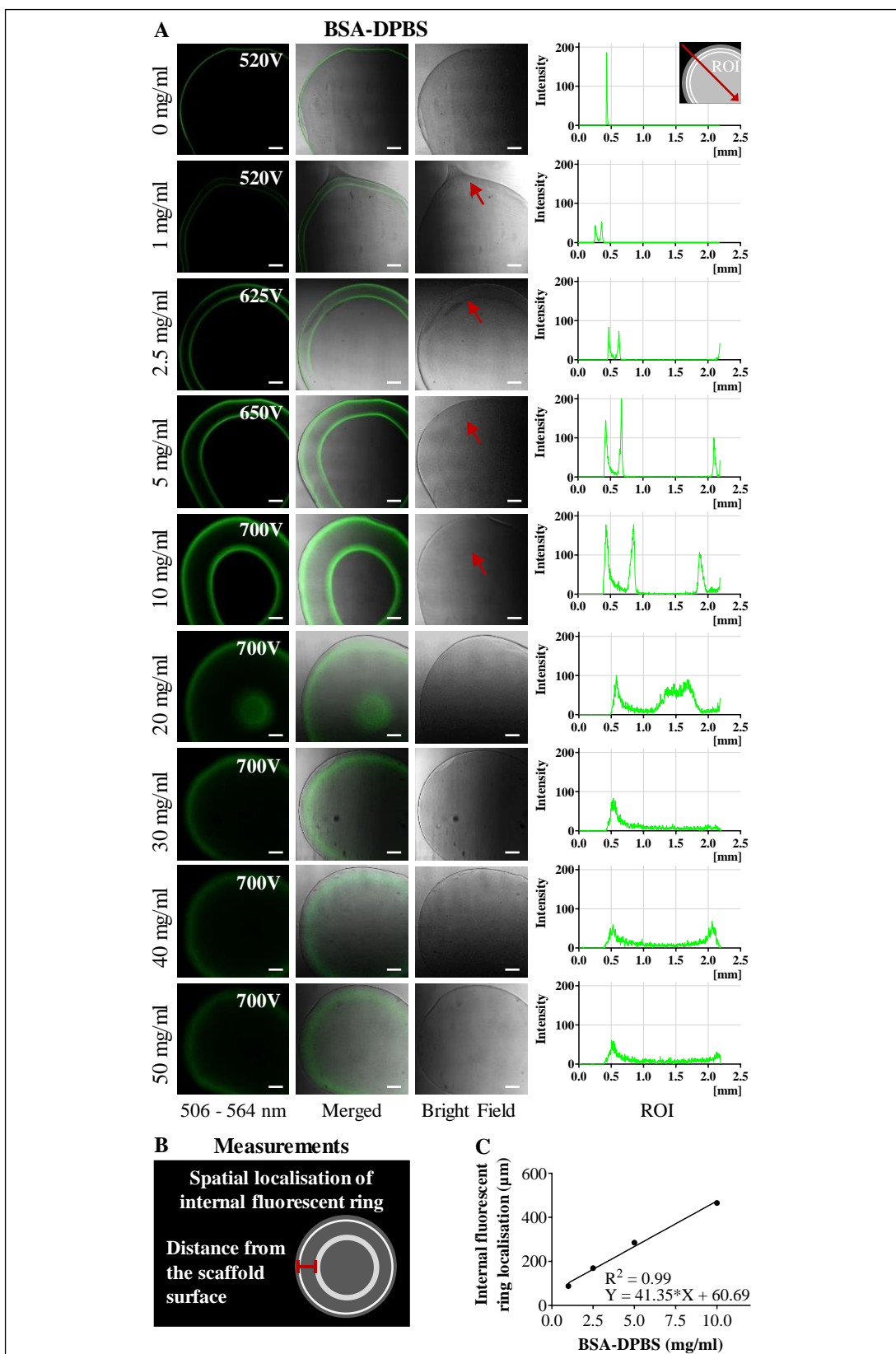


Figure 4.6 Effect of ions in the assembly of nanoclay/protein scaffold. (A) The CLSM images revealed a first fluorescent ring near the surface of all the scaffolds and a second fluorescent ring that localised closer to the core of the scaffolds as the protein concentration of the assembly solution increased. The illustration (B) shows the measurement performed on the images. The linear regression (C) indicated that the displacement of the internal fluorescent ring was concentration dependent ($R^2 = 0.99$). The results represent mean \pm SD for $n = 4$ and the scale bars to 200 μm .

Contrary to earlier experiments, the results indicate that in the presence of ions, the assembly, or stability, of the clay-gels is not dependent on a minimum protein concentration. Moreover, the ions cause the displacement of the internal fluorescent ring towards the core at lower concentrations compared to the water-based samples. Furthermore, in contrast to scaffolds prepared in water, the clay-gels displayed similar size regardless of the concentration of the assembly solution (Fig. 4.7 - A), to confirm this, manual measurements of the diameter of the clay-gel droplets were taken and analysed with one-way ANOVA (mean \pm SD, $n = 4$). The results did not show any significant changes (post hoc Bonferroni, $p > 0.05$) in the clay-gels linear dimensions ($2.119 \pm 0.06 \text{ mm} - 0 \text{ mg/ml}$) as a function of the protein concentration in the presence of ions (Fig. 4.7 - B & C).

Interestingly, and again in contrast to water-based assembly, when comparing the predicted diameter of the scaffold ($2.12 \pm 0.02 \text{ mm}$) calculated from the initial clay-gel volume (methods section - 2.1.2) with the assembled structure, it seems that the linear dimensions did not change (swelling - deswelling) significantly during the assembly in the presence of ions (Fig. 4.7 - C, the black line represent the theoretical diameter).

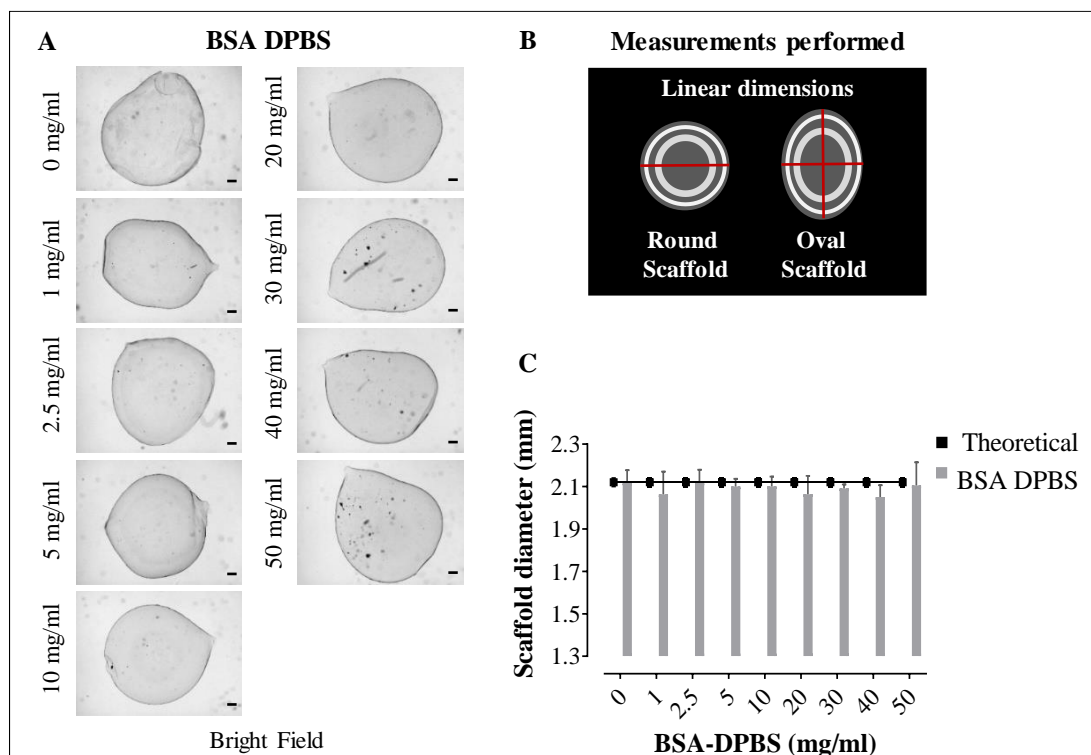


Figure 4.7 Effect of ions in the linear dimensions of nanoclay/protein scaffold. The bright field images (A) and respective statistical analysis (C) reveals no significant changes in the size of the scaffold as the concentration of the assembly solution increases (one-way ANOVA, post hoc Bonferroni, $p > 0.05$). The illustration (B) shows the measurement performed on the images. The results represent mean \pm SD for $n = 4$ and the scale bars to 200 μm .

The results indicate that the addition of ions affects the clay-gel assembly, protein patterning and linear dimensions significantly. Contrary to the previous experiment, all the scaffolds did assemble regardless of the protein concentration, and the scaffolds did not shrink (Fig. 4.4 & 4.7).

Regarding the fluorescent protein pattern, the ions showed a significant impact as well. Compared to the previous experiment; the ions reduced the protein concentration required to form the fluorescent ring, from 20 mg/ml BSA-water to 1 mg/ml BSA-DPBS. Also, it seems that the ions accelerated protein displacement toward the core of the clay-gel droplet and allowed patterning to occur at a lower and broader range of protein concentrations (1 to 10 mg/ml BSA) (Fig. 4.3 & 4.6).

The differences between the water-based and DPBS-based scaffolds represent practical advantages for clay-gel patterning, as well as better representing physiological fluids. For these reasons, subsequent experiments were conducted using DPBS solutions unless otherwise stated.

4.3.1.3 Assembly time

The above results indicate that the diffusion and consequent spatial localisation of the proteins is concentration dependent, which is characteristic of diffusion processes. Thus, it should be expected that the assembly time would also regulate the localisation of the proteins into the clay-gel. To evaluate this, the clay-gels were left to assemble in the presence of BSA for different lengths of time prior to loading with labelled protein (Fig. 4.8 - A).

Overall, the LFM images showed the formation of one distinct fluorescent ring within the green region that moved progressively towards the core of the clay-gel as a function of assembly time until after 160 mins when a distinct fluorescent band could no longer be observed (Fig. 4.8 - B).

As above, measurement of the fluorescent ring was taken with respect to the clay-gel droplet surface to determine the spatial localisation of the FITC BSA (Fig. 4.8 - C). A simple regression was then calculated to study the relationship between the localisation of the FITC BSA and the square root of the assembly time ($\sqrt{\text{min}}$) to model a simple diffusion process (Fick's first law). The results confirm that there is a link between both variables ($p < 0.0001$). A significant regression equation was found with an R^2 of 0.99. The average displacement of the fluorescent ring towards the core of the clay-gel increased $64.62 \mu\text{m}$ for each $\sqrt{\text{min}}$ of assembly time (Fig. 4.8 - D).

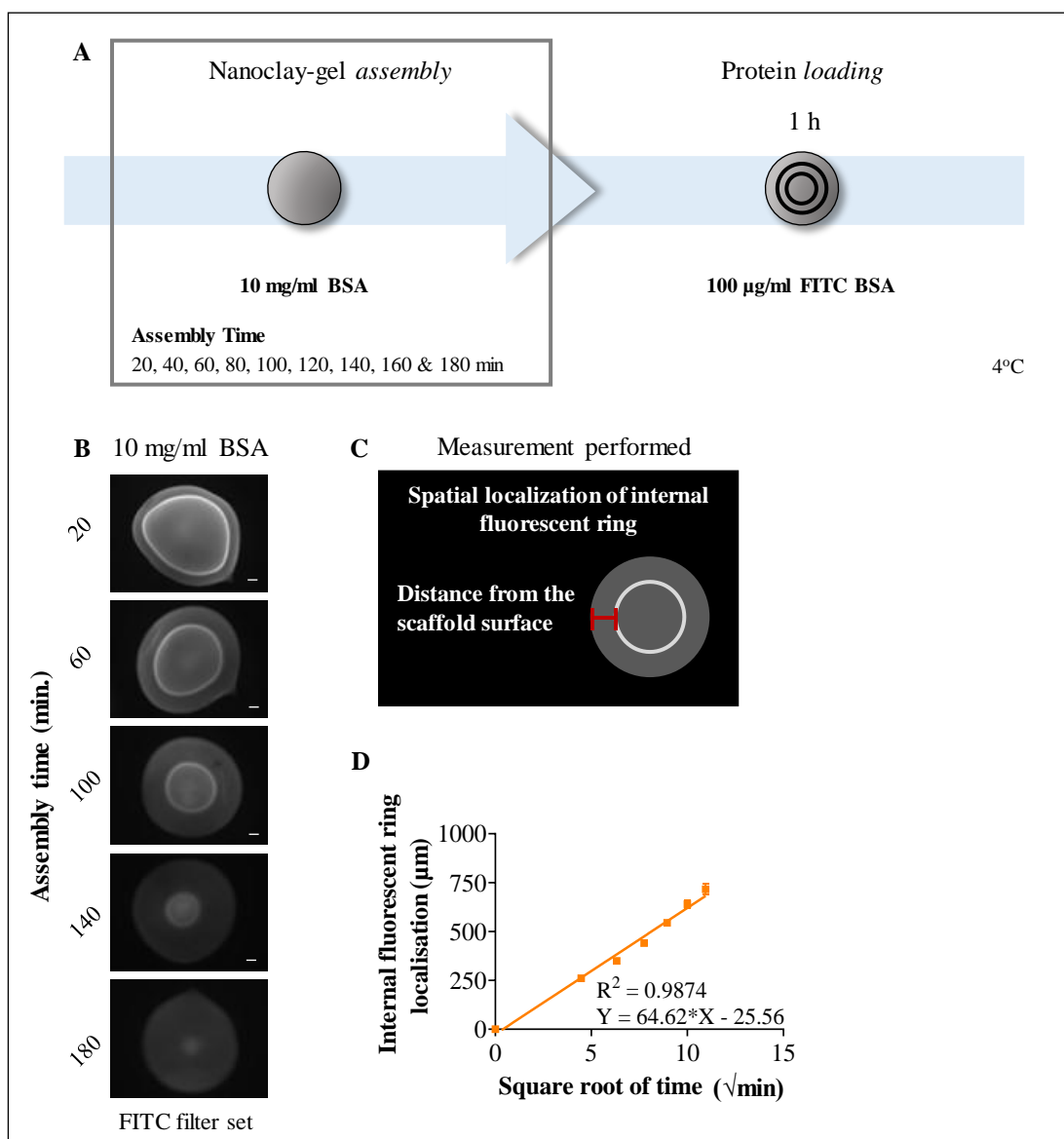


Figure 4.8 Assembly of nanoclay/protein scaffolds as a function of time. (A) Schematic illustration of clay-gels assembled at sequential time points. The (B) LFM images showed a progressive displacement of the fluorescent ring towards the core of the clay-gel as the assembly time increased. Measurement (C) and respective analysis (D) of the fluorescent ring localisation with respect the clay-gel droplet surface confirmed that the displacement of the fluorescent ring starting from the surface (0,0) is proportional to the square root of the assembly time in min (linear regression, $R^2 = 0.99$, $p < 0.0001$). The results were presented as the mean \pm SD for $n = 4$, and the scale bars correspond to 200 μm .

To conclude, the assembly time can be used to control the final localisation of the proteins loaded into the clay-gel droplet.

Since this is a concentration dependent process, as demonstrated earlier (Fig. 4.3 & 4.6), a similar experiment was set up to assess the time taken to assemble the clay-gels with different concentrations of the assembly solution.

Overall, the results show a significant linear regression for all the concentrations (Fig. 4.9 - see respective p values and R^2 on the table).

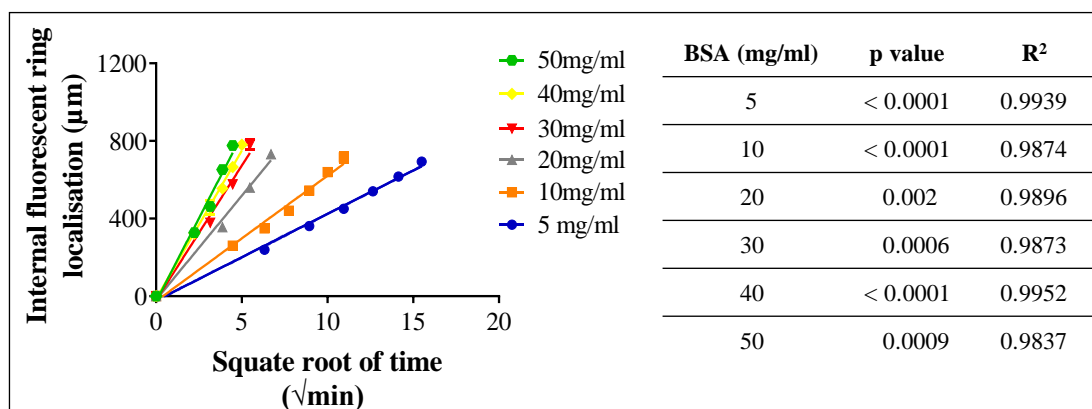


Figure 4.9 Assembly of nanoclay/protein scaffolds as a function of time and concentration of the assembly solution. A linear regression demonstrated that incubation time is proportional to protein concentration. The results were presented as the standard deviation for $n = 4$.

4.3.1.4 Assembly temperature

The objective of the next experiment is to evaluate the effect of the assembly temperature on the nanoclay/protein scaffold, specifically on the localisation of the loaded fluorescent protein and on the clay-gel dimensions. For this, clay-gels were assembled at 4°C and 37°C (for 1 hour), respectively (Fig. 4.10 - A).

Measurements of the fluorescent ring with respect to the clay-gel droplet surface were taken from the LFM images to evaluate the spatial localisation of the proteins (mean \pm SD, $n = 4$) as a function of the assembly temperature. The analysis of variance (two - way ANOVA) of the 10 mg/ml BSA and 20 mg/ml BSA clay-gels showed significant increase in displacement of about 16 % ($p = 0.0012$) and 22 % respectively ($p < 0.0001$) when assembled at 37°C compared to 4°C (Fig. 4.10 - C).

Moreover, to evaluate the dimensions of the clay-gels, a two-way ANOVA was conducted to compare their diameters (mean \pm SD, $n = 4$) as a function of

temperature at a given concentration. The results did not show any significant changes ($p > 0.05$) in the diameter of the clay-gel droplet when assembled at 4°C or 37°C and with different concentrations of the assembly solution (Fig. 4.10 - D).

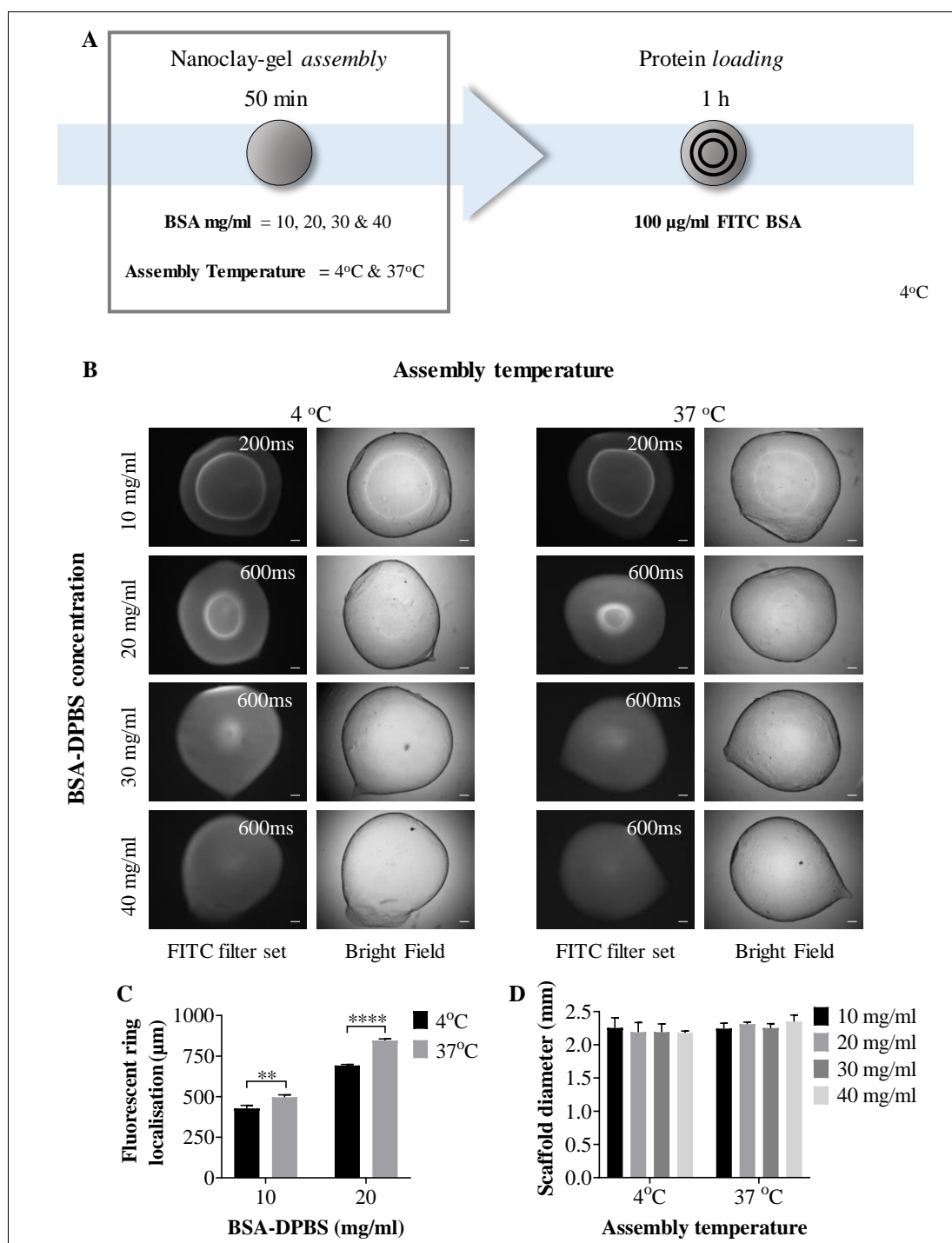


Figure 4.10 Effect of temperature on the scaffold assembly. (A) Schematic illustration of clay-gels assembled at different temperature. The (B) LFM images showed that an increase in the assembly temperature from 4°C to 37°C accelerates the displacement of the fluorescent ring towards the core of the clay-gels. A two-way ANOVA (C) analysis confirmed this observation, the fluorescent ring of the 10 and 20 mg/ml BSA clay-gels assembled at 37°C displaced about 16 % and 22 %, respectively

compared to the 4°C. Evaluation of the diameter of the clay-gel droplets (D) did not show any significant changes as a function of the assembly temperature and concentration of the assembly solution (two-way ANOVA, post hoc Bonferroni, $p > 0.05$). The results were presented as the mean \pm standard deviation of $n = 4$. The scale bars correspond for 200 μm .

Similar to increasing protein concentration, the assembly temperature does not affect the dimensions of the clay-gel scaffold in DPBS but accelerates the displacement of the fluorescent ring towards the core.

4.3.1.5 Assembly with different types of proteins

Previous experiments on section 3.3.2.3 demonstrated that the protein phase of foetal calf serum, more specifically BSA, is key for the nanoclay/protein scaffold assembly and patterning. However, further work is required to determine if this is the result of specific BSA/clay nanoparticle interaction or other type of proteins could be used to produce similar structures.

Moreover, the formation of a “protein corona” should be expected upon contact of clay nanoparticles with BSA, which in turns affect the biological identity, fate and behaviour of the clay nanoparticle, since the coating of biomolecules mediates its interaction with the surrounding environment (Docter et al. 2015). Thus, assembly of the scaffolds with other proteins could be beneficial to functionalize the clay-gels according to the application and potentially improve the recognition, biocompatibility and bioactivity. For these reasons, the objective of the next set of experiments was to determine if the nanoclay/protein scaffolds could be assembled with proteins of different shape and physicochemical properties.

The first experiment was set up to compare the assembly of the clay-gels with a fibril and a globular protein (Fig. 4.11 - A). The confocal images revealed surface binding and no diffusion of the FITC BSA (506 - 564 nm) inside the clay-gels that were assembled with type I collagen. On the contrary, diffusion of FITC BSA was observed in the clay-gels assembled with BSA (Fig 4.11 - B).

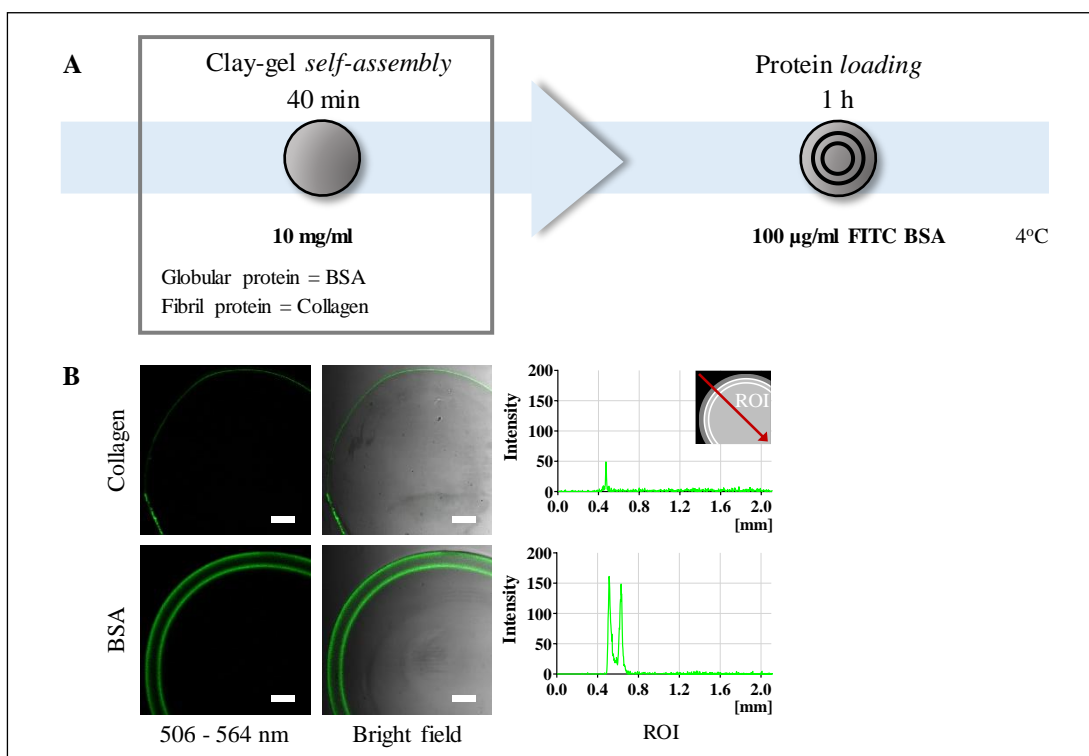


Figure 4.11 Assembly of the nanoclay/protein scaffold with fibril protein vs globular protein. (A) Schematic illustration of the clay-gel assembled with fibril (type I collagen) and globular protein (BSA), respectively. The (B) CLSM images and respective ROI showed the localisation of FITC BSA at the surface of the clay-gel assembled with collagen. On the contrary, the FITC BSA localised inside the clay-gels assembled with BSA. The images correspond to $n = 4$ and the scale bar to $200 \mu\text{m}$.

While a wider range of fibrillar proteins will be required to confirm the requirement of globular proteins in the process, this result provides an initial indication that the assembly process required for patterning of labelled BSA (in this case) is not a generalizable feature of proteins per se.

To further evaluate if the protein patterning is strictly related to the physicochemical properties of BSA, various globular proteins with different size and net charge were used to assemble the clay-gels and then loaded with FITC BSA (Fig. 4.12 - A).

Overall, the results confirm that the nanoclay/protein scaffolds can be assembled with a wide range of globular proteins with different molecular weights (14.3 - 250 kDa) and isoelectric points (4 - 10) (Fig. 4.12 - B).

Qualitative analysis of the bright field images revealed that the proteins have different diffusion path length after 3 hours of incubation, which suggest that the diffusion length is not related to the protein size or charge.

In this regard, comparison of the lysozyme and avidin scaffolds showed similar localisation of the diffusion front (Fig. 4.12 - B, red arrow). Both proteins possess similar isoelectric point (~10) but significantly different molecular weight (14.3 kDa and 68 kDa, respectively). Based on this, it could be assumed that the diffusion coefficient is governed by electrostatic interactions (Fig. 4.12 - B).

Nevertheless, comparison of the BSA and streptavidin scaffolds showed opposite results. Despite the proteins possesses similar isoelectric point (4.8 and 5, respectively) and molecular weight (66.5 kDa and 60 kDa, respectively) it could not be observed the diffusion front of the BSA scaffolds, because it reached saturation as confirmed by the fluorescent image. On the contrary, the bright field image of the streptavidin scaffolds showed the localisation of the diffusion front closer to the clay-gel surface (Fig. 4.12 - B, red arrow).

These results suggest that every protein may interact differently with the clay-gel regardless of the size and net charge. Thus, further work is required to understand what parameters control their diffusion coefficient.

Interesting results were observed when the spatial localisation of the fluorescent protein, corresponding to the FITC BSA emission (506 - 564 nm) was evaluated based on the electrostatic interactions between the assembly and loading proteins. In this regard, the fluorescent ring localised next to the clay-gel surface of those scaffolds assembled with positively charged proteins (lysozyme and avidin). Conversely, the fluorescent protein localised internally on those scaffolds assembled with neutral or negatively charged proteins (myoglobin, casein, BSA streptavidin, hyaluronidase, haemoglobin, immunoglobulin G (IgG) and catalase) (Fig. 4.12).

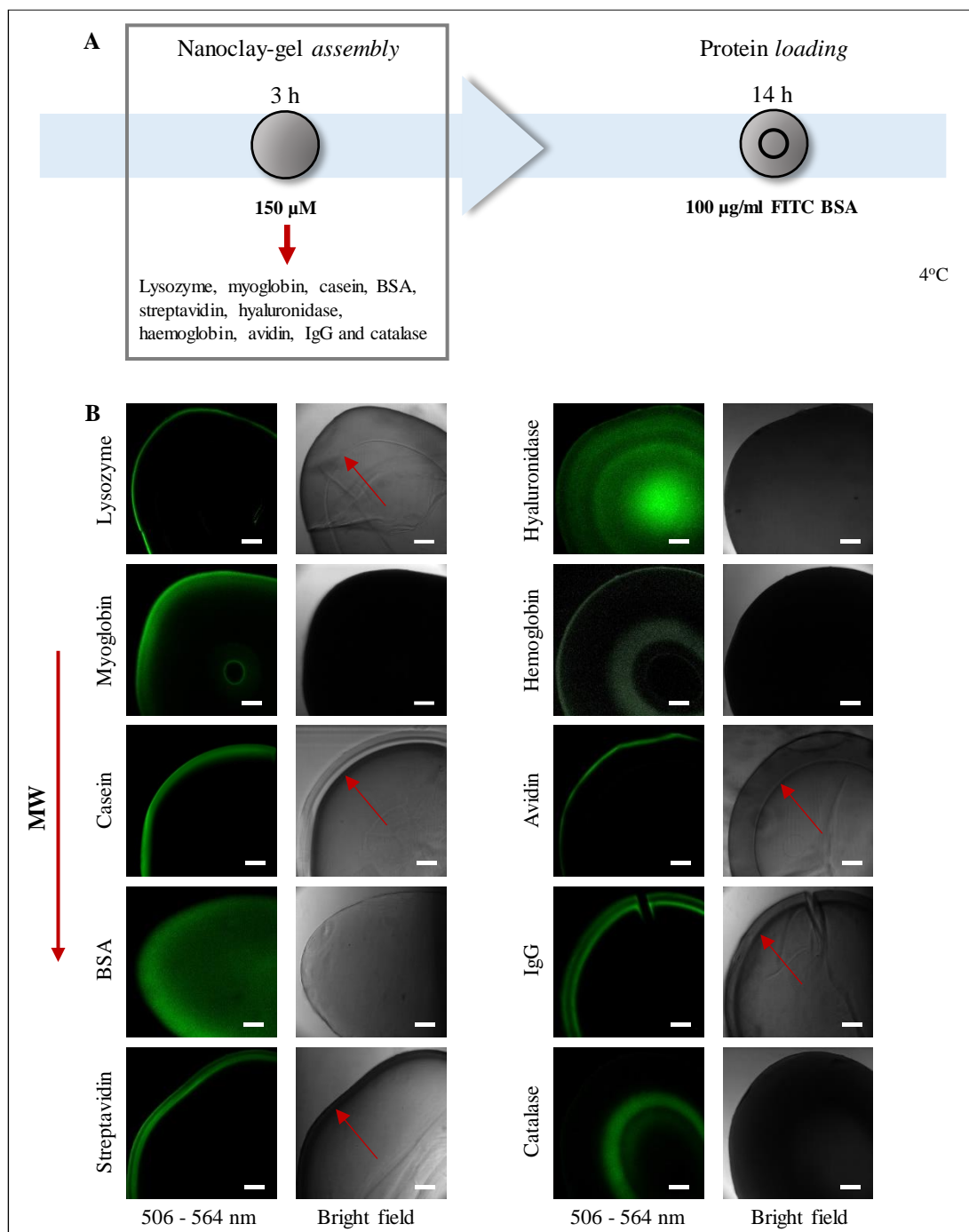


Figure 4.12 Assembly of the nanoclay/protein scaffold with different globular proteins. (A) Schematic illustration of the clay-gels assembled in different globular protein solutions. The (B) confocal images were presented according to the molecular weight of the proteins used to assemble the clay-gels, from the lowest to the highest. The fluorescent pattern distribution differs significantly between the assemblies, except for the lysozyme and avidin that localises next to the surface. The images represent $n = 3$ and the scale bar to 200 μm .

Both proteins, lysozyme and avidin possess an isoelectric point of approximately 10, which makes them positively charged at pH 7 while the FITC BSA with an

isoelectric point of 4.8 would then be negatively charged (Fig. 4.13 - D). According to these facts, it could be hypothesised that the positively charged proteins in the clay-gel prevented the diffusion of the negatively charged FITC BSA due to attractive interactions and accounted for observation of FITC BSA only at the clay-gel surface. With regards to the rest of the proteins used to assemble the clay-gels, there was no attractive protein-protein interaction to hinder the diffusion of FITC BSA inside the clay-gel, because they were neutral and negatively charged (Fig. 4.13 - B & C).

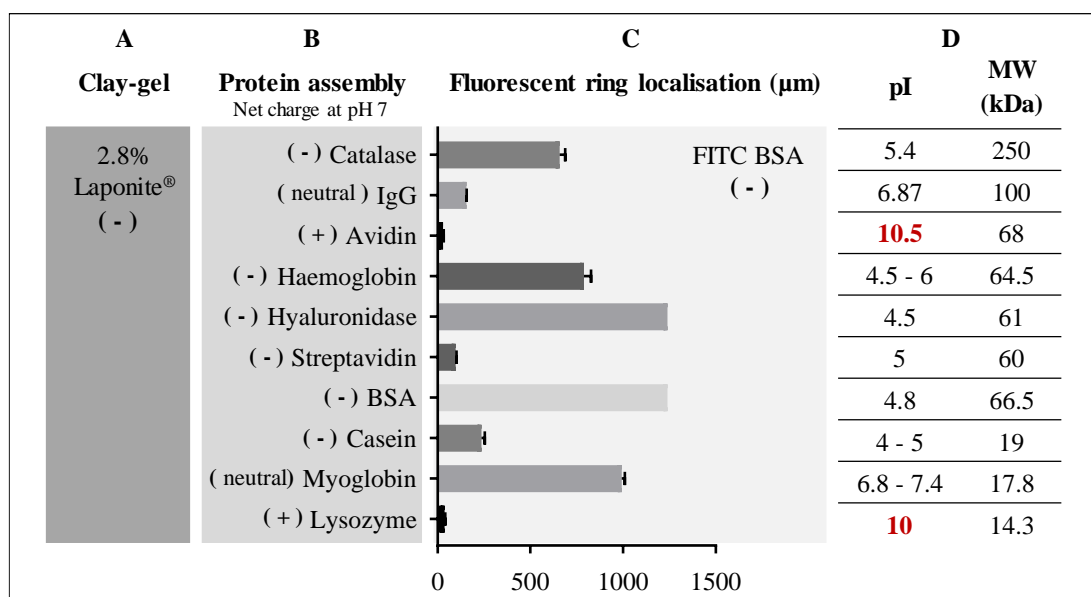


Figure 4.13 Effect of assembly and loading protein interaction in the fluorescent pattern distribution. It was hypothesised that (A) clay-gel acquires the net charge of the (B) protein absorbed at the assembly step. Then, subsequent diffusion and distribution of proteins in the clay-gel, at the loading step, could be the result of electrostatic interactions between the assembly and loading proteins and not the size. The (C) graph shows a descriptive analysis of the localisation of the fluorescent ring with respect to the surface of the clay-gel. It seems that the positively charged proteins (lysozyme and avidin) prevented the diffusion of negatively charged FITC BSA by attraction forces. Contrarily to the rest of the proteins that were neutral and negatively charged and the repulsive forces or none governed the process. The results presented as the mean \pm SD for $n = 3$.

To conclude, a wide range of globular proteins can be used to assemble the scaffolds. Nevertheless, the secondary absorption and localisation of the protein loaded (FITC BSA) could be the result of a protein-protein interaction governed by electrostatic interactions. Further work will be undertaken to study this hypothesis in the next section (4.3.2.3).

4.3.2 Effect of loading variables on the nanoclay/protein scaffold structure

4.3.2.1 Protein absorbed as a function of time

So far, in this chapter, the focus has been on the influence of the initial assembly parameters. This next experiment aims to evaluate the loading of the protein of interest following scaffold assembly. Thus, the first experiment was set to test the maximum loading capacity of the scaffolds as a function of time. For this purpose, assembled clay-gel droplets were loaded with a fluorescent protein, 100 $\mu\text{g/ml}$ FITC BSA, and respective imaging and measurement of the protein absorbed were performed at different time points over the course of 11 days (Fig. 4.14 - A) (methods section - 4.2.2).

The protein assay demonstrates that the scaffolds assembled with BSA reach its maximum absorption capacity at day 7. It absorbs up to $1.51 \pm 0.35 \mu\text{g}$ of BSA per μl of clay-gel, which corresponded to $36.50 \pm 4.07 \%$ of the total protein in the loading solution (Fig. 4.14 - C).

Moreover, the protein absorbed in the BSA scaffold at the day 1 is $0.16 \pm 0.11 \mu\text{g}$ per μl of clay-gel and accordingly to the confocal images, the protein is concentrated in the fluorescent ring. Interestingly, the fluorescent ring also maintains its localisation regardless more protein is being absorbed mainly in the core of the gel as a function of time (Fig. 4.14 - B).

Regarding the DPBS scaffolds, the absorption of 100 $\mu\text{g/ml}$ FITC BSA from the solution was almost complete, with up to $89.99 \pm 0.36 \%$ FITC BSA absorption achieved after 11 days of static incubation. This corresponds to $4.6 \pm 0.46 \mu\text{g}$ of protein per μl of clay (Fig. 4.14 - C). The confocal images revealed the absorption and localisation of the fluorescent protein next to the surface, which diffused progressively towards the core (Fig. 4.14 - B). Both results indicate that the DPBS scaffold did not reach the maximum absorption capacity; thus, more protein may be loaded into the clay-gel.

The bright field images reveal the development of opacity in the scaffolds, assembled with either BSA or DPBS, the spatial distribution of which corresponds to the localisation of the protein absorbed, as observed in the confocal image (Fig. 4.14 - B). Thus, at day 11, the FITC BSA localises in the core mainly and next to the surface of the BSA and DPBS scaffolds, respectively.

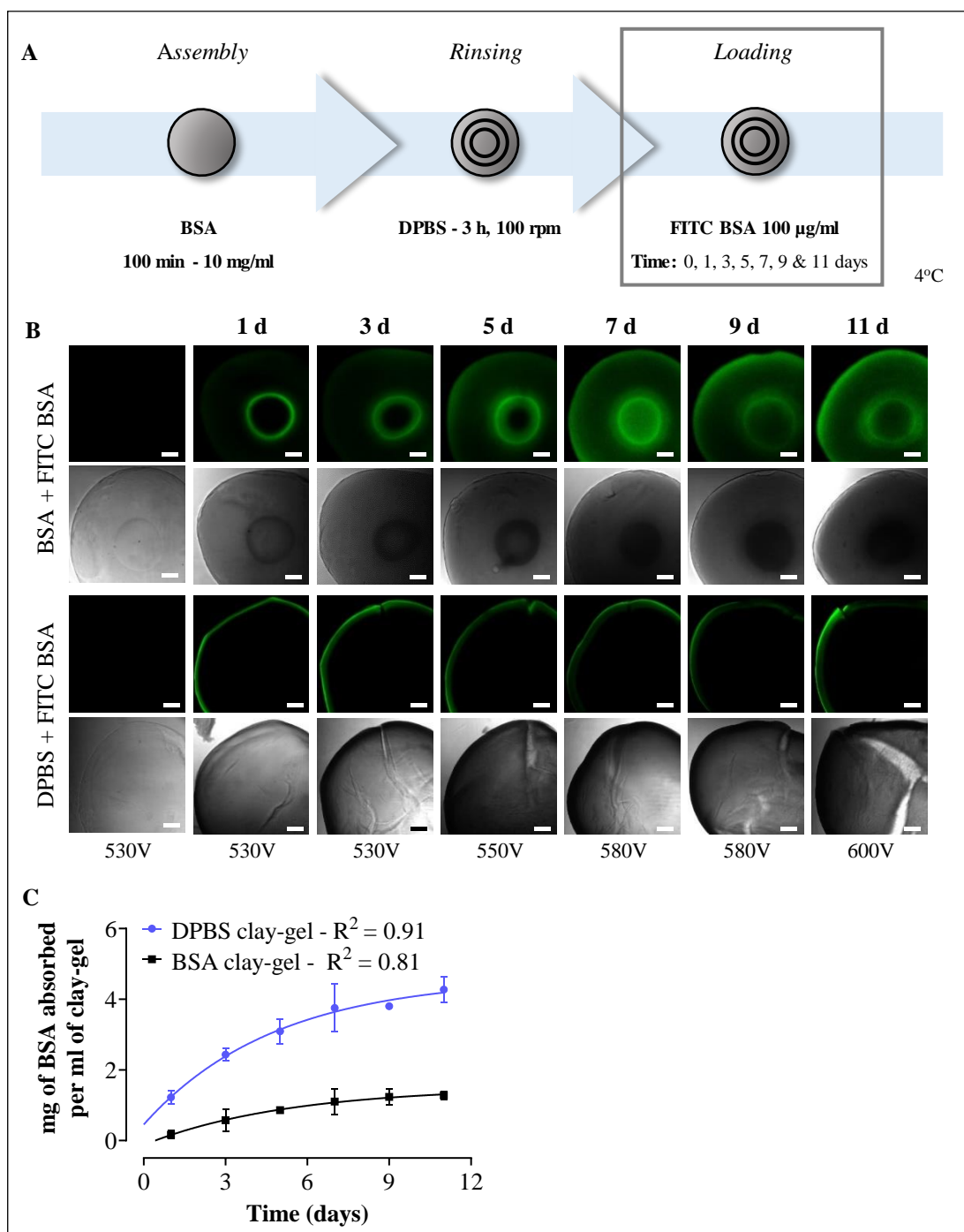


Figure 4.14 Maximum loading capacity of the nanoclay/protein scaffold. (A) Schematic illustration shows the different incubation times of the scaffolds in 100 µg/ml FITC BSA. (B) The confocal images reveal the absorption of FITC BSA (506 - 564 nm) in the clay-gel, as a function of

time. It localises in the core mainly and the surface of the BSA and DPBS scaffolds, respectively (C) A one phase equation predicted the protein absorbed satisfactorily. The BSA scaffold reached its maximum absorption capacity at day 7. Approximately, 36.50 ± 4.07 % of FITC BSA from the solution was absorbed, corresponding to 1.51 ± 0.35 μg per μl of clay-gel. The DPBS scaffold absorbed almost all the FITC BSA, $\sim 89.99 \pm 0.36$ % that corresponds to 4.6 ± 0.46 μg of protein per μl of clay-gel. The half adsorption time or half-life for the BSA and DPBS clay-gels was 3.66 and 3.33 days, respectively, with associated rate constants of 0.19 ± 0.1 and 0.2 ± 0.06 days. The results were presented as the mean \pm standard deviation for $n = 3$. The scale bars correspond to 200 μm .

These results indicate that the BSA scaffolds have significant absorption capacity and it is essential to mention that the protein absorbed is not homogeneously distributed, but localised and, therefore, concentrated in specific areas of the clay-gel as intended.

Further work is needed to understand how the fluorescent ring observed at day 1 was not disturbed by the continuous diffusion of proteins as a function of time, also, why the proteins localise mainly in the core of the clay-gel and not at the rest of the structure.

4.3.2.2 Effect of temperature

Similar to the assembly temperature experiment (section 4.2.1.4), the effect of the loading temperature in the localisation of the fluorescent ring was examined. For this purpose, the clay-gels were assembled at 4°C for 50 min and loaded with 100 $\mu\text{g}/\text{ml}$ FITC BSA for 1 hour at 4°C and 37°C, respectively (Fig. 4.15).

The LFM images showed similar localisation of the fluorescent rings regardless of the loading temperature. This was confirmed by an unpaired sample t-test (mean \pm SD, $n = 5$). Measurement of the fluorescent rings with respect to the clay-gel surface did not show any significant differences between their spatial localisation and the temperature treatment ($p < 0.05$) (Fig. 4.15).

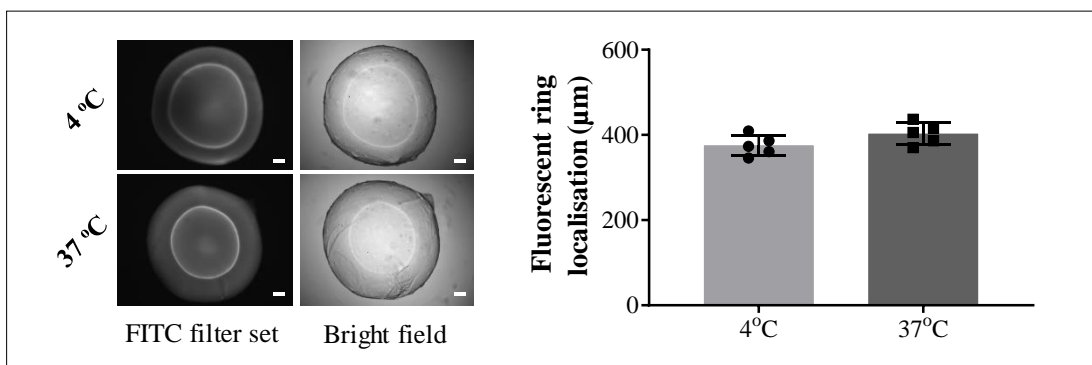


Figure 4.15 Effect of loading temperature on the fluorescent pattern distribution. The images and respective statistical analysis show no significant differences in the spatial localisation of the fluorescent ring in the clay-gel regardless of the loading temperature (unpaired sample t-test, $p < 0.05$). The results were presented as the mean \pm standard deviation for $n = 4$. The scale bars correspond to 200 μm .

The results indicate that the loading temperature does not affect protein localisation after 1 h of incubation. Thus, in the following experiments, the protein will be loaded at 4°C to preserve protein stability, unless otherwise stated.

4.3.2.3 Loading globular proteins

To determine if other proteins different from BSA could be loaded into the scaffolds and evaluate the effect of their size and charge in their spatial localisation into the scaffold, assembled clay-gels were incubated in 1.5 μM of fluorescently labelled lysozyme, casein, BMP-2, streptavidin, BSA, avidin and IgG for 1 h (Fig. 4.16 - A).

The results confirm that the nanoclay/protein scaffolds can be loaded with a wide range of globular proteins with different molecular weights and isoelectric points (Fig. 4.16 - B).

Qualitative analysis of the confocal images indicates that four of the seven proteins tested localised within the scaffold assembled in BSA and three localised at the surface. Interestingly, those that localise at the surface were all positively charged proteins (lysozyme, BMP-2 & avidin). This suggests the possibility that attractive forces between the negatively charged BSA bound to the clay and the positively

charged proteins loaded could hinder the secondary diffusion of the protein into the scaffold structure (Fig. 4.16 - B).

This observation recalls the previous experiment showing that the assembly of scaffolds with positively charged proteins (lysozyme and avidin) did not facilitate the diffusion of the negatively charged BSA, which again localised next to the surface, suggesting that the attractive forces hindered the diffusion of the protein loaded (section 4.3.1.5).

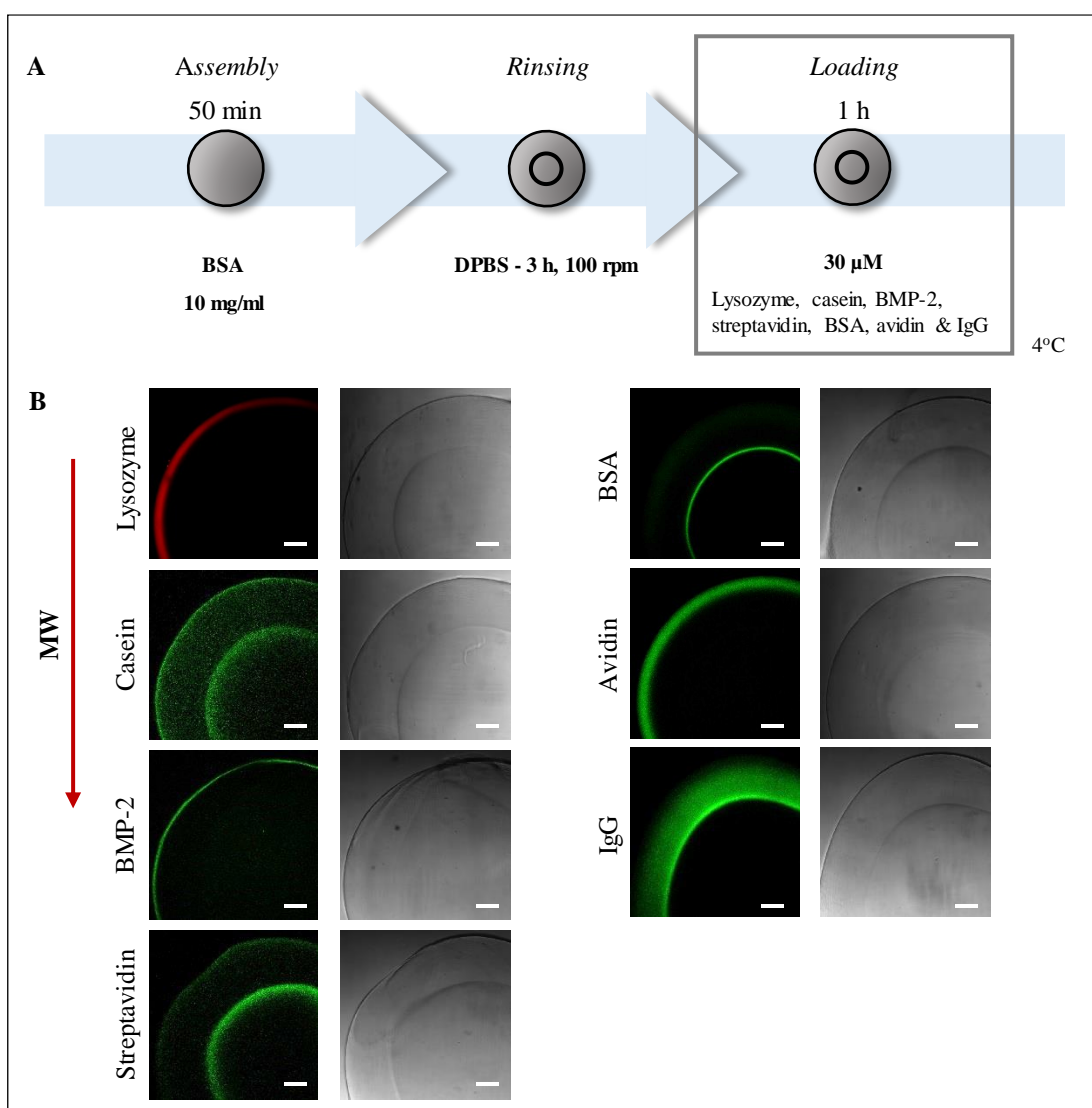


Figure 4.16 Loading different globular proteins into the nanoclay/protein scaffold. (A)

Schematic illustration of BSA scaffolds loaded with different globular protein. (B) The confocal images were presented according to the molecular weight of the proteins used to load the clay-gels, from the lowest to the highest. All the proteins diffused inside the clay-gel except for the lysozyme,

BMP-2 and avidin that localised next to the surface. The images represent $n = 3$ and the scale bar to 200 μm .

While the possibility of the effect of homodimers or homotetramers in the protein-clay or protein-protein interaction cannot be discounted. The experiments performed in this study suggest that the main property of the loaded protein that could be related to their spatial localisation within the gel is the isoelectric point. In this regard, comparison of the scaffolds loaded with lysozyme, BMP-2 and avidin reveal similar spatial localisation near the clay-gel surface (Fig. 4.16). These globular proteins possess similar isoelectric points being positively charged at pH 7. However, they differ significantly in their molecular weight 14.3 kDa, 32 kDa and 68 kDa, respectively. Also, in their quaternary structure, the lysozyme and BMP-2 are homodimeric proteins and the avidin a homotetrameric protein indicating that the net charge of the protein plays a vital role in their spatial localisation. Similar results were observed with the negatively charged proteins, casein, streptavidin, BSA and IgG. The fluorescent proteins diffused into the clay-gel and formed a punctuated gradient. All of them possess different molecular weights, ranging from 19 to 100 kDa. Also, most of them are homodimeric proteins except for the streptavidin, which is a homotetrameric protein. For this reason, it seems unlikely that the quaternary structure of the protein (homodimers or homotetramers), as well the molecular weight to have a significant effect in the diffusion and localisation of the proteins.

It, therefore, seems that the diffusion and localisation of the loaded proteins is governed by electrostatic interactions between the assembly protein and loaded protein. In order to corroborate this hypothesis, clay-gels were assembled and loaded with different permutations of lysozyme and BSA, which are oppositely charged proteins at pH 7 (Fig. 4.17 - A).

The results reveal the localisation of fluorescent proteins next to the surface of the scaffolds that were assembled with lysozyme and BSA and loaded with their respective oppositely charged protein. In contrast, diffusion of the fluorescent molecules was observed on the scaffolds assembled and loaded with proteins of the same net charge (Fig. 4.17 - B).

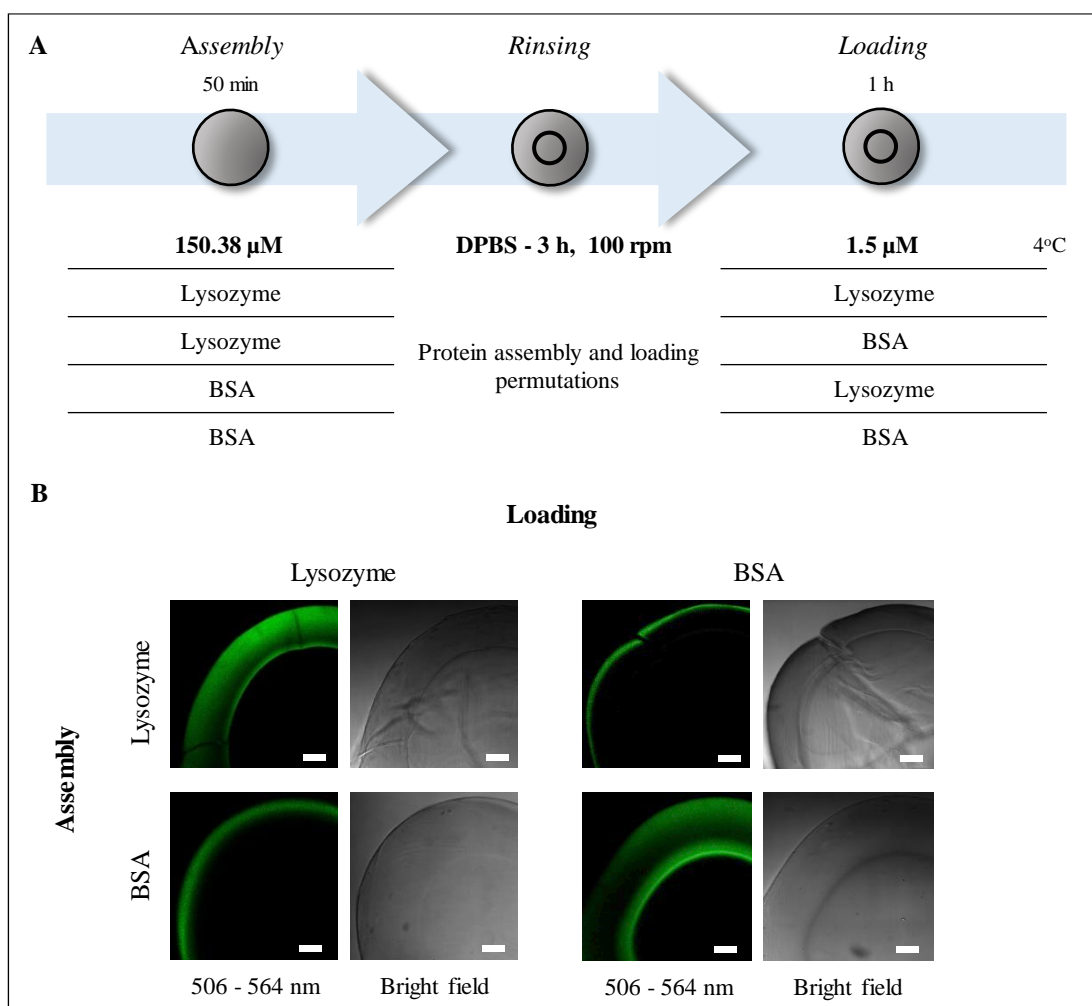


Figure 4.17 Diffusion and localisation of proteins loaded governed by electrostatic interactions.

(A) Schematic illustration of clay-gels assembled and loaded with different permutations of lysozyme and BSA. (B) The confocal images reveal the localisation of the protein next to the clay-gel surface when they are assembled and loaded with oppositely charged proteins (lysozyme \rightarrow BSA & BSA \rightarrow lysozyme). In contrast, diffusion of proteins in the clay-gel was observed when they were assembled and loaded with proteins of the same net charge (lysozyme \rightarrow lysozyme and BSA \rightarrow BSA). The images represent $n = 3$ and the scale bar to 200 μm .

The results suggest that the net charge of the assembly proteins (bound to the clay-gel) and loading proteins raise electrostatic interactions that govern the diffusion of the proteins loaded.

Thus, it seems that the isoelectric point of the protein plays a more critical role than the molecular weight. Therefore, variation in the buffer pH and ionic strength should alter the localisation of the molecules loaded.

4.3.3 Effect of storage variables on the nanoclay/protein scaffold structure

The assembled nanoclay/protein scaffolds in this research project are intended for biomedical applications. Therefore, it is essential to assess the stability of the assembled structure and the effect of storage conditions on the gel over time. In this regard, preliminary experiments were set up to evaluate the effect of the storage solution and temperature on the stability of the scaffold by monitoring the linear dimensions and protein localisation as a function of time.

4.3.3.1 Effect of the storage solution

In order to determine the effect of the storage solution on the scaffolds' stability, clay-gels assembled with BSA were stored in DPBS and water, respectively and evaluated as a function of time (Fig. 4.18 - A).

Qualitative analysis of the scaffolds stored in water showed an increase in size as a function of time (Fig. 4.18 - B). To evaluate this, manual measurements of the clay-gel droplets' diameter were taken and then analysed with one-way ANOVA (mean \pm SD, $n = 6$). The results revealed significant changes (post hoc Bonferroni, $p < 0.0001$) in the linear dimensions of the clay-gels as a function of time (Fig. 4.18 - D). They increased 28.44 ± 4.96 % in size after 3 h of storage in water and remained stable after 3 to 24 h.

Conversely, the scaffolds maintain their linear dimensions when incubated in DPBS as a function of time. This was confirmed by the analysis of variance, which did not show any significant changes (post hoc Bonferroni, $p > 0.05$) in the clay-gels linear dimensions after 24h of storage (Fig. 4.18 - C).

Moreover, the fluorescent ring of the scaffolds stored in water becomes blurred with time, but this is not observed in the scaffolds stored in DPBS (Fig. 4.18 - B).

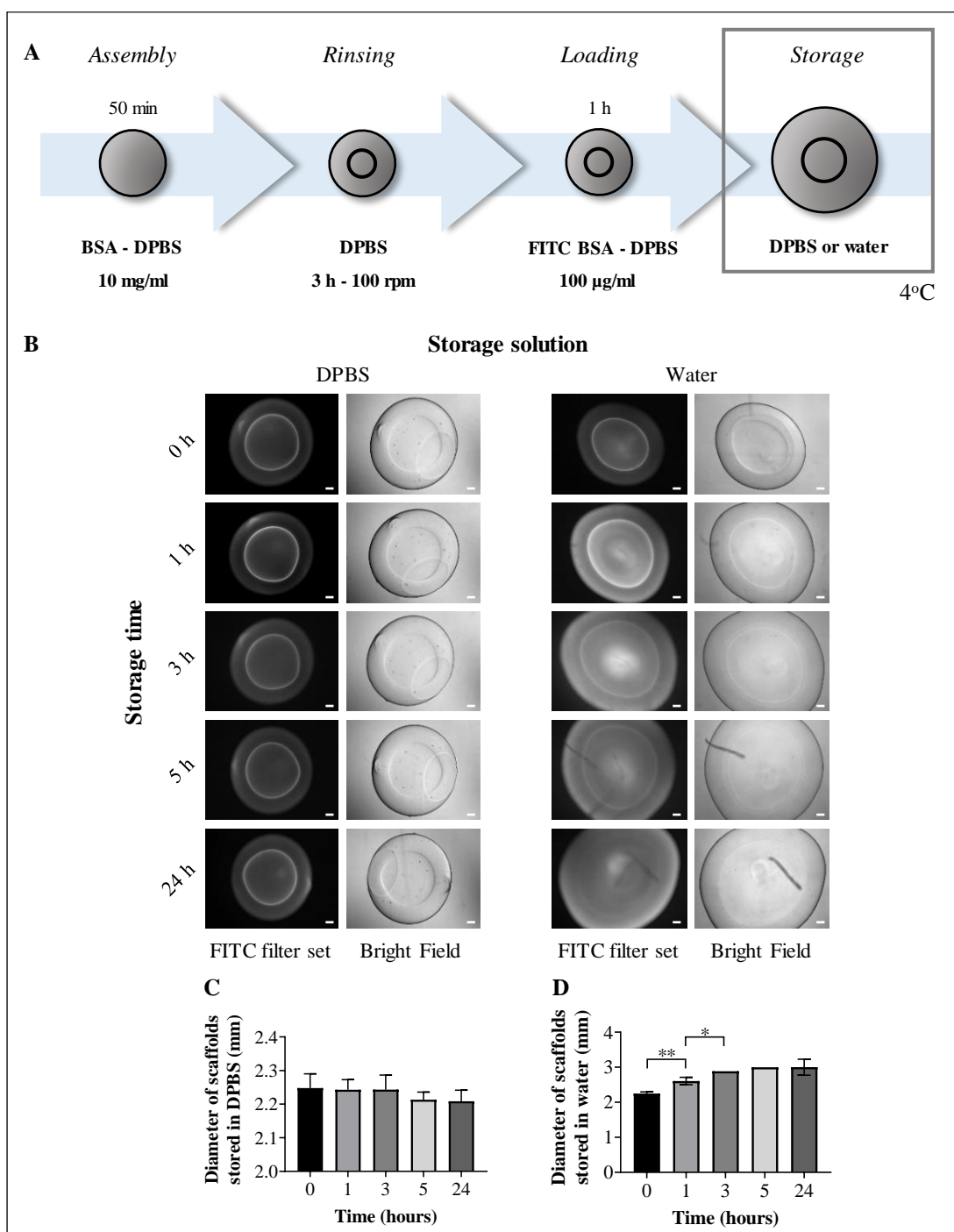


Figure 4.18 Effect of the solvent storage in the nanoclay/protein scaffold. (A) Schematic illustration of assembled BSA scaffolds stored in different solvents, DPBS and water. (B) The LFM images and respective analysis of variance (one-way ANOVA, post hoc Bonferroni) show no changes in the BSA scaffolds stored in DPBS ($p > 0.05$); nevertheless, the scaffolds increased $28.44 \pm 4.96\%$ in size after 3 h of incubation in water and remained stable after 24 h ($p < 0.0001$). The results were presented as the mean \pm standard deviation for $n = 6$ and the scale bar corresponds to 200 μm .

The results indicate that the scaffolds swell in water as a function of time; thus, the presence of ions in the storage solution is necessary to maintain their stability.

Therefore, in the following experiments, the scaffolds were stored in DPBS, unless otherwise stated.

Further research is needed to explore the stability of the scaffold in other solutions, such as physiological saline and/or antimicrobials solutions.

4.3.3.2 Effect of storage temperature

The next experiment was set to evaluate the stability of the clay-gels under different storage temperatures. For this, assembled clay-gels with BSA and DPBS were stored DPBS at 4°C and 37°C - 5 % CO₂, respectively and imaged at different time points (0, 24, 72, 144 hours) (Fig. 4.19 - A).

The LFM images and respective analysis of variance did not any show significant differences in the linear dimensions of the BSA and DPBS scaffolds that were stored at 4°C as a function of time (one-way ANOVA, post hoc Bonferroni $p > 0.05$) (Fig. 4.19 - B & C).

Nevertheless, when stored at 37°C, a significant change in the BSA scaffolds size as a function of time was observed (one-way ANOVA, post hoc Bonferroni $p < 0.0001$). In this regard, the BSA scaffolds decreased progressively up to 25.23 ± 0.96 % in size after 144 h and did not reach stability. Moreover, in comparison with the controls (DPBS scaffolds) did not show significant differences, (one-way ANOVA, post hoc Bonferroni $p > 0.05$). Thus, both scaffolds seem to decrease in size and follow similar trend (Fig. 4.19 - B & D).

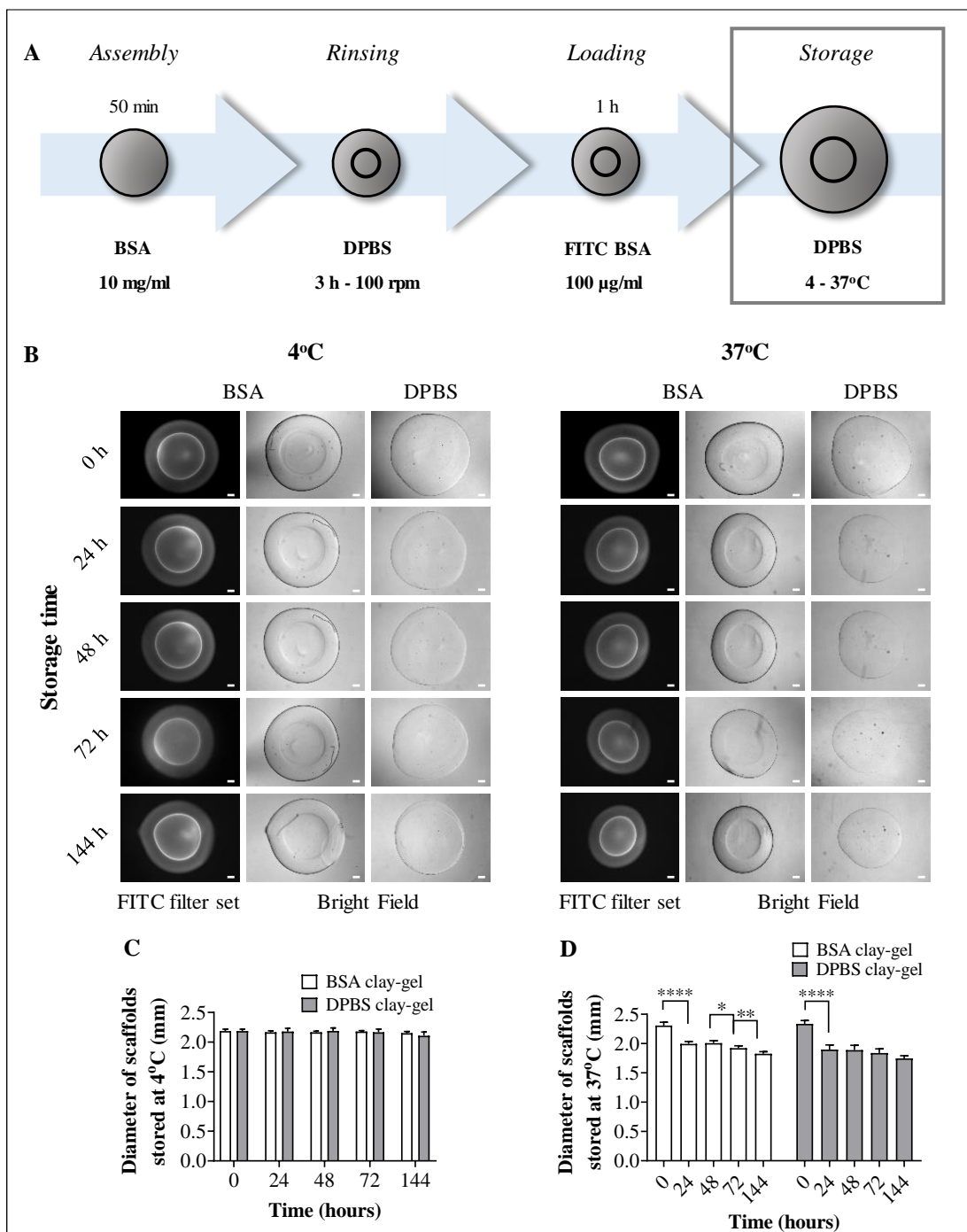


Figure 4.19 Effect of the storage solvent in the nanoclay/protein scaffold. (A) Schematic illustration of assembled BSA and DPBS scaffolds stored in DPBS at 4°C and 37°C. (B) The LFM images and respective analysis of variance (one-way ANOVA, post hoc Bonferroni) show no changes in the BSA and DPBS scaffolds stored at 4°C as a function of time ($p > 0.05$), nevertheless, they decreased $25.23 \pm 0.96\%$ in size after 144h of incubation at 37°C ($p < 0.0001$). The results represent $n = 6$ and the scale bar to 200 μm .

4.3.3.3 Stability as a function of time

To evaluate the stability of the BSA scaffolds, they were stored in DPBS at 4°C and imaged on day 1 and 28. Analysis of the linear dimensions reveals a decrease in size (unpaired t-test, $p < 0.05$) of approximately 4.99 ± 2.86 % from day 1 to day 28 (Fig. 4.20 - A & B).

Similarly, slight changes in the fluorescent ring localisation were observed (unpaired t-test, $p < 0.05$). The statistical analysis revealed a decrease in the distance from the scaffolds' surface of 7.98 ± 0.98 % from day 1 (462.6 ± 21.65 mm) to day 28 (425.6 ± 17.09 mm) (Fig. 4.20 - B).

Interestingly, no sign of infections was observed after 28 days of storage, although a microbial culture is needed to verify this.

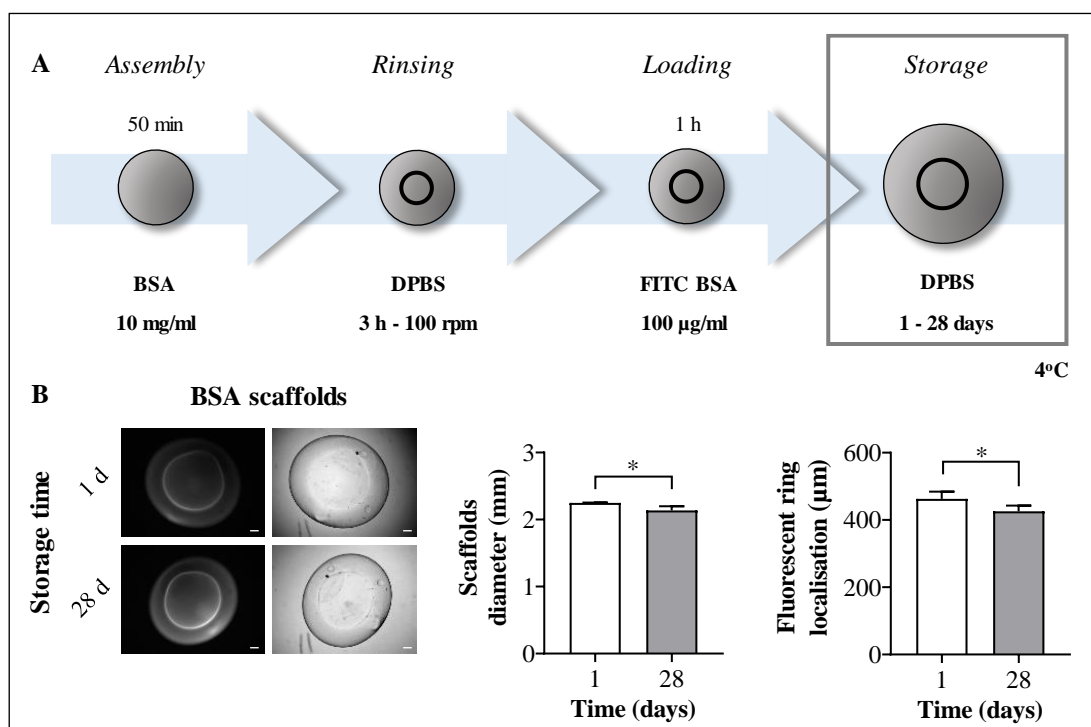


Figure 4.20 Effect of the storage time in the nanoclay/protein scaffold. (A) Schematic illustration of assembled BSA and stored in DPBS at 4°C for 28 days. (B) The LFM images and respective analysis (two-tailed unpaired t-test) shows a slight decrease in the scaffold's linear dimensions of 4.99 ± 2.86 % after 28 days of storage ($p < 0.05$). Similarly, the distance of the fluorescent ring from the scaffold surface decreases 7.98 ± 0.98 % after 28 days of storage ($p < 0.05$). The results were presented as means \pm SD for $n = 4$ and the scale bar corresponds to 200 µm.

In this last section, some environmental parameters that could affect clay-gels durability and stability were evaluated. In this regard, a slight decrease in the size was observed when stored in DPBS at 4°C. Moreover, no sign of infections was detected despite the experiments above described were not performed under aseptic conditions.

Further research is required to establish the shelf life and storage conditions, such as microbial cultures, exploring other storage solutions and the addition of antimicrobials (if necessary), and determining the protein bioactivity to long storage. However, it can be confirmed from these studies that the scaffolds remain stable and preserve the localisation of protein over several weeks in solution.

4.4 Discussion

The first results chapter confirms that the spontaneous formation of the fluorescent-layered structure inside the clay-gel is the product of a complex diffusion process. The detailed analysis demonstrated that two different diffusion processes take place at the assembly and loading steps. Thus, initial treatment of the clay-gel droplet during the assembly process, with either DPBS, DMEM 10 % FCS, 100 % FCS or 30 mg/ml BSA) affects significantly the distribution of the fluorescent protein (FITC BSA) loaded, which could be either at the surface or internally at different distances from the surface. Moreover, it was suggested that the internal distribution of the fluorescent protein loaded co-localised with the apparent diffusion front of the clay-gels assembled in the concentrated protein solution (Fig. 3.12 & 3.20). Therefore, in this chapter it was hypothesised that the fluorescent pattern distribution could be controlled by altering the diffusion process at the assembly step, and in consequence, the localisation of the diffusion front. To evaluate this, the effect of the protein concentration, ions, temperature and time on the clay-gel assembly were studied, which are factors known to result in changes in the solute diffusion rate and distance travelled.

Thus, in the first study, clay-gels assembled with gradients of BSA-water ranging from 20 to 50 mg/ml revealed a linear relationship of concentration with the

localisation of the fluorescent ring inside the scaffold (or diffusion front) (Fig. 4.3 - B & D). These results indicate that the diffusion rate of the assembly protein solution is concentration dependent, which is consistent with Fick's first law of diffusion that postulates that mass transfer occurs in response to the concentration gradient. This is expressed as eq. (1)

$$(1) J = -D \frac{\partial C}{\partial x}$$

where the flux or local rate for movement (J) is proportional to the diffusivity (D) and the negative gradient of concentration ($\partial C/\partial x$), which result from the change in concentration (∂C) due to a change in position (∂x) (Mikhailov et al. 1982). Note that this basic equation does not consider other factors that could affect the diffusivity, but when modelling diffusion. However, it is good practice to begin with the assumption that all diffusion coefficients are equal and independent of temperature, pressure, net charge and other factors, then the assumption can be modified as the different variables are studied.

A similar experiment was performed to evaluate the effect of ions on protein diffusion into the clay-gel as a function of concentration. Again, the fluorescent protein pattern (or diffusion front) localised closer to the core as the protein concentration increased until it could not be observed (Fig. 4.6 - A). Assuming that the fluorescent ring cannot be observed anymore because the clay-gel is saturated, comparison of these results with those above described would suggest that the addition of ions accelerate the clay-gel saturation as a function of the protein concentration. In this regard, the water-based scaffolds reached saturation at 40 mg/ml BSA but the DPBS-based scaffold at 20 mg/ml, both after 50 min of incubation (Fig. 4.3 & 4.6).

The theory regarding the diffusion of charged species in liquid indicates that increase in the solvent ionic strength decreases the diffusion rate of charged macromolecules. This occurs because the electrostatic forces between the macromolecules that mediate the Debye-Hückel screening length decreases with the increase of the ionic strength changing the interactions from repulsive to attractive, which in turns

decreases the diffusion coefficient. For example, Li et al. (2004) demonstrated that the diffusion coefficient of BSA grows with increasing protein concentration, but with the gradual increase in the ionic strength, the diffusion coefficient decreases with the increase in the protein concentration. Similar results were reported by Raj & Flygare (1974) and Anderson et al. (1978). In these scenarios, the Nernst-Planck or Maxwell-Stefan equations, extensions of Fick's law, are generally used because they consider the particle net charge (Anderson et al. 1978 and Hasan & Abdel-Raouf, 2019).

Thus, the theory here described is opposite to the present findings because the addition of ions appears to increase the rate of diffusion of protein into the clay-gel. However, this theory does not take into consideration the interaction between the proteins and the charged diffusive media. In this regard, Lieleg et al. (2010) and Zhang et al. (2015) demonstrate that the attractive interactions between a molecule and a gel network, which would usually hinder diffusion are weakened in the presence of salt leading to a higher diffusion rate. This is because Debye screening becomes more pronounced with the gradual addition of ions, which appears to weaken the probe-gel electrostatic interactions favouring the diffusion.

The discussed studies seem to correlate with the present results because likewise, the diffusion is enhanced in the presence of ions. However, this explanation is not consistent with quite a large literature that has demonstrated that protein adsorption to clays, in fact, tends to increase with the ionic strength, even with neutral or negatively charged proteins. Although the mechanism for this is not clear, some suggest that the ions expose the hydrophobic region of the protein, increasing the hydrophobic interactions and adsorption to the clay (Yu et al. 2013). Others support that the surrounding counter ions decrease the electrostatic repulsion so that the protein diffusion becomes faster and attachment to the surface easier (Bajpai & Sachdeva, 2002 and Möller et al. 2012).

Thus, assuming that in this scenario, a physical reaction between the protein and clay-nanoparticles occurs simultaneously to the diffusion, the process could be accounted for by a reaction-diffusion system, which would be also favoured by the presence of ions as they facilitate the protein adsorption onto the clay nanoparticle

surface accelerating, therefore, the reaction-diffusion of BSA into the clay-gel. It is important to take into consideration that the protein itself will contribute to the ionicity of the system. Although further work is required to verify that the scaffold is assembled via reaction-diffusion. For this, the structural characteristics of the scaffolds will be assessed in the next chapter and compared with other structures that were assembled similarly.

A significant decrease in the size of the water-based scaffolds as a function of the protein concentration was observed (Fig. 4.4) in contrast to the DPBS based scaffolds, which preserved their size (Fig. 4.7). According to these results, it could be assumed that the protein diffusion in the water-based scaffolds is faster because they have shrunk and, therefore, the diffusion distance is shorter. Nevertheless, comparison of the scaffolds assembled with 20 mg/ml BSA-water and BSA-DPBS revealed similar dimensions, but in the presence of ions, the fluorescent ring localised closer to the core (Fig. 4.3 & 4.6) confirming again that the ions do increase the diffusion coefficient.

Notably, all the clay-gels preserved their dimensions in the presence of ions irrespective of the protein concentration, whereas with water, the clay-gel scaffolds only assembled (or stabilised) in protein concentrations over 20 mg/ml (Fig. 4.3 & 4.6). It could be hypothesised that there are some traces of ions in the protein from the manufacturing process sufficient to stabilise the gels in water. However, with the increase in the protein concentration to 50 mg/ml, an increase in the ions concentration would be expected to stabilise the size of the scaffold yet instead it was observed a significant decrease in the dimension of the scaffolds up to 26.4 ± 1.3 % not apparent in DPBS (Fig. 4.4 & 4.7). This suggests that it is the proteins themselves that are sufficient to assemble the scaffolds, albeit in a concentration dependent manner.

Nevertheless, the presence of ions in the assembly solution represents an advantage because they stabilise the size of the scaffold, accelerate the diffusion process and decrease significantly the amount of protein required to create the patterned structure. However, it is not clear how the ions prevent the scaffolds shrinkage and do not interfere but favour the assembly process.

Regarding the effect of the assembly time in the diffusion process, the fluorescent ring localisation was measured with respect to the scaffold surface to determine the distance travelled by the assembly protein solution because the localisation of the fluorescent ring corresponds to the diffusion front. Then, the measured depth of the diffusion of proteins in the clay-gel was used to determine the relationship between the one-dimensional diffusion depth and assembly time according to the equation (2)

$$(2) d = \sqrt{2D * t}$$

where, d is diffusion depth, t is time and D the diffusion coefficient. This equation is a derivation of the Fick's second law equation (3)

$$(3) D = \frac{d^2}{2t}$$

that predicts the relationship between the elapsed time and the square of the length over which diffusion takes (Hasan & Abdel-Raouf, 2019).

In this study, the results confirm a linear relationship between the protein diffusion depth and the squared root of time, regardless of the protein concentration (Fig. 4.8 & 4.9) as postulated by the Fick's second law. Moreover, this indicates that it can effectively predicted the localisation of the fluorescent ring inside the clay-gel by controlling the assembly time and protein concentration simultaneously.

Another factor that affects the diffusion coefficient is temperature. An increase in the temperature implies that the average kinetic energy of the particles increases; thus, the particles begin to move faster and more often. The Stokes-Einstein equation is generally used in these cases. It describes the diffusion of a spherical particle undergoing Brownian motion in a quiescent fluid at a uniform temperature, eq. (4)

$$(4) D = \frac{kT}{6\pi\eta R}$$

where the diffusion coefficient (D) for a particle in a free volume varies linearly with the Boltzmann constant (k) and the absolute temperature (T), and inversely

proportional to the viscosity of the solution (η) and the hydrodynamic radius (R) of the particle (Cruickhank Miller, 1924).

Regarding the present study, the scaffolds assembled at 37°C revealed the localisation of the fluorescent ring closer to the core compared to the scaffolds assembled at 4°C (Fig. 4.10), which suggest that the diffusion process follows the general rule above-described. Thus, the increase in temperature increased the diffusion coefficient of the assembly solution.

Again, taking into consideration the protein/clay interaction, different studies indicate that the adsorption increases with increasing temperature of the medium. This can be accounted for by several facts: 1) increase of temperature brings about an increase in the diffusion of protein molecules (Yu et al. 2013) and 2) it may also cause protein aggregation, both cases increase the protein adsorption (Nakanishi et al. 2001). 3) Moreover, electrostatic attractions are usually weakened with an increase in temperature; thus, a decrease in the adsorption should be expected. Lastly 4) unfolding of the protein at high temperatures may expose the hydrophobic regions of the protein favouring the adsorption through hydrophobic interactions (Simonson & Brooks, 1996, Bajpai & Sachdeva, 2002 and Della Porta et al. 2016).

Therefore, similarly to the ions, the temperature would increase the rate of adsorption accelerating the reaction-diffusion process of the BSA into the clay-gel corroborating the findings.

The final parameters studied at the assembly step focused on the solute properties. Specifically, the molecular weight and isoelectric point. The results revealed that the scaffolds could be assembled various globular proteins regardless of their size and net charge (Fig. 4.12).

Qualitative comparison of the diffusion length suggests that the proteins have different diffusion coefficients, which do not appear related to the protein size or net charge. For example, the bright field image of the scaffold assembled in lysosome and avidin shows similar localisation of the diffusion front. Both proteins have an isoelectric point of approximately 10, but different molecular weights, 14.3 kDa and

68 kDa, respectively. According to this, it could be assumed that the diffusion coefficient is governed by electrostatic interactions (Fig. 4.12 - B, red arrow). Nevertheless, the BSA and streptavidin scaffolds show opposite results. Both proteins possess similar molecular weight (66.5 kDa and 60 kDa, respectively) and isoelectric point (4.8 and 5, respectively). Thus, in the bright field image of the BSA scaffold, the diffusion front could not be observed presumably because it has reached saturation after 3h of incubation, and this was confirmed by the fluorescent image. Nevertheless, the bright field and fluorescent images of the streptavidin scaffolds show the localisation of the diffusion front closer to the clay-gel surface (Fig. 4.12 - B, red arrow). Overall, the results indicate that neither the molecular weight nor the charge of the globular protein determines its diffusion coefficient in the clay-gel. Further work is required to understand how the diffusion is altered by the interaction of each protein with the clay nanoparticles.

Interestingly, the fluorescent pattern distribution of the loaded protein varied significantly with respect to the net charge of the protein used to assemble the scaffolds. In this regard, the FITC BSA localised next to the surface of the clay-gels assembled with a positively charged protein at pH 7. Conversely, the scaffolds assembled with negatively charged proteins and neutral, the FITC BSA diffused in suggesting that the diffusion of the protein loaded through the clay-gel is governed mainly by electrostatic interactions (Fig. 4.12 & 4.13).

To confirm this, the scaffolds were assembled with BSA, a negatively charged protein at pH 7 or lysozyme a positively charged protein at pH 7 and then loaded with either the same or alternatively charged protein, respectively. The results showed the localisation of the fluorescent protein next to the clay-gel surface when they were assembled and loaded with oppositely charged proteins. In contrast, diffusion and localisation of fluorescent proteins in the clay-gel was observed when they were assembled and loaded with proteins of the same net charge, providing further indication that a selective diffusion barrier process governs the secondary diffusion and localisation of molecules, specifically by electrostatic interactions (Fig. 4.17).

In this regard, Lieleg et al. (2010) and Zhang et al. (2015) reported that attractive interactions between macromolecule and a diffusive media hinder the macromolecule diffusion in contrast to the repulsive interactions, which facilitates it. This is consistent with the findings in the present work (Fig. 4.21). Nevertheless, it is not clear whether electrostatic interactions between the clay-protein or protein-protein play the dominant role in this process.

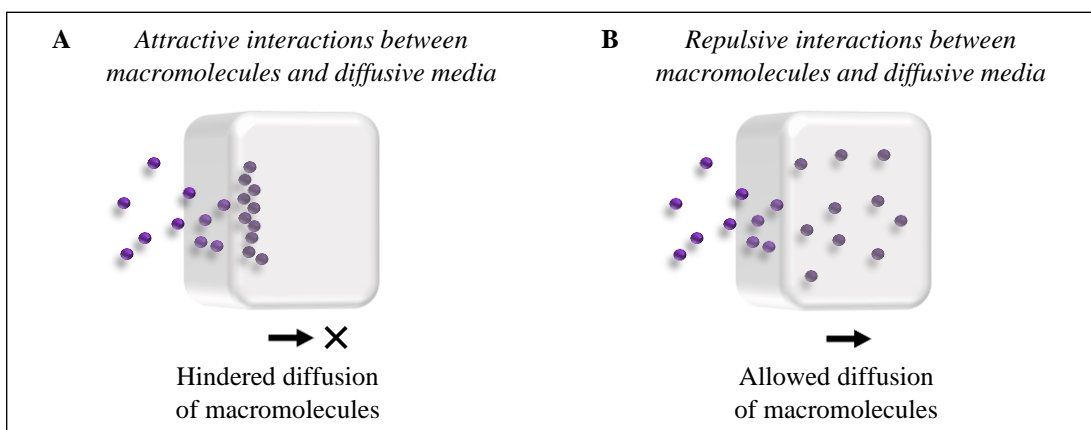


Figure 4.21 Diffusion of charged macromolecules through a charged diffusive media. Schematic illustrations of macromolecules (purple spheres) diffusion (A) hindered or (B) facilitated by attractive or repulsive interactions with the diffusive media (grey box), respectively.

In this regard, two different diffusion mechanisms were proposed. First, it could be envisaged that the proteins, at either the assembly or loading stage, binds according to their net charge with either the positively charged clay-edge or the negatively charged clay-surface (Fig. 4.22 - A), and after the assembly process takes place, there should be a specific region of the nanoparticle unreacted that will then interact with the loaded protein. Thus, if both, the unreacted clay region and the loaded protein have opposite charge, the attractive interaction will hinder the diffusion, and the loaded protein will localise next to the surface (Fig. 4.22 - B & C). On the other hand, if both assembly and loading proteins have the same charge, the repulsive interactions will allow the diffusion of the loaded protein into the clay-gel core (Fig. 4.22 - B & D).

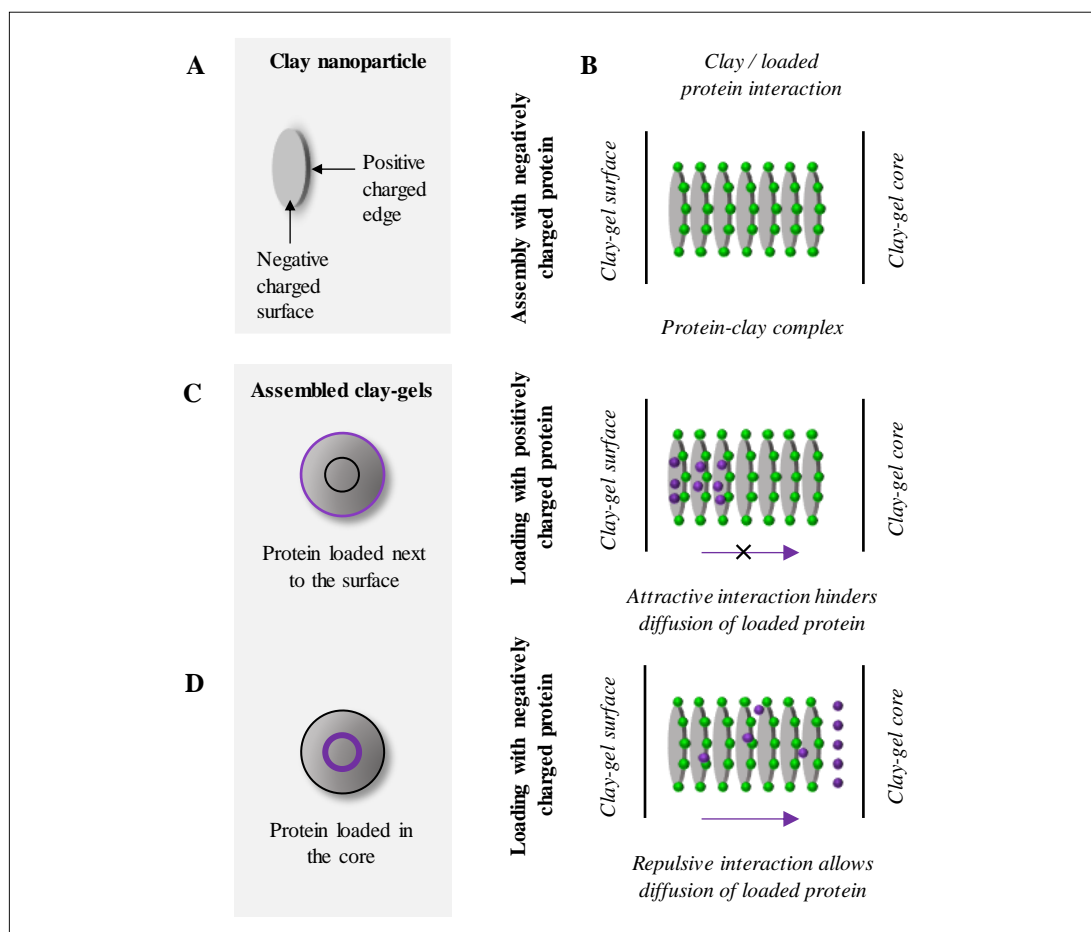


Figure 4.22 Secondary diffusion and localisation of macromolecules governed by clay/protein interaction. (A) The clay-nanoparticle illustration indicates the anisotropic charge distribution, where the edge possesses a weak positive charge and the surface a negative charge. Here is described as a possible mechanism that controls the spatial localisation of the proteins loaded. Thus, (B) assuming a preferential interaction of the proteins with a specific region of the clay nanoparticle due to their charges. At the assembly step, the BSA protein, which is negatively charged (green sphere), should bind and saturate the edges of the clay nanoparticles, which are positively charged. Then, the loaded proteins (purple sphere) would interact with the unreacted surface. Thus, if the loaded protein is positively charged, it will bind to the negatively charged surface of the clay nanoparticle (C) hindering their diffusion. On the contrary, if the protein is negatively charged, it will not interact with the clay and neither the bound protein because both are negatively charged (D) allowing their diffusion into the clay-gel core.

The mechanism above described can be questioned; however, because the literature indicates that negatively charged proteins do not bind only to the positively charged edge of the clay nanoparticle but to the negatively charged surface as well. This phenomenon is called surface patch binding (SPB) also known as “binding on the wrong side of the pH” (Das et al. 2016). This type of anomalous binding explains the

interaction of two macromolecules that possess the same or similar net charge. For example, the binding of proteins to polymers/colloids having a similar net charge (Lesins & Ruckenstein, 1988, Gupta et al. 2007 and Pathak et al. 2017).

In this context, Das et al. (2016) studied the interaction of globular plasma proteins; BSA, human serum albumin (HBS) and β -lactoglobulin (β -Lg) with nanoclays; Laponite® and montmorillonite. At pH > 6, proteins and nanoclays should experience electrostatic repulsion due to the same polarity, since both are negatively charged, but interaction still occurred as demonstrated by the hydrodynamic radius (R_h) analysis, which increased upon binding of clay platelets to the protein surface. (Fig. 4.23 - A). This finding suggests that, in this case, the protein and nanoclays were interacting by SPB.

The authors also conducted zeta potential measurements to demonstrate that the positive surface charge on the protein molecule (3.5 ± 0.5 mV) was neutralised by addition of clay nanoparticles (net negatively charged) indicating that the protein and the clay were interacting through the protein surface charge anisotropy and not the overall protein surface charge, which is negative. Otherwise, the protein and the clay would not interact due to repulsive interactions (Fig. 4.23 - B).

Moreover, the authors observed that the proteins undergo conformational changes in the secondary structure during the SPB. The circular dichroism spectra show that the helical content of protein decreased indicating strong associative interactions between clay nanoparticle and the protein (Fig. 4.23 - C), demonstrating that the heterogeneous charge distribution on the protein surface facilitates the patch binding to the negatively charged surface of the clay nanoparticles, and that change in the proteins' conformation favours the binding (Fig. 4.23 - D).

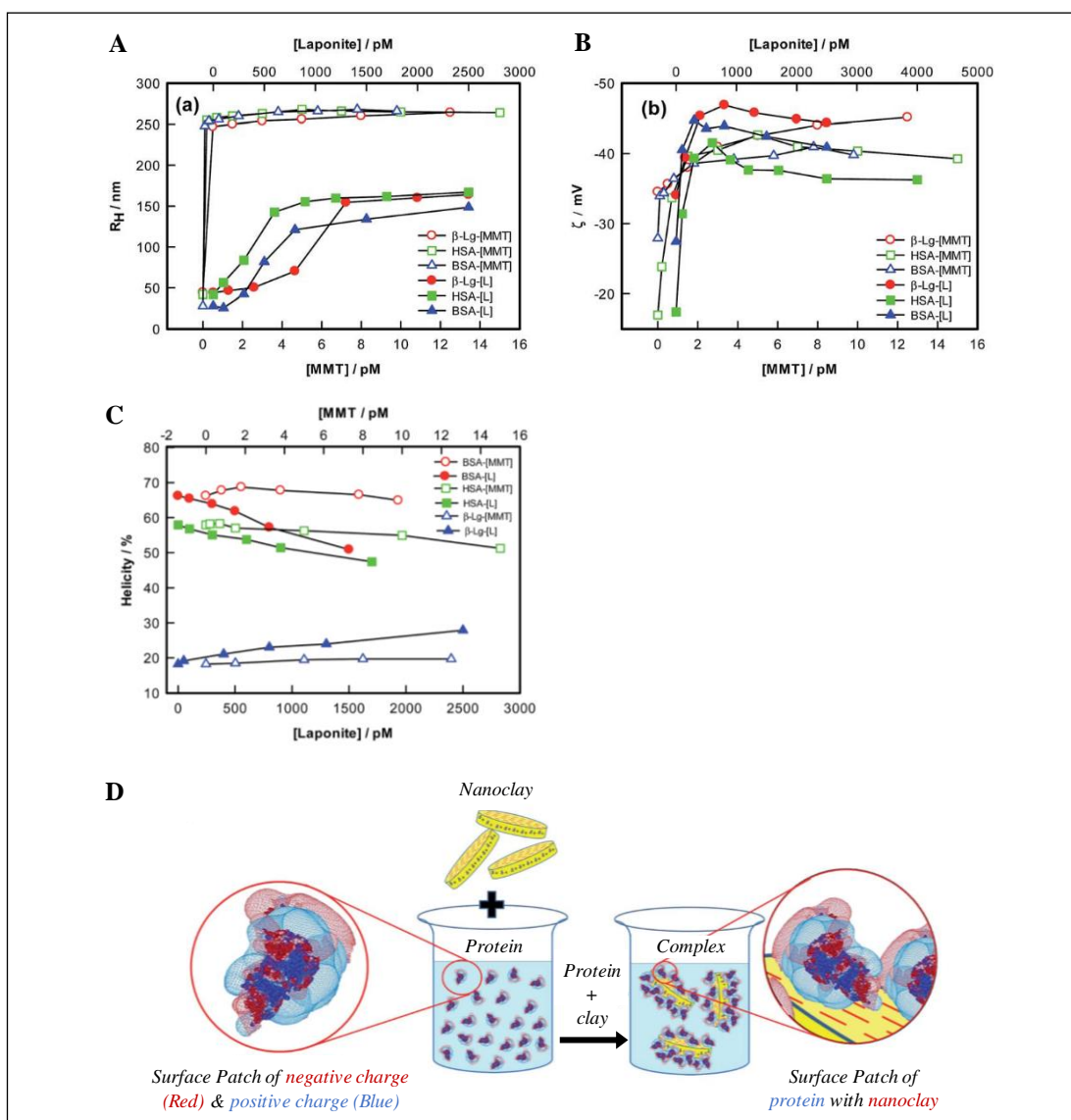


Figure 4.23 Surface patch binding of human serum albumin with Laponite® clay nanoparticle.

Schematic representation of the protein-nanoclay complexation and loss in protein helicity after interaction. The protein binds indiscriminately to the negative surface and positive edge of the clay nanoparticle regardless of the charge. Modified image from Das et al. (2016).

Thus, based on this SPB principle, it was assumed that the assembly protein (negatively charged BSA), binds to all regions of the clay nanoparticle, positive edge and negative surface (Fig. 4.24 - A). So that the formed protein-clay complex would have a negative net charge (-50 ± 5 mV), as reported by Das et al. (2016) (Fig. 4.24 - B). Then, the loaded protein would interact with the protein-clay complex and depending on their repulsive or attractive interaction, the diffusion could be facilitated or hindered, respectively (Fig. 4.24 - B).

This second mechanism seems to explain better the protein/clay interaction at the assembly step but also the localisation of the loaded protein as an alternative to the first mechanism proposed (Fig. 4.22 & 4.24). Most literature indicates that proteins bind to any region of the clay nanoparticle regardless of the charge and in this system, the SPB better account for the likely mode of interaction to generate a charged structure that then filters through electrostatic interactions the loaded proteins.

Nevertheless, further work is required; including, a depletion study to determine the density of the protein per clay nanoparticle because the clay nanoparticles used to assemble the scaffolds are forming a gel and not a sol as reported by Das et al. (2016). The results will help to elucidate if anomalous binding or SPB form the protein-clay complex. In addition, a zeta potential analysis would be essential, since there is no direct evidence that the assembled clay-gel acquires the net charge of the protein used. According to Das et al. (2016), the BSA-clay complex is negatively charged, explaining why the loaded proteins diffuse or not into the gel based on the charge. However, it is not clear yet if the lysozyme-clay complex becomes positively charged, preventing the diffusion of negatively charged proteins.

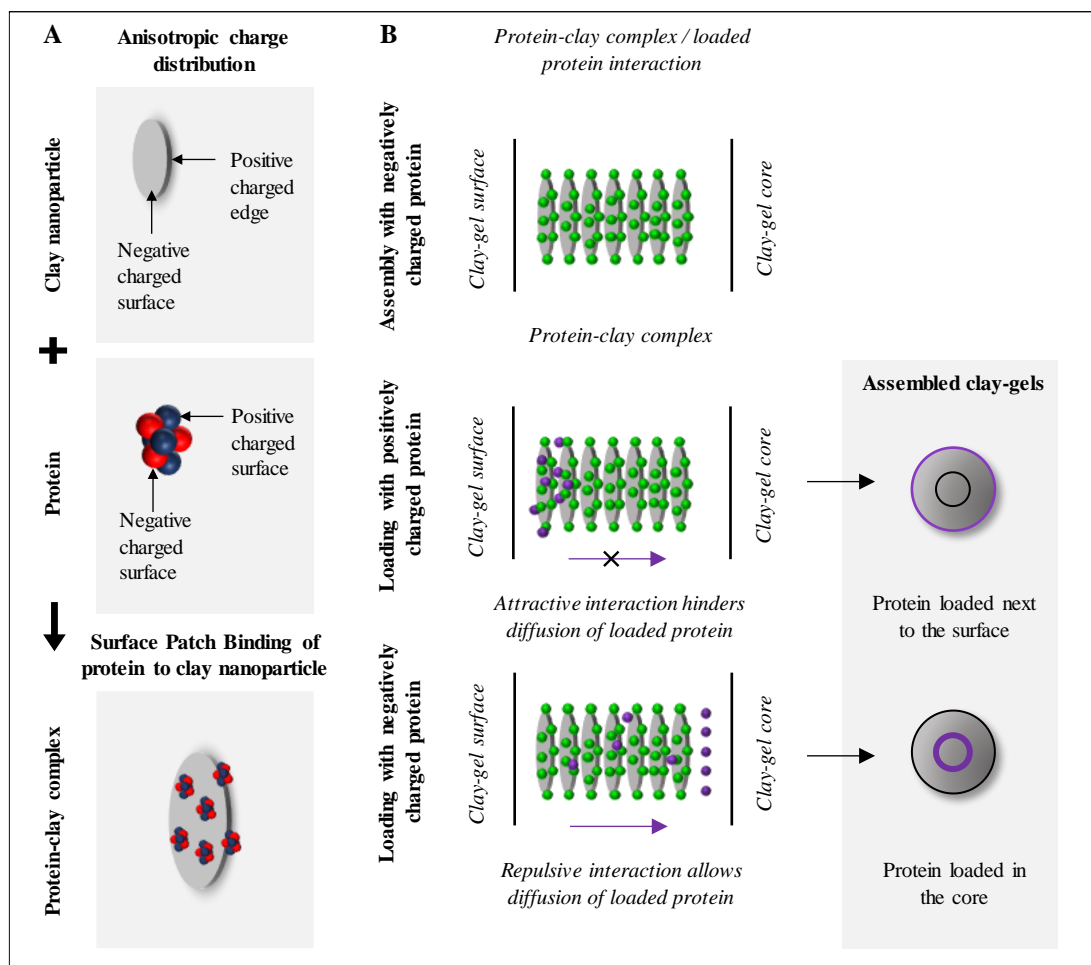


Figure 4.24 Secondary diffusion and localisation of macromolecules governed by protein-clay complex/protein interaction. (A) The clay-nanoparticle and protein illustration indicate the anisotropic charge distribution and their interaction through surface patch binding. Here is described a possible mechanism that controls the spatial localisation of the proteins loaded. Thus, (B) assuming that the assembly protein, negatively charged BSA (green sphere) binds to the edge and surface of the clay nanoparticle, forming a negatively charged protein-clay complex. Then, the positively charged protein loaded (purple sphere) would bind to the negatively charged complex hindering the diffusion. On the contrary, if the protein is negatively charged, it will not interact with the complex because both are negatively charged (D) allowing the diffusion into the clay-gel core.

Thus, towards understanding the clay-protein scaffolds assembly, it was recognised that two different diffusion processes take place at the assembly and loading steps, respectively. 1) A primary diffusion of concentrated protein solution (100 % FCS or 30 mg/ml - BSA) through the clay-gel that then facilitates 2) a secondary diffusion and localisation of low concentrated protein solution (100 μ g/ml - FITC BSA) (Fig. 3.12 & 3.14). For this reason, both phenomena, primary and secondary diffusion,

were studied individually to allow optimising the fabrication parameters and to understand the diffusion mechanism.

In this regard, the results presented so far indicates that variations in the protein concentration, ionic strength, incubation time and temperature affect the diffusion path length of the assembly proteins into the clay-gel, and consequently the spatial localisation of the loaded protein. Furthermore, size and net charge of the protein used at the assembly step influences as well the spatial localisation of the protein loaded. Thus, all these tested variables could be considered as fabrication parameter, which can be used to control de spatial localisation of the loaded proteins into the clay-gel.

Regarding the primary diffusion mechanism studied in the previous chapter, a reaction-diffusion process of concentrated BSA through the clay-gel was suggested to lead the self-assembly of an anisotropic structure that supports the subsequent 3D micropatterning of molecules. In this regard, the new findings support this assumption since changes in concentration, ionic strength and temperature seem to be not only proportional to the diffusion process but to the protein-clay reaction (Ralla et al. 2010 and Yu et al. 2013). Thus, enhancement in the adsorption rate would accelerate clay nanoparticle saturation and with it the diffusion of proteins to the next nanoparticle. Further structural characterisation will be performed in the next chapter to evaluate this assumption.

Concerning the secondary diffusion mechanism, based on previous results, the spatial localisation of the loaded proteins was suggested to be related to a selective diffusion. The new data support this hypothesis and indicates that is a filtering process governed by electrostatic interactions between the protein-clay complex and the loaded proteins, where attractive interactions would hinder the diffusion, and the repulsive interactions facilitate it.

Thus, following this logical sequence of experiments, proceeded to evaluate the effect of loading time and temperature in the 3D micropatterned structure. In this regard, the results show that the scaffolds assembled with BSA reached its maximum absorption capacity at day 7 with $\sim 1.51 \pm 0.35$ μg of BSA per μl of clay-gel.

Interestingly, the fluorescent ring maintained its localisation despite more protein being absorbed in the core of the clay-gel (Fig. 4.14 - B). This suggests that the proteins loaded are strongly bound at the diffusion front, preventing their spontaneous dispersion, which is essential for sustaining the spatial bioactivity of the proteins. Similarly, the loading temperature at 4°C and 37°C does not affect the localisation of the fluorescent ring (Fig. 4.15).

Finally, since the designed clay-gel is intended for biomedical application, the final fabrication parameter evaluated was the storage. Specifically, the storage solvent, temperature and time. Preliminary results suggest that the scaffolds have to be stored in an electrolyte solution to maintain their stability because they swell significantly in water after 3 h of storage (Fig. 4.18 - B).

Regarding the temperature, the results indicate that the ideal storage temperature is 4°C since the scaffold did not show any significant changes at this temperature after 144 h of incubation. This is in contrast to storage at 37°C, at which a significant reduction of the scaffolds' dimensions was observed. Interestingly, the controls (DPBS) showed a similar trend when incubated at 4°C and 37°C, suggesting that the clay nanoparticles govern the scaffolds' stability and not the proteins (Fig. 4.19 - B).

However, a slight decrease in the scaffold size was observed after 28 days of storage in DPBS at 4°C (Fig. 4.20 - B). Further work is required to verify if this is due to evaporation of the solvent or the result of an ageing process of the clay-gel as a function of time.

Interestingly, no sign of infection was detected even though the experiments above described were not performed under aseptic conditions. This could be related to the reported antibacterial properties of the Laponite® nanoparticles (Rawat et al. 2014).

The last experiments demonstrated the effect of some environmental parameters on scaffolds durability and stability. Nevertheless, further research is required to establish the shelf life and storage conditions, such as the use of microbial cultures, exploring other storage solutions, the addition of antimicrobials (if necessary), and determining the protein bioactivity to long storage.

4.5 Conclusions

In this chapter, different factors that affect the scaffold 3D micropatterning were evaluated. The results not only led to the optimisation of the fabrication parameters but began to elucidate the assembly and loading mechanism.

Thus, regarding the fabrication parameters, 1) the assembly step plays a significant role in the anisotropic structure formation and the localisation of the loaded protein. Different factors, known to alter the diffusion coefficient of macromolecules, such as concentration, ionic strength, incubation time and temperature, and the solute size and net charge can be manipulated at the assembly step to predict the 3D localisation of proteins in the clay-gel. 2) Regarding the loading step, the time showed no significant effect of the protein micropatterning, but only the amount of protein loaded. This is crucial to control the concentration of protein to deliver accordingly to the application. 3) Finally, analysis of the storage conditions suggests that the scaffolds are stable in DPBS at 4°C.

With respect to the assembly and loading mechanism, the results suggest that the force that triggers the diffusion of proteins into the clay-gel is the concentration and that the assembly proteins and clay nanoparticles “react” through SPB as the diffusion takes place, saturating the complete nanoparticle, edge and surface. Further characterisation is required to confirm this. Finally, a selective diffusion barrier due to electrostatic interactions between the assembled clay-gel and the loaded protein governs the loading process.

**Chapter 5 CHARACTERISATION OF
THE ARCHITECTURE AND THE
ASSEMBLY MECHANISM OF THE
NANOCLAY/PROTEIN SCAFFOLD**

5.1 Introduction

The previous results suggest that the nanoclay-protein scaffold assembly is the result of a reaction-diffusion process. In this regard, it was hypothesised that the proteins react with the clay nanoparticles as they diffuse into the clay-gel, forming a structure between the protein and clay that facilitates the 3D micro-patterning of proteins.

A reaction-diffusion is a mathematical model proposed in 1952 by Alan Turing, a British mathematician, whose goal was explaining morphogenesis or development of biological tissues by the formation of natural patterns (Turing, 1952). Today the reaction-diffusion model and its variations are widely used to study the self-assembly of numerous natural or synthetic patterned structures, ranging from morphogen gradients, pigmentation on a zebra skin to Liesegang rings, Belousov-Zhabotinskii Reactions and stripes of sand ripples (Ball, 2015). In general, the models describe activating/inhibiting interactions of molecules in a diffusive system, in which the final product is the self-assembly of structures with periodic patterns (Fig. 3.17).

One class of model investigated to great depth are binary reaction-diffusion systems with a reaction front, as this model is believed to explain the fundamental physics of reaction fronts that are usually observed in various chemical and biological systems (Braschler et al. 2011). In this model, two reactants, one diffusive (A) and another static (B) that are initially separated in space react and develop a diffusion front. The propagation of which leaves behind a reaction product (C) (Larralde et al. 1992 and Bazant & Stone, 2000) (Fig. 5.1).

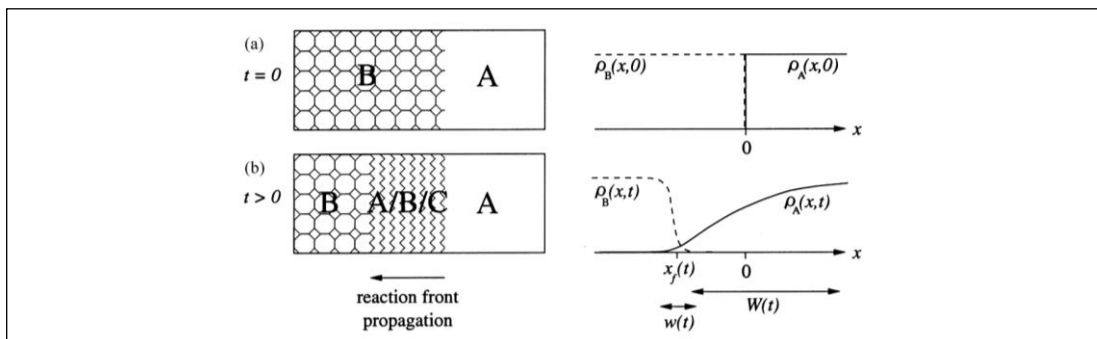


Figure 5.1 The reaction-diffusion fronts with one diffusion and one static reactant. Schematic illustrations on the left and respective concentration sketches on the right shows (a) the diffusing

reactant A separated from the static reactant B. Upon contact, a reaction front propagates into the region rich in reactant B and later leaving a reaction product C (Bazant & Stone, 2000).

Such a model can be used to predict the assembly of physical gels by ionotropic or external gelation, where a polyelectrolyte is immersed in a solution containing ions and the subsequent diffusion of ions crosslink the polyelectrolyte progressively at the reaction front forming a gel (Patil et al. 2010). For example, in the external gelation of alginate beads in a CaCl_2 solution. Upon interaction of an alginate solution with a CaCl_2 solution, a reaction front forms and its progression through the alginate solution leaves a gelled calcium-alginate behind (Braschler et al. 2011 and Ayarza et al. 2017) (Fig. 5.2).

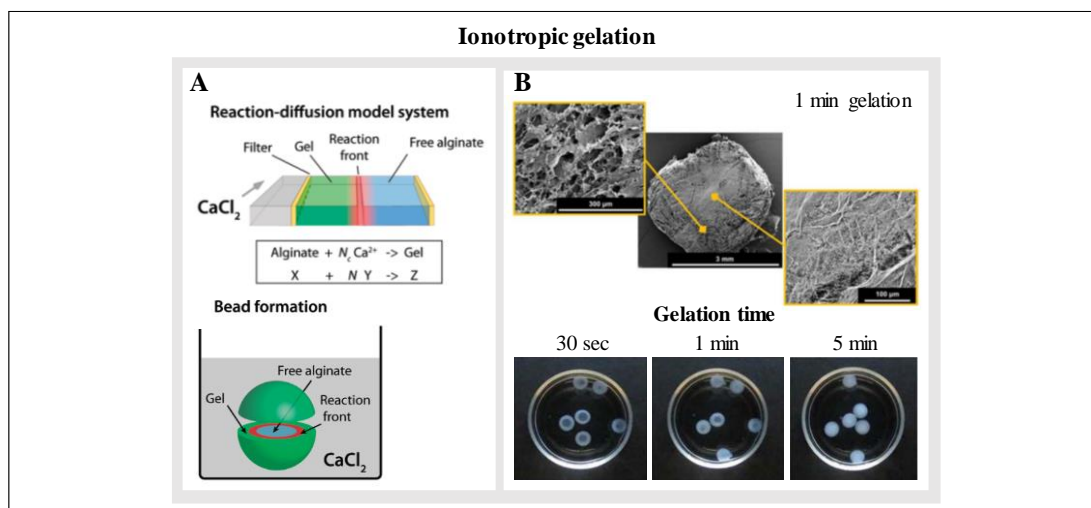


Figure 5.2 Assembly of physical gels by ionotropic gelation. (A) Upon interaction of an alginate solution with a CaCl_2 solution, a reaction front forms and its progression through the alginate solution leaves a gelled calcium-alginate behind (Braschler et al. 2011). (B) The SEM images of partially gelled alginate bead after 1 min of gelation reveals two distinct morphologies. A porous outer region of gelled alginate and a compact inner region of unreacted alginate. Moreover, picture of the alginate beads gelation as a function of time reveals changes in the colour of the structure as the crosslinks occur, which in turn exposes the propagation of the reaction front. (Ayarza et al. 2017).

A physical gel formed by reaction-diffusion characteristically develops distinctive structural features. Such phase transitions (or structural changes) that characteristically result in a higher degree of order. For example, the particles or polymers may acquire a perpendicular or parallel orientation with respect to the diffusion front following the diffusion flux of the gelator (Ziemecka et al. 2013). The phase transitions can be resolved with a range of imaging techniques, such as PLM,

SEM, LFM and TEM. Each of these techniques and the structural information they can provide will be introduced in turn.

The increase in structural order can result in optical anisotropic properties (Fig. 5.3) allowing the phase transition to be visualised under cross-polarised light. In this regard, the particles or polymers may acquire a perpendicular or parallel orientation with respect to the diffusion front depending on the type of reaction. In both cases; however, alignment follows the diffusion flux of the gelator (Ziemecka et al. 2013). Such phenomena have been observed, for example, with the gelation of curdlan, alginate and PBDT gels assembled by a reaction-diffusion mechanism (Dobashi et al. 2005, Maki et al. 2011 and Wu et al. 2014).

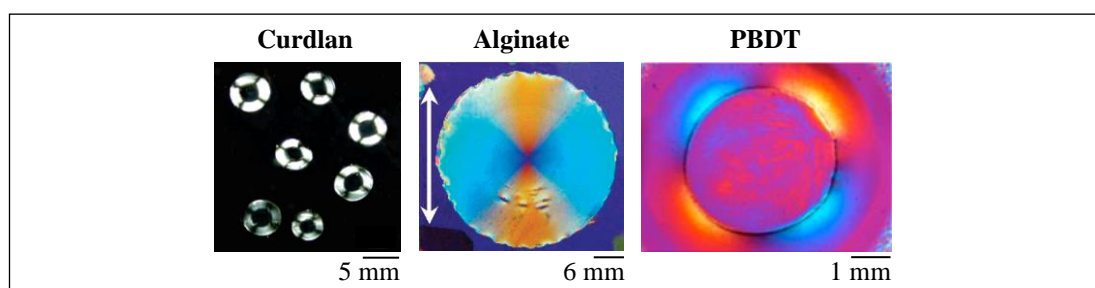


Figure 5.3 Physical gels set by a reaction-diffusion process. Cross-polarised light images of curdlan, alginate and PBDT gels cross-linked by ions diffusion reveals macro beads displaying a radial and symmetrical birefringence, which is indicative of periodical rearrangement of the polymer particle. Modified images from Dobashi et al. 2005, Maki et al. 2011 and Wu et al. 2014, respectively.

In these examples, owing to the circumferential shape of the physical gel and the direction of the reaction-diffusion process towards the core, the polymer particle presents a radial arrangement resulting in the radial and symmetrical birefringence patterns observed under cross-polarised light. In the case of alginate, Maki et al. (2011) indicate that the molecules align along the circumferential direction in the cylindrical gel, which is perpendicular to the direction of gel growth or the Ca^{2+} flow (Fig. 5.3). In addition, this was corroborated by SAXS analysis, which revealed a symmetrical intensity pattern in the direction of the reaction.

SEM imaging can also be used to characterise the phase transition during the reaction-diffusion process of physical gels; specifically, the structure, heterogeneity, and different arrangement of the porous network. For example, Wu et al. (2014)

reported the assembly of PBDT gels by the reaction-diffusion of Ca^{2+} ions. The final structure had 6 different regions, and their respective interfaces could be observed not only by PLM but SEM (Fig. 5.4 - A). In another study performed by Ayarza et al. (2017), the SEM images of partially gelled calcium alginate beads revealed two distinct morphological regions. An outer-gelled region with a porous structure and an inner region, which has not gelled with a compact rough structure (Fig. 5.4 - B).

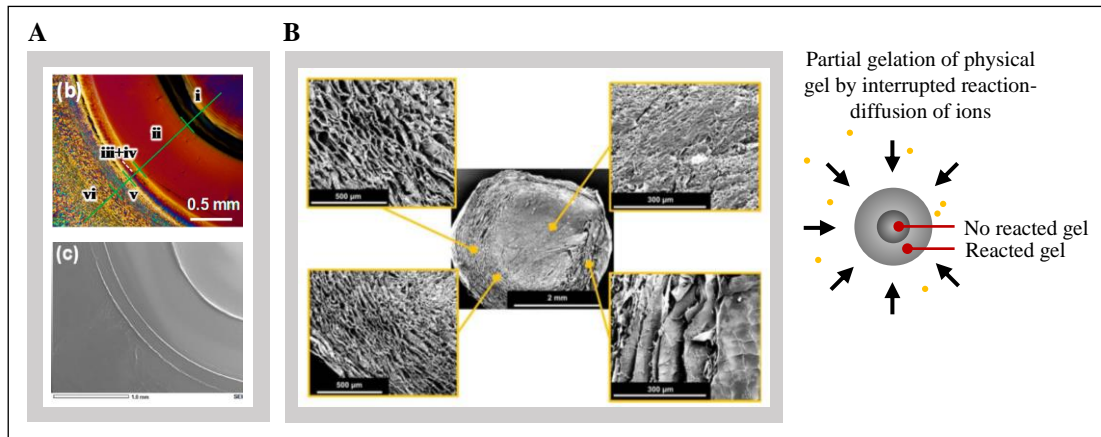


Figure 5.4 SEM characterisation of physical gels cross-linked by diffusion-reaction. (A) PLM images of diffusion of Ca^{2+} through a PBDT gel air-dry reveals the formation of different regions, I - VI. This was confirmed by SEM imaging (Wu et al. 2014). Moreover, (B) SEM images of partly gelled calcium alginate bead reveals two distinct morphological regions. The outer-gelled region shows a porous structure. In contrast, the inner region, which has not gelled, shows a compact rough structure. Note that the alginate samples were immediately frozen into liquid nitrogen after gelation, cut into halves and freeze-dried for SEM imaging (Ayarza et al. 2017), and despite the differences in the samples preparation, a phase transition could be observed.

Another interesting feature that can be evidenced with SEM imaging of fully gelled structures is the distribution of the polymer particle in the gel, which may be homogeneous or inhomogeneous depending on the polymer concentration and molecular weight, and the concentration of the gelator (ions) (Skjak-Braek et al. 1989). Overall, these factors have a direct effect on the relative diffusion rate between the ions and the polymers into the reaction or gelling region. Thus, at low ion concentration, the diffusion rate of polymer is faster with respect to the ions allowing the polymers to diffuse to the periphery of the droplet for cross-linking resulting in an uneven distribution of the polymer. In contrast, at high ion concentration, the diffusion of ions is rather faster than the polymer limiting the diffusion of polymer towards the periphery of the droplet forming a more

homogenous structure (Voo et al. 2016) (Fig. 5.5 - A). For example, SEM images of 2 % w/v calcium alginate beads assembled in 0.1 M CaCl_2 solution revealed larger pores in the centre of the structure in comparison to the periphery, indicating the inhomogeneity of the gel structure. Moreover, the beads assembled with 0.3 M CaCl_2 solution revealed a more homogenous structure. Interestingly, 10% w/v calcium alginate beads had a homogenous structure regardless of the concentration of the CaCl_2 solution (Voo et al. 2016) (Fig. 5.5 - B). Similar results were reported by Skjak-Braek et al. (1989) for alginate, pectate gels, κ -carrageenan and gellan gum gels.

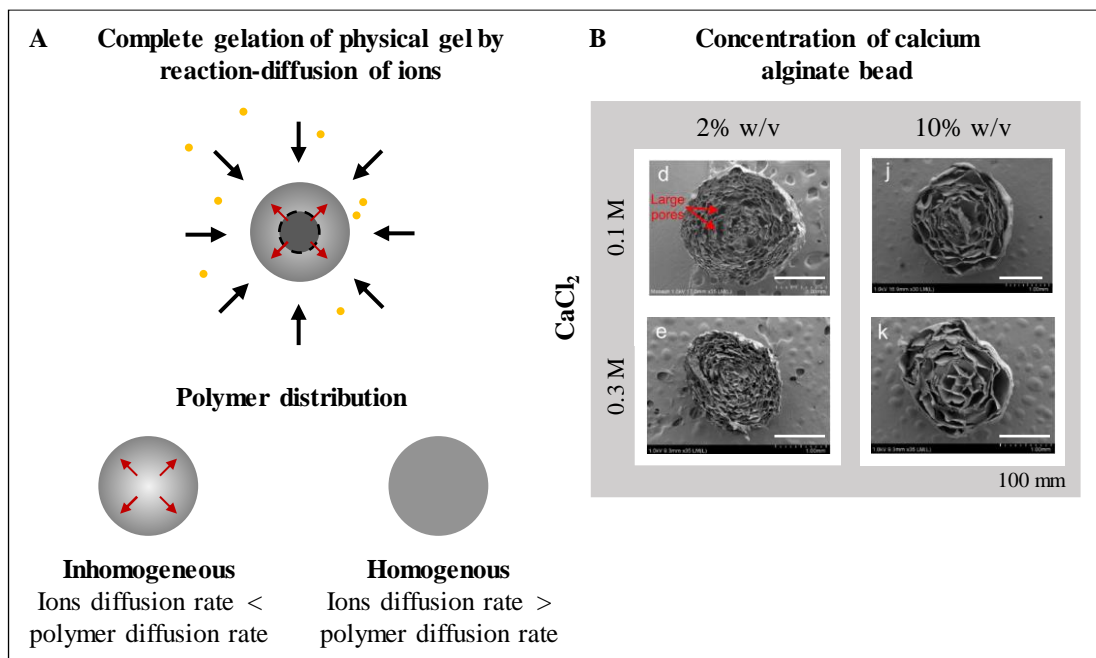


Figure 5.5 Polymer distribution of physical gels assembled via reaction-diffusion characterised by SEM. (A) Schematic illustration of fully reacted physical gel (grey circle) exemplifies the redistribution of the polymer inside the gel droplet based on the relative-diffusion rate of ions (black arrows - yellow dots) towards the core and polymers towards the periphery (red arrows). At low ions concentration, the diffusion of ions is relatively slower in relation to the polymer; therefore, more polymer diffuses and react with ions at the periphery forming an inhomogeneous structure. At high ions concentration, the diffusion of ions is faster in comparison to the polymer limiting its diffusion towards the periphery; thus, the formed structure will be more homogeneous. (B) SEM images of 2% w/v calcium alginate bead assembled with 0.1 M CaCl_2 reveals the formation of an inhomogeneous structure with larger pores in the centre in comparison to the periphery. However, the structure became homogenous when the CaCl_2 concentration was increased to 0.3 M. Moreover, alginate beads of 10 % w/v formed homogenous structures regardless of the ions' concentration. Presumably, the viscosity of the gel slowed the diffusion of polymers towards the periphery (Voo et al. 2016).

Furthermore, TEM imaging can be used to obtain information, such as structural conformation, size, shape and spatial distribution and orientation of the new entity assemble via reaction-diffusion. For example, TEM images of alginate capillaries assembled by ionotropic gelation revealed an alginate network displaying filaments in an anisotropic orientation at the edges of the capillary characteristic of this type of gelation and an isotropic orientation in the bulk (Schuster et al. 2014) (Fig. 5.6 - A). In another system, the TEM images assisted studying structural changes in the network of 2 % alginate beads and 1.5 % alginate/0.5 % chitlac (lactose-modified chitosan). The pure calcium alginate bead revealed an entangled texture with polygonal-like voids. In contrast, alginate/chitlac beads the filaments often coalesced forming patches that then assembled into clusters leaving wider and irregular shaped voids (Brun et al. 2011) (Fig. 5.6 - B).

Addition of molecules to the gelator or changes in their concentration may alter the diffusion rate and with it, the distribution of the polymeric particle in the gel (Skjak-Braek et al. 1989). In this regard, the ionotropic gelation of chitosan using tripolyphosphate (TPP) and pyrophosphate (PPi) as cross-linkers to slow down the diffusion leads to the assembly of structures with homogenous and inhomogeneous distribution polymer networks, respectively, as revealed by the TEM images (Sacco et al. 2016) (Fig. 5.6 - C). Moreover, assembly of Fe₃O₄-chitosan beads in different concentrations of NaOH produces a decrease in the iron oxide particle as the concentration of NaOH increases, and it also alters the spatial distribution of the composed particle (Yang et al. 2012) (Fig. 5.6 - D).

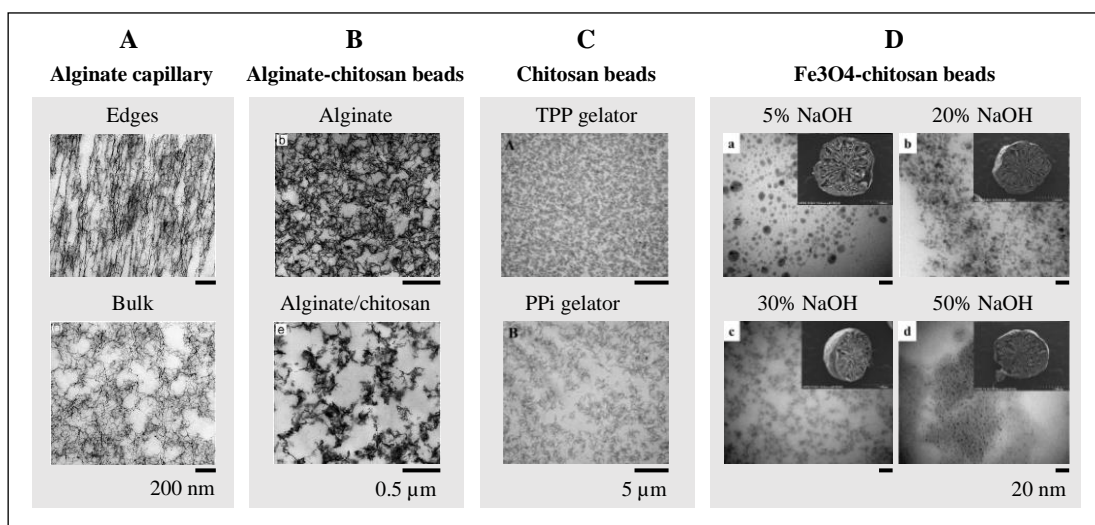


Figure 5.6 TEM imaging analysis of physical gels assembled by reaction-diffusion. (A) External gelation of alginate capillaries develops an anisotropic orientation of alginate filaments at the edges and isotropic orientation in the bulk (Schuster et al. 2014). (B) Assembly of alginate gels reveals a homogenous distribution of the filament and network structure, in comparison to the alginate/chitlac beads, which shows an inhomogeneous structure made of filaments clumps (Brun et al. 2011). (C) Assembly of chitosan beads with TPP cross-linker generates a structure with homogenous distribution of the polymer. In contrast, PPi cross-linker assembled a structure with inhomogeneous distribution of polymer (Sacco et al. 2016). (D) Assembly of Fe₃O₄-chitosan beads with different concentrations of NaOH causes a decrease in size of the iron nanoparticles as the concentration of NaOH increases. It also alters the composite distribution in the gel (Yang et al. 2012).

Thus, gelation via reaction-diffusion process leads to the assembly of a new entity with particular features that can be assessed with different imaging techniques as briefly described-above. Hence, the objectives of this chapter are to characterise the assembly mechanism and structural properties of the scaffolds using a range of imaging techniques, including CLSM, SEM, PLM and TEM. In doing so, the hypothesis that the nanoclay/protein scaffold is assembled by a reaction-diffusion process will be tested.

5.2 Materials and Methods

5.2.1 Scaffold assembly

5 µl droplet of 2.8 % clay-gel were placed in 10 mg/ml BSA-DPBS solution as left to assemble for 50 min at 4°C. Then, the assembled structure was transferred to 100 µg/ml FITC BSA for 1 h at 4°C to load the protein. Finally, the loaded scaffolds were stored and analysed.

The procedure was performed in a 96-well plate containing 200 µl of either the assembly, loading or storage solution. Moreover, one droplet was assembled per well and then transferred to respective treatment solution with a spatula. Also, most of the experiments were performed at 4°C, otherwise stated.

This is the general procedure to assemble the nanoclay/protein scaffold. However, some parameters varied throughout the study and, therefore, further details of the sample preparation can be found in the results.

5.2.2 Characterisation techniques

5.2.2.1 Transmission electron microscopy

The scaffolds were prepared following the protocol provided by the Biomedical Imaging Unit, University of Southampton. Thus, the scaffolds were crosslinked for 1 h at room temperature using a solution of 3 % glutaraldehyde and 4 % formaldehyde in 0.1 M PIPES buffer-pH 7.2. Next, the samples were rinsed with a buffer of 0.1 M PIPES buffer - pH 7.2 twice for 10 min and then transferred to a post fixative solution of 1 % osmium tetroxide in 0.1 M PIPES buffer at pH - 7.2 for 1h. The samples were rinsed again twice with 0.1 M PIPES buffer - pH 7.2 for 10 min and then with distilled water for 30 sec.

In the next step, the samples were incubated in Uranyl acetate for 20 min and then dehydrated by transferring them every 10 min to different dilutions of ethanol, 30, 50, 70 and 95 %, and at the end, they were incubated for 20 min in 100 % ethanol.

To embed the samples in resin, they were treated with acetonitrile and 50:50 acetonitrile:resin solution for 10 min and overnight, respectively. Finally, the samples were transferred to a low viscosity resin (Spurr, Sigma Aldrich) for 6 h. Then, the resin was refreshed and put to polymerise with the sample in an oven 24 hours at 60°C.

Next, the samples were sectioned using an ultramicrotome Reichert Ultracut E ultramicrotome and imaged with a Hitachi HT7700 transmission electron microscope.

5.2.2.2 Scanning electron microscopy

The samples for SEM were prepared similarly to the TEM. However, right after the treatment with 100 % ethanol, they were dried using a Balzers CPD 030 critical point drier. Then, the samples were cut using a razor blade, and since they were brittle, they fell apart as soon as the blade touched the surface. Finally, they were coated gold/palladium using Quorum Q150T ES sputter coater and imaged with a FEI Quanta 250 scanning electron microscope working at 10 kV. The images were taken between X100 to X100,000 magnification with a working distance of approximately 4.5 - 5 mm. The chamber pressure was set to 60 Pa and the spot to 3.0.

5.2.2.3 Polarised Light Microscopy

The scaffolds were transferred to a homemade well plate filled with DPBS to the top and then covered with a thin glass being careful of not introducing any bubbles (Fig. 5.7).

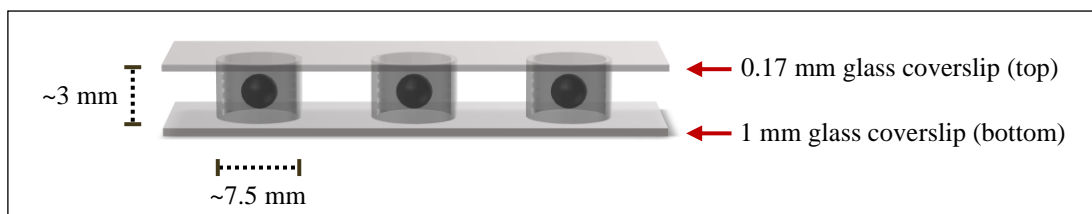


Figure 5.7 Homemade well plate fabricated to analyse the assembled scaffolds under polarised light microscopy.

Formerly to the scaffold imaging, Koehler light was set and the filter NCB11 inserted to balance the colour temperature. Following, crossed polarisers were placed in the optical pathway between the light source and eyepieces to block the light passing through the system. This was confirmed when the field of view looked completely black under the eyepieces. Finally, the lambda plate (Nikon) was adjusted as indicated on the manual instructions and the images collected with a colour camera (Nikon E950). Details of the equipment hardware and software setup are described in table 5.1.

Table 5.1. General Polarised Light Microscope (80i, Nikon) settings.

Objective	CFI Plan Fluor 4x/0.13
Light source	12V100W halogen transmitted illumination
Filters	NCB11 filter colour Polarisers Lambda plate
Camera Nikon E950	sRGB
Image format	Width - 1600 pixels Height - 1200 pixels Bit depth - 24 bits File - JPG.

To evaluate the birefringence of the nanoclay/protein scaffolds in a 2D format, 10 µl of 2.8% clay-gels were placed on a 1 mm thick coverslip, covered with a 0.17 mm coverslip and then transferred to the assembly solution (10 mg/ml BSA - DPBS and DPBS) for 1 h at 4°C. Note that during the sample preparation, a coverslip spacer of 1 mm thick was placed and fixed in between both glasses to obtain samples of the same thickness and secure their stability.

5.2.2.4 Polarised light

Preliminary optical and qualitative characterisation of Laponite® gels as a function of (1) clay concentration, (2) autoclaving, (3) storage temperature and (4) ageing time was performed by means of polarised light. The samples were prepared as described below:

3 ml of different concentrations of Laponite® gels (1 - 4 %) were placed into borosilicate glass vials (15x45 mm, Thermo scientific) to evaluate their

birefringence. To this end, the vials were placed between two crossed polarisers (5x5 cm), which were in the pathway of a cold light source. Finally, a Samsung Galaxy 5 smartphone (manual mode) was used to acquire the polarised images as shown in Fig. 5.8.

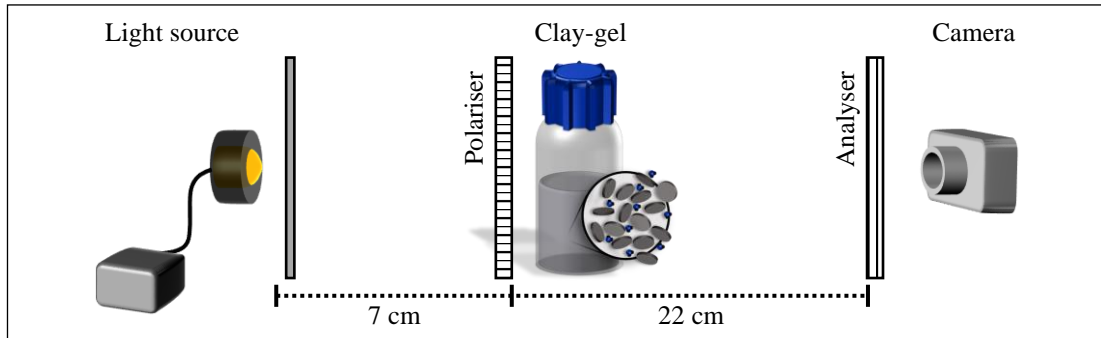


Figure 5.8 Polarised light experiment settings.

5.3 Results

5.3.1 Assembly mechanism of the nanoclay/protein scaffold

Until now, it is evident that the diffusion of proteins into the clay-gel is concentration dependent. In this regard, low concentrations of BSA (100 $\mu\text{g/ml}$) are adsorbed next to the clay-gel surface (Fig. 5.9 - 1B), but upon assembly of the clay-gel with a concentrated solution of BSA (10 mg/ml), the secondary absorption of low concentrated BSA into localised bands within the clay-gel is favoured (Fig. 5.9 - 2B).

The last observation is intriguing, as it is not understood how the assembly of the clay-gel in a concentrated protein solution allows the secondary diffusion of low concentrated BSA and causes its spatial localisation. Thus, to elucidate this, the protein assembly solution was spiked with FITC BSA to follow up its diffusion and evaluate its relationship with the distribution of low concentrated BSA (Fig. 5.9 - A).

The confocal images showed the diffusion of the protein assembly solution (picked with FITC BSA) into the clay-gel (Fig. 5.9 - 3B). Further comparison with the patterned clay-gel (Fig. 5.9 - 2B) revealed a relationship between the spatial localisation of the assembly solution and the loading solution. In this regard, the “diffusion front” of the assembly solution corresponds to the spatial localisation of the “internal fluorescent ring” (Fig. 5.9 - B, yellow arrow) also, that the “assembly protein gradient” correlates with localisation of the “black space lacking FITC BSA” (Fig. 5.9 - B, red arrow).

These observations allowed us to propose a mechanism for the assembly of clay-gels with 3D localisation of proteins. (Fig. 5.9). Thus, the first wave of concentrated protein solution diffuses into the clay-gel, reacts and “saturates” the clay nanoparticles (Fig. 5.9 - 3B - C). Restructuring of this “reacted clay-gel region” with proteins allows a second wave of protein solution to diffuse in and bind to the next available “unsaturated” clay nanoparticles at the interface between the “reacted and unreacted clay-gel” or diffusion front (Fig. 5.9 - 2B & C).

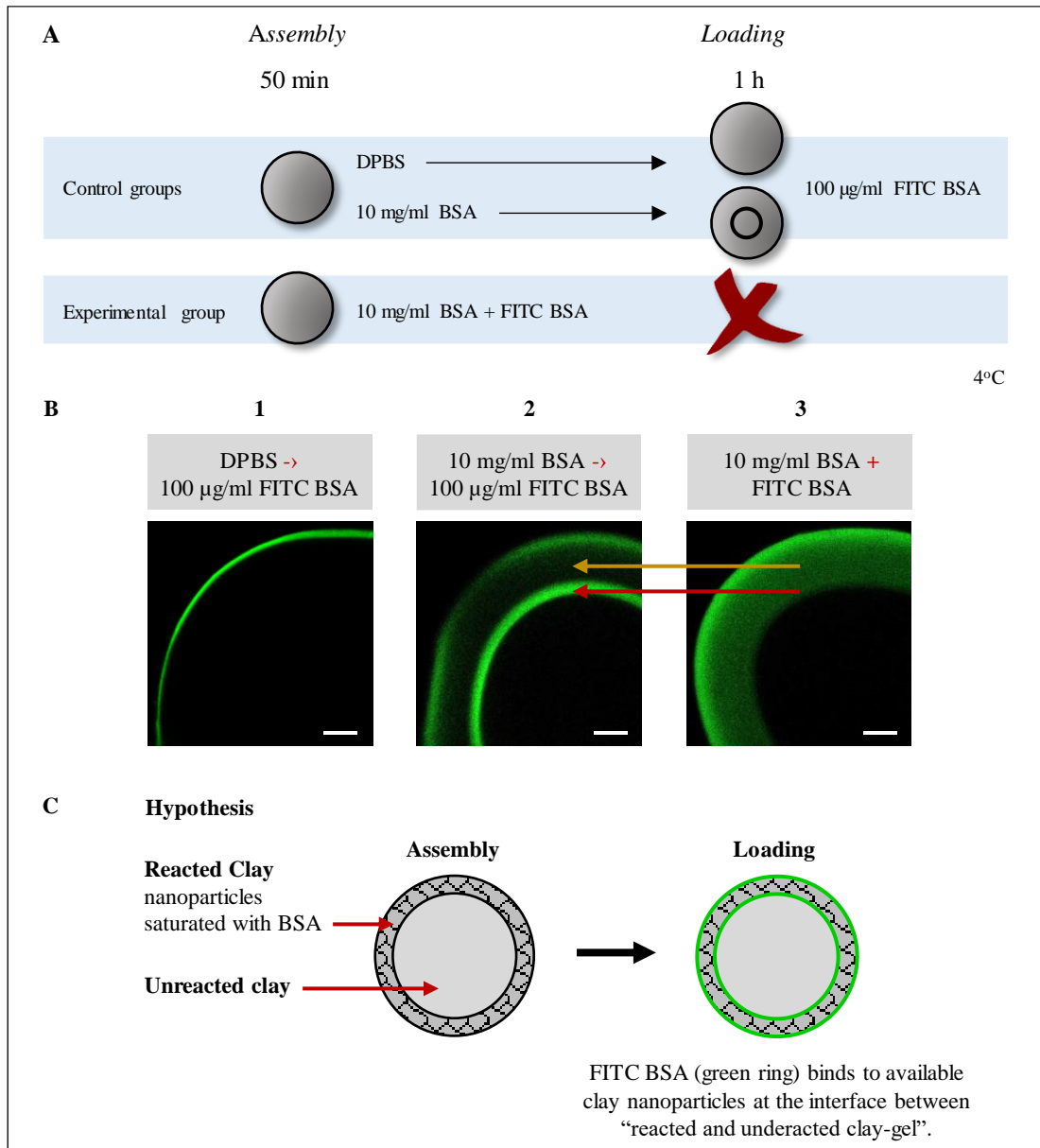


Figure 5.9 Assembly mechanism of nanoclay/protein scaffold. (A) Schematic illustration of the experiment set up to evaluate the relationship between the protein assembly solution and localisation of the secondary loaded protein. The confocal images reveal a link between the localisation of the assembly and loading solutions. (B, red & yellow arrow) The “diffusion front” and “protein gradient” correlates with the spatial localisation of the “fluorescent ring” and “black space lacking FITC BSA” in the patterned clay-gel, respectively. In this regard, (C) it was hypothesised that the concentrated protein solution diffuses into the clay-gel and saturates the nanoparticles. This prevents the subsequent protein wave from binding to the saturated clay nanoparticles until reaching the “diffusion front” or the interface between the “reacted and unreacted clay”. The images represent n = 4 and the scale bar to 200 µm.

Further research is needed to corroborate the above-postulated hypothesis. If it is correct, structural characterisation of the clay-gels should reveal two different phases at the reacted and unreacted clay fraction.

5.3.2 Characterisation of the nanoclay/protein scaffold nano to macroarchitecture

In the previous experiment, it was hypothesised that two different structures compose the nanoclay/protein scaffold. In the regard, the reaction-diffusion process of proteins into the clay-gel generates a “reacted clay fraction” or a “complex structure” of reacted protein/clay nanoparticles, and an “unreacted clay fraction” of pristine clay nanoparticles. Moreover, the interface between these two different structures is crucial for the localisation of the loaded proteins.

Thus, in order to evaluate if the nanoclay/protein scaffold is constituted by two different structures, further characterisation of the clay-gel architecture using SEM, PLM and TEM was performed.

5.3.2.1 Scanning Electron Microscopy

To corroborate the presence of “reacted and unreacted clay” regions in the nanoclay/protein scaffold, clay-gels were assembled with BSA and DPBS and then prepared for SEM imaging by standard chemical cross-linking, ethanol dehydration and critical point drying (CPD) with distilled CO₂ medium (Fig. 5.10 - A) (methods section - 5.2.2.2).

Cross-sections of fractured control clay-gels, plain and DPBS revealed a dense structure with similar texture (Fig. 5.10 - B & C). Interestingly, macroscopic images of the BSA clay-gels revealed a shell/core like structure that separated during the sample preparation for imaging (Fig. 5.10 - D). Magnified images demonstrated that both structures are different. The shell or external fragment had a porous network, whereas the core, or internal fragment displayed a dense structure with a texture similar to that of the controls (Fig. 5.10 - D1 & D2).

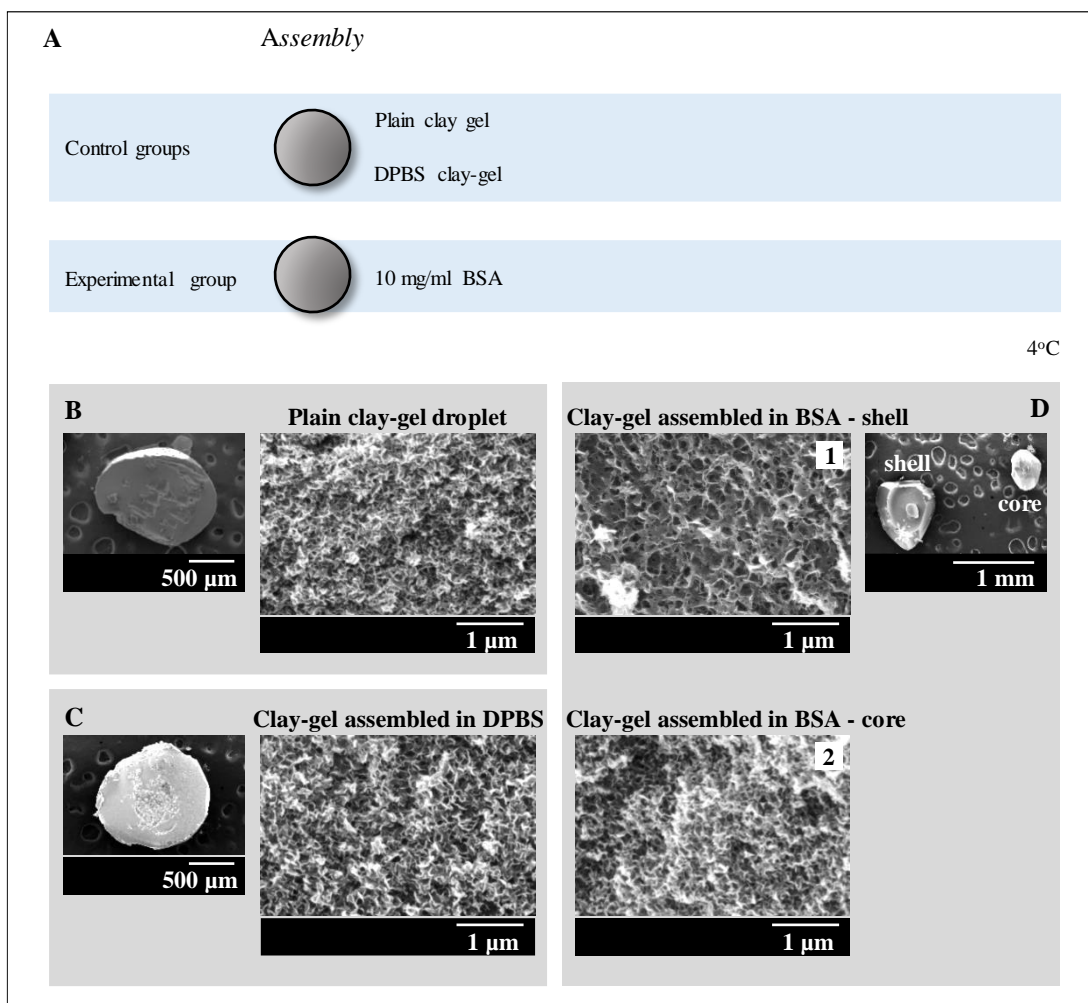


Figure 5.10 Scanning electron microscopy of nanoclay/protein scaffolds. (A) Schematic illustration of clay-gel scaffolds assembled in BSA with respective controls, plain and DPBS clay-gels, to evaluate their nano and microstructure. (D1 & D2) SEM images of cross-section of prepared scaffolds at a magnification of $\times 50,000$ reveal that two different structures form the BSA clay-gels, a porous shell or external fragment and a dense core or internal fragment. (B & C) The latter is similar to the control groups. Representative images for $n = 4$.

Thus, the results indicate that two different structures form the BSA scaffold. In this regard, the porous shell-like fragment seems to correspond to the “reacted” region of the clay-gel droplet, which is formed by the reaction-diffusion of BSA into the clay-gel, and the dense core-like fragment would then correspond to the “unreacted” region of the clay-gel droplet that displays similar features under SEM to the plain and DPBS clay-gels (Fig. 5.11).

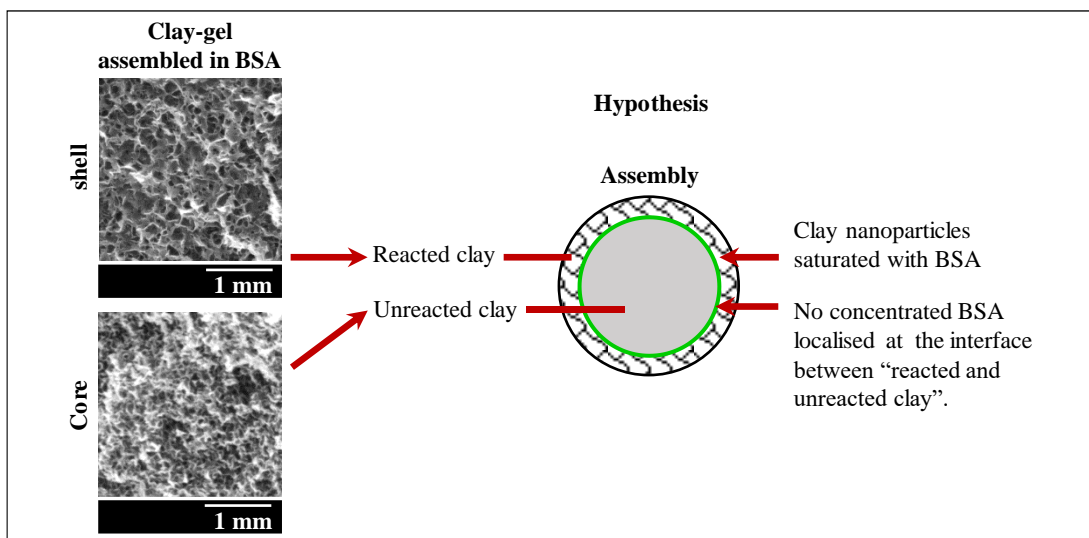


Figure 5.11 Microstructure of clay-gel assembled with BSA. The SEM images reveal a porous shell and a dense core structure, which corresponds with the spatial localisation of the “reacted and unreacted clay” regions, respectively. The result supports the postulated hypothesis. A concentrated protein solution diffused in the clay-gel and saturated the nanoparticles. Then subsequent protein wave cannot bind to the saturated clay nanoparticles but to the next available, which are at the interface between the “reacted and unreacted clay” or “diffusion front”. The images represent $n = 4$.

5.3.2.2 Polarised Light Microscopy

Structural characterisation of nanoclay-protein scaffolds

A characteristic phase transition is observed during the gelation of physical gels by reaction-diffusion, where the new phase develops a higher degree of order as the particles align following the diffusion flux of the gelator (Ziemecka et al. 2013). Moreover, due to the periodical rearrangement of the particles, the gel acquires anisotropic optical properties, which becomes visible under cross-polarised light (Dobashi et al. 2005 and Lin et al. 2010).

In this scenario, the structural change of the reacted/unreacted clay regions observed in the SEM images suggest that the clay-gel undergoes a phase transition. Thus, the next experiment was set up to determine if the new phase or reacted clay region acquires an anisotropic arrangement characteristic of reaction-diffusion gelation by studying its optical properties with PLM (methods section - 5.2.2.3).

Qualitative analysis of the images revealed different birefringence patterns and intensities as a function of the treatment. Hence, the scaffolds assembled with BSA showed a strong circular pattern, which suggests that the anisotropic microstructure of the scaffold possess a radial organisation. In contrast, the DPBS scaffolds displayed a lower and patchy birefringence (Fig. 5.12).

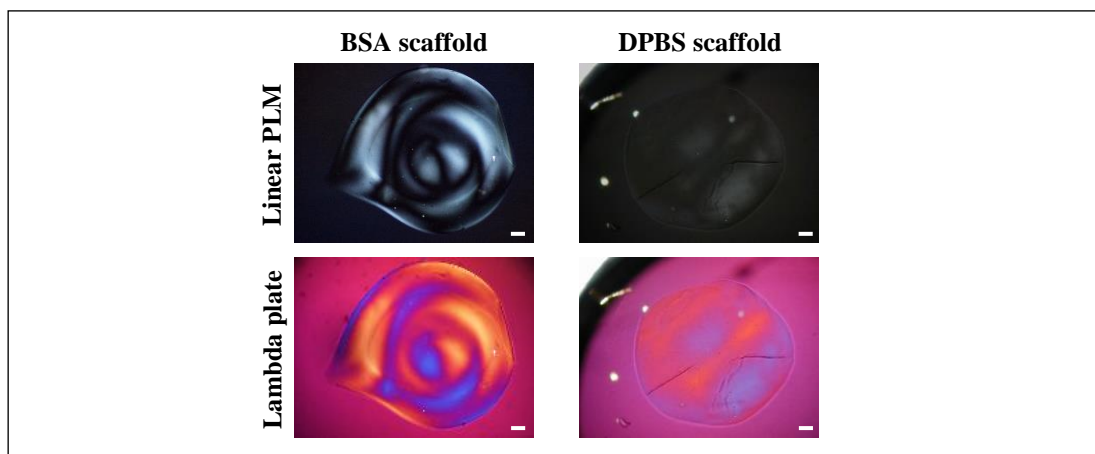


Figure 5.12 Cross-polarised light images of nanoclay/protein scaffolds. The images reveal some degree of order in the scaffolds assemble with proteins or ions. Nevertheless, the BSA scaffolds exhibited a radial-like pattern and refracted light more compared to the scaffolds assembled in DPBS, which displayed patches of low birefringence with the lambda plate. The results imply a higher degree of anisotropic ordering in the BSA scaffold. The images are representative of triplicates, and the scale bar corresponds to 200 μm .

Both BSA and DPBS scaffolds possess some degree of order, but the birefringence pattern and intensity observed indicate that it is higher for the scaffolds treated with BSA. Nevertheless, to determine if the birefringence is related to the reacted clay region and verify that it is not an optical effect due to the shape and thickness of the scaffold, a similar experiment was set up but in a 2D format (1 mm thickness).

In this regard, the PLM exhibited a radial birefringence next to the periphery of the clay-gel treated with BSA with an optical texture parallel to the diffusion direction and perpendicular to the diffusion front. Notably, this anisotropic structure colocalised with the reacted clay region (Fig. 5.13).

Again, PLM images of the DPBS clay-gels exhibited patches of low birefringence with a criss-cross texture. Optically this structure is similar to the unreacted region of the BSA clay-gels, again indicating the equivalence of these structures (Fig. 5.13).

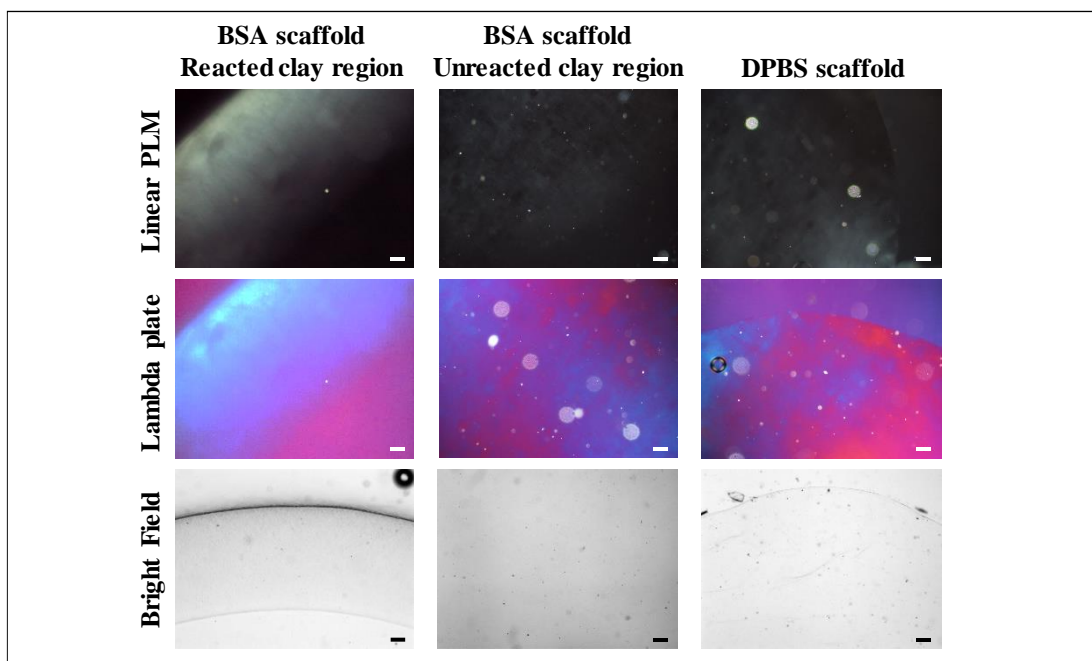


Figure 5.13 Optical analysis of 2D nanoclay/protein scaffolds anisotropic structure. PLM images of the BSA scaffolds reveals that the reacted clay region possesses an anisotropic arrangement with a radial-like birefringence and a texture parallel to the diffusion direction. The unreacted clay region of the BSA scaffolds and DPBS scaffolds exhibit patches of low birefringence and similar textures. The images are representative triplicates, and the scale bar corresponds to 200 μm .

The reacted clay region possesses a significant degree of order. Nevertheless, some birefringence could also be perceived in the unreacted clay region (Fig. 5.13), suggesting that the material has some inherent degree of order, which increases with the diffusion process. The existence of such background ordering of nanoparticles was confirmed in PLM images of 2.8 % clay-gel in its native state that exhibited low birefringence and crisscrossed texture, again similar to the unreacted clay region of the BSA scaffolds (Fig. 5.14 vs 5.13).

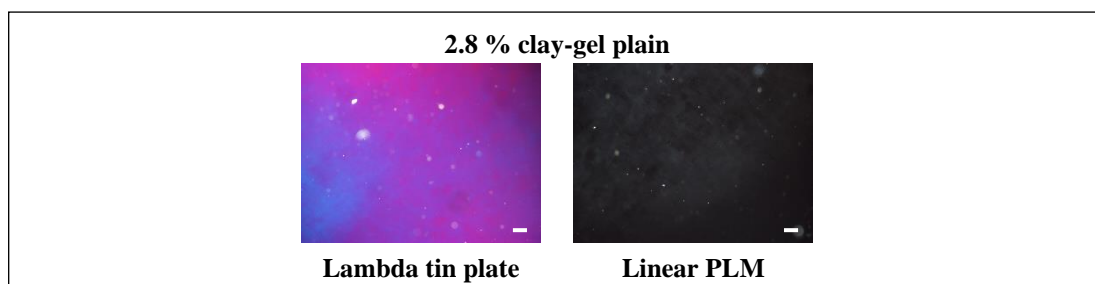


Figure 5.14 Optical analysis of 2.8 % clay-gel anisotropic structure.

The results indicate that 2.8 % clay-gel possess some degree of order, which seems to increase with the reaction-diffusion of proteins. Further characterisation of the clay-gel will be described in the next section to determine if the scaffold assembly is related to a particular ordered state: gel, glass, nematic phase or other states.

Structural characterisation of clay-gel

The polarised light images of 2.8 % autoclaved clay-gel revealed some birefringence (Fig. 5.15), suggesting that its ordered state is a nematic phase similar to the results reported by Mouchid et al. (1995) and Gabriel et al. (1996). Nevertheless, the authors did not expose the clay nanoparticle dispersion to a temperature/pressure treatment. Thus, proceeded to evaluate if the autoclaving step and/or the concentration of the dispersion were accountable for the birefringence observed in the system. For this, dispersions of clay nanoparticles in water with different concentrations ranging from 1 to 4 % were prepared. Then the dispersions, either autoclaved or non-autoclaved were evaluated under cross-polarised light (methods section - 5.2.2.4).

Qualitative analysis of the images showed significant changes as a function of autoclaving step and concentration, specifically at 3 %, where the autoclaved clay-gel developed birefringent patches compared to the non-autoclaved, which did not double refract the light (Fig. 5.15 - red squares).

Furthermore, the 4 % non-autoclaved clay-gel showed birefringent patches with smooth textures. However, after the autoclaving step, the birefringence increased significantly, and the patches acquired a rough texture. A close view showed some aggregates with a rectangular shape (Fig. 5.15).

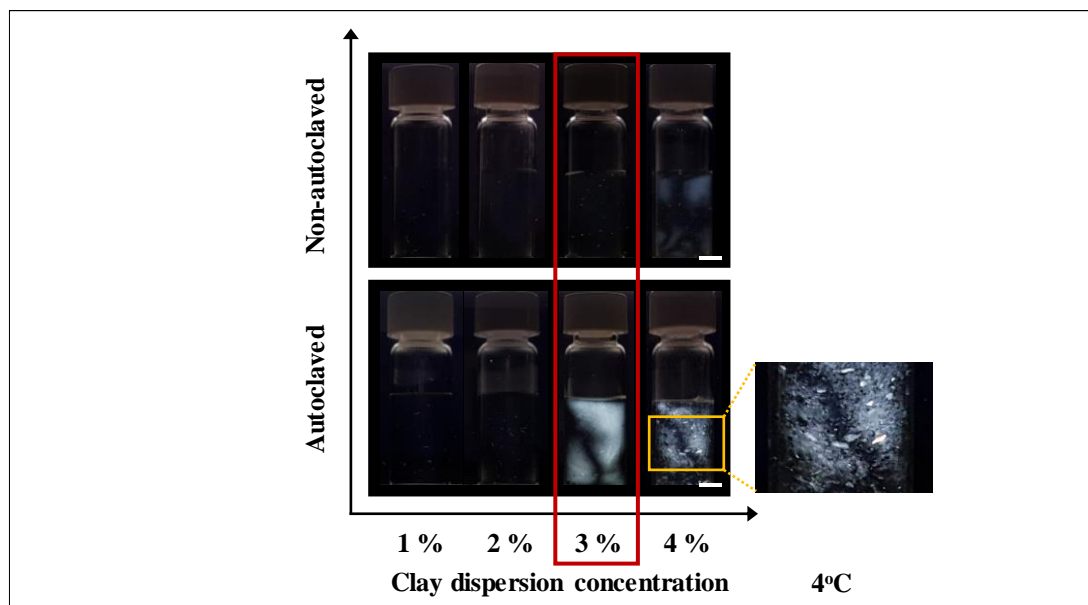


Figure 5.15 Crossed polarising images of clay dispersions presented as a function of autoclave treatment and concentration. Images are representative of triplicates and the scale bar to 5 mm.

Regarding, the 2.8 % clay-gel, it revealed similar optical properties to the 3 % displaying birefringent patches with a thread-like texture only in the autoclaved samples (Fig. 5.8 - A). In addition, the birefringence was preserved even after vigorous shearing suggesting that the periodic arrangement attained is irreversible (Fig. 5.8 - B).

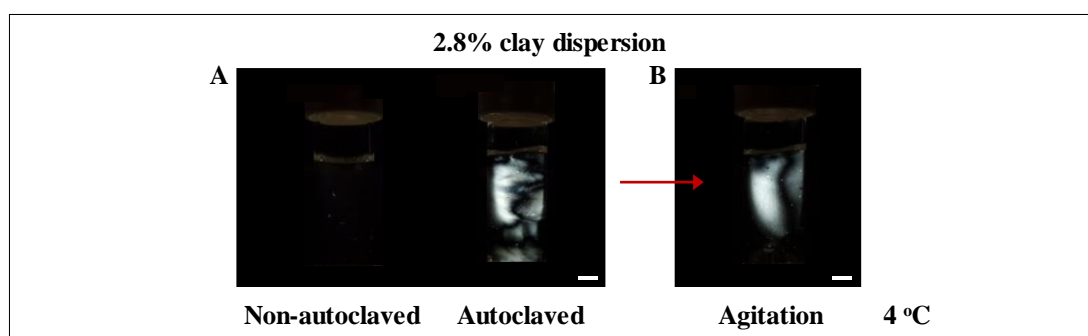


Figure 5.16 Crossed polarising images of 2.8 % clay-gel. (A) Cross-polarised light image of 2.8 % clay-gel reveals some birefringence with nematic thread-like texture after the autoclave treatment. Moreover, (B) after vigorous shearing with a vortex set to 2700 rpm for one minute, the birefringence was preserved. Images are representative of triplicates and the scale bar to 5 mm.

Next, cross-polarised light images of the same samples were taken after one month of storage to evaluate the stability of the ordered state. In this regard, it could not

observe apparent changes in the birefringence intensity and neither a phase separation of the clay dispersions suggesting that the ordered state attained is stable.

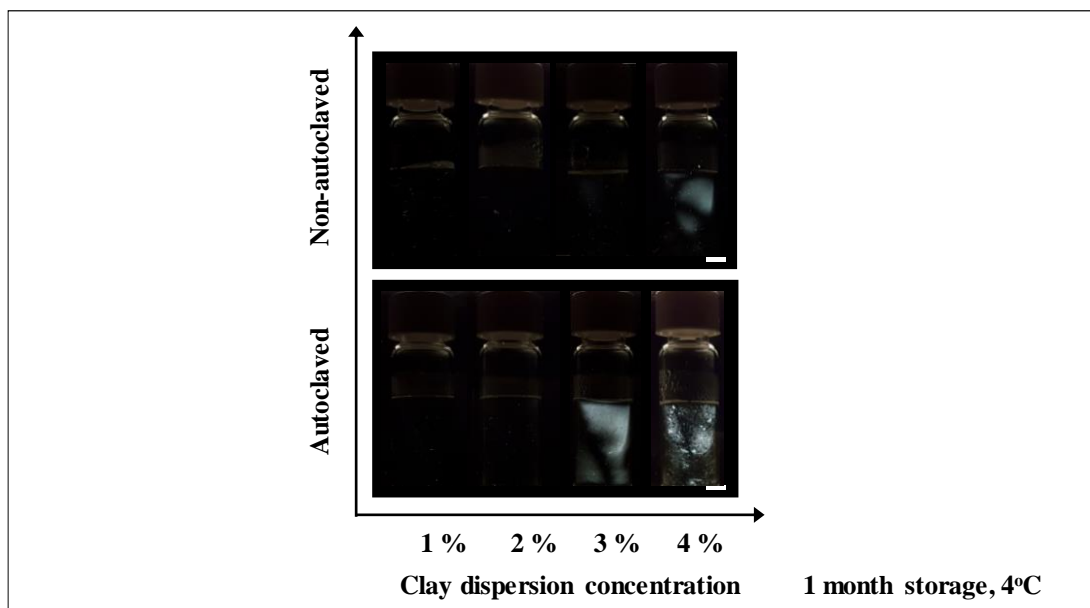


Figure 5.17 Crossed polarising images of clay dispersions after one month of storage. The images were presented as a function of autoclave treatment and concentration. Images are representative of triplicates and the scale bar to 5 mm.

These results indicate that the autoclaving step introduces some degree of order as a function of concentration, specifically, at 2.8 and 3 % clay-gel and that it is retained despite shearing and storage time (Fig. 5.16 - 5.17).

Lastly, to determine if the assembled nanoclay/protein scaffolds is strictly related to 2.8 % clay-gel autoclaved, the scaffolds were assembled with different concentration of clay dispersions, ranging from 1 % to 4 % and either autoclaved or non-autoclaved.

Stable gel formation was achieved only with concentrations above 3 % and 2 % for non-autoclaved and autoclaved clay dispersions, respectively (Fig. 5.18).

According to previous results, the 2 % clay-gel autoclaved and 3 % non-autoclaved do not display any birefringence (Fig. 5.15). However, upon diffusion of BSA molecules, radial and symmetrical birefringent patterns were apparent in both cases (Fig. 5.18). In contrast, 3% and 4% clay-gels autoclaved and 4% non-autoclaved

revealed some birefringence on the previous experiment (Fig. 5.15), and the assembled scaffolds displayed a stronger birefringence and the lambda images suggest that it is symmetrical (Fig. 5.18).

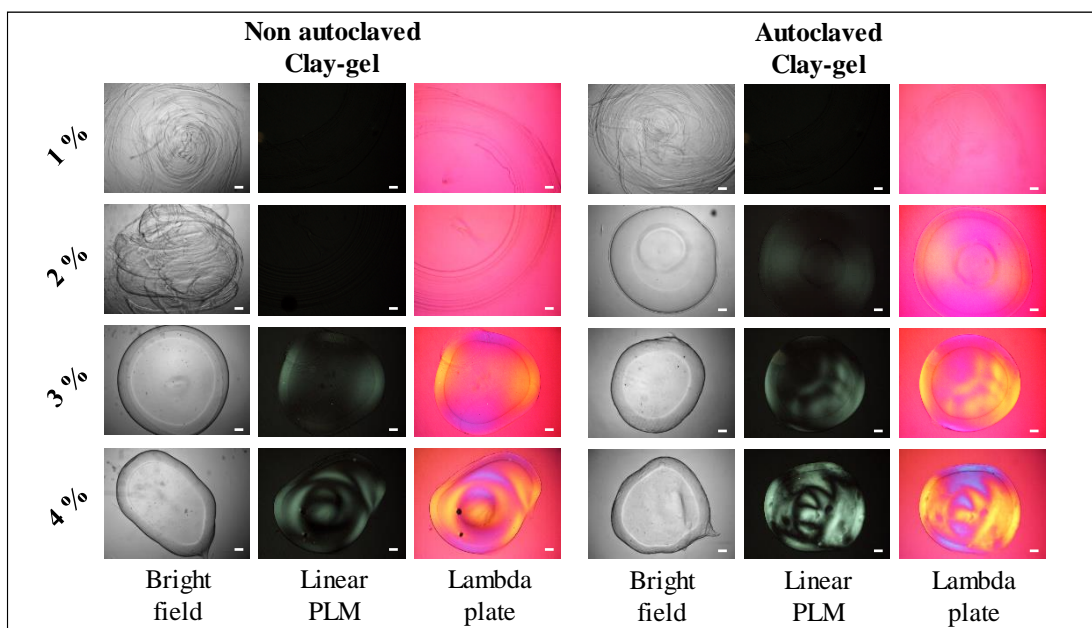


Figure 5.18 Optical analysis of 3D nanoclay/protein scaffolds assembled with different clay-gel concentrations. The polarised light images revealed some birefringence in the scaffolds assembled, which increases as a function of clay-gel concentration. The images are representative of triplicates, and the scale bar to 200 μm .

These results indicate that there are two different sources of birefringence in this system. One is intrinsic to the clay-gel, and the other is related to the diffusion of the BSA into the clay-gel. The last is consistent with a reaction-diffusion process.

5.3.2.3 Transmission Electron Microscopy

As well as the rearrangement of gelling molecules, changes in the spatial concentration of gel molecules during reaction-diffusion have also been reported (Wu et al. 2014). To evaluate such structural changes, clay-gels in their native state and assembled with BSA and DPBS were prepared for TEM imaging by standard fixation with chemical cross-linking, ethanol dehydration and embedding in epoxy resin (Fig. 5.19 - A) (methods section - 5.2.2.1).

The TEM images revealed spindle-like structures of about ~25 nm length, which corresponds to the clay nanoparticles (Laponite®) (Fig. 5.19 - B). This is consistent with the cryo-TEM images reported by (Jatav & Joshi, 2014). Qualitative analysis of the images suggests that the nanoparticles possess different spatial concentration for each treatment with a random orientation. Except for the reacted clay region of the BSA scaffolds, which nanoparticles seem to have a preferred orientation and they might be aligned following the diffusion flux of the protein (Fig. 5.19 - B3, red arrow). Moreover, it seems that the nanoparticles concentration is significantly lower in the unreacted region of the BSA scaffolds (Fig. 5.19 - B4) in contrast to the reacted region and control (DPBS and plain clay-gel). Based on this, it could be suggested that there is a depletion of nanoparticles from the unreacted region to the reacted region during the reaction-diffusion process.

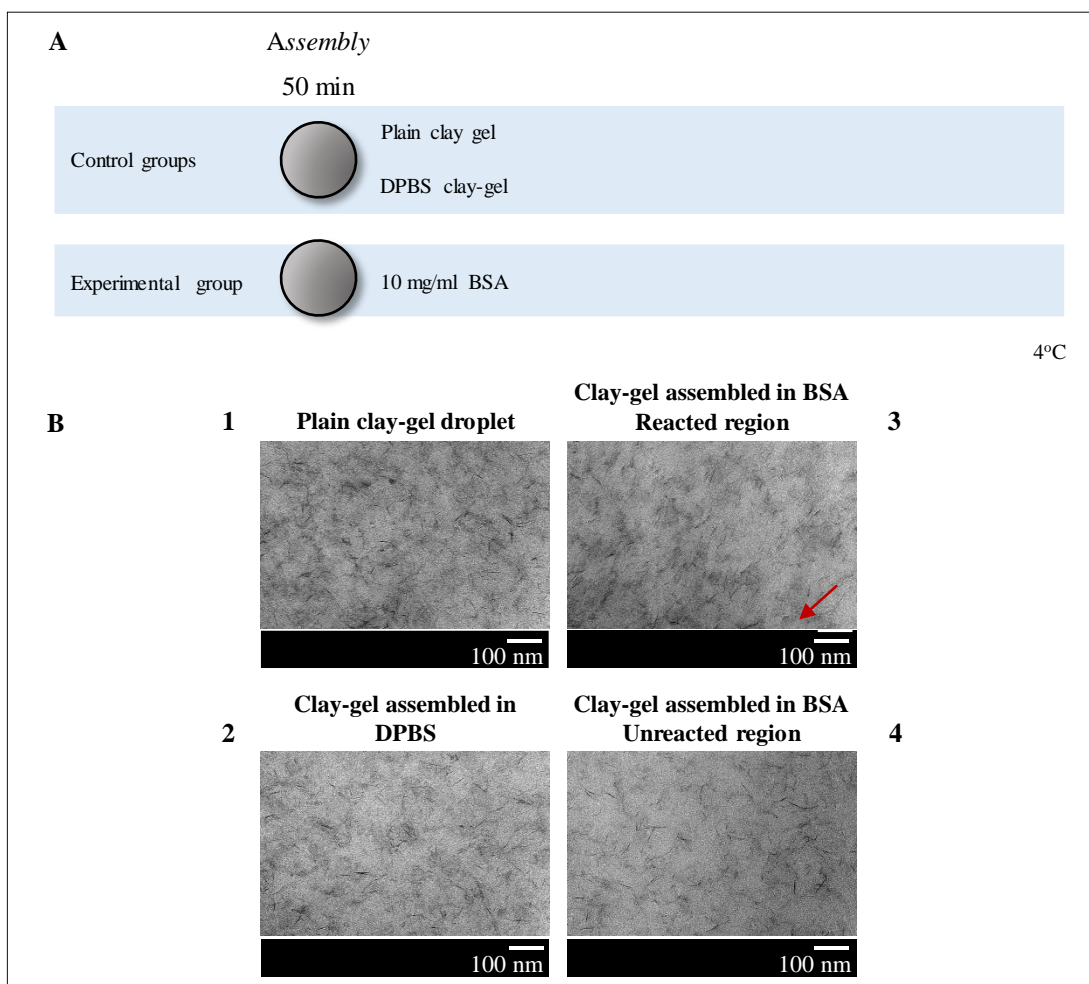


Figure 5.19 Transmission electron microscopy of nanoclay/protein scaffolds. (A) Schematic illustration of scaffolds assembled in BSA with respective controls, plain and DPBS clay-gels to evaluate their nanostructure. (B) TEM images (of x 200,000 magnification) revealed spindle-like

structures of ~25 nm length, regardless of the scaffolds' treatment, which corresponds to the clay nanoparticles. Moreover, (B1, B2 & B4) the nanoparticles seem to have a random orientation except for the reacted clay-gel region of the BSA scaffold, which seems to have some preferential orientation (B3 - red arrow). The images are representative of triplicates and the scale bars to 100 nm.

Nevertheless, it is crucial to recognise that the sample preparation for TEM imaging is harsh, which may alter the clay-gels nanostructure and respective analysis. Thus, other less or non-destructive techniques, such as SAXS, cryo-TEM or Raman spectroscopy may be useful to evaluate the distribution of clay nanoparticles concentration and their spatial orientation after the scaffold assembly.

5.3.2.4 Maximum adsorption capacity of the clay-gel droplet

As demonstrated in previous experiments, the nanoclay/protein scaffolds are assembled by a reaction-diffusion process, where the reaction is the adsorption of proteins to clay nanoparticles. This physical reaction leads to the self-assembly of a structure with a periodic arrangement.

In order to develop a preliminary model of the scaffolds' structural assembly, the adsorption capacity of clay-gels at equilibrium was measured to give an indication of the density of proteins per clay nanoparticle in the structure. For this, clay-gels were placed in a BSA solution for different incubation times. The supernatant was then analysed by absorbance to quantify the protein concentration (Fig 5.20 - A) (methods section - 4.2.2).

The results indicate that a 5 μ l clay-gel droplet can adsorb approximately 1.93 ± 0.32 mg/ml of BSA (Fig. 5.20 - B). Further comparison of the protein concentration with respective diffusion path length suggests that the maximum saturation is reached at ~3h (Fig. 4.8 & 5.20).

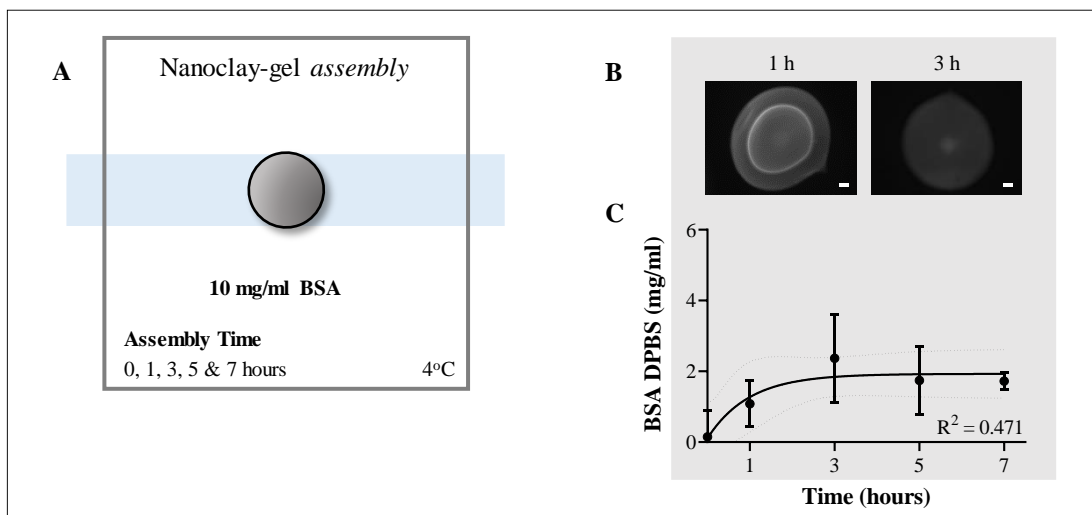


Figure 5.20 Maximum adsorption capacity of the clay-gel droplet. (A) The illustration shows the assembly of clay-gels in BSA solution for different incubation times. (C) Protein concentration analysis of supernatants indicates that the clay-gel adsorbs 1.93 ± 0.32 mg/ml BSA. Further (B) comparison with diffusion path length images suggests that the saturation is reached at ~ 3 h of incubation. Images and results are representative of triplicates and the scale bar to $200 \mu\text{m}$.

Assuming that there are 7.04×10^{17} clay nanoparticles per gram of Laponite® (calculated elsewhere, Felbeck et al. 2015), the number density of particles in 28 mg/ml droplet would be 1.97×10^{16} per cm^3 , which is equivalent to 1 particle every 50730 nm^3 (when divided by $1 \times 10^{21} \text{ nm}^3$).

Regarding the BSA, which is $66,463 \text{ g/mol}$, every $66,463$ grams of BSA contains 6.022×10^{23} (Avogadro's number) BSA molecules. Thus, in 77.12 ± 12.77 mg per ml of Laponite®, there should be $6.99 \pm 1.16 \times 10^{17}$ molecules of BSA, corresponding to approximately 34.94 ± 5.78 BSA molecules per clay nanoparticle. The last calculation is based on a volume of interest around individual clay nanoparticle of 50000 nm^3 . Also, it was assumed that the protein, BSA, formed a monolayer on individual clay nanoparticle, surface and edge, and no protein entrapment or sharing with other clay nanoparticles was considered.

5.4 Discussion

In the first and second results chapter, it was hypothesised that the scaffold assembly was the result of a reaction-diffusion process, where the BSA molecules react and diffuse into the clay-gel in a concentration dependent manner. The assembled structure facilitates the subsequent diffusion and localisation of loaded proteins into the scaffold.

An interesting feature was observed in the assembled structure, an apparent ring that colocalised with the spatial localisation of the loaded proteins. Both structures displaced together when different diffusion factors were altered at the assembly step, such as concentration, ionic strength, time and temperature (section 4.3.1). For this reason, it was assumed that this ring was the diffusion front where the loaded proteins localised as well.

This assumption has been corroborated in the current chapter. In this regard, confocal images revealed that the diffusion front generated by the assembly solution correlates with the spatial localisation of the loaded protein in the 3D micropatterned clay-gels (Fig. 5.9 - B).

Again, these findings further clarify the scaffold assembly mechanism and structural conformation. Thus, considering that the clay nanoparticles saturated with BSA molecules form a “reacted clay-gel region”, then the loaded FITC BSA would diffuse through this new structure and bind to the next available clay nanoparticles, which should be at the interface between the “reacted and unreacted clay-gel” or diffusion front (Fig. 5.9 - C). If this is correct, structural characterisation of the assembled clay-gels should reveal two different phases.

In this regard, SEM imaging analysis supports that the assembled protein/clay-gel structure may consist of both “reacted and unreacted clay-gel regions”. Interestingly, during the preparation of the sample a shell/core structure separated and the SEM images revealed that the shell or possible “reacted clay-gel region” had a porous network whereas the core or “unreacted clay-gel region” displayed a dense structure

with a texture similar to that of the controls, DPBS scaffold and native clay-gel (Fig. 5.10 - D1 & D2).

Similar results were reported by Ayarza et al. (2017), SEM images of partially gelled calcium alginate beads showed two distinct morphological regions. An outer-gelled region with a porous structure and an inner region, which has not gelled with a compact rough structure (Fig. 5.4 - B). Although it could be argued that the alginate and clay-gel structures differ significantly in term of composition, type of reaction and sample preparation for SEM imaging, the assembly mechanism is similar, a reaction-diffusion process. In this regard, the nanoclay/protein scaffolds were assembled through a physical reaction triggered by proteins-clay interaction instead of a chemical reaction between calcium ions-alginate, also, the gelator molecules are proteins, not ions.

Paradoxically, the samples preparation for conventional SEM imaging is meant to preserve their structure. The standard protocol consists of the chemical cross-linking of the sample and a controlled drying process to prevent dimensional changes. Nevertheless, alterations in the morphology are almost unavoidable, mainly due to the cross-linking process (Hafez & Kenemans, 1982 and Talbot & White, 2013). Thus, the images can provide an idea of the porosity and interconnectivity and other features, but it needs to be corroborated with other techniques. This fact must be taken into consideration during the analysis.

In this scenario, the SEM images revealed that the nanoclay/protein scaffold is constituted by two structures with distinct morphologies, a porous shell-like fragment and a dense core like-fragment. It is challenging to infer direct information about the porosity or interconnectivity percentage because the chemical cross-linking may have altered both parameters, as previously discussed. However, it is safe to conclude that the native clay-gels undergo structural changes upon diffusion of BSA molecules (Fig. 5.11).

Similar to the SEM results, the PLM imaging revealed conformational changes in the structure and the presence of two different phases. In this regard, imaging of 3D scaffolds assembled in BSA and DPBS under conventional cross-polarised light and

retardation plates revealed that both are birefringent structures. However, the birefringence pattern and intensity are different. The BSA scaffold showed a strong semicircular pattern, which suggests that the anisotropic microstructure of the scaffold possess some radial organisation. In contrast, the DPBS scaffolds displayed a lower and patchy birefringence (Fig. 5.12).

Interestingly, a similar experiment but in a 2D format revealed a strong and radial birefringence in relation to the reacted-clay region. In contrast, a low and patchy birefringence was detected in the unreacted-clay region, which was comparable to the control (Fig. 5.13).

Further comparison with pristine 2.8 % clay-gel indicates that the birefringent patches observed in the DPBS samples are from the pristine clay-gel, suggesting that the material possesses some degree of organisation prior to contact with proteins or ions (Fig. 5.14).

It is important to take into consideration that the thickness, shape and concentration of the sample affect significantly the birefringence and therefore the analysis of the acquired images. In this regard, it could be argued that the polarised light images of the samples, 2.12 mm dia. droplet, 1 mm thick 2D gels and 5 mm dia. clay-gel vials are not comparable because as it is known, the birefringence grows larger with increasing specimen thickness and as well the propagation of the direction varies with the medium. However, the result of the experimental groups and respective controls seems to be consistent regardless of the sample thickness and presentation.

Similarly, the protein in the system may contribute with the birefringence observe, since they are optically active chiral molecules, which means that polarised light interacts with the molecule so that the angle of the plane of oscillation rotates (Vitkin et al. 2002).

Further work is required to study the polarisation phenomena in more details. For this, a LC-PolScope could be used to measure the birefringence, refractive index and determine the fast and slow axis of the samples.

The metastable state of 2.8% Laponite® remains controversial (Jatav & Joshi, 2016). Some suggest that clay nanoparticle dispersions at this concentration form a nematic phase (Mourchid et al. 1995 and Gabriel et al. 1996), but others indicate that it is a gel (Jatav & Joshi, 2017) or a repulsive-glass (Jabbari-Farouji et al. 2008 and Ruzicka & Zaccarelli, 2011) and that the birefringent observed with increase in temperature is due to water evaporation so that the nanoparticles are forced to rearrange to occupy less space (Lemaire et al. 2002). This inconsistency has been related to differences in the material preparation, experimental setup and analysis technique (Barbara Ruzicka & Zaccarelli, 2011).

In this project, polarised light images of 2.8 % autoclaved clay-gel revealed a threaded texture (Fig. 5.14), suggesting that the metastable state of the material is a nematic phase similar to the results reported Mourchid et al. (1995) and Gabriel et al. (1996), where the clay-nanoparticles present some periodical arrangement with the long axes roughly parallel. However, the authors did not expose the clay nanoparticle dispersion to a temperature/pressure treatment. For this reason, an experiment was set up to evaluate if the autoclaving step and/or the concentration of the dispersion were accountable for the birefringence observed.

Qualitative analysis of non-autoclaved clay-gel showed no birefringence, except for the 4 %, which could be a fractal structure of aggregated nanoparticles stacks that did not exfoliate completely after 1 h of agitation. Regarding the autoclaved clay-gels, non-double refraction of light was detected on the 1 and 2 %. However, the 2.8 and 3 % developed an important birefringence with a smooth texture. Moreover, the birefringence texture observed in the 4 % non-autoclaved clay-gel turned from smooth to rough (Fig. 5.15). Overall, the results indicate that the autoclaving step introduced some degree of order into the clay-gel, which increased as a function of concentration.

Owing to the thermal treatment that the clay nanoparticle dispersion was subjected to; specifically, an autoclaving cycle of 121°C and 15 PSI for 30 min, the periodic rearrangement of the nanoparticles could be due to water evaporation or an ageing process that was speeded by the temperature and pressure. The latter assumption appears to correlate better with the results because after the autoclaving step some

water is added to the clay-nanoparticle dispersions to compensate for the evaporation and the birefringence is not diminished (Fig. 5.15 & 5.16).

The physical ageing of soft glassy materials, such as clay nanoparticles dispersions (Gupta et al. 2012), is the evolution towards the lowest energy state. The process is accompanied by the structural rearrangement of molecules, and below the glass transition temperature, the system may evolve through different metastable configuration within a time scale of minutes to hours or years. Nevertheless, when it is heated above the glass transition temperature, a lower energy metastable state is reached in a shorter time by fluidisation of the jammed state (Liu & Nagel, 1998, Trappe et al. 2001 and Nguyen et al. 2015). Therefore, it is hypothesised that the clay nanoparticles have experienced an unjamming transition due to the thermal treatment enabling their preferential reorientation towards a lower state of energy and more stable conformation. The final rearrangement generates the consequently birefringence observed.

Moreover, the results suggest that the autoclaving treatment of 2.8 % clay-gel leads to an irreversible ageing state. Since the material did not rejuvenate after vigorous shearing, retaining its characteristic birefringence (Fig. 5.16 - B), as reported by Shahin & Joshi, (2010). In addition, after one month of storage at 4°C, no apparent evolution was observed. The clay-gel displayed similar birefringence with no phase separation (Gupta et al. 2012) (Fig. 5.16 vs 5.17).

Regarding the nanoparticles' arrangement in the birefringent gel, a house of card organisation would conflict with the nematic ordering because the structure formed would be isotropic. This fact indirectly supports the repulsive glass organisation. Another possibility would be a new metastable configuration (Gabriel et al. 1996). Thus, further work is required to understand the phase transition, interaction and organisation of the nanoparticles in the birefringent gel. For this, different techniques, such as dynamic mechanical analysis, dynamic light scattering, PLM and SAXS may be used to study the metastable state of the material.

Until now, it has been demonstrated that 2.8 % autoclaved clay-gel possess some degree of order. Thus, an experiment was set up to determine if the assembly of the

nanoclay/protein scaffolds was related to this particular state of matter. The results revealed that the scaffold assembly is not specific to an anisotropic clay-gel since isotropic clay-gels, 2 % autoclaved and 3 % non-autoclaved did assemble as well (Fig. 5.18).

Notably, upon diffusion of BSA molecules through the isotropic clay-gels, the assembled scaffolds developed a radial birefringence characteristic of reaction-diffusion systems (Wu et al. 2014). In contrast, the anisotropic clay-gel showed stronger and semi-circular birefringent patches. Therefore, it can be concluded that there are two different sources of birefringence in this system. One is intrinsic to the clay-gel, and the other is related to the diffusion of BSA into the clay-gel.

Next, the clay-gels were imaged with TEM. Qualitative analysis of the nanoparticles distribution suggests a depletion of the nanoparticles from the unreacted region (core) to the reacted region (periphery). This phenomenon has been described to occur during the external gelation of physical gels by reaction-diffusion. For example, Leong et al. (2016) indicate that cross-linking of alginate beads by external gelation initiates at the periphery of the droplets. Thus, the particles are drawn toward the periphery to enable cross-linking. The final structure possesses a heterogeneous distribution of alginate networks, being higher at the periphery in comparison to the centre of the bead (Fig. 5.21). Similar results were reported by Wu et al. (2014), the authors observed an abrupt decrease in PBDT content in the isotropic region or core.

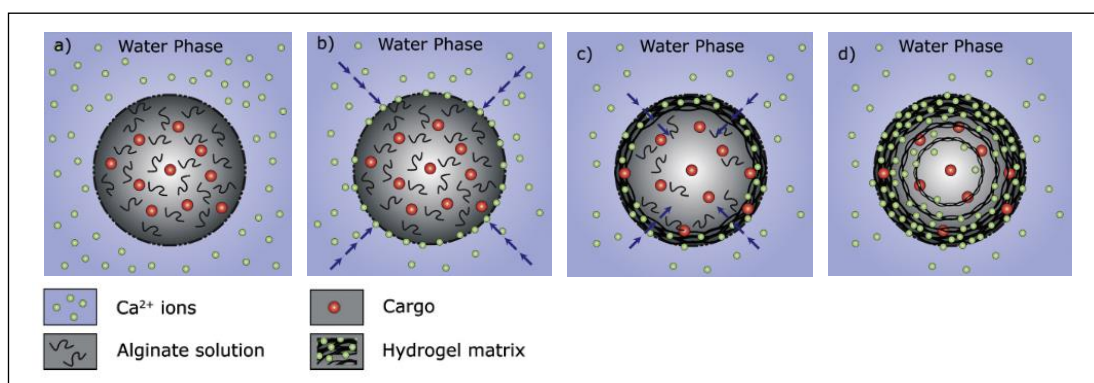


Figure 5.21 Mechanism of external gelation for bead formation. (a) Contact of the alginate droplet with a calcium solution initiates the (b) inward diffusion of calcium ions into the gel with simultaneous (c) gelation. During the process, the alginate fibres are depleted from the centre of the

bead to the periphery. (d) After the gelation is completed, the formed structure will have a heterogeneous distribution of alginate networks, which is higher at the periphery in comparison to the centre of the bead. Modified image from Leong et al. (2016).

Further qualitative analysis of the TEM images reveals a random organisation of the clay nanoparticles in the control samples and unreacted clay region (core) except for the reacted clay region (periphery), which seems to have a preferential orientation. Presumably, the clay nanoparticles are aligned following the diffusion flux of the gelator, which is characteristic of reaction-diffusion systems (Ziemecka et al. 2013).

Considering that the samples preparation may have introduced structural changes in the clay-gel (Hayat, 1981 and Park et al. 2016), other techniques, such as SAXS, atomic force microscopy (AFM), cryo-TEM, cryo-SEM, environmental-SEM or Raman spectroscopy should be considered to resolve the structure, distribution of clay nanoparticles concentration and their spatial orientation.

Until now, it has been proven that the nanoclay/protein scaffolds are assembled by a reaction-diffusion process, where the reaction is the adsorption of proteins to clay nanoparticles. This physical reaction leads to the self-assembly of a structure with a periodic arrangement. Therefore, studying the adsorption capacity of the clay-gel results valuable towards developing a preliminary model of the scaffolds' structural assembly based on the density of proteins per clay nanoparticle.

Thus, in order to evaluate the adsorption capacity of the clay-gel, a supernatant depletion assay was performed. The results indicate that 34.94 ± 5.78 BSA molecules bind per clay nanoparticle (section 5.3.2.4), which is near the estimated protein adsorbed. For this, the dimensions of the Laponite® clay nanoparticle and the BSA were considered.

Assuming that the proteins may bind to different regions of the Laponite® clay nanoparticle, the surface area of the nanoparticle surface and the edge were calculated as a total or individually. The results indicate that a nanoparticle with an average dimension of 25 nm diameter and 1 nm in height has a total surface area of 1060.29 nm^2 , and the surface and edge, 982 nm^2 and 78.29 nm^2 , respectively.

Regarding the surface area occupied by BSA, Jachimska et al. 2016 and Kubiak-Ossowska et al. 2017 evaluated by atomic force microscopy (AFM) and molecular dynamics (MD) the structure of BSA adsorbed on silica. For this purpose, the authors assumed that the BSA has a triangle shape (N form) that may interact with the silica surface with two different orientations, the triangular face facing the surface (flat-on) or standing on the rectangular edge (side-on) (Fig. 5.22 - A).

Based on the information provided by the above-described studies, the theoretical density of the proteins adsorbed onto the clay nanoparticle was estimated considering the protein orientation and the region of the clay nanoparticle they bind to. Thus, based on the AFM calculated footprint, 29 and 38 BSA molecules (flat-on or side-on, respectively) should bind to the surface & edge (1060.29 nm^2) of the clay nanoparticle, and according to MD calculations, 33 and 23 BSA molecules (flat-on or side-on, respectively) should bind (Fig. 5.22 - B & C).

A	BSA orientation Triangle shape	B		C		
		Method/BSA size [nm]	AFM (9.2 * 9.2 * 9.2 * 3.0)	MD (9.1*8.5*8.0*5.4)		
	Flat on		Flat on	Side on	Flat on	Side on
	Side on					
		Footprint of BSA [nm ²]	36.7	27.6	32.7	46.1
		Proteins per clay nanoparticle				
		Surface & edge A = 1060.29 nm ²	29	38	33	23
		Surface A = 982 nm ²	27	36	30	21
		Edge A = 78.29 nm ²	2	3	2	2

Figure 5.22 Estimated adsorbed protein per clay nanoparticle. (A) Illustration of the BSA triangle shape and different adsorbed orientation, the triangular face facing the surface (flat-on) or standing on the rectangular edge (side-on). (B) Here is presented AFM and MD data of the estimated footprint area of a single BSA adsorbed onto a silica surface with flat-on and side-on orientations (Jachimska et al. 2016 and Kubiak-Ossowska et al. 2017). (C) The theoretical density of the proteins adsorbed onto the clay nanoparticle was calculated considering the protein orientation and the region of the clay nanoparticle they bind to.

In this study, the calculated protein adsorbed by a protein depletion indicates that 34.94 ± 5.78 BSA binds per molecules, which is similar to the theoretical values

above described. Based on this information, a 3D modelling software (Vectary) was used to visualise the protein density with respect to a single clay nanoparticle and to explore their possible spatial interaction and distribution. For this purpose, 37 BSA molecules and one clay nanoparticles were drawn. Image of non-interacting protein/clay nanoparticles revealed a protein-rich environment (Fig. 5.23 - A). To model the protein/clay interaction and spatial distribution, it was taking into consideration the protein adsorption mechanisms already reported, such as electrostatic interactions and hydrophobic/hydrophilic interactions. Thus, based on the protein/clay charge, the negatively charged BSA would bind to the positively charged edges. It could also be due to hydrophobic interactions between the siloxane bridges and the hydrophobic residues of the protein exposed (Yu et al. 2013). Moreover, according to the SPB interaction, the BSA would bind to the clay nanoparticle surface and edge due to protein surface charge anisotropy (Das et al. 2016) (Fig. 5.23 - B & C).

Therefore, according to the 3D models' assumptions, the proteins bound to the clay nanoparticles edges (78.29 nm^2) look densely packed; thus, multiple layers must be formed to bind 37 BSA molecules. On the contrary, when the 37 BSA molecules are bound either at the surface + edge (1060.29 nm^2) or only the surface (982 nm^2) of the clay nanoparticle, the protein seems to form a monolayer in the most packed conformation. Thus, the last assumption correlated better with protein/clay adsorption studies, which indicates that BSA molecules bind to the surface of the clay nanoparticles despite both are negatively charged (Yu et al. 2013 and Das et al. 2016).

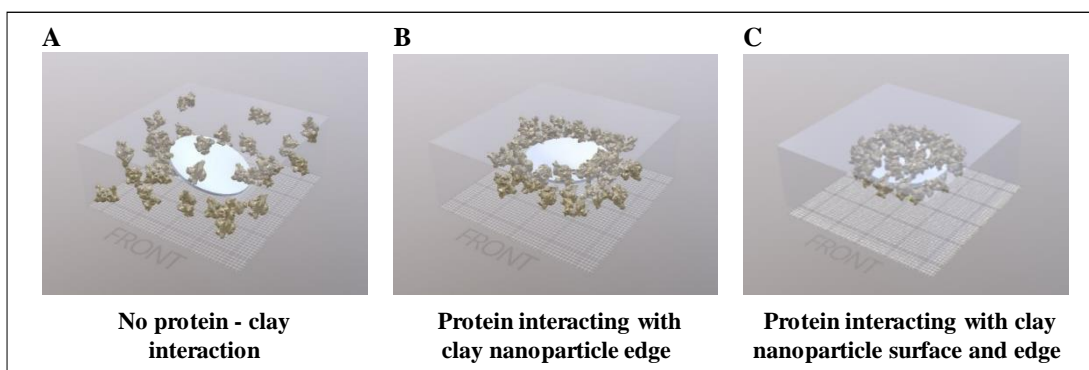


Figure 5.23 Density of proteins per clay-nanoparticles 3D models. Images displayed a $20 \times 50 \times 50 \text{ nm}$ (50000 nm^3) volume of interest around an individual clay particle with 37 molecules of BSA. (A)

The non-interaction protein images reveal a significant protein density with respect to the clay-nanoparticle. (B) The negatively charged BSA may localise at the positively charged clay-nanoparticle edge, due to electrostatic interactions, or due to hydrophobic interactions between the siloxane bridges (at the edges) and the hydrophobic residues of the protein exposed. (C) Another scenario would be that the proteins bind to the surface and edge of the clay-nanoparticles driven by electrostatic interactions with the protein surface charge anisotropy. This type of interaction is known as surface patch binding (SPB). An on-line software known as Vectary was used to produce the 3D models and the image A & B were kindly provided by Jonathan Dawson, University of Southampton.

Nevertheless, there are certain limitations about this last study that need to be acknowledged. Although the theoretical and measured values reveal some similarities, it must be to consider that the theoretical estimations were performed based on the interaction of proteins with an individual clay nanoparticle. However, in this system, the clay nanoparticles are not dispersed but interacting with each other through electrostatic interactions, either forming a gel or a glass, and this could potentially affect the protein-clay interaction.

Finally, a detailed analysis of the structural characteristics indicates that the self-assembled scaffold possessed several hierarchical levels of organisation, which is commonly observed in natural self-assembled structures, such as bone or seashells. In this regard, the Level I (nm) would be constituted by gel of clay nanoparticles aligned with the long axis roughly parallel and proteins in solution. Level II (nm), reacted clay nanoparticle saturated by protein. Level III (nm - μm), periodic arrangement of reacted clay nanoparticles aligned following the diffusion flux of the gelator. Level IV (nm - μm), nanoclay/protein scaffolds constituted by reacted and underacted clay-gel. Level V (μm - mm) punctuated regular pattern or gradual gradient of proteins within the scaffold. Level VI (cm), packed spheres of gels filling a bone gap providing a complex environment (Fig. 5.24)

Thus, the scaffold assembles not only mimic the gradients of biochemical cues but also present some hierarchical organisation, which could potentially, affect the biological activity of the structure.

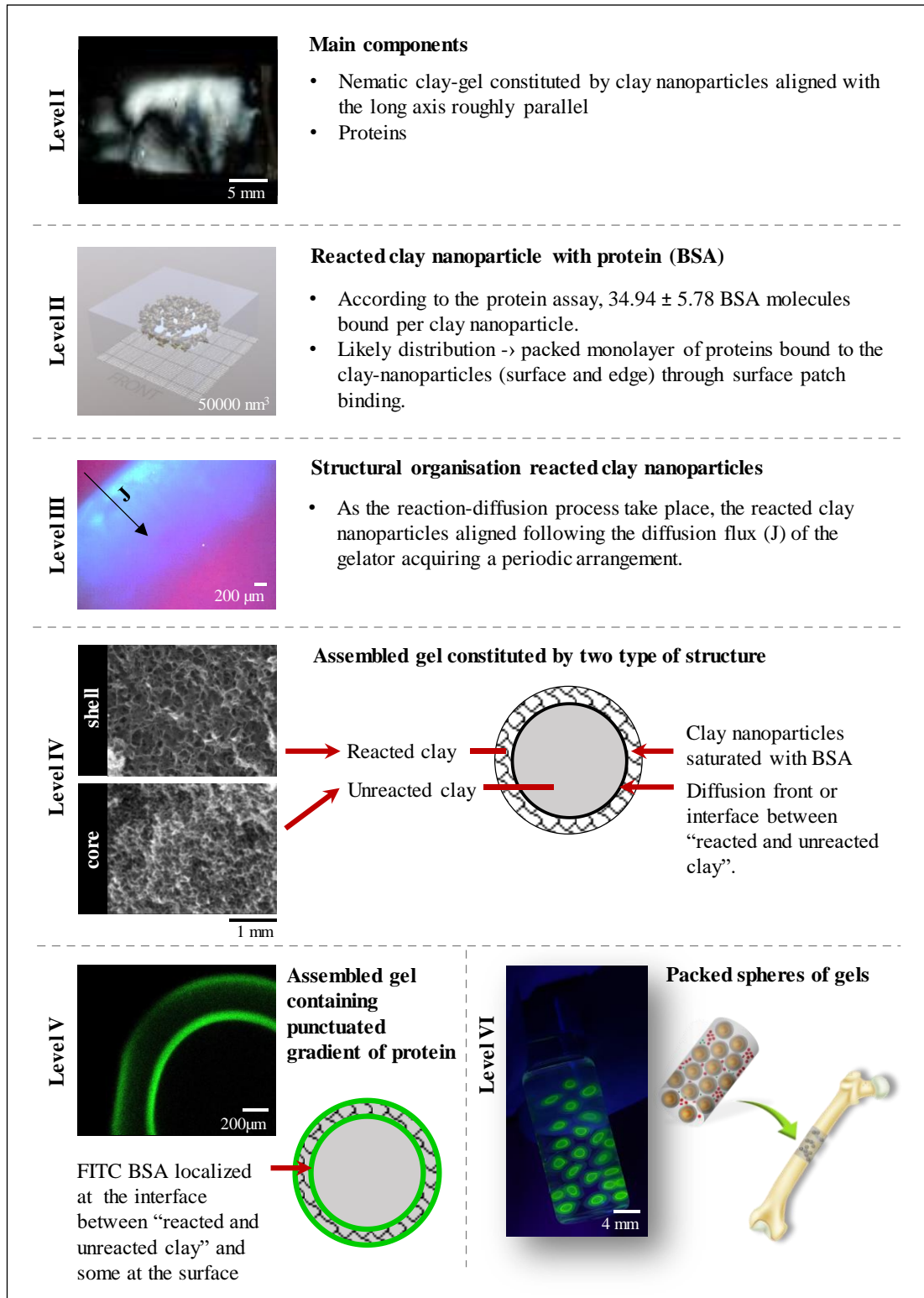


Figure 5.24 Hierarchical levels of organisation of the nanoclay/protein scaffold.

5.5 Conclusions

In this chapter, different imaging techniques, including CLSM, SEM, PLM and TEM were employed to characterise the nanoclay-protein scaffolds structure. The results provided some insights about the structural conformation at different length scales and a better understanding of the assembly mechanism.

In this regard, PLM and SEM images confirmed that a reaction-diffusion process is responsible for the scaffold assembly, where the proteins (or gelator) react with the clay nanoparticles and simultaneously diffuse through the clay-gel in a concentration dependent manner. The process leads to the formation of a protein-clay complex structure with a periodical arrangement. Furthermore, the CLSM images demonstrated that the diffusion front or the interface between the reacted and unreacted clay-gel region is responsible for the spatial localisation of loaded proteins into the clay-gel.

Regarding, the TEM study, the images suggest there is a depletion of nanoparticles from the core to the periphery of the droplet; also, that the nanoparticles in the reacted clay-gel region have some degree of order. Both observations are characteristic of physical gels assembled by reaction-diffusion. Nevertheless, further characterisation is required to confirm this and understand the nanostructure of the scaffold.

Thus, understanding the effect of different fabrication parameters (studied on the previous chapter) and the assembly mechanism (elucidated in this chapter) open new opportunities to assemble structure containing more complex gradients of proteins. In this regard, the versatility of the system was assessed in the next chapter.

**Chapter 6 EXPLORING THE
VERSATILITY AND FUNCTIONALITY
OF THE NANOCLAY/PROTEIN
SCAFFOLDS**

6.1 Introduction

During embryogenesis, gradients of signalling molecules presented as periodic patterns, instruct the specialisation of naïve cells with a determined spatial order in a concentration and time-dependent manner. Moreover, the multiplicity of signalling pathways coordinate the formation of functional organ systems (Sanz-Ezquerro et al. 2017). Part of this process has been observed during healing tissues as well. For this reason, significant efforts have been made to recapitulate the spatio-temporal signalling of molecules through delivery systems with controlled release profiles and more recently with the design of 3D micropatterned structures (Censi et al. 2012, Vermonden et al. 2012 and Shadish et al. 2019).

Thus, in this project, it has been developed a method to self-assemble scaffolds of clay nanoparticles containing 3D micropatterning of proteins to control cell fate. In previous results' chapters, the assembly and loading mechanism of the scaffold was elucidated. Hence, based on this understanding, this chapter aims to evaluate the versatility of the platform to meet specific application-based requirements, such as different sizes, shapes or protein micropattern distribution.

In this regard, the adaptation of the size is essential for the delivery route into the human body. Macroscopic hydrogels in the order of millimetres to centimetre are usually implanted surgically (e.g. bone graft) or injected to repair large defects. Moreover, micro hydrogels can be introduced as transepithelial or local injection, and when smaller than 5 μm as oral or pulmonary delivery owing to their fast clearance and enhanced penetration through tissues barriers (reviewed by Li & Mooney, 2016). Finally, nano hydrogels between 5 to 250 nm size are suitable for systemic drug administration due to their extravasation into tissues, fast cellular internalisation and clearance (reviewed by Alexis et al. 2008). Generally, the adaptation of the size goes along the geometrical shape. For example, the configuration may allow recreating complex cell microenvironments to repair large defects (e.g. 3D printed hydrogels with different grip patterns) or facilitate their pass through blood vessels or extravasation into tissues as a delivery system (e.g. liposomes or carbon nanotubes) (Agrahari, 2017).

Regarding the micropatterning of molecules, they may be presented as simultaneous positive or negative, gradual or punctuated gradients of multiple molecules during development and tissue regeneration. For example, the ventral and dorsal patterning of neural progenitors during the neural tube development is controlled not only by the spatiotemporal distribution of BMP, Wnt and Shh but also their “graded” signalling (Briscoe & Small, 2015 and Zagorski et al. 2017) (Fig. 6.1 A). In contrast, digits form from the limb bud undifferentiated cells through periodic patterns of alternated digital and interdigital fates. Studies indicate that this process is finely orchestrated by “restricted” spatio-temporal signalling of BMP-2, Sox9 and Wnt (Raspopovic et al. 2014 and Zuniga & Zeller, 2014) (Fig. 6.1 - B).

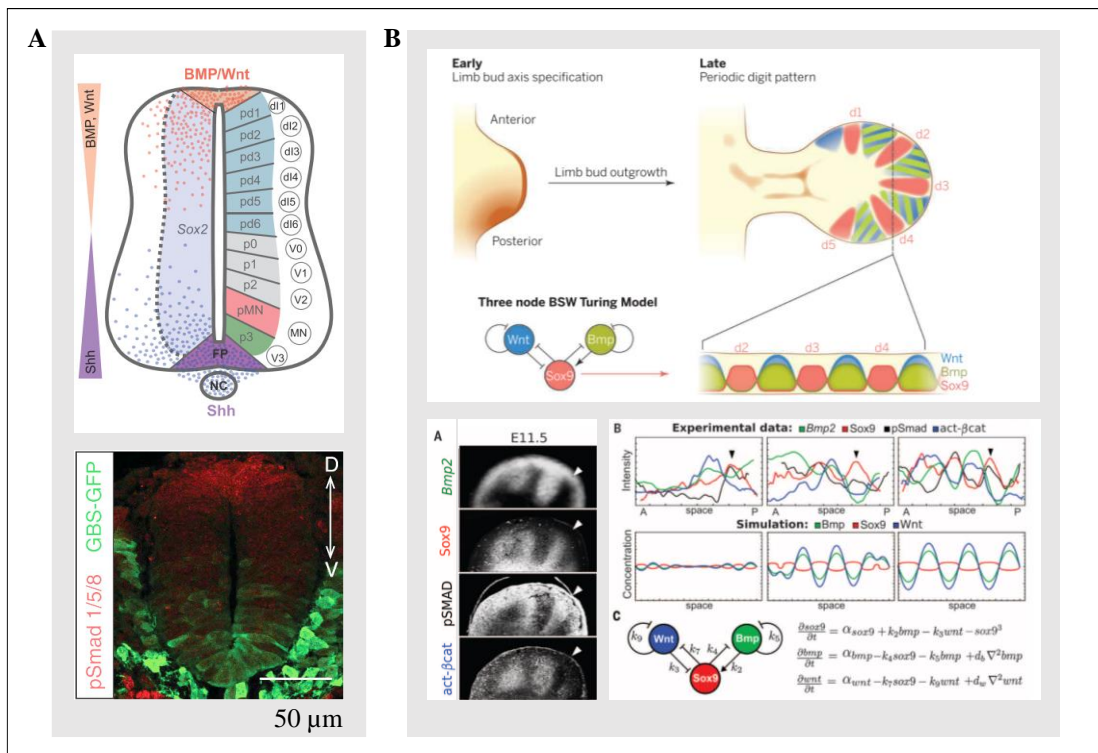


Figure 6.1 Signalling patterning during development. (A) Graded signalling patterning of BMP-2 (pSmad) and Wnt (GBS-GFP) during neural tube developments leads the patterning of neural progenitor (Briscoe & Small, 2015 and Zagorski et al. 2017) In contrast, restricted spatio-temporal patterns of BMP-2, Sox9, BMP (pSmad) and Wnt (act-βcat) signalling governs the alternated digital and interdigital fates of undifferentiated cells from the limb bud (Raspopovic et al. 2014 and Zuniga & Zeller, 2014).

Therefore, based on the understanding of the assembling and loading mechanism of the nanoclay/protein scaffold. The objectives of this chapter are to 1) evaluate the versatility of the system to generate complex protein gradients. Also, to 2) assembled

structure of a range of dimensions and sizes containing proteins patterns and finally to assess the bioactivity of the scaffold in vivo. In doing so, the hypothesis that nanoclay/protein scaffold containing 3D gradient of proteins is able to control and enhance spatio temporal bone formation.

6.2 Materials and Methods

6.2.1 Assembly of nanoclay/protein scaffolds

6.2.1.1 Assembly of nanoclay/protein scaffolds with punctuated protein patterns

To assemble the scaffolds, 5 μ l droplet of 2.8 % clay-gel were placed in 200 μ l of BSA DPBS (20 mg/ml) for 5 min and then transferred to FITC BSA-DPBS (200 μ g/ml) for 20 min to load the first protein ring. This process was repeated three more times to load a total of four rings of FITC BSA. However, the assembly time was increased by a factor of 5 min to obtain spaced rings. The whole process was performed at 4°C and analysed with CLSM (Table 6.1).

A similar procedure was used to generate a scaffold with a dual punctuated gradient of proteins by simply alternating the loading protein solutions, BSA Alexa Fluor™ 647 (BSA AF 647) and IgG Alexa Fluor™ 488 (IgG AF 488).

Table 6.1 Experimental setup to assembled nanoclay/protein scaffolds with multiple punctuate gradient of proteins. Here are described the different incubation times and concentrations of the assembly protein solutions (As), BSA DPBS (BD) and BSA water (BW). Also, for the loading solutions (Ln), FITC BSA (FB).

n = 3	Treatment							
	1		2		3		4	
# of rings	As	Ln	As	Ln	As	Ln	As	Ln
1	BD	FB						
2	BD	FB	BW	FB				
3	BD	FB	BW	FB	BW	FB		
4	BD	FB	BW	FB	BW	FB	BW	FB
Protein Concentration	20 mg/ml	200 μ g/ml	20 mg/ml	200 μ g/ml	20 mg/ml	200 μ g/ml	20 mg/ml	200 μ g/ml
Incubation Time	5 min	20 min	10 min	20 min	15 min	20 min	20 min	20 min

6.2.1.2 Assembly of nanoclay/protein scaffolds with dual gradual protein patterns

To create a nanoclay/protein scaffold containing a dual gradual gradient of proteins with overlapped positive and negative concentrations, 5 μl of 2.8 % clay-gel were placed in a concentrated BSA solution (10 mg/ml) containing 100 $\mu\text{g/ml}$ FITC BSA. Simultaneously, 600 $\mu\text{g/ml}$ of BSA AF 647 solution was fed into the assembly solution using a syringe pump. The feeding rate and volume were adjusted to control the diffusion and localisation of the proteins into the scaffold. In this regard, half and complete diffusion through the scaffold were achieved with feeding times of 50 min and 150 min, respectively. Finally, the scaffolds were stored in DPBS and imaged with CLSM (Fig. 6.2).

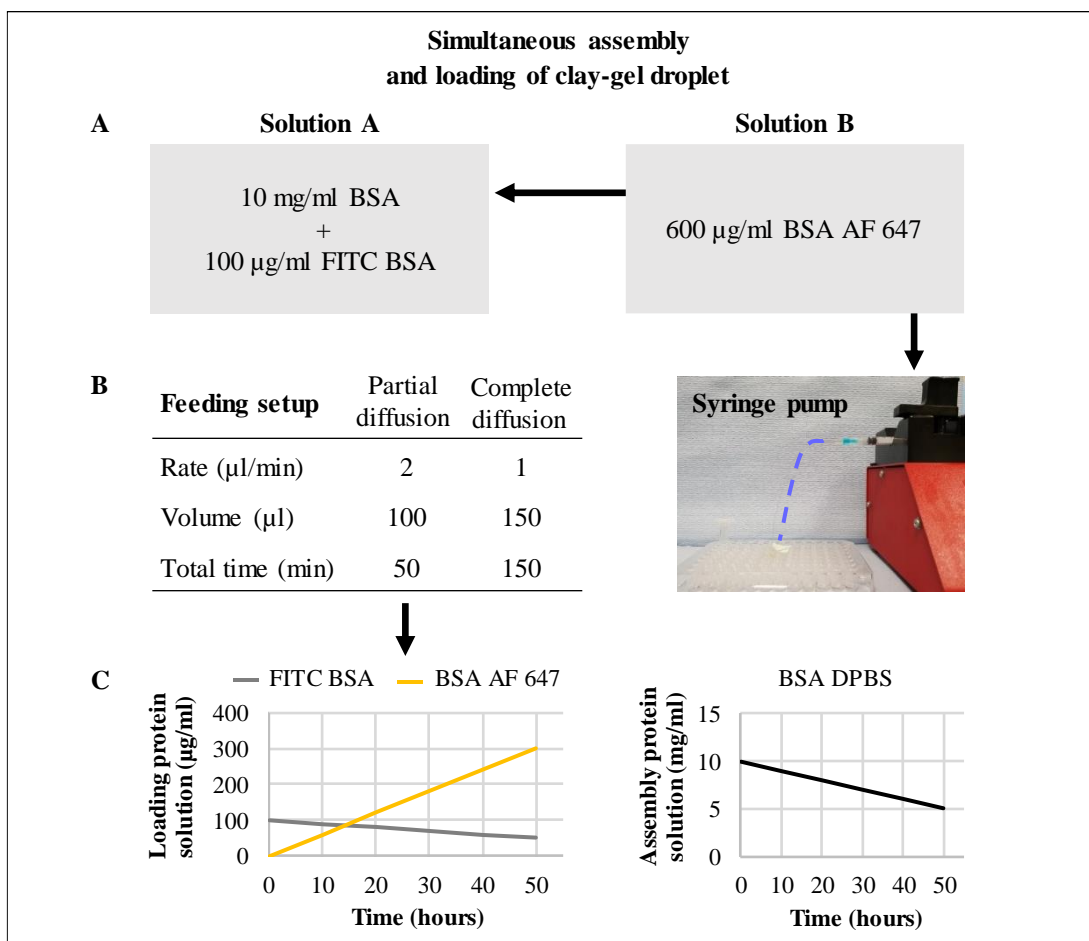


Figure 6.2 Experimental setup to assemble nanoclay/protein scaffolds with dual gradual protein patterns. (A) Clay-gel droplet was placed in the “solution A” comprising the assembly and loading solution, which was fed with a “solution B” comprising the second loading solution using a syringe pump. (B) Different feeding time was set up to control the diffusion path length to obtain scaffolds

either partial or complete diffusion. (C) Theoretical dynamic changes of the loading and assembly solutions were projected as a function of time. The graphs show overlapping positive and negative gradients of the loading solutions and a negative gradient of the assembly solution.

6.2.1.3 Functionalization of clay-gel prior to assembly

To improve the porosity and mechanical properties of the scaffolds, 2.8 % clay-gel was mixed with different polymeric solutions, type I collagen - FITC or alginate, in a polymer/clay nanoparticle ratio of 1/100. The scaffolds were assembled by placing a 5 μ l droplet of respective composites in 10 mg/ml BSA solution. After 50 min, they were transferred to 100 μ g/ml BSA AF 647 to load the protein. Finally, the scaffolds were stored in DPBS and imaged with CLSM.

6.2.1.4 Assembly of nanoclay/protein scaffolds of different size and shape

The results suggest that the original size and shape of the clay-gel is stabilised upon contact with the assembly solution. To evaluate this, a micropipette was used to assemble clay-gel droplets with different sizes by adjusting the volume dispensed. However, to make microdroplets, an atomiser spray bottle was used. Furthermore, to vary the shape, the clay-gel was dispensed into the assembly solution using a syringe to obtain clay-gel strings. Similarly, the front side of the syringe barrel was removed to assemble clay-gel cylinders.

The assembly solution used in this experiment was FCS, and the incubation time was adjusted according to the clay-gel volume used. Furthermore, the assembled scaffolds were loaded with different fluorescent proteins, and to visualise their spatial localisation they were imaged with a fluorescent microscope, a CLSM or a bench-top UV light transilluminator. For more details of the experiment setup, refer to table 6.2.

Table 6.2 Experimental setup to assembled nanoclay/protein scaffolds of different size and shape.

Clay-gel preparation				
Concentration	2.8 %			
Dispersion time	1 h - RT			
Sterilisation treatment	Autoclaving			
Storage temperature	4°C			
	Macro droplet	Micro droplet	Cylinder	Strings
Assembly				
Assembly solution concentration	60 % FCS DPBS	1.2 % FCS DPBS	100 % FCS	100 % FCS
Assembly solution volume (ml)	2	5	2	4
Clay-gel volume (µl)	5, 10, 15 & 20	1000	200 & 1000	500
Equipment to make the scaffold	Micropipette	Atomiser spray	Syringe (1 & 5ml)	Syringe (1ml)
Assembly container	6 well plate	Small petri-dish	24 well plate	Glass bottle (5ml)
Incubation temperature (°C)	4	4	4	4
Incubation time	50, 90, 130 & 170 min	10min	14 & 72hours	30min
Loading				
Loading solution concentration	100 µg/ml FITC BSA	100 µg/ml FITC BSA	100 - 250 µg/ml FITC - BSA Rho - BSA FITC - Casein FITC - Streptavidin	100 µg/ml FITC BSA
Loading solution volume (ml)	2	0.5	2	4
Temperature (°C)	4	4	4	4
Time (h)	48	1	96	1
Storage				
Solution	DPBS	DPBS	DPBS	DPBS
Volume (ml)	2	0.5 ml	2	4
Temperature (°C)	4	4	4	4
Note:	Made between 15 to 20 droplets per well	After assembly and loading steps, the microdroplets were recovered with a micro-centrifuge (10 min 4°C - 1.3 rcf)	The front side of the barrel was removed to make the scaffold	

6.2.2 Biological activity assessment of nanoclay/protein scaffolds

Prior to implantation of the scaffold in the subcutaneous mouse model, different fabrication parameters were assessed, including the assembly, rinsing, loading and bioactivity of the protein to be loaded. Also, the delivery system to maintain the integrity of the scaffolds during the in vivo experiment. Next, some of the procedures used are described.

6.2.2.1 *ELISA*

A human BMP ELISA kit from R&D system was used to quantify the BMP-2 adsorbed by the nanoclay/protein scaffold after 1 and 3 hours of incubation in 50 µg/ml BMP-2. First, all the reagent and samples were brought to room temperature and prepared as described next.

1. The wash buffer was diluted 4 times with deionised water. The prepared volume was enough to do eight washes.
2. The substrate solution was prepared by mixing the reagent A and B in equal volumes within 15 min before use. The volume was calculated according to the numbers of well used.
3. The calibrator diluent RD5P was diluted in a 1:10 ratio with deionised water within 15 min before use. This solution was then used to dilute down the standards and samples.
4. The BMP-2 standard dilutions were prepared using the BMP-2 Infuse™ from Medtronic and the calibrator diluent RD5P in polypropylene tubes.

Table 6.3 BMP-2 Infuse™ standards dilutions.

Serial dilution (pg/ml)	4000	2000	1000	500	250	125	62.5	0
BMP-2 stock (20,000pg/ml)	1ml ->	500 ->	500 ->	500 ->	500 ->	500 ->	500 ->	x
Diluent RD5P		500	500	500	500	500	500	500

5. The samples were diluted with the calibrator diluent RD5P to concentrations enough to fit inside the standard curve.

Next, the standards and samples were assayed in duplicates. For this, 100 µl of Assay Diluent RD1-19 were added to each well and then 50 µl of the standards and samples. The reaction was covered and left to incubate for 2 h at room temperature on the orbital shaker. Then, the wells were aspirated and washed with 400 µl of diluted wash buffer four times. Next, 200 µl of BMP-2 conjugate was added to each well, covered it again and left to incubate for 2 h at room temperature on the orbital shaker. Then, repeated the aspiration and washing step and proceeded to add 200 µl

of the substrate solution to each well and left to incubate for 30 min at room temperature on the bench-top protected from the light. Finally, added 50 μ l of the stop solution to each well and the optical density of the reaction was measured using a microplate reader set to 450 nm.

6.2.2.2 *Bioactivity assay*

To evaluate the bioactivity of the BMP-2 (InfuseTM), C2C12 cells or immortalised mouse myoblast cell line were seeded in 24 well plates with a density of 10^5 per well. They were cultured with DMEM containing 2 % FCS and 1 % Penicillin-Streptomycin solution at 37°C, 5 % CO₂ for 24 h. Then, the culture media was refreshed with media containing different dilutions of BMP-2 (0, 100, 200, 400 and 800 ng/ml) and cultured the cells over 72 h.

Finally, at day 3, proceeded to do an alkaline phosphatase (ALP) staining, which is a highly expressed enzyme in C2C12 myoblast when differentiates into osteoblastic lineage. For this, the cells were washed with DPBS and fixed with 95 % ethanol for 10 min. Then, the ethanol was removed, washed with DPBS and left to dry. Freshly prepared ALP staining solution, 19.2 ml deionised water containing 800 μ l Naphthol AS MX (Sigma Aldrich) and 0.0048 g Fast Violet salt (Sigma Aldrich) was added to each well and incubated at 37°C for up to 60 min, checking the colour change every 10 min.

6.2.2.3 *3D printed holders*

In order to maintain the integrity of the scaffold, a holder of polylactic acid (PLA) (Ultimaker) was made. For this purpose, the extrusion printer Ultimaker 3 extended was used and respective Ultimaker Cure software to design it. The holder frame was ~1 mm thickness and had a cylindrical shape with eight posts. The final internal dimension was ~6x6 mm, enough space to fit the scaffold.

The printed structures were then refined. Four posts out of eight were removed and the sharp edges were smoothed with a scalpel and sandpaper. Finally, they were sterilised with an antibiotic/antimycotic solution (AB/AM) (Sigma Aldrich). For this,

they were incubated in 10X AB/AM - DPBS solution for 1 h. Next, they were incubated in 1X AB/AM - DPBS and DPBS solutions for 24 hours, respectively. Note that the incubations were performed at 4°C to maintain the bioactivity of the reagent and on a rocker to increase the perfusion of the solutions throughout the holder.

6.2.2.4 *Subcutaneous mouse model*

The animal study was conducted in compliance with ethical approval, obtained under project licence PPL P96B16FBD, and the Biomedical Research Facility of the University of Southampton provided the animals and facilities to perform the study. Thus, F1 hybrid mice male were anaesthetized with an intraperitoneal injection of buprenorphine solution, Buprenodale® multidose 0.3 mg/ml solution (Dechra). A midline dorsal incision was made. Then, two clay-gel cylinders inside respective PLA holders were implanted on each side and wounds closed with 5-0 suture PDS™ 45 cm (Ethicon). The total number of mice used for this preliminary study were two, carrying scaffolds loaded or not with BMP-2.

The micro CT scans were performed using Brunker Skyscan 1176 at day 1 and 30. For this, the mice were anaesthetized with isoflurane each time. Finally, the images were reconstructed using NRecon, and analysed using CTAn software.

To retrieve the samples, the mice were euthanized by carbon dioxide followed by cervical dislocation to assure depth.

6.2.2.5 *Histology*

Retrieved samples were fixed with 4 % formaldehyde (ACROS organics™), which was refreshed after 1 h and left for 2 more days at 4°C on the rocker. The fixed samples underwent decalcification in 5 % EDTA (Fisher) - 0.1 M Tris (Sigma Aldrich) solution with a pH of 7.3 for 3 days at room temperature on a rocker. They were then dehydrated with different ethanol dilutions (50, 70, 90 & 100%) followed by 100 % HistoClear® (National Diagnostics™), embedded in wax (2 h - 72°C), sectioned at 10 µm thickness and placed over a coverslip. Finally, the sections were

dewaxed using HistoClear® and ethanol, and stained with alcian blue/sirius red to visualise the presence of sulphated glycosaminoglycans and collagen within the constructs. Briefly, the sections were stained with freshly prepared Weigert's Haematoxylin solution (Clin-Tech limited) for 10 min followed with Eosin (Clin-Tech limited) for 2 - 4 min, but after washing them with water and dipping 3 times in 1 % HCL - 70 % ethanol solution. Next, they were stained in 0.5 % alcian blue (ACROS organics™) for 10 min, treated with freshly prepared 1% molybdophosphoric acid (ACROS organics™) for 20 min and stained with 0.3 % sirius red (Sigma Aldrich) for 1 h.

Finally, the stained sections were dehydrated, mounted in p-xylene bis-pyridinium bromide (DPX) (Fisher) and observed under an Olympus dotSlide Virtual Microscopy System (microscope frame BX51) with attached Olympus CC12 microscope camera at 20X magnification by using Olympus OlyVIA software.

6.3 Results

6.3.1 Assembly of nanoclay/protein scaffolds with multiple protein patterns

Previous results demonstrate that the structured clay-gel scaffolds are assembled through a reaction-diffusion process. In this regard, a concentrated protein solution (assembly solution) diffuses into the clay-gel, which progressively react and saturate the clay nanoparticles. Then, later addition of no concentrated protein solution (loading solution) diffuses through the restructured gel and localise in the diffusion front where the interface between the reacted and unreacted clay nanoparticles is. The result is the formation of the protein pattern; in this case, a single fluorescent ring inside the clay-gel.

Thus, if this assembly mechanism is correct, it should be able to create multiple protein patterns inside the clay-gel by displacing the diffusion front with the assembly solution to allow the loading of more proteins in the new reacted-unreacted clay interface (Fig 6.3 - A). To test this hypothesis, sequential assembly and loading steps were repeated four times to assemble the scaffolds (Fig 6.3 - B). The concentration of the protein solutions and incubation times were adjusted to control the formation and localisation of the new diffusion fronts as described in the methods section - 6.2.1.1.

The confocal images reveal the progressive formation of four fluorescent rings towards the clay-gel core as a function of the treatment cycles. Interestingly, it seems that earlier loaded protein on reacted/unreacted clay interface is not disturbed by the secondary diffusion waves involved in the assembly process (Fig 6.3 - C).

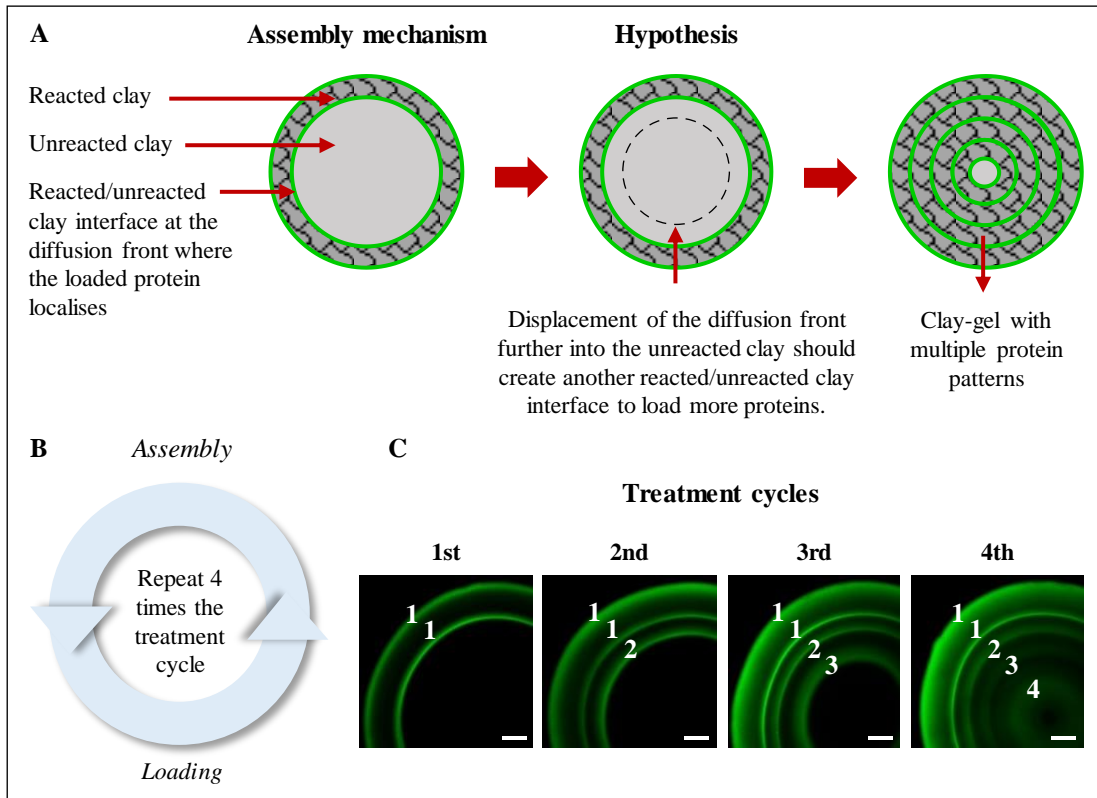


Figure 6.3 Assembly of nanoclay/protein scaffolds with a punctuated concentration of protein gradients. (A) Schematic illustration with a hypothesis to generate multiple protein patterns inside the clay-gel based on the scaffold assembly mechanism, also (B) respective protocol to test the hypothesis. (C) The confocal images reveal the formation of punctuated concentration of protein gradients in the scaffolds. The images represent $n = 3$ and the scale bar to 200 μm .

The results serve to add further confirmation of the proposed assembly mechanism and validates the hypothesis above stated regarding the multiple protein pattern formation. To conclude, it is possible to create punctuated concentration gradients of proteins in the scaffolds by simply alternating the assembly and loading step, controlling the concentration of the protein solutions and the scaffolds incubation time.

It is known that concentration gradients of different morphogens or bioactive molecule are found during bone development and repair, such as BMP-2 and VEGF. Thus, to mimic this dual signalling, the scaffolds were assembled and loaded with two different model proteins, BSA AF 647 and IgG AF 488

The confocal images reveal the formation of alternated fluorescent rings corresponding to BSA (red ring) and IgG (green ring) inside the clay-gel as a function of the treatment cycle (Fig. 6.4).

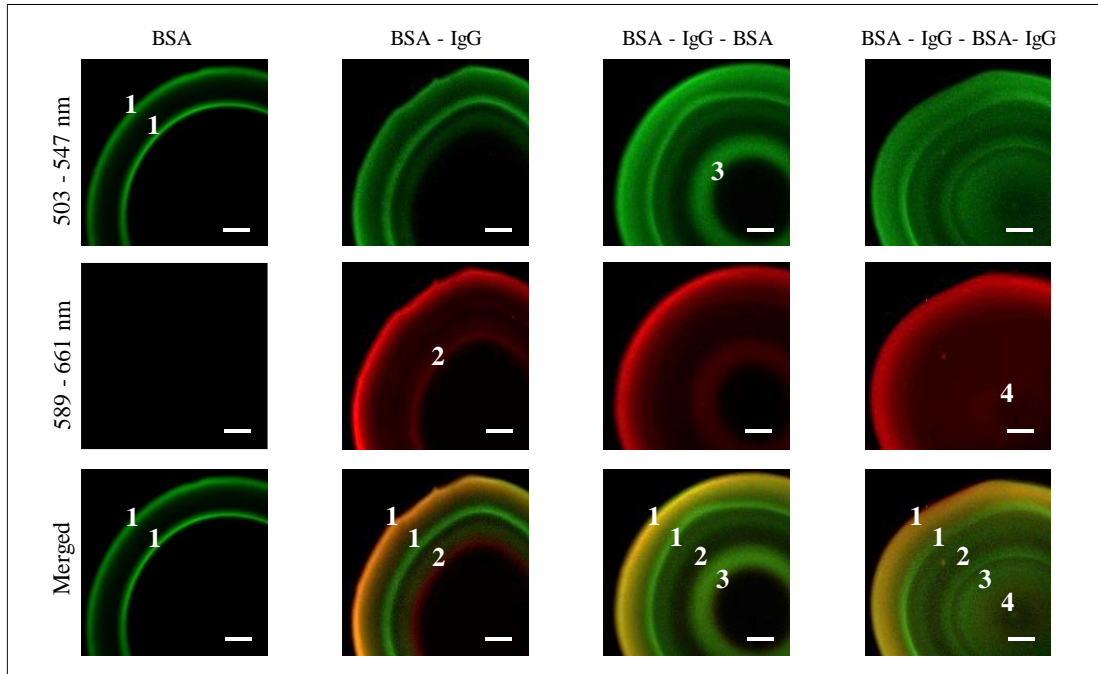


Figure 6.4 Assembly of nanoclay/protein scaffolds with a punctuated concentration of protein gradients. The confocal images reveal the punctuated concentration gradients of BSA (red ring) and IgG (green ring) in the clay-gel scaffolds. The images represent $n = 3$ and the scale bar to $200 \mu\text{m}$.

The results are promising since they demonstrated understanding and control over the scaffold assembly. In this regard, the versatile fabrication system allows the design and manufacture of different proteins gradients inside the clay-gel. Moreover, the 3D localisation of the patterned proteins does not seem to be affected by secondary diffusion waves, which is essential to maintain local protein concentrations.

Morphogens are presented in the form of 3D gradients. Nevertheless, it is still not known their distribution during bone formation or regeneration, is it punctual or gradual? Is the concentration positive or negative? In the next experiments, the possibility to generate different protein gradient patterning was explored.

When studying the assembly mechanism of the clay-gel scaffolds in the previous results chapter (5.3.1), a gradual diffusion of concentrated BSA spiked with FITC

BSA into the clay-gel was observed, and based on this observation, next experiment was set up to assemble scaffolds holding a dual but gradual gradient of proteins with overlapped positive and negative concentration profiles. For this, the assembly and loading steps were combined, and dynamic but linear changes in the concentration of the different protein solutions were introduced as a function of time using a syringe pump. Further details of the experiment can be found in the methods section - 6.2.1.2.

The confocal images reveal a gradual diffusion of FITC BSA (green gradient) and BSA AF 647 (red gradient) inside the clay-gel scaffolds (Fig. 6.5). Further analysis demonstrates the intersection of both positive and negative protein gradients (Fig. 6.5 - graph).

Moreover, changes in the assembly time led to partial or complete diffusion of the dual protein gradients in the clay-gel (Fig. 6.5 - A vs B).

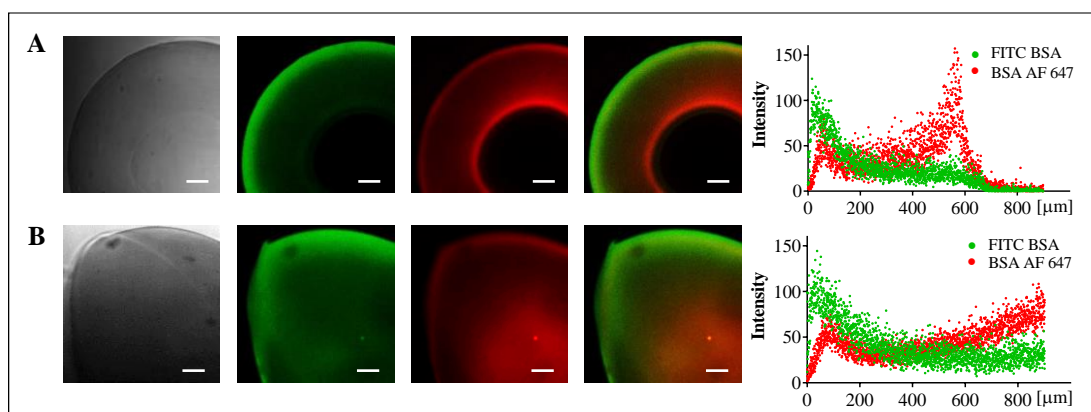


Figure 6.5 Assembly of nanoclay/protein scaffolds with a gradual concentration of protein gradients. The confocal images and respective intensity profile graph revealed a gradual diffusion of FITC BSA (green gradient) and BSA AF 647 (red gradient) inside the clay-gels. (A vs B) Changes in assembly time allowed generating gradients with different magnitude and steepness. The images represent $n = 3$ and the scale bar to 200 μm .

This approach demonstrated that it is possible to generate a dual gradual gradient of proteins in a 3D clay-gel through a simple and controlled reaction-diffusion process.

6.3.2 Scalable and mouldable clay-gels

The design and synthesis of biomimetic gels not only involves mimicking tissues composition, nano and microstructure, mechanical properties or functionality. Significant attention must be paid to the gel dimensions and shapes as well. In this regard, the possibility to scale up the 3D micropatterned clay-gels and to vary their shape was explored.

Scaling up the scaffold implies using higher volumes of clay-gel, which would then require increasing the concentrations of the protein solution and adjusting the assembly time. Regarding the scaffold shape, it seems that the clay-gel maintains its original shape upon contact with the assembly solution, either containing proteins or ions. Therefore, it should be possible to pre-shape the clay-gel with a mould before the assembly step.

Thus, the next experiments were set up to evaluate the clay-gel versatility to assemble structures of different dimensions and shapes. In this regard, clay-gel macro and microdroplets, cylinders and strings were assembled using different equipment to mould them, such as a micropipette, an atomiser spray bottle or a syringe. Further details of the experiment can be found in the methods section - 6.2.1.4.

Qualitative analysis of the fluorescent images indicates that it is possible to assemble clay-gel droplets of 5 to 20 μ l without altering the protein pattern distribution and micro-resolution. Also, the assembly of microdroplets with FITC BSA localised in the core (Fig. 6.6 - A & B).

Furthermore, clay-gel cylinders of \sim 0.4 mm dia. by 1.2 mm thick and 1 cm dia. by 0.9 cm thick were assembled and loaded with different model proteins. Specifically, FITC BSA, tetramethylrhodamine isothiocyanate BSA (TRITC BSA), FITC casein and FITC streptavidin. Transversal cross-section of the clay-gel cylinders exposed the protein pattern distribution, which would correspond with the previous results (Fig. 6.6 - C, D, E, F & G), demonstrating that neither the size nor the shape alters the assembly and protein loading process.

Moreover, a butterfly-like protein pattern was observed in clay-gels cylinders that had partial transversal cuts at the beginning of the assembly process. This indicates that introducing defects in the clay-gel alters the protein pattern distribution (Fig. 6.6 - H). Finally, the results revealed that the assembly of clay-gel strings with internal protein patterns was possible (Fig. 6.6 - I).

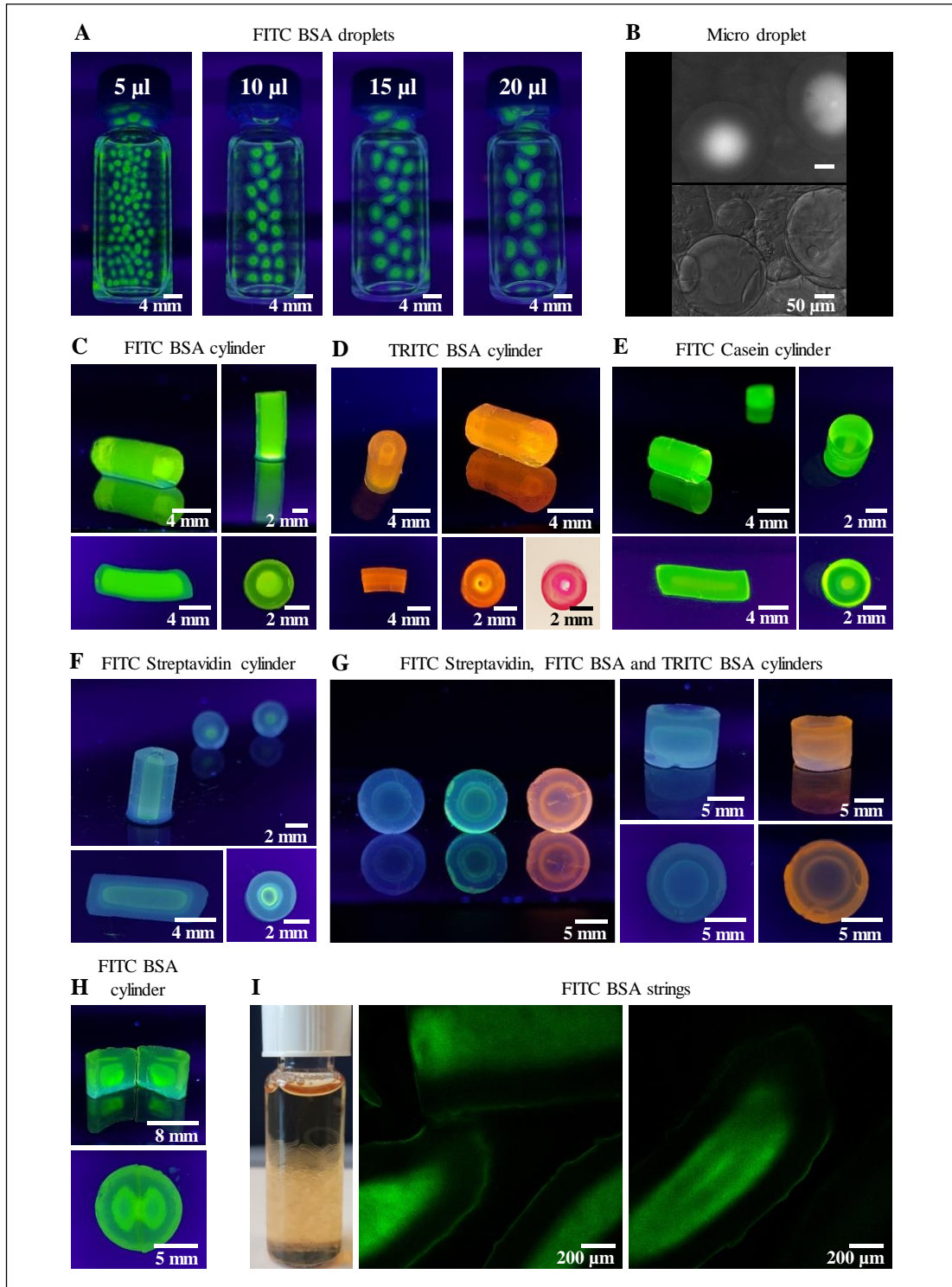


Figure 6.6 Assembly of nanoclay/protein scaffolds of different size and shape. (A) Droplets assembled with different volumes of clay-gel, from 5 to 20 μ l and loaded with FITC BSA. (B) Clay-gel microdroplets loaded with FITC BSA. Clay-gel cylinders of 200 μ l loaded with (C) FITC BSA, (D) TRITC BSA, (E) FITC casein and (F) FITC streptavidin. (G) Clay-gel cylinders of 1 mm loaded with FITC streptavidin, FITC BSA and TRITC BSA (from left to right). (H) Clay-gel cylinder with butterfly FITC BSA pattern. (I) Clay-gel strings loaded with FITC BSA.

Again, the versatility of the clay-gel and the fabrication method developed allows the assembly of scaffolds with different size and shape. More importantly, the micro-resolution of the protein pattern is not lost regardless of the dimensional changes introduced. Overall, the scalable and mouldable properties of the clay-gels open new opportunities to build customised structures for numerous applications.

6.3.3 Functionalization of clay-gel prior to assembly

Previous experiments indicate that the minimum density of clay nanoparticles required to assemble the nanoclay/protein scaffold is approximately 2 % (Fig. 5.18) suggesting that any excess of unreacted clay nanoparticles is not vital. Therefore, it was hypothesised that clay-gels with a concentration above 2 %, and which excess of clay nanoparticles are reacted can still assemble 3D patterned scaffolds. To evaluate this, 2.8 % clay-gels were mixed with type I collagen - FITC and alginate in a ratio of 1/100 prior to the assembly process. Then, the scaffolds were loaded with BSA AF 647 and imaged with CLSM (methods section - 6.2.1.3).

The confocal images reveal the formation of a fluorescent ring inside the clay-gel droplets regardless of the initial clay-gel treatment with collagen or alginate (Fig. 6.7).

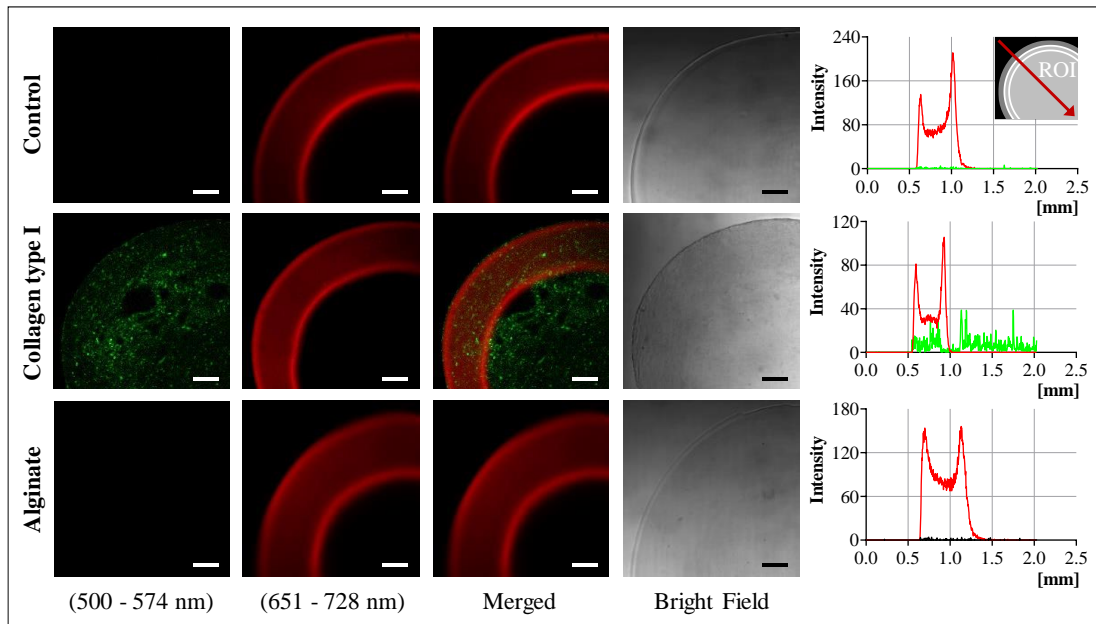


Figure 6.7 Assembly of nanoclay/protein scaffolds with functionalized clay-gel. The confocal images reveal the diffusion and localisation of BSA (labelled with Alexa Fluor 647) inside the scaffolds that were assembled with 2.8 % clay-gel containing type I collagen (labelled with FITC) or alginate. The images represent $n = 4$ and the scale bar to 200 μm .

These results raise the possibility to improve not only the bioactivity of the scaffold but to tune its porosity and mechanical properties with the addition of natural or synthetic polymers. Future work is needed to characterise these newly assembled structures.

6.3.4 Biological activity of nanoclay/protein scaffolds

Note that previous studies have demonstrated the biocompatibility and bioactivity of human bone marrow stem cells to clay-gels in 2D and 3D format containing growth factors, such as BMP-2 and VEGF (Gibbs et al. 2016, Shi et al. 2018 and Page et al. 2019). However, none of them reports cells invasion, which could be related to the viscosity and porosity of the gel. Conversely, different *in vivo* studies have shown cell invasion and migration, and bone and blood vessels growth within clay-gels containing either BMP-2 or VEGF (Dawson & Oreffo, 2013 and Page et al. 2019). In this regard, cells invasion seems crucial to demonstrate the bioactivity of 3D patterned nanoclay/protein scaffolds, therefore, an *in vivo* study appears appropriate.

Thus, to evaluate the bioactivity of nanoclay/protein scaffolds loaded with BMP-2 towards bone formation, the scaffolds were implanted in a subcutaneous mouse model. However, before this, different fabrication parameters of the scaffolds were assessed, including the assembly, loading, rinsing and bioactivity of the protein to be loaded. Also, a delivery system to maintain the integrity of the scaffolds during the in vivo study was reviewed.

6.3.4.1 *Assembly*

In this preliminary experiment, a clay-gel cylinder of 5x5 mm was assembled. For this purpose, 100 μ l of 2.8 % clay-gel was dispensed in 2 ml of 40 mg/ml BSA-DPBS using a 1 ml syringe, which front side of the barrel was removed. However, since the incubation time to generate a protein pattern inside this large structure is unknown, the next experiment was set up to assemble clay-gel cylinders for 3, 6 and 24 h and load them with 100 μ g/ml FITC BSA for 1 h. Finally, to visualise the spatial localisation the protein within the gel, a bench-top UV light transilluminator was used. The results indicated that after 6 hours, the scaffold was almost saturated as the protein pattern was right in the core. In this regard, it seems that the adequate assembly time is 3 h, as the protein pattern localised at \sim 1.3 mm from the scaffold's surface, which possesses \sim 5 mm in diameter (Fig. 6.8 - A).

6.3.4.2 *Rinsing*

To remove the excess of the assembly solution (BSA-DPBS), the scaffolds were transferred to 2 ml of DPBS and rinsed with an orbital shaker at 100 rpm - 4°C. The solution was refreshed a few times until no protein was detected by the protein assay. The results indicate that it takes \sim 19 h of continuous rinsing with 3 solution refreshment to remove the excess of protein from the scaffold (details of the protein assay can be found in the main methods - 4.2.2) (Fig. 6.8 - B).

6.3.4.3 *Loading*

Gibbs et al. 2016 demonstrated that delivery of 40 to 500 ng/ml BMP-2 with Laponite® clay-gel in a subcutaneous mouse model is sufficient to trigger bone

formation. In this regard, the scaffolds in this preliminary study should be loaded with ~0.5 to 1 $\mu\text{g/ml}$ of BMP-2. However, the incubation time necessary to load this amount of protein is unknown. Thus, to evaluate this, clay-gel cylinders were assembled, rinsed and transferred to 10 and 50 $\mu\text{g/ml}$ FITC BSA for 3, 6 and 24 h at 4°C to load the protein. Finally, the protein absorbed was measured with a fluorometric protein assay.

The results indicate that the scaffolds incubated in 10 $\mu\text{g/ml}$ FITC BSA absorbed 1.16 ± 0.03 $\mu\text{g/ml}$ at 26 h. However, the process is significantly slower in comparison to the scaffolds incubated in 50 $\mu\text{g/ml}$ FITC BSA, which absorbed 1.41 ± 0.33 $\mu\text{g/ml}$ at 3 h. For this reason, in the next experiment, 50 $\mu\text{g/ml}$ BMP-2 Infuse™ solution (Medtronic) was used to load the scaffold, and the amount of protein absorbed was measured at 1 h and 3 h (Fig. 6.8 - C, right).

The ELISA results indicate that the nanoclay/protein scaffold absorbed 20.52 ± 6.40 $\mu\text{g/ml}$ and 27.09 ± 7 $\mu\text{g/ml}$ BMP-2 after 1 and 3 h of incubation. These concentrations are over those expected. However, as they are under the ultra-physiological concentrations used in the clinic, the scaffolds containing 20.52 ± 6.40 $\mu\text{g/ml}$ were used for the in vivo study (refer to methods section - 6.2.2.1 for the ELISA procedure) (Fig. 6.8 - C, left).

6.3.4.4 *Bioactivity assay*

To confirm the bioactivity of the BMP-2, an in vitro study was set up using C2C12 cells and an alkaline phosphatase assay (refer to method section - 6.2.2.2). The results indicate that the ALP activity of C2C12 cells increased with increasing concentrations of BMP-2, especially over 200 ng/ml (Fig. 6.8 - D).

6.3.4.5 *Holder*

In order to maintain the integrity of scaffolds when implanted subcutaneously, a cylindrical cage of PLA was fabricated using an extrusion 3D printer. The designed structure had enough internal space (6x6 mm) to fit the scaffold (5x5 mm). It was constituted by 2 rings of PLA forming the side of the cages, which were held

together by 8 posts. Moreover, one of the rings was crossed to maintain the scaffold in place, and the overall frame thickness was ~1 mm. Finally, the structure was refined by smoothing the sharp edges, removing four of the post and sterilising them as described in the methods section - 6.2.2.3 (Fig. 6.8 - E).

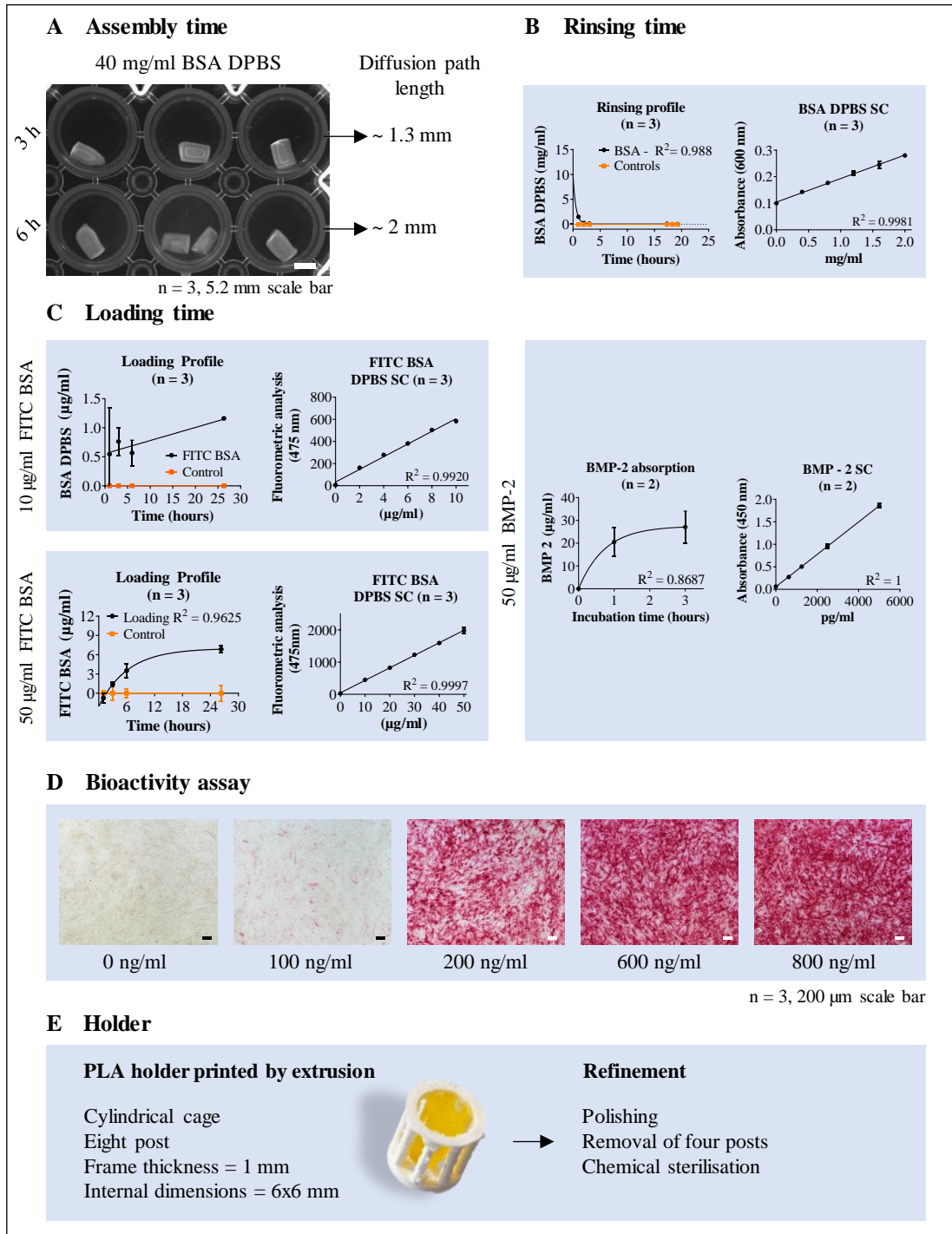


Figure 6.8 Optimisation of the scaffolds' fabrication parameters. (A) The results indicate that adequate assembly time of 100 μ l Of 2.8 % clay-gel in 40 mg/ml BSA DPBS is 3 h at 4°C. (B) Furthermore, it takes ~19 h of rinsing to remove the excess of assembly solution, BSA DPBS. (C) The

ELISA results indicate that the scaffolds uptake 20.52 ± 6.40 $\mu\text{g/ml}$ at 1 h of incubation, 4°C. (D) In vitro bioactivity assay of BMP-2 performed with C2C12 and ALP staining reveals an increase in the ALP activity as a function of BMP-2 concentration. (E) 3D printed holder of PLA containing a cylindrical clay-gel loaded with FITC BSA. The holder consists of a cylindrical cage, which was refined and chemically sterilised before implantation in the mouse model.

6.3.4.6 *Subcutaneous mouse model*

For this purpose, the scaffolds were scaled up to be able to detect with micro CT imaging the spatial localisation of the new bone with respect to the clay-gel and protein localisation. To preserve their integrity and protein localisation in the subcutaneous pocket, the scaffolds were placed inside a 3D printed PLA holder prior to implantation (Fig. 6.9 - A). Further details of the procedure can be found in the methods section - 6.2.2.4.

In this first pilot, the results indicate that the PLA holders help to maintain the scaffold integrity after one month and still allow tissue ingrowth. In this regard, micro CT reconstruction of the implanted constructs revealed the formation of a dense structure inside the holders regardless of the presence of BMP-2. To evaluate the nature of these structures, a histological study was performed. Transversal sections of the controls stained with alcian blue/sirius red (A&S) for glycosaminoglycans /collagen, respectively, revealed a blue central structure with a circular shape surrounded by soft tissue and holder pillar vestiges. A closer look reveals some infiltration of cells next to the edges. Owing to the spatial localisation of the circular structure, it was likely to be the nanoclay/protein scaffold, which was also detected with the micro CT regardless of the absence of bone (Fig. 6.9 - B).

Regarding the experimental group containing BMP-2, the histological sections reveal a yellow central structure surrounded by a halo of infiltrating cells, followed by soft tissue and holder pillar vestiges. Interestingly, new bone with a semi-circle shape, containing marrow and adjacent to the cells was observed. In this regard, it can be concluded that the central and adjacent density observed in the micro CT reconstructions corresponds to the scaffold and new bone, respectively (Fig. 6.9 - B). Details of the histological procedure, sectioning and staining, can be found in the methods section - 6.2.2.5.

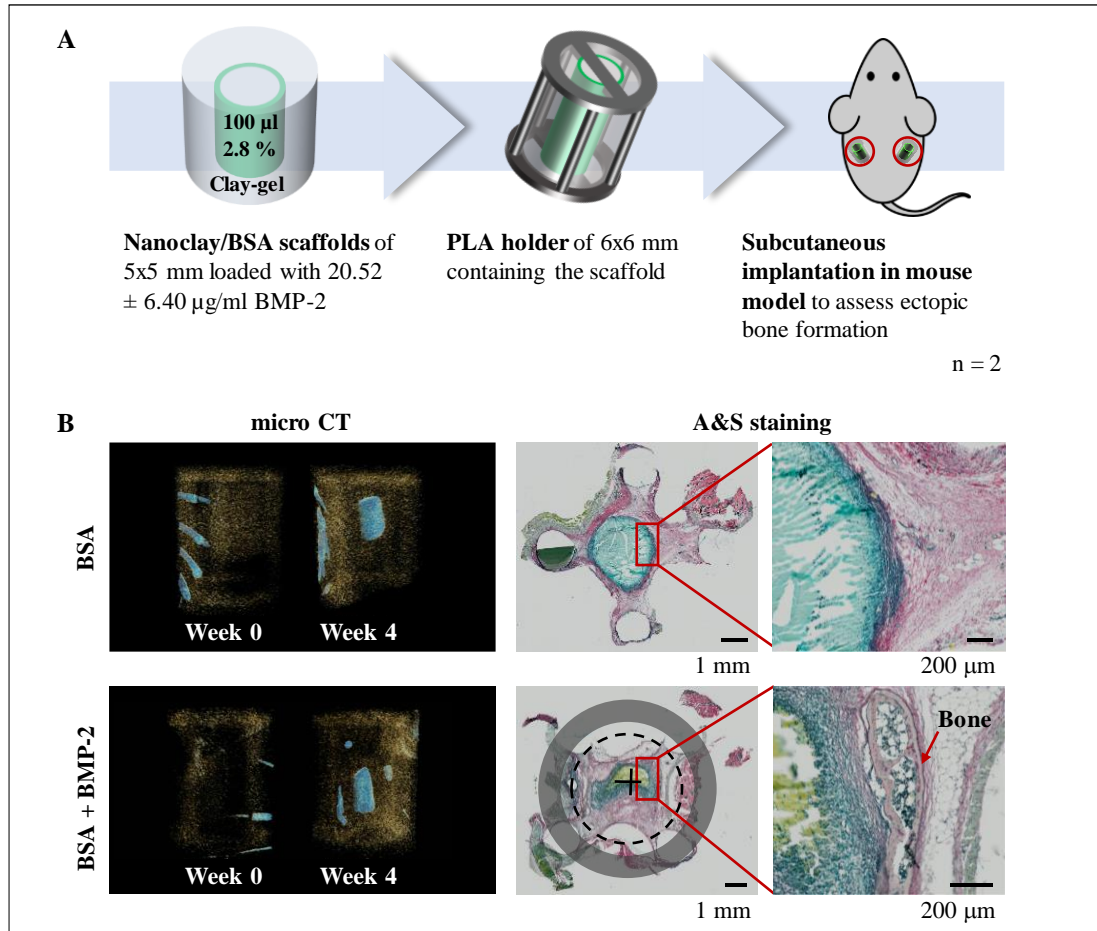


Figure 6.9 Biological activity of nanoclay/protein scaffolds. (A) Nanoclay/protein scaffolds assembled with BSA, loaded with $20.52 \pm 6.40 \mu\text{g/ml}$ BMP-2 and placed inside a 3D printed PLA holder were implanted in a subcutaneous mouse model to evaluate the ectopic bone formation. (B) The micro CT reconstructions of both control and experimental group reveal the formation of dense structures after four weeks. To understand the nature of these structures, transversal sections were stained with alcian blue/sirius red. In the controls, the scaffold stained in blue and looked intact after 1 month. Regarding, the experimental group containing BMP-2, the scaffold stained in yellow and looked smaller after 1 month when compared to the control. Also, had a larger infiltrate of cells, suggesting that the cells have invaded and degraded progressively the scaffold and during this process they encounter the BMP-2 forming localised new bone (n = 2).

Thus, this in vivo study reveals that it is possible to control the spatial localisation of newly formed bone with a punctuated gradient of BMP-2 albeit variably across the cross-section of the patterned scaffold.

6.4 Discussion

The aim of the chapter has been to explore the versatility of the system to design scaffolds with distinct micropatterns of biochemical cues, dimensions and shapes to generate structures with customised physico-chemical cues for bone tissue regeneration.

Regarding the protein micropatterning, it has been demonstrated that it is possible to create multiple patterns of two different proteins inside the clay-gel droplet by simply alternating the assembly and loading step and by controlling the concentration of the protein solutions and the incubation time (Fig. 6.3 & 6.4). This result is in agreement with the assembling mechanism proposed in the previous result chapter, where the protein assembly solution diffuses into the clay-gel and progressively reacts with and saturates the clay nanoparticles. Later the protein loading solution diffuses through the restructured gel and binds to the unreacted clay nanoparticles at the diffusion front or interface between the reacted and unreacted clay nanoparticles (Fig. 5.9). By repeating this process, it has been demonstrated the possibility to generate fresh diffusion fronts to bind subsequently introduced proteins. Interestingly, the protein patterns appear to be firmly bound, as they do not seem disturbed by subsequent assembly protein solution waves.

Again, taking advantage of the assembly and loading mechanism, it was produced a scaffold holding a dual but gradual gradient of proteins with overlapping positive and negative concentration profiles by loading the protein with the assembly solution and altering their concentration over time as the reaction-diffusion process takes place. In this regard, the negative gradient formed by the linear decrease in concentration of the protein solution A (BSA FITC) as the concentration of protein solution B (BSA AF 647) increased, creating the positive gradient (Fig. 6.5).

Development and tissue regeneration processes are finely coordinated by diffusive molecules, known as morphogens, which spatio-temporal patterns regulate the fate of naïve cells towards the formation of complex tissues and functional organ systems. Recently, several *in vitro* platforms have been developed in attempts to recreate

spatio-temporal patterns of morphogens to shed light on these complex developmental events. Major advances in this area have been achieved by hydrogel microfluidic technology since the dynamic and precise delivery of biomolecules in space and time through an engineered culture substrate have proven the potential to direct successfully the differentiation and spatial localisation of stem cells. In this regard, Cosson & Lutolf (2014) reported the in situ neural differentiation of embryonic stem cells through the spatio-temporal control of the morphogen retinoic acid (RA) using a microfluidic hydrogel chip. Notably, analysis of the embryonic stem cells size and Sox1-GFP reporter expression revealed a concentration dependent effect of RA on neural induction after 6 hours onwards, being stronger closer to the source. A more complex platform was presented by Demers et al. (2016) to mimic spinal cord patterning. For this, the microfluidic device comprised multiple channels to generate four separate gradients of RA and purmorphamine to activate the sonic hedgehog pathway, BMP-4, and FGF. Changing the concentration of the morphogens demonstrated spatial control over the motor neuron differentiation of embryonic stem cells throughout the gel especially when combining RA and purmorphamine gradients.

These models emphasize the importance of introducing 3D micropatterns of biochemical cues into the design of scaffolds for TERM applications. Here it has been demonstrated the versatility of the system to produce 3D scaffolds containing punctuated or gradual gradients of different morphogens in a very simple, precise and effective manner. Future work will focus on evaluating the biological implications and optimising the presentation of the morphogen to control cell differentiation towards effective bone regeneration.

Other important factors that need to be considered in the scaffold design are the dimensions and shapes since their adaptation determines the delivery route into the body and the spatio-temporal functionality, which in turn influences the vascularization, degradation rate, drug release, and other physical and mechanical signalling, which are crucial for bone repair. Here, it has been demonstrated the versatility of the nanoclay/protein scaffolds fabrication to generate structures with different dimensions from 0.2 to 1 mm and shapes, such as droplets, cylinders and strings without affecting the protein patterning and resolution, as they are scale-up

(Fig. 6.6). In this regard, this new system provides the opportunity to design customised bone scaffolds with clinical relevance.

In order to evaluate the bioactivity of the nanoclay/protein scaffolds loaded with BMP-2, assembled scaffolds with and without patterned BMP-2 were implanted in a subcutaneous mouse model. A 3D printed PLA holder was utilised to maintain the scaffold integrity over the implantation period. To be able to correlate the bone formation with the spatial localisation of the BMP-2 inside the scaffold, large cylinders of about 6x6 mm were manufactured, since smaller scaffold would potentially reabsorb faster and the micro CT would not be able to resolve the structure formed.

Unexpectedly, the reconstruction of the micro CT images showed dense structures inside the PLA holder of both control and study group after 4 weeks. However, the histological analysis demonstrated that they have different origins. In this regard, a transversal cross-section of the controls, or clay-gels assembled with BSA, revealed an almost intact circular scaffold with little cell infiltration. Unpublished data generated by the bone & joint group at University of Southampton showed spontaneous calcium deposition within Laponite® gels following implantation, which may account for the observed increase in density of these uncolonised regions of the scaffold. Notably; however, this has only been observed in higher (> 3.5 %) concentration Laponite® gels.

In contrast, the study group containing BMP-2 revealed a more active process. The dimensions of the scaffold were reduced in comparison to the control. Also, it was surrounded by a large halo of cell infiltration, suggesting that the scaffold was degraded gradually by cells, a process that appears to be enhanced by the presence of BMP-2. Moreover, new bone formed adjacent to the scaffold was observed and it seems to correspond with the cylindrical shape and dimension of the scaffold. In this regard, it is possible that the cells encountered the bound BMP-2, formed the new bone and continued their path towards the core of the scaffold.

A study performed by Gibbs et al. (2016) reported the formation of ectopic bone in a subcutaneous mouse model triggered by low doses of BMP-2 delivered with

Laponite® gel. Interestingly, the loading mode defined the osteogenic pathway. In this regard, direct or intramembranous bone formation was observed after 28 days when 1 µg of BMP-2 was applied exogenously to the trabecular bone graft TGF-β perfused with 2.5 % clay-gel at the point of implantation. The authors of this study suggest that this might be related to the high concentration of BMP-2 adsorbed in close relation with the trabecular bone graft. In contrast, endochondral bone formation was observed when the BMP-2 was encapsulated in the clay-gel.

Interestingly, in the present study, mature trabecular bone colonised with haematopoietic tissue was observed within the nanoclay/protein scaffold loaded with BMP-2. However, earlier time points need to be studied to better clarify the osteogenic pathway or intervening steps that precede the formation of bone tissue within patterned BMP-2 scaffolds.

Furthermore, these results demonstrate a progressive degradation of 100 µl of 2.8 % clay-gel loaded with 20.52 ± 6.40 µg/ml BMP-2 at 4 weeks, which appears in close relation with the cell infiltration. In contrast, histological images published Gibbs et al. (2016) reveals cells invasion and fragmentation of 20 µl of 2.5 % clay-gel containing 1 µg BMP-2, which remain in place at 28 days. Similar results were reported by Page et al. (2019). They indicate that after implantation of 50 µl of 3 % Laponite® gel containing 2 µg VEGF, a substantial volume of the material remained at 21 days. However, it was fragmented with cells and tissue present throughout the material (Fig. 6.7).

Thus, this new system seems to favour the progressive degradation of the clay-gel assembled with BSA, but only when loaded with BMP-2. In comparison to the studies above-described, it does not seem to be related to the clay-gel concentration or volume, but the protein concentration or the loading mode. This is important to take into consideration as the degradation affects the overall spatio-temporal bioactivity of the scaffold.

These results are promising; however, further work is required to improve the biological activity of the scaffold as only a relatively small section of the BMP-2 loaded region of the scaffold generated new bone formation. Future experiments will,

therefore, focus on optimising the loading of BMP-2 and its concentration within the scaffold.

Another factor that may need to be improved, is the mechanical properties of the scaffolds in order to be able to implant them without the PLA holder. In this regard, the addition of polymers with the clay-gel nanoparticles prior to the assembly was proposed. The preliminary results showed that the incorporation of collagen or alginate does not affect the 3D micropatterning of proteins (Fig. 6.7). However, further work is required to evaluate the threshold polymer/clay ratio and the effect on the mechanical properties and their structure as it is expected changes in the porosity and degradation rate as well. Numerous studies have demonstrated the positive effect of clay nanoparticles in the mechanical properties of hydrogels. They could either improve the rheological properties of bioinks for 3D printing by extrusion or as a cross-linker to generate hydrogels with good mechanical strength (Wang et al. 2010 and Dávila & d'Ávila, 2019). However, in this context, the clay-gel would be the major phase, and the addition of other molecules are expected to strengthen the internal interactions.

6.5 Conclusions

In this chapter, it has been demonstrated the versatility of the system to self-assemble nanoclay/protein scaffolds with different dimensions and shapes containing more than one protein and with different pattern distributions. This provides exciting opportunities to generate structures with customised physico-chemical and biological properties able to direct effective bone formation. In this regard, the first in vivo study revealed that the punctuated localisation of BMP-2 inside the scaffold has the potential to control the spatio-temporal formation of bone. However, further work optimising the scaffold design is required to improve the bioactivity.

Moreover, improvement of the mechanical properties and degree of porosity is necessary to maintain the stability of the scaffold without a holder and facilitate cell invasion, respectively. For this purpose, the incorporation of another hydrogel into the clay-gel was proposed. Preliminary results indicate that the scaffolds' 3D protein

micropatterning is not altered, but further structural and rheological characterisation is required to optimise the scaffold.

Thus, this self-assembled, biocompatible and cost/time effective nanotechnology based on clay nanoparticles and proteins provides new opportunities for bone tissue engineering and regenerative medicine, as a therapeutic device and model to study developmental processes.

Chapter 7 DISCUSSION AND FUTURE DIRECTIONS FOR RESEARCH

7.1 Discussion

7.1.1 Achievements of this study

The main aim of this thesis was to exploit the physico-chemical properties of clay colloids to achieve self-assembly and patterning of protein gels to recapitulate the cellular microenvironment found during bone development and regeneration and to establish this new technology as a therapeutic delivery system of protein gradients to enhanced stem-cell driven regeneration of bone tissue. In doing so, the project tested the hypothesis that bottom-up self-assembly of nanoclay/protein scaffolds can be harnessed to achieve microscale control of protein gradients to deliver and sustain localised niches for enhanced bone tissue regeneration.

The current thesis achieved the above aims by:

- The development of a method to self-assemble clay-gels containing a 3D pattern of proteins;
- The implementation of a fluorescent imaging technique to evaluate the spatial localisation of the fluorescent proteins loaded;
- The implementation of imaging techniques (CLSM, PLM and SEM) to characterise the structure and study the assembly mechanism;
- The optimisation of the fabrication parameters to control the spatial localisation of proteins;
- The demonstration that the thixotropic property of clay-gels is critical in the assembly of structures with different dimensions and shapes;
- The demonstration that nanoclay/protein scaffolds containing a punctuated gradient of BMP-2 control the spatiotemporal formation of bone *in vivo*.

The conducted research led to the following findings:

- Addition of concentrated clay-gel in a protein-rich solution triggers a reaction-diffusion process that (a) assembles the scaffold and (b) creates a template where the proteins of interest will localise;

- The assembled structure presents a hierarchical organisation;
- Manipulation of the assembly parameters, including the concentration of the protein-rich solution, ionic strength, incubation time and temperature, and the protein size and net charge affect the reaction-diffusion process; as a result, the 3D spatial localisation of the proteins loaded inside the gel;
- Alternating the assembly and loading solutions generate scaffolds containing multiple and punctuated protein gradients;
- Simultaneous dynamic changes in concentration of the assembly and loading solutions generate a dual and gradual gradient of proteins with overlapping positive and negative gradients;
- The versatility of the system allows to assemble structures with distinct dimensions and shapes using different devices (micropipettes, atomiser spray bottle and syringes) that predetermine the form and volume of thixotropic clay-gel prior to contact with the assembly solution;
- The 3D protein patterning is not altered with variations in scaffold dimensions or shape;
- 4 weeks after subcutaneous implantation of nanoclay/protein scaffolds with punctuated localisation of BMP-2 in a mouse model, the scaffold guided the formation of localised bone with marrow.

In chapter 3, a method for assembling clay-gels containing 3D patterning of proteins was developed. In this regard, a spontaneous patterning of molecules was observed when concentrated colloidal clay-gels were placed in a protein-rich solution (DMEM 10 % FCS, 100 % FCS of 30 mg/ml BSA) and were then transferred to a low concentrated proteins solution (100 µg/ml FITC BSA). It was clear that the protein patterning was the result of a complex diffusion process triggered by BSA molecules in a concentration-dependent manner and, therefore, concluded that two distinct diffusion processes take place; 1) a primary diffusion of concentrated protein solution through the clay-gel that then facilitates 2) a secondary diffusion and localisation of low concentrated protein solution. To our knowledge, this is the first report describing the assembly of a scaffold with a 3D gradient of molecules involving non-covalent clay-gel and physiological-like fluids opening new avenues of research for biomimetic drug delivery systems.

In chapter 4, the effect of different fabrication parameters in the 3D patterning of proteins inside the gel was studied. The results led to optimising the assembly process and also provided insight into the assembly and loading mechanism. In this regard, it was concluded that the assembly step is vital in the formation and localisation of the protein loaded since the manipulation of different factors known to alter the diffusion path length of macromolecules, such as concentration, ionic strength, incubation time and temperature. Also, the solute size and net charge altered the spatial localisation of protein pattern. Regarding the assembly and loading mechanism, it was suggested that the diffusion of the assembly solution occurs via “reaction-diffusion” and that the diffusion and spatial localisation of the loading solution occur via “selective diffusion barrier” potentially governed by electrostatic interactions between the assembled structure and loaded protein.

In chapter 5, structural characterisation of the nanoclay/protein scaffold was performed using different imaging techniques, including CLSM, SEM and PLM. The results provided insight into the structural conformation at different length scales and a better understanding of the assembly mechanism. In this regard, PLM and SEM images confirmed that a reaction-diffusion process is responsible for the scaffold assembly, where the proteins (or gelator) react with the clay nanoparticles and simultaneously diffuse through the clay-gel in a concentration-dependent manner. The process led to the formation of a protein-clay complex structure with a periodical arrangement. Furthermore, the CLSM images demonstrated that the diffusion front or the interface between the reacted and unreacted clay-gel region is responsible for the spatial localisation of loaded proteins into the clay-gel.

In chapter 6, the versatility of the system to generate structures containing different gradients of proteins, such as punctuated or gradual with overlapped positive and negative gradients was demonstrated. Also, the possibility to assemble structures of with a range of dimensions (0.2 - 1 mm) and shapes (droplets, cylinders and strings) providing the opportunity to develop customised structures for bone regeneration or in vitro developmental studies. Finally, the bioactivity of the scaffolds was assessed in vivo. The assembled gels were loaded with BMP-2 and implanted subcutaneously in a mouse model, revealing the potential of punctuated BMP-2 gradient to control the spatio-temporal formation of bone.

7.1.2 A discussion of main findings and their context

Developmental and regenerative processes are finely coordinated by the signalling of diffusive molecules, known as morphogens, that regulate the fate of naïve cells towards the formation of complex tissues and functional organ systems in time and concentration dependent manner. Recently, several in vitro platforms have been developed in attempts to recreate spatio-temporal patterns of morphogens to shed light on these complex developmental events. Major advances in this area have been achieved by hydrogel microfluidic technology since the dynamic and precise delivery of biomolecules in space and time through an engineered culture substrate have proven the potential to direct successfully the differentiation and spatial localisation of stem cells.

In this regard, Cosson & Lutolf (2014) reported the in situ neural differentiation of embryonic stem cells through the spatio-temporal control of the morphogen retinoic acid (RA) using a microfluidic hydrogel chip. Notably, analysis of the embryonic stem cells size and Sox1-GFP reporter expression revealed a concentration dependent effect of RA on neural induction after 6 hours onwards, being stronger closer to the source. A more complex platform was presented by Demers et al. (2016) to mimic spinal cord patterning. For this, the microfluidic device comprised multiple channels to generate four separate gradients of RA and purmorphamine to activate the sonic hedgehog pathway, BMP-4, and FGF. Changing the concentration of the morphogens demonstrated spatial control over the motor neuron differentiation of embryonic stem cells throughout the gel especially when combining RA and purmorphamine gradients. These models emphasise the importance of introducing 3D micropatterns of biochemical cues into the design of scaffolds for TERM applications.

In this study, it has been demonstrated the versatility of the new clay-gel system to produce 3D scaffolds containing punctuated or gradual gradients of different proteins in a very simple and effective manner similar to those observed during development. The protein patterning is related to the unique sorptive properties and large surface area of the clay nanoparticle that allows spontaneous and firm binding of proteins at the interface between the reacted and unreacted clay-gels regions. Prior to this

project, it has not has been reported the patterning of proteins using gels assembled via reaction-diffusion systems, such as alginate (Dai et al. 2009). Moreover, a proof of concept experiment performed as part of the patent application using chitosan gels, which is a positively charged molecule, revealed no formation of any protein pattern.

Interestingly, in 1952, Turing proposed that morphogenesis occurs through a reaction-diffusion process, where morphogen reacts and diffuse through tissues forming patterns of signals to regulate the development of functional organs. This is one of the most debated developmental theories. However, with the gradual increase in computer simulation that predicts the dynamic properties of patterns formation, it is starting to gain acceptance. Thus, the clay-gel system developed in this study not only recapitulates the spatiotemporal localisation of biochemical cues but a possible fundamental development process since a reaction-diffusion system has been used to create patterns of proteins. Through this biomimetic approach, it is aimed to control cells fate to enhance the regeneration of hard and soft tissues and the outcomes would not only benefit patients but to deepen the understanding of developmental processes.

7.1.3 Limitations of the study and indications for future research

Throughout this study, the use of fluorescent proteins became a reliable tool to visualise the spatial localisation of proteins loaded within the nanoclay/protein scaffold. The results facilitated optimising the fabrication parameters, elucidating the assembly mechanism and demonstrating the versatility of the system to assemble complex structures of different dimensions and shapes without altering the protein gradient. Some analyses required manual measurement of features to describe the phenomena observed, such as the diffusion path length of proteins through the scaffold as a function of time, concentration or ionic strength. Therefore, it is essential to consider human error in this type of analysis. However, in order to minimise it, a CLSM was used to acquire images with improved resolution in comparison to the fluorescent microscope.

Furthermore, PLM images revealed a radial birefringence that develops upon assembly of the scaffolds in the protein-ring solution, suggesting that the clay nanoparticles are being realigned following the diffusion flux of the gelator (protein) as the reaction-diffusion process takes place. However, the results do not provide information about the spatial orientation of the nanoparticle with respect to the diffusion front. For this purpose, other techniques, such as SAXS will be considered to resolve the structure. Moreover, the sample preparation and analysis technique used for PLM must be improved to obtain qualitative data about the optical properties of the clay-gel and the scaffolds. For this purpose, a LC-PolScope could be used to measure the birefringence, refractive index and determine the fast and slow axis of the sample.

The SEM imaging analysis was also crucial to determine that the assembly mechanism of the scaffold was a reaction-diffusion process. The images revealed a change in phase as the scaffolds were assembled. In this regard, the reacted region formed a porous shell and the unreacted region a dense core. However, no further information could be inferred from the images about the porosity, interconnectivity and other features because alterations in the morphology are almost unavoidable during the sample preparation, mainly due to the cross-linking process (Hafez & Kenemans, 1982 and Talbot & White, 2013). In this regard, other techniques, such as environmental or cryo-SEM could be used to evaluate the structure of the scaffold as they do not require any sample processing before imaging.

Similarly, TEM images showed changes in the scaffolds structure, suggesting a depletion of nanoparticles towards the diffusion front and possible reorientation across the long axis perpendicular to the diffusion front. These are standard features observed in gels that were assembled via reaction-diffusion (Leong et al. 2016). Nevertheless, it is known that the sample preparation for TEM imaging is harsh and may alter the clay-gels nanostructure and respective analysis. Thus, other less or non-destructive techniques, such as SAXS may be useful to evaluate the distribution of clay nanoparticles concentration, spatial orientation, periodic arrangement and spacing after the scaffold assembly. Similarly, cryo-TEM or Raman spectroscopy could be used to support the SAXS nanostructure analysis.

Until now, little is known about the protein clay interaction and conformational changes of the protein. The supernatant depletion assay suggested that a monolayer of proteins coats the clay nanoparticles. However, the error of the measurements was significant. Thus, to address this, the experiment must be repeated with larger samples to increase the sensitive of the assay. Also, another technique that could provide an inside view is the fluorescence lifetime imaging, performed with a CLSM.

In this study, scaffolds loaded with a punctuated gradient of BMP-2 were implanted in a subcutaneous mouse model to assess their bioactivity. The results revealed the formation of localised bone containing marrow. However, further work is required to improve the biological activity of the scaffold as only a relatively small section of the BMP-2 loaded region of the scaffold generated new bone formation. Future experiments will, therefore, focus on optimising the loading of BMP-2 and its concentration within the scaffold before evaluating bone formation in a femoral critical-size bone defect.

Another factor that may need to be improved, is the mechanical properties of the scaffolds in order to implant them without the PLA holder. In this regard, the addition of polymers to the clay-gel nanoparticles prior to the assembly was proposed. The preliminary results showed that the incorporation of collagen or alginate does not affect the 3D micropatterning of proteins. However, further work is required to evaluate the threshold polymer/clay ratio and related effects on the mechanical properties and structural characteristic of the scaffolds. For this purpose, it can be used a rheometer and an SEM-EDS analysis to perform initial analysis.

Finally, in this study, the bioactivity of the scaffolds in vitro was not assessed. For this purpose, it is proposed using cells that can migrate inside hydrogels, such as NIH-3T3 cell and HT-1080 fibrosarcoma cell line or primary rat dorsal root ganglia cells. However, it needs to be taken into consideration that this concentrated clay-gel lack of effective porosity and even encapsulated cells are not able to move (according to unpublished data generated by the bone & joint research group at the University of Southampton). To address this issue, the addition of other natural or synthetic hydrogels was proposed to engineer nanoclay/protein constructs with

porous interconnected network, opening the opportunity to use this platform for in vitro developmental studies.

7.2 Concluding remarks

To our knowledge, this is the first report describing the assembly of a scaffold with 3D gradient of biochemical cues involving non-covalent clay-gel. This study provides a detailed method to self-assemble nanoclay/protein scaffolds containing patterns of proteins and the effect of different fabrication parameters, which can be used to fine-tune the spatial localisation of the proteins within the gel. Furthermore, the structural characterisation presented in this study allowed understanding the assembly mechanism and, therefore, the assembly of more complex structures with different dimensions, shapes and protein gradients. Finally, the in vivo study reported in this thesis shows that a punctuated gradient of BMP-2 can localise the spatio-temporal formation of bone. These findings open new avenues of research for biomimetic drug delivery systems not only for fracture repair but also for other tissues in patients. In addition, they provide a framework to build a device to study developmental processes in vitro and in vivo.

Appendix

Reagent

Table A.1 Nanoclay/gel scaffold assembly

Reagents	Product code	Lot number	Supplier
Albumin from bovine serum (BSA) Alexa Fluor™ 647 conjugate	A34785	1932509	Invitrogen by Thermo Fisher Scientific
Albumin bovine - fluorescein isothiocyanate conjugate (lyophilised powder)	A9771-50MG 1002533088	SLBP519V	Sigma-Aldrich
Albumin Tetramethylrhodamine isothiocyanate bovine (lyophilised powder)	A2289-10MG 1002402447	SLBQ0215V	Sigma-Aldrich
Alginic acid sodium salt from brown algae	71238	---	Sigma-Aldrich
Avidin from egg white	A9275-5MG 1002567715	SLBS4417	Sigma-Aldrich
Bovine serum albumin reagent graded powder, heat shock treated (100gr)	BP1600-100	64-1341	Fisher Scientific
Catalase from bovine liver	C1345-1G 1002593381	SLBW3156	Sigma-Aldrich
Casein - fluorescein isothiocyanate from bovine milk (type III, essentially salt-freeze, lyophilised powder)	C0528-10MG 1001763953	015H7170V	Sigma-Aldrich
Casein sodium salt from bovine milk	C8654-500G 101728295	BCBP6469V	Sigma-Aldrich
Collagen - type I solution from rat tail	1002467066	SLBS8676	Sigma-Aldrich
DAPI dilactate (4',6-diamidino-2- phenylindole)	D3571	---	Sigma-Aldrich
Dulbecco's Modified Eagle's Medium with 4.5g/L Glucose and with L- Glutamine (500ml)	12-604F	---	BioWhittaker®, Lonza
Dulbecco's phosphate-buffered saline without calcium and magnesium	17-512F	---	BioWhittaker®, Lonza
D-(+)-Glucose	G-7528	69H00161	Sigma-Aldrich
DyLight™ 488 NHS-Ester (1mg)	46402	TC2545501	Thermo Fisher Scientific

DyLight™ 633 NHS-Ester (1mg)	46414	---	Thermo Fisher Scientific
DyLight™ 800 NHS-Ester (3 vials)	1860510	SI2448717	Thermo Fisher Scientific
DHA (cis-4, 7, 10, 13, 16, 19-Docosahexaenoic acid)	D2534-25mg 1001970314	SLBL3090V	Sigma-Aldrich
DQ™ Collagen type I from bovine skin - fluorescein conjugate	D12060	1829167	Invitrogen by Thermo Fisher Scientific
FITC-Avidin	434411	1805238	Invitrogen by Thermo Fisher Scientific
Foetal Calf Serum	10270	42F0461K	Life technologies - Thermo Fisher Scientific
Haemoglobin from bovine blood (lyophilised powder)	H2500-1G 1001974960	SLBF3496V	Sigma-Aldrich
Hyaluronidase from bovine testes (Type I – S, lyophilized powder)	H3506-1G 1002514208	SLBR7365V	Sigma-Aldrich
IgG from bovine serum	I5506-10MG 1002594884	SLBM2612V	Sigma-Aldrich
IgG (H+L) Alexa Fluor® 488 goat anti-mouse	A11001	898287	Invitrogen by Thermo Fisher Scientific
Laponite® XLG powder	---	SR# 4573	BYK additive limited
Lysozyme from chicken egg white	L6876-1G 1002566788	SLBT5161	Sigma-Aldrich
Myoglobin from equine heart	M1882- 250MG 1002436883	SLBF8560V	Sigma-Aldrich
Protein Assay - Dye reagent concentrate (450ml)	500-0006	---	Bio RAD
Penicillin-Streptomycin	P0781-20ML	---	Sigma Aldrich
rhBMP-2, component of large II Infuse® Bone Graft Kit	7510904	111509AA	Medtronic
Sodium hydroxide, extra pure pellets	134070010	A0224034	ACROS organics™
Streptavidin from Streptomyces avidinii	S4762-5MG	016M4188V	Sigma-Aldrich
Streptavidin-FITC from Streptomyces avidinii	S3762-1MG	---	Sigma-Aldrich

Table A.2 Histological analysis

Reagents	Product code	Lot number	Supplier
Alcian Blue 8GX, certified	400460100	A0402660	ACROS organics™
Direct Red 80 - Sirius Red	365548-25G 1001428065	MKBBK7017V	Sigma-Aldrich
Diaminoethanetetra-acetic acid disodium salt dihydrate (EDTA)	D/0650/60	1665046	Fisher
Ethanol	BP2818-4	---	Fisher
Histo-clear®	HS-200	---	National Diagnostics™
Hydrochloric acid ACS reagent, 37% solution in water	423795000	A0317959	ACROS organics™
p-xylene bis-pyridinium bromide, phthalate free mountain medium (DPX)	D/5330/05	1668809	Fisher
Paraformaldehyde 96% extra pure	416780010	A0372619	ACROS organics™
Phosphomolybdc acid hydrate-80%	206381000	A0404881	ACROS organics™
Trisma®base	T1503-1KG 1002302339	SLBR3760V	Sigma Aldrich
Weigert's solution 1 (Alcoholic Haematoxylin)	640494	C168-48-05	Clin-Tech limited
Weigert's solution 2 (Acidified Ferric Chloride)	640504	C165-24-09	Clin-Tech limited

Table A.3 SEM and TEM analyses

Reagents	Supplier
Ethanol	Biomedical Imaging Unit, University of Southampton
Formaldehyde	
Glutaraldehyde	
PIPES	
Spurr Low Viscosity Embedding Kit - EM0300. Sigma-Aldrich	
Uranyl acetate	

Table A.4 Biological activity assessment of nanoclay/protein scaffolds

Reagents	Product code	Lot number	Supplier
5-0 suture PDS™ 45 cm			Ethicon
Antibiotic/antimycotic solution x100 stabilised	A59955-100ml	005M4754V	Sigma Aldrich
Buprenodale® Multidose 0.3 mg/ml solution (Buprenorphine)	---	---	Dechra
100% Ethanol	BP2818-4	---	Fisher
Fast Violet salt	F163	---	Sigma Aldrich
F1 hybrid mice male	---	---	Biomedical research facility, University of Southampton
human BMP ELISA kit	SBP200	---	R&D
Polylactic acid Ultimaker	RAL 9010	---	Ultimaker
Naphthol AS-MX phosphate	855-20ML	---	Sigma Aldrich

Labware*Table A.5 Material used for nanoclay/gel scaffold assembly*

Labware	Manufacture
6, 12, and 96 well plate, clear flat bottom, sterile	Sigma Aldrich
96 well plate, clear, U bottom	Sigma Aldrich
μ-slide 8 well glass bottom	Ibidi
Glass bottle 5 ml (15x45 mm)	Thermo scientific

Equipment*Table A.6 Equipment*

Equipment	Manufacture
3D printer Ultimaker 3 extended	Ultimaker
Aladdin syringe pumps - Al-1000	Aladdin
Benchtop autoclave Classic prestige medical 210002	Prestige Medical
Brunker Skyscan 1176	Brunker
Confocal laser scanning microscope - TCS SP5	Leica
Critical point dryer - Bal-tec - CPD 030	Irchel
dotSlide Virtual Microscopy System - BX51	Olympus

Dual-intensity chromate-vue transilluminator - TM-20	UVP, INC.
Drying cabinet - IWC200	Genlab
HM 325 Rotary Microtome - 902100	Thermo Scientific™
InGenius LHR: Gel Documentation System	SYNGENE
Inverted Microscope AxioVert - 200	Carl Zeiss
Centrifuge 5415R	Eppendorf
Microplate reader - GloMax® Discover System - GM3000	Promega
Micropipette 10µl	Eppendorf
Micropipette 100, 200, 1000µl	STARLAB
NANOpure Diamond™ - D11911	Barnstead
Nikon Photomicroscope - Eclipse 80i	Nikon
Nikon Polarizer First Order Red Full Wave Plate Lambda λ Compensator for Eclipse	Nikon
Nikon colour camera E950	Nikon
Orbital shaker - PSU - 10i	Grant-bio
Paraffin Embedding Station - Blockmaster III	Raymond A Lamb
Paraffin Section Flotation Bath - MH8517	Electrothermal
Quorum Q150T ES carbon and sputter coater	Quorum
Scanning Electron Microscope FEI Quanta - 250	FEI Quanta
Slide drying bench - MH6616	Electrothermal
Fisherbrand™ Isotemp™ Stirring Hotplate - 15303518	Fisher Scientific
Transmission Electron Microscope - Hitachi HT7700	Hitachi
Ultramicrotome Reichert Ultracut E	Reichert-Jung
Vacuum Heating and Drying Oven Heraeus vacutherm - VT 6025	Thermo Scientific™
Vortex-T Genie 2	Scientific Industries
Zeiss™ Cold Light Source - KL 2500 LCD	Fisher

References

- Abe, K., Kawamata, I., Nomura, S. M., & Murata, S. (2019). Programmable reactions and diffusion using DNA for pattern formation in hydrogel medium. *Molecular Systems Design & Engineering*, 4, 639–643. <https://doi.org/10.1039/c9me00004f>
- Adair, J. H., Suvaci, E., & Sindel, J. (2001). Surface and Colloid Chemistry. In *Encyclopedia of Materials: Science and Technology* (Vol. 3, Issue 1, pp. 1–10). Elsevier. <https://doi.org/10.1016/B0-08-043152-6/01622-3>
- Agrahari, V. (2017). The exciting potential of nanotherapy in brain-tumor targeted drug delivery approaches. *Neural Regeneration Research*, 12(2), 197. <https://doi.org/10.4103/1673-5374.200796>
- Agrawal, V., & Sinha, M. (2017). A review on carrier systems for bone morphogenetic protein-2. *Journal of Biomedical Materials Research Part B: Applied Biomaterials*, 105(4), 904–925. <https://doi.org/10.1002/jbm.b.33599>
- Aguilar, J. P., Lipka, M., Primo, G. A., Licon-Bernal, E. E., Fernández-Pradas, J. M., Yaroshchuk, A., Albericio, F., & Mata, A. (2018). 3D Electrophoresis-Assisted Lithography (3DEAL): 3D Molecular Printing to Create Functional Patterns and Anisotropic Hydrogels. *Advanced Functional Materials*, 28(15), 1–10. <https://doi.org/10.1002/adfm.201703014>
- Ahmed, E. M. (2015). Hydrogel: Preparation, characterization, and applications: A review. *Journal of Advanced Research*, 6(2), 105–121. <https://doi.org/10.1016/j.jare.2013.07.006>
- Alexander, C., Zuniga, E., Blitz, I. L., Wada, N., le Pabic, P., Javidan, Y., Zhang, T., Cho, K. W., Crump, J. G., & Schilling, T. F. (2011). Combinatorial roles for BMPs and endothelin 1 in patterning the dorsal-ventral axis of the craniofacial skeleton. *Development*, 138(23), 5135–5146. <https://doi.org/10.1242/dev.067801>
- Alexis, F., Pridgen, E., Molnar, L. K., & Farokhzad, O. C. (2008). Factors Affecting the Clearance and Biodistribution of Polymeric Nanoparticles. *Molecular Pharmaceutics*, 5(4), 505–515. <https://doi.org/10.1021/mp800051m>
- Amini, A. R., Laurencin, C. T., & Nukavarapu, S. P. (2012). Bone tissue engineering: Recent advances and challenges. *Critical Reviews in Biomedical Engineering*, 40(5), 363–408. <https://doi.org/10.1615/CritRevBiomedEng.v40.i5.10>
- Amsden, B. (1998). Solute Diffusion within Hydrogels. Mechanisms and Models. *Macromolecules*, 31(23), 8382–8395. <https://doi.org/10.1021/ma980765f>
- Anderson, J. L., Rauh, F., & Morales, A. (1978). Particle diffusion as a function of concentration and ionic strength. *Journal of Physical Chemistry*, 82(5), 608–616. <https://doi.org/10.1021/j100494a022>
- Artel. (2019). *Lab Report 5: Setting tolerances for pipettes in the laboratory*. http://www.labautopedia.com/mw/index.php/Setting_tolerances_for_pipettes_in

_the_laboratory

- Ashe, H. L. (2006). The interpretation of morphogen gradients. *Development*, 133(3), 385–394. <https://doi.org/10.1242/dev.02238>
- Au, P.-I., Hassan, S., Liu, J., & Leong, Y.-K. (2015). Behaviour of LAPONITE® gels: Rheology, ageing, pH effect and phase state in the presence of dispersant. *Chemical Engineering Research and Design*, 101, 65–73. <https://doi.org/10.1016/j.cherd.2015.07.023>
- Augat, P., & Schorlemmer, S. (2006). The role of cortical bone and its microstructure in bone strength. *Age and Ageing*, 35(SUPPL.2), 27–31. <https://doi.org/10.1093/ageing/afl081>
- Awasthi, V., & Joshi, Y. M. (2009). Effect of temperature on aging and time-temperature superposition in nonergodic laponite suspensions. *Soft Matter*, 5(24), 4991–4996. <https://doi.org/10.1039/b915105b>
- Ayarza, J., Coello, Y., Nakamatsu, J., Ayarza, J., Coello, Y., & Nakamatsu, J. (2017). International Journal of Polymer Analysis and SEM – EDS study of ionically cross-linked alginate and alginic acid bead formation bead formation. *International Journal of Polymer Analysis and Characterization*, 22(1), 1–10. <https://doi.org/10.1080/1023666X.2016.1219834>
- Ayoub, A., Roshan, C. P., Gillgrass, T., Naudi, K., & Ray, A. (2016). The clinical application of rhBMP-7 for the reconstruction of alveolar cleft. *Journal of Plastic, Reconstructive and Aesthetic Surgery*, 69(1), 101–107. <https://doi.org/10.1016/j.bjps.2015.09.004>
- Aziz, M. S., & El sherif, A. Y. (2015). Biomimicry as an approach for bio-inspired structure with the aid of computation. *Alexandria Engineering Journal*, 55(1), 707–714. <https://doi.org/10.1016/j.aej.2015.10.015>
- Bae, K. H., & Kurisawa, M. (2016). Emerging hydrogel designs for controlled protein delivery. *Biomaterials Science*, 4(8), 1184–1192. <https://doi.org/10.1039/c6bm00330c>
- Bai, X., Gao, M., Syed, S., Zhuang, J., Xu, X., & Zhang, X.-Q. (2018). Bioactive hydrogels for bone regeneration. *Bioactive Materials*, 3(4), 401–417. <https://doi.org/10.1016/j.bioactmat.2018.05.006>
- Bajpai, A. K., & Sachdeva, R. (2002). Study on the adsorption of hemoglobin onto bentonite clay surfaces. *Journal of Applied Polymer Science*, 85(8), 1607–1618. <https://doi.org/10.1002/app.10698>
- Ball, P. (2015). Forging patterns and making waves from biology to geology: a commentary on Turing (1952) ‘The chemical basis of morphogenesis.’ *Philosophical Transactions of the Royal Society B: Biological Sciences*, 370(1666), 20140218. <https://doi.org/10.1098/rstb.2014.0218>
- Bazant, M. Z., & Stone, H. A. (2000). Asymptotics of reaction-diffusion fronts with one static and one diffusing reactant. *Physica D: Nonlinear Phenomena*, 147(1–2), 95–121. [https://doi.org/10.1016/S0167-2789\(00\)00140-8](https://doi.org/10.1016/S0167-2789(00)00140-8)
- Bier, E., & De Robertis, E. M. (2015). BMP gradients: A paradigm for morphogen-mediated developmental patterning. *Science*, 348(6242), aaa5838–aaa5838.

<https://doi.org/10.1126/science.aaa5838>

- Bose, S., Roy, M., & Bandyopadhyay, A. (2012). Recent advances in bone tissue engineering scaffolds. *Trends in Biotechnology*, *30*(10), 546–554.
<https://doi.org/10.1016/j.tibtech.2012.07.005>
- Bouyer, M., Guillot, R., Lavaud, J., Plettinx, C., Olivier, C., Curry, V., Boutonnat, J., Coll, J.-L., Peyrin, F., Josserand, V., Bettega, G., & Picart, C. (2016). Surface delivery of tunable doses of BMP-2 from an adaptable polymeric scaffold induces volumetric bone regeneration. *Biomaterials*, *104*, 168–181.
<https://doi.org/10.1016/j.biomaterials.2016.06.001>
- Boyde, A. (2012). Scanning Electron Microscopy of Bone. In M. H. Helfrich & S. H. Ralston (Eds.), *Bone Research Protocols* (pp. 365–400). Humana Press.
https://doi.org/10.1007/978-1-61779-415-5_24
- Bragdon, B., Moseychuk, O., Saldanha, S., King, D., Julian, J., & Nohe, A. (2011). Bone Morphogenetic Proteins : A critical review. *Cellular Signalling*, *23*(4), 609–620. <https://doi.org/10.1016/j.cellsig.2010.10.003>
- Braschler, T., Valero, A., Colella, L., Pataky, K., Brugger, J., & Renaud, P. (2011). Link between alginate reaction front propagation and general reaction diffusion theory. *Analytical Chemistry*, *83*(6), 2234–2242.
<https://doi.org/10.1021/ac103118r>
- Breuls, R., Jiya, T., & Smit, T. (2008). Scaffold stiffness influences cell behavior: opportunities for skeletal tissue engineering. *The Open Orthopaedics Journal*, *2*, 103–109. <https://doi.org/10.2174/1874325000802010103>
- Briscoe, J., & Small, S. (2015). Morphogen rules: design principles of gradient-mediated embryo patterning. *Development*, *142*(23), 3996–4009.
<https://doi.org/10.1242/dev.129452>
- Brun, F., Accardo, A., Marchini, M., Ortolani, F., Turco, G., & Paoletti, S. (2011). Texture analysis of TEM micrographs of alginate gels for cell microencapsulation. *Microscopy Research and Technique*, *74*(1), 58–66.
<https://doi.org/10.1002/jemt.20874>
- Campana, V., Milano, G., Pagano, E., Barba, M., Cicione, C., Salonna, G., Lattanzi, W., & Logroscino, G. (2014). Bone substitutes in orthopaedic surgery: from basic science to clinical practice. *Journal of Materials Science: Materials in Medicine*, *25*(10), 2445–2461. <https://doi.org/10.1007/s10856-014-5240-2>
- Carreira, A. C., Alves, G. G., Zambuzzi, W. F., Sogayar, M. C., & Granjeiro, J. M. (2014). Bone Morphogenetic Proteins: Structure, biological function and therapeutic applications. *Archives of Biochemistry and Biophysics*, *561*, 64–73.
<https://doi.org/10.1016/j.abb.2014.07.011>
- Censi, R., Di Martino, P., Vermonden, T., & Hennink, W. E. (2012). Hydrogels for protein delivery in tissue engineering. *Journal of Controlled Release*, *161*(2), 680–692. <https://doi.org/10.1016/j.jconrel.2012.03.002>
- Cha, J.-K., Jung, U.-W., Thoma, D. S., Hämmerle, C. H. F., & Jung, R. E. (2018). Osteogenic efficacy of BMP-2 mixed with hydrogel and bone substitute in peri-implant dehiscence defects in dogs: 16 weeks of healing. *Clinical Oral Implants*

- Research*, 29(3), 300–308. <https://doi.org/10.1111/clr.13117>
- Cheever, M., Master, A., & Versteegen, R. (2017). A Method for Differentiating Fetal Bovine Serum from Newborn Calf Serum. *BioProcessing Journal*, 16, 1–6. <https://doi.org/10.12665/j16oa.cheever>
- Chen, J., & Zou, X. (2019). Self-assemble peptide biomaterials and their biomedical applications. *Bioactive Materials*, 4(February 2019), 120–131. <https://doi.org/10.1016/j.bioactmat.2019.01.002>
- Cho, T. J., Gerstenfeld, L. C., & Einhorn, T. A. (2002). Differential temporal expression of members of the transforming growth factor β superfamily during murine fracture healing. *Journal of Bone and Mineral Research*, 17(3), 513–520. <https://doi.org/10.1359/jbmr.2002.17.3.513>
- Christian, J. L. (2012). Morphogen gradients in development: from form to function. *Wiley Interdisciplinary Reviews: Developmental Biology*, 1(1), 3–15. <https://doi.org/10.1002/wdev.2>
- Cipelletti, L., & Ramos, L. (2005). Slow dynamics in glassy soft matter. *Journal of Physics: Condensed Matter*, 17, R253–R285. <https://doi.org/10.1088/0953-8984/17/6/R01>
- Clarke, B. (2008). Normal Bone Anatomy and Physiology. *Clin J Am Soc Nephrol*, 3, 131–139. <https://doi.org/10.2215/CJN.04151206>
- Conway, J. D., Shabtai, L., Bauernschub, A., & Specht, S. (2014). BMP-7 Versus BMP-2 for the Treatment of Long Bone Nonunion. *Orthopedics*, 37(12), 1049–1057. <https://doi.org/10.3928/01477447-20141124-50>
- Cosson, S., & Lutolf, M. P. (2015). Hydrogel microfluidics for the patterning of pluripotent stem cells. *Scientific Reports*, 4(1), 4462. <https://doi.org/10.1038/srep04462>
- Cruickshank Miller, C. (1924). The Stokes-Einstein Law Diffusion. *Proc. Royal Soc. Lond. A*, 17(5), 724–748.
- Cui, H., Webber, M. J., & Stupp, S. I. (2010). Self-assembly of peptide amphiphiles: From molecules to nanostructures to biomaterials. *Biopolymers*, 94(1), 1–18. <https://doi.org/10.1002/bip.21328>
- Dai, H., Li, X., Long, Y., Wu, J., Liang, S., Zhang, X., Zhao, N., & Xu, J. (2009). Multi-membrane hydrogel fabricated by facile dynamic self-assembly. *Soft Matter*, 5(10), 1987. <https://doi.org/10.1039/b821363a>
- Dai, X., Knupp, S. A., & Xu, Q. (2012). Patterning nanoparticles in a three-dimensional matrix using an electric-field-assisted gel transferring technique. *Langmuir*, 28(5), 2960–2964. <https://doi.org/10.1021/la204288g>
- Daluiski, A., Engstrand, T., Bahamonde, M. E., Gamer, L. W., Agius, E., Stevenson, S. L., Cox, K., Rosen, V., & Lyons, K. M. (2001). Bone morphogenetic protein-3 is a negative regulator of bone density. *Nature Genetics*, 27(1), 84–88. <https://doi.org/10.1038/83810>
- Das, K., Rawat, K., & Bohidar, H. B. (2016). Surface patch binding induced interaction of anisotropic nanoclays with globular plasma proteins. *RSC*

- Advances*, 6(106), 104117–104125. <https://doi.org/10.1039/C6RA11669H>
- Dathe, K., Kjaer, K. W., Brehm, A., Meinecke, P., Nürnberg, P., Neto, J. C., Brunoni, D., Tommerup, N., Ott, C. E., Klopocki, E., Seemann, P., & Mundlos, S. (2009). Duplications Involving a Conserved Regulatory Element Downstream of BMP2 Are Associated with Brachydactyly Type A2. *American Journal of Human Genetics*, 84(4), 483–492. <https://doi.org/10.1016/j.ajhg.2009.03.001>
- Datta, H. K., Ng, W. F., Walker, J. A., Tuck, S. P., & Varanasi, S. S. (2008). The cell biology of bone metabolism. *Journal of Clinical Pathology*, 61(5), 577–587. <https://doi.org/10.1136/jcp.2007.048868>
- Dávila, J. L., & d'Ávila, M. A. (2019). Rheological evaluation of Laponite/alginate inks for 3D extrusion-based printing. *International Journal of Advanced Manufacturing Technology*, 101(1–4), 675–686. <https://doi.org/10.1007/s00170-018-2876-y>
- Dawson, J. I., Kanczler, J. M., Yang, X. B., Attard, G. S., & Oreffo, R. O. . (2011). Clay Gels For the Delivery of Regenerative Microenvironments. *Advanced Materials*, 23(29), 3304–3308. <https://doi.org/10.1002/adma.201100968>
- Dawson, J. I., & Oreffo, R. O. C. (2013). Clay: New opportunities for tissue regeneration and biomaterial design. *Advanced Materials*, 25(30), 4069–4086. <https://doi.org/10.1002/adma.201301034>
- Dawson, M., Wirtz, D., & Hanes, J. (2003). Enhanced Viscoelasticity of Human Cystic Fibrotic Sputum Correlates with Increasing Microheterogeneity in Particle Transport. *Journal of Biological Chemistry*, 278(50), 50393–50401. <https://doi.org/10.1074/jbc.M309026200>
- De Witte, T.-M., Fratila-Apachitei, L. E., Zadpoor, A. A., & Peppas, N. A. (2018). Bone tissue engineering via growth factor delivery: from scaffolds to complex matrices. *Regenerative Biomaterials*, 5(4), 197–211. <https://doi.org/10.1093/rb/rby013>
- Deforest, C. A., Polizzotti, B. D., & Anseth, K. S. (2009). Sequential click reactions for synthesizing and patterning three-dimensional cell microenvironments. *Nature Materials*, 8(8), 659–664. <https://doi.org/10.1038/nmat2473>
- DeForest, C. A., & Tirrell, D. A. (2015). A photoreversible protein-patterning approach for guiding stem cell fate in three-dimensional gels. *Nature Materials*, 14(5), 523–531. <https://doi.org/10.1038/nmat4219>
- Dehsorkhi, A., Castelletto, V., & Hamley, I. W. (2014). Self-assembling amphiphilic peptides. *Journal of Peptide Science*, 20(7), 453–467. <https://doi.org/10.1002/psc.2633>
- Del Mercato, L. L., Ferraro, M. M., Baldassarre, F., Mancarella, S., Greco, V., Rinaldi, R., & Leporatti, S. (2014). Biological applications of LbL multilayer capsules: From drug delivery to sensing. *Advances in Colloid and Interface Science*, 207(1), 139–154. <https://doi.org/10.1016/j.cis.2014.02.014>
- Del Río, J. A., & Whitaker, S. (2016). Diffusion of Charged Species in Liquids. *Scientific Reports*, 6(1), 35211. <https://doi.org/10.1038/srep35211>

- Della Porta, V., Bramanti, E., Campanella, B., Tiné, M. R., & Duce, C. (2016). Conformational analysis of bovine serum albumin adsorbed on halloysite nanotubes and kaolinite: a Fourier transform infrared spectroscopy study. *RSC Advances*, 6(76), 72386–72398. <https://doi.org/10.1039/C6RA12525E>
- Demers, C. J., Soundararajan, P., Chennampally, P., Cox, G. A., Briscoe, J., Collins, S. D., & Smith, R. L. (2016). Development-on-chip: in vitro neural tube patterning with a microfluidic device. *Development*, 143(11), 1884–1892. <https://doi.org/10.1242/dev.126847>
- Despanie, J., Dhandhukia, J. P., Hamm-Alvarez, S. F., & MacKay, J. A. (2016). Elastin-like polypeptides: Therapeutic applications for an emerging class of nanomedicines. *Journal of Controlled Release*, 240, 93–108. <https://doi.org/10.1016/j.jconrel.2015.11.010>
- Dobashi, T., Furusawa, K., Kita, E., Minamisawa, Y., & Yamamoto, T. (2007). DNA liquid-crystalline gel as adsorbent of carcinogenic agent. *Langmuir*, 23(3), 1303–1306. <https://doi.org/10.1021/la061412+>
- Dobashi, T., Yoshihara, H., Nobe, M., Koike, M., Yamamoto, T., & Konno, A. (2005). Liquid crystalline gel beads of Curdlan. *Langmuir*, 21(1), 2–4. <https://doi.org/10.1021/la047901w>
- Docter, D., Westmeier, D., Markiewicz, M., Stolte, S., Knauer, S. K., & Stauber, R. H. (2015). The nanoparticle biomolecule corona: lessons learned – challenge accepted? *Chemical Society Reviews*, 44(17), 6094–6121. <https://doi.org/10.1039/C5CS00217F>
- Douglas, J. (2018). Weak and Strong Gels and the Emergence of the Amorphous Solid State. *Gels*, 4(1), 19. <https://doi.org/10.3390/gels4010019>
- Draenert, F. G., Nonnenmacher, A. L., Kämmerer, P. W., Goldschmitt, J., & Wagner, W. (2013). BMP-2 and bFGF release and in vitro effect on human osteoblasts after adsorption to bone grafts and biomaterials. *Clinical Oral Implants Research*, 24(7), 750–757. <https://doi.org/10.1111/j.1600-0501.2012.02481.x>
- Ducy, P., & Karsenty, G. (2000). The family of bone morphogenetic proteins. *Kidney International*, 57(6), 2207–2214. <https://doi.org/10.1046/j.1523-1755.2000.00081.x>
- Edgar, C. M., Chakravarthy, V., Barnes, G., Kakar, S., Gerstenfeld, L. C., & Einhorn, T. A. (2007). Autogenous regulation of a network of bone morphogenetic proteins (BMPs) mediates the osteogenic differentiation in murine marrow stromal cells. *Bone*, 40(5), 1389–1398. <https://doi.org/10.1016/j.bone.2007.01.001>
- Ekegren, C., Edwards, E., de Steiger, R., & Gabbe, B. (2018). Incidence, Costs and Predictors of Non-Union, Delayed Union and Mal-Union Following Long Bone Fracture. *International Journal of Environmental Research and Public Health*, 15(12), 2845. <https://doi.org/10.3390/ijerph15122845>
- El Bialy, I., Jiskoot, W., & Reza Nejadnik, M. (2017). Formulation, Delivery and Stability of Bone Morphogenetic Proteins for Effective Bone Regeneration. *Pharmaceutical Research*, 34(6), 1152–1170. <https://doi.org/10.1007/s11095->

017-2147-x

- Elsalanty, M. E., & Genecov, D. G. (2009). Bone Grafts in Craniofacial Surgery. *Craniofacial Trauma & Reconstruction*, 2(3), 125–134. <https://doi.org/10.1055/s-0029-1215875>.
- Entchev, E. V., & González-Gaitán, M. A. (2002). Morphogen Gradient Formation and Vesicular Trafficking. *Traffic*, 3(2), 98–109. <https://doi.org/10.1034/j.1600-0854.2002.030203.x>
- Fei, Y., Xu, R., & Hurley, M. M. (2012). Stem cell-based bone repair. *Am J Stem Cell*, 1(2), 106–113.
- Felbeck, T., Mundinger, S., Lezhnina, M. M., Staniford, M., Resch-Genger, U., & Kynast, U. H. (2015). Multifold Fluorescence Enhancement in Nanoscopic Fluorophore-Clay Hybrids in Transparent Aqueous Media. *Chemistry - A European Journal*, 21(20), 7582–7587. <https://doi.org/10.1002/chem.201406416>
- Feng, X. (2009). Chemical and Biochemical Basis of Cell-Bone Matrix Interaction in Health and Disease. *Curr Chem Biol*. 2009, 3(2), 975–990. <https://doi.org/10.2174/187231309788166398.Chemical>
- Fernandez-Yague, M. A., Abbah, S. A., McNamara, L., Zeugolis, D. I., Pandit, A., & Biggs, M. J. (2015). Biomimetic approaches in bone tissue engineering: Integrating biological and physicommechanical strategies. *Advanced Drug Delivery Reviews*, 84, 1–29. <https://doi.org/10.1016/j.addr.2014.09.005>
- Florencio-Silva, R., Da Silva Sasso, G. R., Sasso-Cerri, E., Simões, M. J., & Cerri, P. S. (2015). Biology of Bone Tissue: Structure, Function, and Factors That Influence Bone Cells. *BioMed Research International*, 2015, 421746, 1–17. <https://doi.org/10.1155/2015/421746>
- Freshney, R. I. (2005). Culture of Animal Cells: A Manual of Basic Techniques. In *Culture of Animal Cells* (Fifth). John Wiley & Sons, Inc. <https://doi.org/10.1002/9780471747598>
- Fu, K., Pack, D. W., Klibanov, A. M., & Langer, R. (2000). Visual Evidence of Acidic Environment Within Degrading Poly(lactic-co-glycolic acid) (PLGA) Microspheres. *Pharmaceutical Research*, 17(1), 100–106. <https://doi.org/10.1023/A:1007582911958>
- Furusawa, K., Sato, S., Masumoto, J. I., Hanazaki, Y., Maki, Y., Dobashi, T., Yamamoto, T., Fukui, A., & Sasaki, N. (2012). Studies on the formation mechanism and the structure of the anisotropic collagen gel prepared by dialysis-induced anisotropic gelation. *Biomacromolecules*, 13(1), 29–39. <https://doi.org/10.1021/bm200869p>
- Gabriel, J. C. P., Sanchez, C., & Davidson, P. (1996). Observation of nematic liquid-crystal textures in aqueous gels of smectite clays. *Journal of Physical Chemistry*, 100(26), 11139–11143. <https://doi.org/10.1021/jp961088z>
- Gaharwar, A. K., Cross, L. M., Peak, C. W., Gold, K., Carrow, J. K., Brokesh, A., & Singh, K. A. (2019). 2D Nanoclay for Biomedical Applications: Regenerative Medicine, Therapeutic Delivery, and Additive Manufacturing. *Advanced*

- Materials*, 31(23), 1900332. <https://doi.org/10.1002/adma.201900332>
- Gaharwar, A. K., Kishore, V., Rivera, C., Bullock, W., Wu, C. J., Akkus, O., & Schmidt, G. (2012). Physically Crosslinked Nanocomposites from Silicate-Crosslinked PEO: Mechanical Properties and Osteogenic Differentiation of Human Mesenchymal Stem Cells. *Macromolecular Bioscience*, 12(6), 779–793. <https://doi.org/10.1002/mabi.201100508>
- Gaharwar, A. K., Mihaila, S. M., Swami, A., Patel, A., Sant, S., Reis, R. L., Marques, A. P., Gomes, M. E., & Khademhosseini, A. (2013). Bioactive Silicate Nanoplatelets for Osteogenic Differentiation of Human Mesenchymal Stem Cells. *Advanced Materials*, 25(24), 3329–3336. <https://doi.org/10.1002/adma.201300584>
- Gallet, A., Staccini-Lavenant, L., & Therond, P. P. (2008). Cellular Trafficking of the Glypican Dally-like Is Required for Full-Strength Hedgehog Signaling and Wingless Transcytosis. *Developmental Cell*, 14(5), 712–725. <https://doi.org/10.1016/j.devcel.2008.03.001>
- Gandhi, N. S., & Mancera, R. L. (2012). Prediction of heparin binding sites in bone morphogenetic proteins (BMPs). *Biochimica et Biophysica Acta (BBA) - Proteins and Proteomics*, 1824(12), 1374–1381. <https://doi.org/10.1016/j.bbapap.2012.07.002>
- Gautschi, O. P., Frey, S. P., & Zellweger, R. (2007). Bone morphogenetic proteins in clinical applications. *ANZ Journal of Surgery*, 77(8), 626–631. <https://doi.org/10.1111/j.1445-2197.2007.04175.x>
- Geckil, H., Xu, F., Zhang, X., Moon, S., & Demirci, U. (2010). Engineering hydrogels as extracellular matrix mimics. *Nanomedicine*, 5(3), 469–484. <https://doi.org/10.2217/nnm.10.12.Engineering>
- Gibbs, D. M. R., Black, C. R. M., Hulsart-Billstrom, G., Shi, P., Scarpa, E., Oreffo, R. O. C., & Dawson, J. I. (2016). Bone induction at physiological doses of BMP through localization by clay nanoparticle gels. *Biomaterials*, 99, 16–23. <https://doi.org/10.1016/j.biomaterials.2016.05.010>
- Goldstein, A. M., Brewer, K. C., Doyle, A. M., Nagy, N., & Roberts, D. J. (2005). BMP signaling is necessary for neural crest cell migration and ganglion formation in the enteric nervous system. *Mechanisms of Development*, 122(6), 821–833. <https://doi.org/10.1016/j.mod.2005.03.003>
- Gong, X., Wang, Z., & Ngai, T. (2014). Direct measurements of particle–surface interactions in aqueous solutions with total internal reflection microscopy. *Chem. Commun.*, 50(50), 6556–6570. <https://doi.org/10.1039/C4CC00624K>
- Griffith, D. L., Keck, P. C., Sampath, T. K., Rueger, D. C., & Carlson, W. D. (1996). Three-dimensional structure of recombinant human osteogenic protein 1: Structural paradigm for the transforming growth factor β superfamily. *Proceedings of the National Academy of Sciences of the United States of America*, 93(2), 878–883. <https://doi.org/10.1073/pnas.93.2.878>
- Gupta, A. N., Bohidar, H. B., & Aswal, V. K. (2007). Surface patch binding induced intermolecular complexation and phase separation in aqueous solutions of similarly charged gelatin-chitosan molecules. *Journal of Physical Chemistry B*,

- 111(34), 10137–10145. <https://doi.org/10.1021/jp070745s>
- Gupta, R., Baldewa, B., & Joshi, Y. M. (2012). Time temperature superposition in soft glassy materials. *Soft Matter*, 8(15), 4171. <https://doi.org/10.1039/c2sm07071e>
- Güven, S., Chen, P., İnci, F., Tasoglu, S., Erkmen, B., & Demirci, U. (2015). Multiscale assembly for tissue engineering and regenerative medicine. *Trends in Biotechnology*, 33(5), 269–279. <https://doi.org/10.1016/j.tibtech.2015.02.003>
- Hafez, E. S. E., & Kenemans, P. (1982). *Atlas of Human Reproduction By Scanning Electron Microscopy* (E. S. E. Hafez & P. Kenemans (eds.); 1st ed.). Springer Netherlands. <https://doi.org/10.1007/978-94-011-8140-2>
- Hahn, M. S., Miller, J. S., & West, J. L. (2006). Three-dimensional biochemical and biomechanical patterning of hydrogels for guiding cell behavior. *Advanced Materials*, 18(20), 2679–2684. <https://doi.org/10.1002/adma.200600647>
- Hasan, A. M. A., & Abdel-Raouf, M. E.-S. (2019). Cellulose-Based Superabsorbent Hydrogels. In I. H. Mondal (Ed.), *Cellulose-Based Superabsorbent Hydrogels. Polymers and Polymeric Composites: A Reference Series* (pp. 245–267). Springer, Cham. https://doi.org/10.1007/978-3-319-77830-3_11
- Hayat, E. (1981). *Fixation for Electron Microscopy*. Academic Press.
- He, X., Ma, J., & Jabbari, E. (2008). Effect of Grafting RGD and BMP-2 Protein-Derived Peptides to a Hydrogel Substrate on Osteogenic Differentiation of Marrow Stromal Cells. *Langmuir*, 24(21), 12508–12516. <https://doi.org/10.1021/la802447v>
- Hedgepeth, C. M., Conrad, L. J., Zhang, J., Huang, H., Lee, V. M. Y., & Klein, P. S. (1997). Activation of the Wnt Signaling Pathway: A Molecular Mechanism for Lithium Action. *Developmental Biology*, 185(1), 82–91. <https://doi.org/10.1006/dbio.1997.8552>
- Henkel, J., Woodruff, M. A., Epari, D. R., Steck, R., Glatt, V., Dickinson, I. C., Choong, P. F. M., Schuetz, M. A., & Huttmacher, D. W. (2013). Bone Regeneration Based on Tissue Engineering Conceptions — A 21st Century Perspective. *Bone Research*, 1(3), 216–248. <https://doi.org/10.4248/BR201303002>
- Hernandez, D. S., Ritschdorff, E. T., Seidlits, S. K., Schmidt, C. E., & Shear, J. B. (2016). Functionalizing micro-3D-printed protein hydrogels for cell adhesion and patterning. *Journal of Materials Chemistry B*, 4(10), 1818–1826. <https://doi.org/10.1039/C5TB02070K>
- Hernlund, E., Svedbom, A., Ivergård, M., Compston, J., Cooper, C., Stenmark, J., McCloskey, E. V., Jönsson, B., & Kanis, J. A. (2013). Osteoporosis in the European Union: medical management, epidemiology and economic burden. A report prepared in collaboration with the International Osteoporosis Foundation (IOF) and the European Federation of Pharmaceutical Industry Associations (EFPIA). *Archives of Osteoporosis*, 8(1–2), 136. <https://doi.org/10.1007/s11657-013-0136-1>
- Herrera, J., Olmo, N., Turnay, J., Sicilia, A., Bascones, A., Gavilanes, J., & Lizarbe,

- M. (1995). Implantation of sepiolite-collagen complexes in surgically created rat calvaria defects. *Biomaterials*, *16*(8), 625–631. [https://doi.org/10.1016/0142-9612\(95\)93860-G](https://doi.org/10.1016/0142-9612(95)93860-G)
- Hettiaratchi, M. H., Rouse, T., Chou, C., Krishnan, L., Stevens, H. Y., Li, M.-T. A., McDevitt, T. C., & Guldborg, R. E. (2017). Enhanced in vivo retention of low dose BMP-2 via heparin microparticle delivery does not accelerate bone healing in a critically sized femoral defect. *Acta Biomaterialia*, *59*, 21–32. <https://doi.org/10.1016/j.actbio.2017.06.028>
- Hoare, T. R., & Kohane, D. S. (2008). Hydrogels in drug delivery: Progress and challenges. *Polymer*, *49*(8), 1993–2007. <https://doi.org/10.1016/j.polymer.2008.01.027>
- Hözl, K., Lin, S., Tytgat, L., Van Vlierberghe, S., Gu, L., & Ovsianikov, A. (2016). Bioink properties before, during and after 3D bioprinting. *Biofabrication*, *8*(3), 032002. <https://doi.org/10.1088/1758-5090/8/3/032002>
- Hu, W., Wang, Z., Xiao, Y., Zhang, S., & Wang, J. (2019). Advances in crosslinking strategies of biomedical hydrogels. *Biomaterials Science*, *7*(3), 843–855. <https://doi.org/10.1039/c8bm01246f>
- Hustedt, J. W., & Blizzard, D. J. (2014). The controversy surrounding bone morphogenetic proteins in the spine: a review of current research. *The Yale Journal of Biology and Medicine*, *87*(4), 549–561. <http://www.ncbi.nlm.nih.gov/pubmed/25506287>
- Hynes, R. O. (2002). Integrins. *Cell*, *110*, 673–687. <https://doi.org/10.1016/B978-012439510-7/50078-4>
- Ikada, Y. (2006). Challenges in tissue engineering. *Journal of The Royal Society Interface*, *3*(10), 589–601. <https://doi.org/10.1098/rsif.2006.0124>
- Jabbari-Farouji, S., Tanaka, H., Wegdam, G. H., & Bonn, D. (2008). Multiple nonergodic disordered states in Laponite suspensions: A phase diagram. *Physical Review E*, *78*(6), 061405. <https://doi.org/10.1103/PhysRevE.78.061405>
- Jabbarzadeh, E., Blanchette, J., Shazly, T., & Khademhosseini, A. (2012). Vascularization of Biomaterials for Bone Tissue Engineering : Current Approaches and Major Challenges. *Current Angiogenesis*, *1*(3), 180–191.
- Jachimska, B., Tokarczyk, K., Łapczyńska, M., Puciul-Malinowska, A., & Zapotoczny, S. (2016). Structure of bovine serum albumin adsorbed on silica investigated by quartz crystal microbalance. *Colloids and Surfaces A: Physicochemical and Engineering Aspects*, *489*, 163–172. <https://doi.org/10.1016/j.colsurfa.2015.10.033>
- Jain, M., & Matsumura, K. (2016). Polyampholyte- and nanosilicate-based soft bionanocomposites with tailorable mechanical and cell adhesion properties. *Journal of Biomedical Materials Research Part A*, *104*(6), 1379–1386. <https://doi.org/10.1002/jbm.a.35672>
- James, A. W., LaChaud, G., Shen, J., Asatrian, G., Nguyen, V., Zhang, X., Ting, K., & Soo, C. (2016). A Review of the Clinical Side Effects of Bone Morphogenetic Protein-2. *Tissue Engineering Part B: Reviews*, *22*(4), 284–297.

<https://doi.org/10.1089/ten.teb.2015.0357>

- Jatav, S., & Joshi, Y. M. (2014). Chemical stability of Laponite in aqueous media. *Applied Clay Science*, 97–98, 72–77. <https://doi.org/10.1016/j.clay.2014.06.004>
- Jatav, S., & Joshi, Y. M. (2016). Analyzing a fractal gel of charged oblate nanoparticles in a suspension using time-resolved rheometry and DLVO theory. *Faraday Discussions*, 186, 199–213. <https://doi.org/10.1039/C5FD00128E>
- Jatav, S., & Joshi, Y. M. (2017). Phase Behavior of Aqueous Suspension of Laponite: New Insights with Microscopic Evidence. *Langmuir*, 33(9), 2370–2377. <https://doi.org/10.1021/acs.langmuir.7b00151>
- Javier, A. L., Doan, L. T., Luong, M., Reyes de Mochel, N. S., Sun, A., Monuki, E. S., & Cho, K. W. Y. (2012). Bmp Indicator Mice Reveal Dynamic Regulation of Transcriptional Response. *PLoS ONE*, 7(9), e42566. <https://doi.org/10.1371/journal.pone.0042566>
- Jeon, O., Song, S. J., Yang, H. S., Bhang, S. H., Kang, S. W., Sung, M. A., Lee, J. H., & Kim, B. S. (2008). Long-term delivery enhances in vivo osteogenic efficacy of bone morphogenetic protein-2 compared to short-term delivery. *Biochemical and Biophysical Research Communications*, 369(2), 774–780. <https://doi.org/10.1016/j.bbrc.2008.02.099>
- Johansson, L., Skantze, U., & Lofroth, J. E. (1991). Diffusion and interaction in gels and solutions. 2. Experimental results on the obstruction effect. *Macromolecules*, 24(22), 6019–6023. <https://doi.org/10.1021/ma00022a018>
- Johnell, O., & Kanis, J. A. (2006). An estimate of the worldwide prevalence and disability associated with osteoporotic fractures. *Osteoporosis International*, 17(12), 1726–1733. <https://doi.org/10.1007/s00198-006-0172-4>
- Jurkić, L. M., Capanec, I., Pavelić, S. K., & Pavelić, K. (2013). Biological and therapeutic effects of ortho-silicic acid and some ortho-silicic acid-releasing compounds: New perspectives for therapy. *Nutrition & Metabolism*, 10(1), 2. <https://doi.org/10.1186/1743-7075-10-2>
- Katagiri, T., & Watabe, T. (2016). Bone Morphogenetic Proteins. *Cold Spring Harbor Perspectives in Biology*, 8(6), a021899. <https://doi.org/10.1101/cshperspect.a021899>
- Kavanagh, G. M., & Ross-Murphy, S. B. (1998). Rheological characterisation of polymer gels. *Progress in Polymer Science*, 23(3), 533–562. [https://doi.org/10.1016/S0079-6700\(97\)00047-6](https://doi.org/10.1016/S0079-6700(97)00047-6)
- Khansari, M. M., Sorokina, L. V., Mukherjee, P., Mukhtar, F., Shirdar, M. R., Shahidi, M., & Shokuhfar, T. (2017). Classification of Hydrogels Based on Their Source: A Review and Application in Stem Cell Regulation. *JOM*, 69(8), 1340–1347. <https://doi.org/10.1007/s11837-017-2412-9>
- Kicheva, A., & González-Gaitán, M. (2008). The Decapentaplegic morphogen gradient: a precise definition. *Current Opinion in Cell Biology*, 20(2), 137–143. <https://doi.org/10.1016/j.ceb.2008.01.008>
- King, W. J., & Krebsbach, P. H. (2012). Growth factor delivery: How surface interactions modulate release in vitro and in vivo. *Advanced Drug Delivery*

- Reviews*, 64(12), 1239–1256. <https://doi.org/10.1016/j.addr.2012.03.004>
- Kini, U., & Nandeesh, B. (2012). Physiology of Bone Formation, Remodeling, and Metabolism Usha Kini and B. N. Nandeesh 2. In I. Fogelman, H. Van Der Wall, & G. Gnanasegaran (Eds.), *Radionuclide and Hybrid Bone Imaging* (pp. 29–55). Springer-Verlag Berlin Heidelberg. <https://doi.org/10.1007/978-3-642-02400-9>
- Kloen, P., Di Paola, M., Borens, O., Richmond, J., Perino, G., Helfet, D. L., & Goumans, M. J. (2003). BMP signaling components are expressed in human fracture callus. *Bone*, 33(3), 362–371. [https://doi.org/10.1016/S8756-3282\(03\)00191-1](https://doi.org/10.1016/S8756-3282(03)00191-1)
- Kornberg, T. B. (2012). The Imperatives of Context and Contour for Morphogen Dispersion. *Biophysj*, 103(11), 2252–2256. <https://doi.org/10.1016/j.bpj.2012.10.025>
- Krishnakumar, G. S., Roffi, A., Reale, D., Kon, E., & Filardo, G. (2017). Clinical application of bone morphogenetic proteins for bone healing: a systematic review. *International Orthopaedics*, 41(6), 1073–1083. <https://doi.org/10.1007/s00264-017-3471-9>
- Kubiak-Ossowska, K., Tokarczyk, K., Jachimska, B., & Mulheran, P. A. (2017). Bovine Serum Albumin Adsorption at a Silica Surface Explored by Simulation and Experiment. *Journal of Physical Chemistry B*, 121(16), 3975–3986. <https://doi.org/10.1021/acs.jpcc.7b01637>
- Lagzi, I., Kowalczyk, B., & Grzybowski, B. A. (2010). Liesegang Rings Engineered from Charged Nanoparticles. *Journal of the American Chemical Society*, 132(1), 58–60. <https://doi.org/10.1021/ja906890v>
- Lai, S. K., O’Hanlon, D. E., Harrold, S., Man, S. T., Wang, Y.-Y., Cone, R., & Hanes, J. (2007). Rapid transport of large polymeric nanoparticles in fresh undiluted human mucus. *Proceedings of the National Academy of Sciences*, 104(5), 1482–1487. <https://doi.org/10.1073/pnas.0608611104>
- Lander, A. D., Nie, Q., & Wan, F. Y. M. (2002). Do morphogen gradients arise by diffusion? *Developmental Cell*, 2(6), 785–796. [https://doi.org/10.1016/S1534-5807\(02\)00179-X](https://doi.org/10.1016/S1534-5807(02)00179-X)
- Landis, W. J. (1995). The strength of a calcified tissue depends in part on the molecular structure and organization of its constituent mineral crystals in their organic matrix. *Bone*, 16(5), 533–544. [https://doi.org/10.1016/8756-3282\(95\)00076-P](https://doi.org/10.1016/8756-3282(95)00076-P)
- Larralde, H., Araujo, M., Havlin, S., & Stanley, H. E. (1992). Reaction front for A+BC diffusion-reaction systems with initially separated reactants. *Physical Review A*, 46(2), 855–859. <https://doi.org/10.1103/PhysRevA.46.855>
- Le Dréau, G., & Martí, E. (2012). Dorsal-ventral patterning of the neural tube: A tale of three signals. *Developmental Neurobiology*, 72(12), 1471–1481. <https://doi.org/10.1002/dneu.22015>
- Lee, J., Cuddihy, M. J., & Kotov, N. A. (2008). Three-Dimensional Cell Culture Matrices: State of the Art. *Tissue Engineering Part B: Reviews*, 14(1), 61–86.

<https://doi.org/10.1089/teb.2007.0150>

- Lee, U. N., Day, J. H., Haack, A. J., Lu, W., Theberge, A. B., & Berthier, E. (2019). Layer-by-Layer Fabrication of 3D Hydrogel Structures Using Open Microfluidics. *BioRxiv*, 687251. <https://doi.org/10.1101/687251>
- Lemaire, B. J., Panine, P., Gabriel, J., & Davidson, P. (2002). The measurement by SAXS of the nematic order parameter of laponite gels. *Europhysics Letters*, 59(1), 55–61. <https://doi.org/10.1209/epl/i2002-00159-8>
- Leong, J.-Y., Lam, W.-H., Ho, K.-W., Voo, W.-P., Lee, M. F.-X., Lim, H.-P., Lim, S.-L., Tey, B.-T., Poncelet, D., & Chan, E.-S. (2016). Advances in fabricating spherical alginate hydrogels with controlled particle designs by ionotropic gelation as encapsulation systems. *Particuology*, 24(2016), 44–60. <https://doi.org/10.1016/j.partic.2015.09.004>
- Lesins, V., & Ruckenstein, E. (1988). Patch controlled attractive electrostatic interactions between similarly charged proteins and adsorbents. *Colloid & Polymer Science*, 266(12), 1187–1190. <https://doi.org/10.1007/BF01414409>
- Li, J., & Mooney, D. J. (2016). Designing hydrogels for controlled drug delivery. *Nature Reviews Materials*, 1(12), 16071. <https://doi.org/10.1038/natrevmats.2016.71>
- Li, P. R., Wei, J. C., Chiu, Y. F., Su, H. L., Peng, F. C., & Lin, J. J. (2010). Evaluation on cytotoxicity and genotoxicity of the exfoliated silicate nanoclay. *ACS Applied Materials and Interfaces*, 2(6), 1608–1613. <https://doi.org/10.1021/am1001162>
- Li, S., Xing, D., & Li, J. (2004). Dynamic light scattering application to study protein interactions in electrolyte solutions. *Journal of Biological Physics*, 30(4), 313–324. <https://doi.org/10.1007/s10867-004-0997-z>
- Li, Z., Torgersen, J., Ajami, A., Mühleder, S., Qin, X., Husinsky, W., Holnthoner, W., Ovsianikov, A., Stampfl, J., & Liska, R. (2013). Initiation efficiency and cytotoxicity of novel water-soluble two-photon photoinitiators for direct 3D microfabrication of hydrogels. *RSC Advances*, 3(36), 15939–15946. <https://doi.org/10.1039/c3ra42918k>
- Lieleg, O., Baumgärtel, R. M., & Bausch, A. R. (2009). Selective filtering of particles by the extracellular matrix: An electrostatic bandpass. *Biophysical Journal*, 97(6), 1569–1577. <https://doi.org/10.1016/j.bpj.2009.07.009>
- Lieleg, O., & Ribbeck, K. (2011). Biological hydrogels as selective diffusion barriers. *Trends in Cell Biology*, 21(9), 543–551. <https://doi.org/10.1016/j.tcb.2011.06.002>
- Lieleg, O., Vladescu, I., & Ribbeck, K. (2010). Characterization of particle translocation through mucin hydrogels. *Biophysical Journal*, 98(9), 1782–1789. <https://doi.org/10.1016/j.bpj.2010.01.012>
- Lienemann, P. S., Lutolf, M. P., & Ehrbar, M. (2012). Biomimetic hydrogels for controlled biomolecule delivery to augment bone regeneration. *Advanced Drug Delivery Reviews*, 64(12), 1078–1089. <https://doi.org/10.1016/j.addr.2012.03.010>

- Limongi, T., Tirinato, L., Pagliari, F., Giugni, A., Allione, M., Perozziello, G., Candeloro, P., & Di Fabrizio, E. (2017). Fabrication and Applications of Micro/Nanostructured Devices for Tissue Engineering. *Nano-Micro Letters*, 9(1), 1–13. <https://doi.org/10.1007/s40820-016-0103-7>
- Lin, P., Lin, S., Wang, P. C., & Sridhar, R. (2014). Techniques for physicochemical characterization of nanomaterials. *Biotechnology Advances*, 32(4), 711–726. <https://doi.org/10.1016/j.biotechadv.2013.11.006>
- Lin, S. C., Minamisawa, Y., Furusawa, K., Maki, Y., Takeno, H., Yamamoto, T., & Dobashi, T. (2010). Phase relationship and dynamics of anisotropic gelation of carboxymethylcellulose aqueous solution. *Colloid and Polymer Science*, 288(6), 695–701. <https://doi.org/10.1007/s00396-010-2193-y>
- Liu, A. J., & Nagel, S. R. (1998). Jamming is not just cool any more. *Nature*, 396, 21–22. <https://doi.org/10.1038/23819>
- Liu, W., Zhang, Y. S., Heinrich, M. A., De Ferrari, F., Jang, H. L., Bakht, S. M., Alvarez, M. M., Yang, J., Li, Y. C., Trujillo-de Santiago, G., Miri, A. K., Zhu, K., Khoshakhlagh, P., Prakash, G., Cheng, H., Guan, X., Zhong, Z., Ju, J., Zhu, G. H., ... Khademhosseini, A. (2017). Rapid Continuous Multimaterial Extrusion Bioprinting. *Advanced Materials*, 29(3), 1–8. <https://doi.org/10.1002/adma.201604630>
- Liu, Y., Luo, D., & Wang, T. (2016). Hierarchical Structures of Bone and Bioinspired Bone Tissue Engineering. *Small*, 12(34), 4611–4632. <https://doi.org/10.1002/sml.201600626>
- Long, F., & Ornitz, D. M. (2013). Development of the Endochondral Skeleton. *Cold Spring Harbor Perspectives in Biology*, 5(1), a008334. <https://doi.org/10.1101/cshperspect.a008334>
- Louët, S. (2004). Reagent safety issues surface for cell / tissue therapies. *Nature Biotechnology*, 22(3), 253–254.
- Lovrak, M., Hendriksen, W. E. J., Maity, C., Mytnyk, S., van Steijn, V., Eelkema, R., & van Esch, J. H. (2017). Erratum: Free-standing supramolecular hydrogel objects by reaction-diffusion. *Nature Communications*, 8(1), 16128. <https://doi.org/10.1038/ncomms16128>
- Luo, Y., & Shoichet, M. S. (2004). A photolabile hydrogel for guided three-dimensional cell growth and migration. *Nature Materials*, 3(4), 249–253. <https://doi.org/10.1038/nmat1092>
- Macdonald, M. L., Samuel, R. E., Shah, N. J., Padera, R. F., Beben, Y. M., & Hammond, P. T. (2011). Tissue integration of growth factor-eluting layer-by-layer polyelectrolyte multilayer coated implants. *Biomaterials*, 32(5), 1446–1453. <https://doi.org/10.1016/j.biomaterials.2010.10.052>
- Mackie, E. J., Ahmed, Y. A., Tatarczuch, L., Chen, K.-S., & Mirams, M. (2008). Endochondral ossification: How cartilage is converted into bone in the developing skeleton. *The International Journal of Biochemistry & Cell Biology*, 40(1), 46–62. <https://doi.org/10.1016/j.biocel.2007.06.009>
- Maes, C., Kobayashi, T., Selig, M. K., Torrekens, S., Roth, S. I., Mackem, S.,

- Carmeliet, G., & Kronenberg, H. M. (2010). Article Osteoblast Precursors , but Not Mature Osteoblasts , Move into Developing and Fractured Bones along with Invading Blood Vessels. *Developmental Cell*, *19*(2), 329–344. <https://doi.org/10.1016/j.devcel.2010.07.010>
- Maki, Y., Ito, K., Hosoya, N., Yoneyama, C., Furusawa, K., Yamamoto, T., Dobashi, T., Sugimoto, Y., & Wakabayashi, K. (2011). Anisotropic structure of calcium-induced alginate gels by optical and small-angle X-ray scattering measurements. *Biomacromolecules*, *12*(6), 2145–2152. <https://doi.org/10.1021/bm200223p>
- Malda, J., Visser, J., Melchels, F. P., Jüngst, T., Hennink, W. E., Dhert, W. J. A., Groll, J., & Hutmacher, D. W. (2013). 25th Anniversary Article: Engineering Hydrogels for Biofabrication. *Advanced Materials*, *25*(36), 5011–5028. <https://doi.org/10.1002/adma.201302042>
- Mann, S. (1988). Molecular recognition in biomineralization. *Nature*, *332*, 119–124. <https://doi.org/10.1038/332119a0>
- Mann, S. (2001). *Biomineralization: Principles and Concepts in Bioinorganic Materials Chemistry*. Oxford University Press.
- Marsell, R., & Einhorn, T. A. (2011). The biology of fracture healing. *Injury*, *42*(6), 551–555. <https://doi.org/10.1016/j.injury.2011.03.031>
- Maselko, J., Reckley, J. S., & Showalter, K. (1989). Regular and irregular spatial patterns in an immobilized-catalyst Belousov-Zhabotinsky reaction. *Journal of Physical Chemistry*, *93*(7), 2774–2780.
- Mason, B. N., Califano, J. P., & Reinhart-king, C. A. (2012). Matrix Stiffness : A Regulator of Cellular Behavior and Tissue Formation. In S. K. Bhatia (Ed.), *Engineering Biomaterials for Regenerative Medicine* (1st ed., pp. 19–38). Springer-Verlag. <https://doi.org/10.1007/978-1-4614-1080-5>
- Matsubara, H., Hogan, D. E., Morgan, E. F., Mortolock, D. P., Einhorn, A., & Gerstenfeld, L. C. (2013). *NIH Public Access*. *51*(1), 168–180. <https://doi.org/10.1016/j.bone.2012.02.017.Vascular>
- Mehta, M., Schmidt-Bleek, K., Duda, G. N., & Mooney, D. J. (2012). Biomaterial delivery of morphogens to mimic the natural healing cascade in bone. *Advanced Drug Delivery Reviews*, *64*(12), 1257–1276. <https://doi.org/10.1016/j.addr.2012.05.006>
- Meijer, G. J., Bruijn, J. D. De, Koole, R., & Blitterswijk, C. A. Van. (2007). Cell-Based Bone Tissue Engineering. *PLoS Medicine*, *4*(2), 260–264. <https://doi.org/10.1371/journal.pmed.0040009>
- Michel, M., Toniazzo, V., Ruch, D., & Ball, V. (2012). Deposition mechanisms in layer-by-layer or step-by-step deposition methods: from elastic and impermeable films to soft membranes with ion exchange properties. *ISRN Materials Science*, *2012*, 1–13. <https://doi.org/10.5402/2012/701695>
- Migliorini, E., Valat, A., Picart, C., & Cavalcanti-Adam, E. A. (2016). Tuning cellular responses to BMP-2 with material surfaces. *Cytokine & Growth Factor Reviews*, *27*, 43–54. <https://doi.org/10.1016/j.cytogfr.2015.11.008>
- Mikhailov, M. D., Ozisik, M. N., & Shishedjiev, B. K. (1982). Diffusion in

- Heterogeneous Media. *Journal of Heat Transfer*, 104(4), 781–787.
<https://doi.org/10.1115/1.3245200>
- Min, J., Braatz, R. D., & Hammond, P. T. (2014). Tunable Staged Release of Therapeutics from Layer-by-Layer Coatings with Clay Interlayer Barrier. *Biomaterials*, 35(8), 2507–2517.
<https://doi.org/10.1016/j.biomaterials.2013.12.009>
- Miri, A. K., Mirzaee, I., Hassan, S., Mesbah Oskui, S., Nieto, D., Khademhosseini, A., & Zhang, Y. S. (2019). Effective bioprinting resolution in tissue model fabrication. *Lab on a Chip*, 19(11), 2019–2037.
<https://doi.org/10.1039/C8LC01037D>
- Moghaddam, A., Breier, L., Haubruck, P., Bender, D., Biglari, B., Wentzensen, A., & Zimmermann, G. (2016). Non-unions treated with bone morphogenic protein 7: Introducing the quantitative measurement of human serum cytokine levels as promising tool in evaluation of adjunct non-union therapy. *Journal of Inflammation (United Kingdom)*, 13(1), 1–9. <https://doi.org/10.1186/s12950-016-0111-x>
- Möller, J., Schroer, M. A., Erkamp, M., Grobelny, S., Paulus, M., Tiemeyer, S., Wirkert, F. J., Tolan, M., & Winter, R. (2012). The effect of ionic strength, temperature, and pressure on the interaction potential of dense protein solutions: From nonlinear pressure response to protein crystallization. *Biophysical Journal*, 102(11), 2641–2648. <https://doi.org/10.1016/j.bpj.2012.04.043>
- Mosiewicz, K. A., Kolb, L., Van Der Vlies, A. J., Martino, M. M., Lienemann, P. S., Hubbell, J. A., Ehrbar, M., & Lutolf, M. P. (2013). In situ cell manipulation through enzymatic hydrogel photopatterning. *Nature Materials*, 12(11), 1072–1078. <https://doi.org/10.1038/nmat3766>
- Mountziaris, P. M., & Mikos, A. G. (2008). Modulation of the Inflammatory Response for Enhanced Bone Tissue Regeneration. *Tissue Eng Part B Rev*, 14(2), 179–186. <https://doi.org/10.1089/ten.teb.2008.0038>
- Mourad, M. C. ., Wijnhoven, J. E. G. ., van 't Zand, D. ., van der Beek, D., & Lekkerkerker, H. N. . (2006). Gelation versus liquid crystal phase transitions in suspensions of plate-like particles. *Philosophical Transactions of the Royal Society A: Mathematical, Physical and Engineering Sciences*, 364(1847), 2807–2816. <https://doi.org/10.1098/rsta.2006.1856>
- Mourchid, A., Delville, A., Lambard, J., Lécolier, E., & Levitz, P. (1995). Phase Diagram of Colloidal Dispersions of Anisotropic Charged Particles: Equilibrium Properties, Structure, and Rheology of Laponite Suspensions. *Langmuir*, 11(6), 1942–1950. <https://doi.org/10.1021/la00006a020>
- Mourchid, A., Lécolier, E., Van Damme, H., & Levitz, P. (1998). On Viscoelastic, Birefringent, and Swelling Properties of Laponite Clay Suspensions: Revisited Phase Diagram. *Langmuir*, 14(17), 4718–4723.
<https://doi.org/10.1021/la980117p>
- Mousa, M., Evans, N. D., Oreffo, R. O. C., & Dawson, J. I. (2018). Clay nanoparticles for regenerative medicine and biomaterial design: A review of clay bioactivity. *Biomaterials*, 159, 204–214.

<https://doi.org/10.1016/j.biomaterials.2017.12.024>

- Mredha, M. T. I., Tran, V. T., Jeong, S. G., Seon, J. K., & Jeon, I. (2018). A diffusion-driven fabrication technique for anisotropic tubular hydrogels. *Soft Matter*, *14*(37), 7706–7713. <https://doi.org/10.1039/c8sm01235k>
- Muller, P., Rogers, K. W., Yu, S. R., Brand, M., & Schier, A. F. (2013). Morphogen transport. *Development*, *140*(8), 1621–1638. <https://doi.org/10.1242/dev.083519>
- Nakanishi, K., Sakiyama, T., & Imamura, K. (2001). On the adsorption of proteins on solid surfaces, a common but very complicated phenomenon. *Journal of Bioscience and Bioengineering*, *91*(3), 233–244. [https://doi.org/10.1016/S1389-1723\(01\)80127-4](https://doi.org/10.1016/S1389-1723(01)80127-4)
- Narita, T., Ohnishi, I., Tokita, M., & Oishi, Y. (2008). Macroscopic pattern formation of liquid crystal in κ -carrageenan gel. *Colloids and Surfaces A: Physicochemical and Engineering Aspects*, *321*(1–3), 117–120. <https://doi.org/10.1016/j.colsurfa.2008.01.037>
- Narita, T., & Tokita, M. (2006). Liesegang Pattern Formation in κ -Carrageenan Gel. *Langmuir*, *22*(1), 349–352. <https://doi.org/10.1021/la0522350>
- Nguyen, A. T., Sathe, S. R., & Yim, E. K. F. (2016). From nano to micro: topographical scale and its impact on cell adhesion, morphology and contact guidance. *Journal of Physics: Condensed Matter*, *28*(18), 183001. <https://doi.org/10.1088/0953-8984/28/18/183001>
- Nguyen, H. K., Prevosto, D., Labardi, M., Capaccioli, S., & Lucchesi, M. (2015). Irreversibly Adsorbed Layer in Supported Ultrathin Polymer Film Investigated by Local Dielectric Spectroscopy. In S. Napolitano (Ed.), *Non-equilibrium Phenomena in Confined Soft Matter: Irreversible Adsorption, Physical Aging and Glass Transition at the Nanoscale* (pp. 161–185). Springer International Publishing. https://doi.org/10.1007/978-3-319-21948-6_7
- Nicholson, C., & Syková, E. (1998). Extracellular space structure revealed by diffusion analysis. *Trends in Neurosciences*, *21*(5), 207–215. [https://doi.org/10.1016/S0166-2236\(98\)01261-2](https://doi.org/10.1016/S0166-2236(98)01261-2)
- O'Brien, F. J. (2011). Biomaterials & scaffolds for tissue engineering. *Materials Today*, *14*(3), 88–95. [https://doi.org/10.1016/S1369-7021\(11\)70058-X](https://doi.org/10.1016/S1369-7021(11)70058-X)
- Oftadeh, R., Perez-Viloria, M., Villa-Camacho, J. C., Vaziri, A., & Nazarian, A. (2015). Biomechanics and Mechanobiology of Trabecular Bone: A Review. *Journal of Biomechanical Engineering*, *137*(1), 1–15. <https://doi.org/10.1115/1.4029176>
- Ohshima, H. (2014). Interaction of colloidal particles. In *Colloid and Interface Science in Pharmaceutical Research and Development* (pp. 1–28). Elsevier. <https://doi.org/10.1016/B978-0-444-62614-1.00001-6>
- Oryan, A., Monazzah, S., & Bigham-Sadegh, A. (2015). Bone injury and fracture healing biology. *Biomedical and Environmental Sciences*, *28*(1), 57–71. <https://doi.org/10.3967/bes2015.006>
- Ovsianikov, A., Li, Z., Torgersen, J., Stampfl, J., & Liska, R. (2012). Selective Functionalization of 3D Matrices Via Multiphoton Grafting and Subsequent

- Click Chemistry. *Advanced Functional Materials*, 22(16), 3429–3433.
<https://doi.org/10.1002/adfm.201200419>
- Ozbolat, I. T., & Hospodiuk, M. (2016). Current advances and future perspectives in extrusion-based bioprinting. *Biomaterials*, 76, 321–343.
<https://doi.org/10.1016/j.biomaterials.2015.10.076>
- Page, D. J., Clarkin, C. E., Mani, R., Khan, N. A., Dawson, J. I., & Evans, N. D. (2019). Injectable nanoclay gels for angiogenesis. *Acta Biomaterialia*, 100(5), 378–387. <https://doi.org/10.1016/j.actbio.2019.09.023>
- Palmer, L., Newcomb, C., Kaltz, S., Spoerke, E., & Samuel, I. (2008). Biomimetic Systems for Hydroxyapatite Mineralization Inspired By Bone and Enamel Liam. *Chem Rev.*, 108(11), 4754–4783.
<https://doi.org/10.1021/cr8004422.Biomimetic>
- Park, C., Kim, H., Rhyu, I. J., & Uhm, C. (2016). How to get well-preserved samples for transmission electron microscopy. *Applied Microscopy*, 46(4), 188–192.
<https://doi.org/10.9729/AM.2016.46.4.188>
- Park, S.-J., & Seo, M.-K. (2011). Intermolecular Force. In *Interface Science and Technology* (Vol. 18, pp. 1–57). <https://doi.org/10.1016/B978-0-12-375049-5.00001-3>
- Parkinson, I. H., & Fazzalari, N. L. (2013). Characterisation of Trabecular Bone Structure. In M. J. Silva (Ed.), *Stud Mechanobiol Tissue Eng Biomater* (1st ed., Issue November 2010, pp. 31–51). Springer-Verlag Berlin Heidelberg.
https://doi.org/10.1007/8415_2011_113
- Patel, Z. S., Yamamoto, M., Ueda, H., Tabata, Y., & Mikos, A. G. (2008). Biodegradable gelatin microparticles as delivery systems for the controlled release of bone morphogenetic protein-2. *Acta Biomaterialia*, 4(5), 1126–1138.
<https://doi.org/10.1016/j.actbio.2008.04.002>
- Pathak, J., Priyadarshini, E., Rawat, K., & Bohidar, H. B. (2017). Complex coacervation in charge complementary biopolymers: Electrostatic versus surface patch binding. *Advances in Colloid and Interface Science*, 250, 40–53.
<https://doi.org/10.1016/j.cis.2017.10.006>
- Patil, J. S., Kamalapur, M. V., Marapur, S. C., & Kadam, D. V. (2010). Iontropic gelation and polyelectrolyte complexation: The novel techniques to design hydrogel particulate sustained, modulated drug delivery system: A review. *Digest Journal of Nanomaterials and Biostructures*, 5(1), 241–248.
- Petka, W. A. (1998). Reversible Hydrogels from Self-Assembling Artificial Proteins. *Science*, 281(5375), 389–392. <https://doi.org/10.1126/science.281.5375.389>
- Polo-Corrales, L., Latorre-Esteves, M., & Ramirez-Vick, J. E. (2014). Scaffold design for bone regeneration. *Journal of Nanoscience and Nanotechnology*, 14(1), 15–56. <https://doi.org/10.1166/jnn.2014.9127>
- Poon, B., Kha, T., Tran, S., & Dass, C. R. (2016). Bone morphogenetic protein-2 and bone therapy: Successes and pitfalls. *Journal of Pharmacy and Pharmacology*, 68(2), 139–147. <https://doi.org/10.1111/jphp.12506>
- Raj, T., & Flygare, W. H. (1974). Diffusion studies of bovine serum albumin by

- quasielastic light scattering. *Biochemistry*, 13(16), 3336–3340.
<https://doi.org/10.1021/bi00713a024>
- Ralla, K., Sohling, U., Riechers, D., Kasper, C., Ruf, F., & Scheper, T. (2010). Adsorption and separation of proteins by a smectitic clay mineral. *Bioprocess and Biosystems Engineering*, 33(7), 847–861. <https://doi.org/10.1007/s00449-010-0408-8>
- Raspopovic, J. (2014). *No Title {TL} - 566. 566 {VN}-(6196)*, 10–15.
<https://doi.org/10.5061/dryad.jm6pj>
- Rawat, K., Agarwal, S., Tyagi, A., Verma, A. K., & Bohidar, H. B. (2014). Aspect Ratio Dependent Cytotoxicity and Antimicrobial Properties of Nanoclay. *Applied Biochemistry and Biotechnology*, 174(3), 936–944.
<https://doi.org/10.1007/s12010-014-0983-2>
- Reddi, A. H. (2003). Cartilage morphogenetic proteins: role in joint development, homeostasis, and regeneration. *Annals of the Rheumatic Diseases*, 62 Suppl 2(Suppl 2), ii73–ii78. https://doi.org/10.1136/ard.62.suppl_2.ii73
- Reznikov, N., Shahar, R., & Weiner, S. (2014). Bone hierarchical structure in three dimensions. *Acta Biomaterialia*, 10(9), 3815–3826.
<https://doi.org/10.1016/j.actbio.2014.05.024>
- Roberts, T. T., & Rosenbaum, A. J. (2012). Bone grafts, bone substitutes and orthobiologics: the bridge between basic science and clinical advancements in fracture healing. *Organogenesis*, 8(4), 114–124.
<https://doi.org/10.4161/org.23306>
- Rodríguez-Cabello, J. C., Martín, L., Alonso, M., Arias, F. J., & Testera, A. M. (2009). “Recombinamers” as advanced materials for the post-oil age. *Polymer*, 50(22), 5159–5169. <https://doi.org/10.1016/j.polymer.2009.08.032>
- Ruedinger, F., Lavrentieva, A., Blume, C., Pepelanova, I., & Scheper, T. (2015). Hydrogels for 3D mammalian cell culture: a starting guide for laboratory practice. *Applied Microbiology and Biotechnology*, 99(2), 623–636.
<https://doi.org/10.1007/s00253-014-6253-y>
- Ruzicka, B., Zaccarelli, E., Zulian, L., Angelini, R., Sztucki, M., Moussaïd, A., Narayanan, T., & Sciortino, F. (2010). Observation of empty liquids and equilibrium gels in a colloidal clay. *Nature Materials*, 10(1), 56–60.
<https://doi.org/10.1063/1.4794601>
- Ruzicka, Barbara, & Zaccarelli, E. (2011). A fresh look at the Laponite phase diagram. *Soft Matter*, 7(4), 1268. <https://doi.org/10.1039/c0sm00590h>
- Sabet, F. A., Raeisi Najafi, A., Hamed, E., & Jasiuk, I. (2016). Modelling of bone fracture and strength at different length scales: a review. *Interface Focus*, 6(1), 20150055. <https://doi.org/10.1098/rsfs.2015.0055>
- Sacco, P., Paoletti, S., Cok, M., Asaro, F., Abrami, M., Grassi, M., & Donati, I. (2016). Insight into the ionotropic gelation of chitosan using tripolyphosphate and pyrophosphate as cross-linkers. *International Journal of Biological Macromolecules*, 92, 476–483. <https://doi.org/10.1016/j.ijbiomac.2016.07.056>
- Sakr, O. S., Jordan, O., & Borchard, G. (2016). Sustained protein release from

- hydrogel microparticles using layer-by-layer (LbL) technology. *Drug Delivery*, 23(8), 2747–2755. <https://doi.org/10.3109/10717544.2015.1069422>
- Samorezov, J. E., & Alsberg, E. (2015). Spatial regulation of controlled bioactive factor delivery for bone tissue engineering. *Advanced Drug Delivery Reviews*, 84, 45–67. <https://doi.org/10.1016/j.addr.2014.11.018>
- Santo, V. E., Gomes, M. E., Mano, J. F., & Reis, R. L. (2012). From nano- to macro-scale: nanotechnology approaches for spatially controlled delivery of bioactive factors for bone and cartilage engineering. *Nanomedicine*, 7(7), 1045–1066. <https://doi.org/10.2217/nmm.12.78>
- Sanz-Ezquerro, J. J., Münsterberg, A. E., & Stricker, S. (2017). Editorial: Signaling Pathways in Embryonic Development. *Frontiers in Cell and Developmental Biology*, 5(76), 1–3. <https://doi.org/10.3389/fcell.2017.00076>
- Sawala, A., Sutcliffe, C., & Ashe, H. L. (2012). Multistep molecular mechanism for Bone morphogenetic protein extracellular transport in the Drosophila embryo. *Proceedings of the National Academy of Sciences*, 109(28), 11222–11227. <https://doi.org/10.1073/pnas.1202781109>
- Scheufler, C., Sebald, W., & Hülsmeier, M. (1999). Crystal structure of human bone morphogenetic protein-2 at 2.7 Å resolution. *Journal of Molecular Biology*, 287(1), 103–115. <https://doi.org/10.1006/jmbi.1999.2590>
- Schuster, E., Eckardt, J., Hermansson, A. M., Larsson, A., Lorén, N., Altskär, A., & Ström, A. (2014). Microstructural, mechanical and mass transport properties of isotropic and capillary alginate gels. *Soft Matter*, 10(2), 357–366. <https://doi.org/10.1039/c3sm52285g>
- Semenov, S. N., Markvoort, A. J., Gevers, W. B. L., Piruska, A., De Greef, T. F. A., & Huck, W. T. S. (2013). Ultrasensitivity by molecular titration in spatially propagating enzymatic reactions. *Biophysical Journal*, 105(4), 1057–1066. <https://doi.org/10.1016/j.bpj.2013.07.002>
- Setiawati, R., & Rahardjo, P. (2018). Osteogenesis and Bone Regeneration. In Haisheng Yang (Ed.), *IntechOpen*. <https://doi.org/10.5772/intechopen.82452>
- Shadish, J. A., Benuska, G. M., & DeForest, C. A. (2019). Bioactive site-specifically modified proteins for 4D patterning of gel biomaterials. *Nature Materials*, 18(9), 1005–1014. <https://doi.org/10.1038/s41563-019-0367-7>
- Shah, N. J., Macdonald, M. L., Beben, Y. M., Padera, R. F., Samuel, R. E., & Hammond, P. T. (2011). Tunable dual growth factor delivery from polyelectrolyte multilayer films. *Biomaterials*, 32(26), 6183–6193. <https://doi.org/10.1016/j.biomaterials.2011.04.036>
- Shahin, A., & Joshi, Y. M. (2010). Irreversible aging dynamics and generic phase behavior of aqueous suspensions of laponite. *Langmuir*, 26(6), 4219–4225. <https://doi.org/10.1021/la9032749>
- Shahin, A., & Joshi, Y. M. (2011). Interface-Induced Anisotropy and the Nematic Glass/Gel State in Jammed Aqueous Laponite Suspensions. *Langmuir*, 27(23), 14045–14052. <https://doi.org/10.1021/la202398v>
- Shen, B., Bhargav, D., Wei, A., Williams, L. A., Tao, H., Ma, D. D. F., & Diwan, A.

- D. (2009). BMP-13 emerges as a potential inhibitor of bone formation. *International Journal of Biological Sciences*, 5(2), 192–200. <https://doi.org/10.7150/ijbs.5.192>
- Shi, P., Kim, Y. H., Mousa, M., Sanchez, R. R., Oreffo, R. O. C., & Dawson, J. I. (2018). Self-Assembling Nanoclay Diffusion Gels for Bioactive Osteogenic Microenvironments. *Advanced Healthcare Materials*, 7(15), 1–11. <https://doi.org/10.1002/adhm.201800331>
- Simonson, T., & Brooks, C. L. (1996). Charge screening and the dielectric constant of proteins: Insights from molecular dynamics. *Journal of the American Chemical Society*, 118(35), 8452–8458. <https://doi.org/10.1021/ja960884f>
- Skjåk-Bræk, G., Grasdalen, H., & Smidsrød, O. (1989). Inhomogeneous polysaccharide ionic gels. *Carbohydrate Polymers*, 10(1), 31–54. [https://doi.org/10.1016/0144-8617\(89\)90030-1](https://doi.org/10.1016/0144-8617(89)90030-1)
- Spicer, C. D., Pashuck, E. T., & Stevens, M. M. (2018). Achieving Controlled Biomolecule-Biomaterial Conjugation [Review-article]. *Chemical Reviews*, 118(16), 7702–7743. <https://doi.org/10.1021/acs.chemrev.8b00253>
- Suliman, S., Xing, Z., Wu, X., Xue, Y., Pedersen, T. O., Sun, Y., Døskeland, A. P., Nickel, J., Waag, T., Lygre, H., Finne-Wistrand, A., Steinmüller-Nethl, D., Krueger, A., & Mustafa, K. (2015). Release and bioactivity of bone morphogenetic protein-2 are affected by scaffold binding techniques in vitro and in vivo. *Journal of Controlled Release*, 197, 148–157. <https://doi.org/10.1016/j.jconrel.2014.11.003>
- Talbot, M. J., & White, R. G. (2013). Methanol fixation of plant tissue for Scanning Electron Microscopy improves preservation of tissue morphology and dimensions. *Plant Methods*, 9(1), 1–7. <https://doi.org/10.1186/1746-4811-9-36>
- Tanaka, H., Jabbari-Farouji, S., Meunier, J., & Bonn, D. (2005). Kinetics of ergodic-to-nonergodic transitions in charged colloidal suspensions: Aging and gelation. *Physical Review E*, 71(2), 1–10. <https://doi.org/10.1103/PhysRevE.71.021402>
- Tanaka, Hajime, Meunier, J., & Bonn, D. (2004). Nonergodic states of charged colloidal suspensions: Repulsive and attractive glasses and gels. *Physical Review E*, 69(3), 031404. <https://doi.org/10.1103/PhysRevE.69.031404>
- Tannoury, C., & An, H. (2014). Complications with the use of bone morphogenetic protein 2 (BMP-2) in spine surgery. *The Spine Journal*, 14(3), 552–559. <https://doi.org/10.1016/j.spinee.2013.08.060>
- Thiruvengadathan, R., Korampally, V., Ghosh, A., Chanda, N., Gangopadhyay, K., & Gangopadhyay, S. (2013). Nanomaterial processing using self-assembly-bottom-up chemical and biological approaches. *Reports on Progress in Physics*, 76(6), 066501. <https://doi.org/10.1088/0034-4885/76/6/066501>
- Thyparambil, A. A., Wei, Y., & Latour, R. A. (2015). Experimental characterization of adsorbed protein orientation, conformation, and bioactivity. *Biointerphases*, 10(1), 019002. <https://doi.org/10.1116/1.4906485>
- Tickle, C. (1999). Morphogen gradients in vertebrate limb development. *Seminars in Cell and Developmental Biology*, 10(3), 345–351.

<https://doi.org/10.1006/scdb.1999.0294>

- Timin, A. S., Gould, D. J., & Sukhorukov, G. B. (2017). Multi-layer microcapsules: fresh insights and new applications. *Expert Opinion on Drug Delivery*, *14*(5), 583–587. <https://doi.org/10.1080/17425247.2017.1285279>
- Tomás, H., Alves, C. S., & Rodrigues, J. (2018a). Laponite®: A key nanoplatform for biomedical applications? *Nanomedicine: Nanotechnology, Biology, and Medicine*, *14*(7), 2407–2420. <https://doi.org/10.1016/j.nano.2017.04.016>
- Tomás, H., Alves, C. S., & Rodrigues, J. (2018b). *Laponite ® : A key nanoplatform for biomedical applications ? 14*, 2407–2420. <https://doi.org/10.1016/j.nano.2017.04.016>
- Torgersen, J., Qin, X. H., Li, Z., Ovsianikov, A., Liska, R., & Stampfl, J. (2013). Hydrogels for two-photon polymerization: A toolbox for mimicking the extracellular matrix. *Advanced Functional Materials*, *23*(36), 4542–4554. <https://doi.org/10.1002/adfm.201203880>
- Trappe, V., Prasad, V., Cipelletti, L., Segre, P. N., & Weitz, D. A. (2001). Jamming phase diagram for attractive particles. *Nature*, *411*(6839), 772–775. <https://doi.org/10.1038/35081021>
- Tsuji, K., Bandyopadhyay, A., Harfe, B. D., Cox, K., Kakar, S., Gerstenfeld, L., Einhorn, T., Tabin, C. J., & Rosen, V. (2006). BMP2 activity, although dispensable for bone formation, is required for the initiation of fracture healing. *Nature Genetics*, *38*(12), 1424–1429. <https://doi.org/10.1038/ng1916>
- Turing, A. M. (1952). The chemical basis of morphogenesis. *Philosophical Transactions of the Royal Society of London. Series B, Biological Sciences*, *237*(641), 37–72. <https://doi.org/10.1098/rstb.1952.0012>
- U.S. Dept. of HHS. (2004). Bone health and osteoporosis: a report of the Surgeon General. *US Health and Human Services*, 437. <https://www.ncbi.nlm.nih.gov/books/NBK45513/>
- Uludag, H., D’Augusta, D., Palmer, R., Timony, G., & Wozney, J. (1999). Characterization of rhBMP-2 pharmacokinetics implanted with biomaterial carriers in the rat ectopic model. *Journal of Biomedical Materials Research*, *46*(2), 193–202. [https://doi.org/10.1002/\(SICI\)1097-4636\(199908\)46:2<193::AID-JBM8>3.0.CO;2-1](https://doi.org/10.1002/(SICI)1097-4636(199908)46:2<193::AID-JBM8>3.0.CO;2-1)
- Urist, M. R. (1965). Bone : Formation by Autoinduction. *Science*, *150*(3698), 893–899. <https://doi.org/10.1126/science.150.3698.893>
- Urist, M. R., & Strates, B. S. (1971). Bone Morphogenetic protein. *Journal of Dental Research*, *50*(6), 1392–1406. <https://doi.org/10.1177/00220345710500060601>
- Vaccaro, A. R., Whang, P. G., Patel, T., Phillips, F. M., Greg, D., Albert, T. J., Hilibrand, A. S., Brower, R. S., Kurd, M. F., Appannagari, A., Patel, M., & Fischgrund, J. S. (2008). The safety and efficacy of OP-1 (rhBMP-7) as a replacement for iliac crest autograft for posterolateral lumbar arthrodesis : minimum 4-year follow-up of a pilot study. *The Spine Journal*, *8*(3), 457–465. <https://doi.org/10.1016/j.spinee.2007.03.012>
- Van Vlierberghe, S., Dubruel, P., & Schacht, E. (2011). Biopolymer-based hydrogels

- as scaffolds for tissue engineering applications: A review. *Biomacromolecules*, *12*(5), 1387–1408. <https://doi.org/10.1021/bm200083n>
- Vander Straeten, A., Bratek-Skicki, A., Germain, L., D’Haese, C., Eloy, P., Fustin, C. A., & Dupont-Gillain, C. (2017). Protein-polyelectrolyte complexes to improve the biological activity of proteins in layer-by-layer assemblies. *Nanoscale*, *9*(44), 17186–17192. <https://doi.org/10.1039/c7nr04345g>
- Vermonden, T., Censi, R., & Hennink, W. E. (2012). Hydrogels for protein delivery. *Chemical Reviews*, *112*(5), 2853–2888. <https://doi.org/10.1021/cr200157d>
- Vincent, J. F. V. (2008). Biomimetic materials chemistry. *Biochimie*, *23*(12), 3140–3147. [https://doi.org/10.1016/0300-9084\(96\)89517-4](https://doi.org/10.1016/0300-9084(96)89517-4)
- Vitkin, I., Laszlo, R., & Whyman, C. (2002). Effects of molecular asymmetry of optically active molecules on the polarization properties of multiply scattered light. *Optics Express*, *10*(4), 222. <https://doi.org/10.1364/OE.10.000222>
- Von Bubnoff, A., Peiffer, D. A., Blitz, I. L., Hayata, T., Ogata, S., Zeng, Q., Trunnell, M., & Cho, K. W. Y. (2005). Phylogenetic footprinting and genome scanning identify vertebrate BMP response elements and new target genes. *Developmental Biology*, *281*(2), 210–226. <https://doi.org/10.1016/j.ydbio.2005.02.014>
- Voo, W.-P., Ooi, C.-W., Islam, A., Tey, B.-T., & Chan, E.-S. (2016). Calcium alginate hydrogel beads with high stiffness and extended dissolution behaviour. *European Polymer Journal*, *75*, 343–353. <https://doi.org/10.1016/j.eurpolymj.2015.12.029>
- Walmsley, G. G., Mcardle, A., Tevlin, R., Momeni, A., Atashroo, D., Hu, M. S., Feroze, A. H., Wong, V. W., Lorenz, P. H., Longaker, M. T., Wan, D. C., & Surgery, R. (2015). Nanotechnology in bone tissue engineering. *Nanomedicine*, *11*(5), 1253–1263. <https://doi.org/10.1016/j.nano.2015.02.013>. Nanotechnology
- Wang, Q., Mynar, J. L., Yoshida, M., Lee, E., Lee, M., Okuro, K., Kinbara, K., & Aida, T. (2010). High-water-content mouldable hydrogels by mixing clay and a dendritic molecular binder. *Nature*, *463*, 339–343. <https://doi.org/10.1038/nature08693>
- Wang, S., Wu, Y., Guo, R., Huang, Y., Wen, S., Shen, M., Wang, J., & Shi, X. (2013). Laponite nanodisks as an efficient platform for doxorubicin delivery to cancer cells. *Langmuir*, *29*(16), 5030–5036. <https://doi.org/10.1021/la4001363>
- Wang, X., Nyman, J. S., & Reyes, M. (2010). *Fundamental Biomechanics in Bone Tissue Engineering* (K. A. Athanasiou (ed.)). Morgan & Claypool.
- Weatherholt, A. M., Fuchs, R. K., & Warden, S. J. (2013). Specialized connective tissue: bone, the structural framework of the upper extremity. *J Hand Ther*, *25*(2), 123–132. <https://doi.org/10.1016/j.jht.2011.08.003>. Specialized
- Wei, G., Jin, Q., Giannobile, W. V., & Ma, P. X. (2007). The enhancement of osteogenesis by nano-fibrous scaffolds incorporating rhBMP-7 nanospheres. *Biomaterials*, *28*(12), 2087–2096. <https://doi.org/10.1016/j.biomaterials.2006.12.028>
- Weiner, S., & Wagner, H. D. (1998). THE MATERIAL BONE: Structure-

- Mechanical Function Relations. *Annu. Rev. Mater. Sci*, 28, 271–298.
<https://doi.org/10.1146/annurev.matsci.28.1.271>
- Weiner, Stephen, & Addadi, L. (1997). Design strategies in mineralized biological materials. *Journal of Materials Chemistry*, 7(5), 689–702.
<https://doi.org/10.1039/a604512j>
- Wen, X., Sh, D., & Zhang, N. (2005). Applications of Nanotechnology in Tissue Engineering. In H. S. Nalwa (Ed.), *Handbook of Nanostructured Biomaterials and Their Applications in Nanobiotechnology* (Vol. 1, pp. 1–22). American Scientific Publishers.
- Whitesides, G. M., & Boncheva, M. (2002). Beyond molecules: Self-assembly of mesoscopic and macroscopic components. *Proceedings of the National Academy of Sciences*, 99(8), 4769–4774.
<https://doi.org/10.1073/pnas.082065899>
- Whitesides, G., Mathias, J., & Seto, C. (1991). Molecular self-assembly and nanochemistry: a chemical strategy for the synthesis of nanostructures. *Science*, 254(5036), 1312–1319. <https://doi.org/10.1126/science.1962191>
- Williams, R., Ryves, W. J., Dalton, E. C., Eickholt, B., Shaltiel, G., Agam, G., & Harwood, A. J. (2004). A molecular cell biology of lithium. *Biochemical Society Transactions*, 32(5), 799–802. <https://doi.org/10.1042/BST0320799>
- Wilson, C. G., Martín-Saavedra, F. M., Vilaboa, N., & Franceschi, R. T. (2013). Advanced BMP gene therapies for temporal and spatial control of bone regeneration. *Journal of Dental Research*, 92(5), 409–417.
<https://doi.org/10.1177/0022034513483771>
- Wosnick, J. H., & Shoichet, M. S. (2008). Three-dimensional chemical patterning of transparent hydrogels. *Chemistry of Materials*, 20(1), 55–60.
<https://doi.org/10.1021/cm071158m>
- Wu, Z. L., Takahashi, R., Sawada, D., Arifuzzaman, M., Nakajima, T., Kurokawa, T., Hu, J., & Gong, J. P. (2014). In situ observation of Ca²⁺ diffusion-induced superstructure formation of a rigid polyanion. *Macromolecules*, 47(20), 7208–7214. <https://doi.org/10.1021/ma501699d>
- Wylie, R. G., Ahsan, S., Aizawa, Y., Maxwell, K. L., Morshead, C. M., & Shoichet, M. S. (2011). Spatially controlled simultaneous patterning of multiple growth factors in three-dimensional hydrogels. *Nature Materials*, 10(10), 799–806.
<https://doi.org/10.1038/nmat3101>
- Xu, C., Breedveld, V., & Kopeček, J. (2005). Reversible hydrogels from self-assembling genetically engineered protein block copolymers. *Biomacromolecules*, 6(3), 1739–1749. <https://doi.org/10.1021/bm050017f>
- Yamamoto, T., Tomita, N., Maki, Y., & Dobashi, T. (2010). Dynamics in the process of formation of anisotropic chitosan hydrogel. *Journal of Physical Chemistry B*, 114(31), 10002–10009. <https://doi.org/10.1021/jp102207w>
- Yan, D., & Lin, X. (2009). Shaping Morphogen Gradients by Proteoglycans. *Cold Spring Harbor Perspectives in Biology*, 1(3), a002493.
<https://doi.org/10.1101/cshperspect.a002493>

- Yang, C.-H., Wang, C.-Y., Huang, K.-S., Yeh, C.-S., Wang, A. H.-J., Wang, W.-T., & Lin, M.-Y. (2012). Facile Synthesis of Radial-Like Macroporous Superparamagnetic Chitosan Spheres with In-Situ Co-Precipitation and Gelation of Ferro-Gels. *PLoS ONE*, 7(11), e49329. <https://doi.org/10.1371/journal.pone.0049329>
- Yang, D., Moon, S., & Lee, D.-W. (2017). Surface Modification of Titanium with BMP-2/GDF-5 by a Heparin Linker and Its Efficacy as a Dental Implant. *International Journal of Molecular Sciences*, 18(1), 229. <https://doi.org/10.3390/ijms18010229>
- Yang, J., Shi, P., Tu, M., Wang, Y., Liu, M., Fan, F., & Du, M. (2014). Bone morphogenetic proteins: Relationship between molecular structure and their osteogenic activity. *Food Science and Human Wellness*, 3(3–4), 127–135. <https://doi.org/10.1016/j.fshw.2014.12.002>
- Yoshizawa, S., Brown, A., Barchowsky, A., & Sfeir, C. (2014). Magnesium ion stimulation of bone marrow stromal cells enhances osteogenic activity, simulating the effect of magnesium alloy degradation. *Acta Biomaterialia*, 10(6), 2834–2842. <https://doi.org/10.1016/j.actbio.2014.02.002>
- Yu, W. H., Li, N., Tong, D. S., Zhou, C. H., Lin, C. X. (Cynthia), & Xu, C. Y. (2013). Adsorption of proteins and nucleic acids on clay minerals and their interactions: A review. *Applied Clay Science*, 80–81, 443–452. <https://doi.org/10.1016/j.clay.2013.06.003>
- Yu, Y. Y., Lieu, S., Lu, C., Miclau, T., Marcucio, R. S., & Colnot, C. (2010). Immunolocalization of BMPs, BMP antagonists, receptors, and effectors during fracture repair. *Bone*, 46(3), 841–851. <https://doi.org/10.1016/j.bone.2009.11.005>
- Zagorski, M., Tabata, Y., Brandenberg, N., Lutolf, M. P., Tkačik, G., Bollenbach, T., Briscoe, J., & Kicheva, A. (2017). Decoding of position in the developing neural tube from antiparallel morphogen gradients. *Science*, 356(6345), 1379–1383. <https://doi.org/10.1126/science.aam5887>
- Zara, J. N., Siu, R. K., Zhang, X., Shen, J., Ngo, R., Lee, M., Li, W., Chiang, M., Chung, J., Kwak, J., Wu, B. M., Ting, K., & Soo, C. (2011). High Doses of Bone Morphogenetic Protein 2 Induce Structurally Abnormal Bone and Inflammation In Vivo. *Tissue Engineering Part A*, 17(9–10), 1389–1399. <https://doi.org/10.1089/ten.tea.2010.0555>
- Zhang, X., Hansing, J., Netz, R. R., & Derouchey, J. E. (2015). Particle transport through hydrogels is charge asymmetric. *Biophysical Journal*, 108(3), 530–539. <https://doi.org/10.1016/j.bpj.2014.12.009>
- Zhao, W., Jin, X., Cong, Y., Liu, Y., & Fu, J. (2013). Degradable natural polymer hydrogels for articular cartilage tissue engineering. *Journal of Chemical Technology and Biotechnology*, 88(3), 327–339. <https://doi.org/10.1002/jctb.3970>
- Zhou, S., Lo, W., Suhaimi, J. L., Digman, M. A., Gratton, E., & Nie, Q. (2012). Article Free Extracellular Diffusion Creates the Dpp Morphogen Gradient of the Drosophila Wing Disc. *Current Biology*, 22(8), 668–675.

<https://doi.org/10.1016/j.cub.2012.02.065>

Ziemecka, I., Koper, G. J. M., Olive, A. G. L., & Van Esch, J. H. (2013). Chemical-gradient directed self-assembly of hydrogel fibers. *Soft Matter*, 9(5), 1556–1561. <https://doi.org/10.1039/c2sm27095a>

Zuniga, A., & Zeller, R. (2014). In Turing's hands--the making of digits. *Science*, 345(6196), 516–517. <https://doi.org/10.1126/science.1257501>